

TECHNISCHE UNIVERSITÄT MÜNCHEN

TUM School of Natural Sciences

**Investigation of the Evolution from
Nanostructured Metal Clusters to Thin
Metal Films on Diblock Copolymer
Templates**

Marc Gensch, M.Sc.

Vollständiger Abdruck der von der TUM School of Natural Sciences der Technischen Universität München zur Erlangung des akademischen Grades eines

Doktors der Naturwissenschaften (Dr. rer. nat.)

genehmigten Dissertation.

Vorsitzender: Prof. Dr. Martin Zacharias

Prüfer der Dissertation: 1. Prof. Dr. Peter Müller-Buschbaum
2. Prof. Dr. Friedrich C. Simmel

Die Dissertation wurde am 06.12.2022 bei der Technischen Universität München eingereicht und durch die TUM School of Natural Sciences am 02.02.2023 angenommen.

Abstract

The present work investigates the metal growth on diblock copolymer templates. It compares the growth with that on corresponding homopolymers in order to reveal a deeper understanding of the metal-polymer interaction between the first appearing metal clusters and the polymer template and the chemical interactions. The focus is on *in situ* X-ray scattering methods to follow the metal cluster formation during sputter deposition and their size evolution to model the metal cluster growth on different copolymer films, namely polystyrene-block-poly(methyl methacrylate) (PS-*b*-PMMA) and poly(methyl methacrylate)-block-poly(3-hexylthiophene-2,5-diyl) (PMMA-*b*-P3HT). The formation, cluster sizes and shapes are additionally confirmed by complementary microscopy methods. The chemical interaction of the metal-polymer interface defines the resulting nanostructure and the later emerging nanogranular layer. The electrical and optical properties are followed during the sputter deposition and are affected by different metal and polymer types and the insular-to-metal transition, while showing plasmonic effects in the early stages of cluster growth. The results will offer the possibility to tailor distinct metal cluster layers for sensors, electrodes, organic photovoltaic applications and organic electronics using polymer template-guided sputter deposition.

Zusammenfassung

Die vorliegende Arbeit untersucht das Metallwachstum auf Diblock Copolymer Templaten. Das Wachstum wird mit den auf Homopolymeren in Beziehung gesetzt, um ein tieferes Verständnis der Metall-Polymer-Wechselwirkung und des Metallwachstums zu erlangen. Der Schwerpunkt liegt auf *In situ* Röntgenstreuungsmethoden, um die Metallcluster Bildung und deren Wachstumsentwicklung zu verfolgen. Dieses Wachstum wird auf verschiedenen Copolymer Typen wie z.B. polystyrol-block-polymethylmethacrylat (PS-*b*-PMMA) und polymethylmethacrylat-block-poly(3-hexylthiophene-2,5-diyl) (PMMA-*b*-P3HT) untersucht und Wachstumsmodelle entwickelt. Die Anordnung der Cluster, die Clustergrößen und -formen werden zusätzlich durch ergänzende mikroskopische Methoden bestätigt. Die chemischen Spektren für die frühe Metall-Polymer-Wechselwirkung zeigt einen hohen Einfluss der chemischen Verbindungen auf die resultierende Nanostruktur und deren späteren entstehenden nanogranularen Schicht. Die elektrischen und optischen Eigenschaften werden während der Sputterabscheidung verfolgt und zeigt für verschiedene Metall- und Polymertypen eine Auswirkung des Übergangs von der Metallcluster Bildung zum dünnen leitfähigen Metallfilm. Die optischen Eigenschaften während der Metallabscheidung zeigt für verschiedene Ag- und Al-Cluster in den frühen Wachstumsstadien

plasmonische Effekte. Die Ergebnisse werden dazu beitragen, maßgeschneiderte Metallclusterschichten mithilfe der Sputterdeposition für Sensoren, Elektroden, organische photovoltaische Anwendungen und organische Elektronik zu entwickeln.

Contents

List of abbreviations	vii
1. Introduction	1
2. Theoretical aspects	7
2.1. Polymer Fundamentals	7
2.1.1. Polymer Principles	7
2.1.2. Phase Separation	8
2.1.3. Diblock Copolymers	9
2.1.4. Semi-Conducting Polymers	11
2.2. Sputter Deposition	14
2.2.1. Fundamentals	15
2.2.2. Radio frequency (RF) vs. Magnetron Sputtering	16
2.2.3. Thin Film Formation	18
2.3. Scattering Basics	20
2.3.1. X-ray Introduction	21
2.3.2. Grazing-Incidence Small-Angle X-ray Scattering (GISAXS)	27
2.3.3. Grazing-Incidence Wide-Angle X-ray Scattering (GIWAXS)	30
3. Characterization methods	33
3.1. Imaging Methods	33
3.1.1. Atomic force microscopy (AFM)	33
3.1.2. Scanning electron microscope (SEM)	35
3.2. Spectroscopic Methods	37
3.2.1. X-ray photoelectron spectroscopy (XPS)	37
3.2.2. Fourier-transform infrared (FTIR) spectroscopy	38
3.2.3. Ultraviolet–visible (UV-vis) spectroscopy	39
3.3. Electronic Methods	42
3.3.1. Resistance Measurements	42
3.4. Scattering Methods	44
3.4.1. GISAXS	44

3.4.2. GIWAXS	46
4. Sample preparation	49
4.1. Materials	49
4.1.1. Substrate Materials	49
4.1.2. Polymers	50
4.1.3. Metals	53
4.2. Thin Film Preparation	53
4.2.1. Substrate Cleaning	54
4.2.2. Spin-Coating	54
4.2.3. Solvent Vapor Annealing	56
4.2.4. Metal Sputter Deposition	56
5. Sputter Deposition of Nanogranular Ag Layers during on PS-<i>b</i>-PMMA	61
5.1. Microscopic analysis of polymer-template assisted Ag growth	63
5.1.1. AFM, FESEM and <i>ex-situ</i> GISAXS analysis	63
5.2. Chemical interaction of the metal with the polymer	70
5.2.1. XPS and FTIR analysis	70
5.3. <i>In situ</i> GISAXS and resistivity measurements on different polymer templates	75
5.4. Correlation of the optical relative reflectance change and Ag growth on PS- <i>b</i> -PMMA	83
5.5. Summary	85
6. Selective Ag Nanocluster Metallization on Partially Conjugated PMMA-<i>b</i>- P3HT Templates	87
6.1. Topography characterization	89
6.1.1. AFM, SAXS, WAXS and static GISAXS analysis	89
6.1.2. FESEM analysis	97
6.2. Surface chemistry characterization	100
6.2.1. XPS and FTIR analysis	100
6.3. In situ GISAXS on different polymer templates	107
6.4. Summary	118
7. Aluminum Nanocluster Layers Growing on Partially Conjugated PMMA-<i>b</i>- P3HT Templates	119
7.1. Optical reflectance and morphology change during sputter deposition . . .	121
7.2. Chemical interaction of Al with the polymer components	124
7.3. Scattering analysis	130
7.4. Comparison of the Al decoration on the polymer types	134

7.5. Growth model	140
7.6. Summary	142
8. Selective Wetting of Au versus Ag on PLA-<i>b</i>-P3HT Templates	143
8.1. Morphological comparison of Au and Ag on PLA- <i>b</i> -P3HT with AFM . . .	143
8.2. Morphological comparison of Au and Ag on PLA- <i>b</i> -P3HT with GISAXS .	146
8.3. Summary	149
9. Conclusion and outlook	151
A. Appendix chapter 4	155
B. Appendix chapter 5	159
C. Appendix chapter 7	163
Bibliography	169
List of publications	193
Acknowledgements	199

List of abbreviations

2D-FFT	2D-fast fourier transformation
AFM	atomic force microscopy
BHJ	bulk-heterojunction
D_{ptv}	peak-to-valley distance
DBC	diblock copolymer
DWBA	distorted wave Born approximation
FTIR	Fourier transformed infrared spectroscopy
FWHM	full width at half maximum
GISAXS	grazing-incidence small angle x-ray scattering
GIWAXS	grazing-incidence wide angle x-ray scattering
HOMO	highest occupied molecular orbital
IMT	insulator-to-metal transition
LMA	local monodisperse approximation
LUMO	lowest unoccupied molecular orbital
ODT	order disorder transition
P(LA- <i>b</i> -3HT)	poly(lactide- <i>block</i> -3-hexyl thiophene)
P(MMA- <i>b</i> -3HT)	poly(methyl methacrylate- <i>block</i> -3-hexyl thiophene)
P(S- <i>b</i> -MMA)	poly(styrene- <i>block</i> -methyl methacrylate)
P3HT	poly(3-hexyl-thiophene), $(C_{10}H_{14}S)_n$
PLA	polylactide, $(C_3H_4O_2)_n$

PMMA	poly(methyl methacrylate), $(C_5H_8O_2)_n$
PS	polystyrene, $(C_8H_8)_n$
QCM	quartz crystal microbalance
SDD	sample-detector distance
SEM	scanning electron microscopy
SSL	strong segregation limit
SVA	solvent vapor annealing
UV-vis	UV-vis spectroscopy
WSL	weak segregation limit
XPS	x-ray photoelectron spectroscopy

1. Introduction

Diblock copolymer (DBC) templates are used for a variety of applications e.g. nanolithography, drug delivery systems, templating of nanoparticles, photovoltaics, battery applications and sensors. [1–16] Controlling the structure of the metal clusters, the polymer template or both on the nanoscale allows for tailoring the optical and electrical properties for the fabrication of more efficient organic electronics such as transistors, electrodes or photovoltaics. [17–21] The metal nanostructures control the localized plasmonic effects, where the incoming electromagnetic light excites plasmons, and therefore the conduction band electrons inside the metal nanoparticles oscillate coherently. [22, 23] The sizes of the metal clusters must be smaller than the wavelength of the incoming light. The importance of the nanoscale dimensions for optical and electronic devices is of high interest for industry to fabricate more efficient and smaller devices in future with high control of the resulting nanostructure of the metal, polymer and other inorganic layers. This can be used e.g. for sensor applications and for the enhancement of the performance of organic photovoltaics. [19, 24–26]

The devices consist of different layers stacked together: the layers may be organic, inorganic or for most devices a mixture of organic and inorganic layers. The contact, intermixing and therefore the interfaces between these layers, plays a crucial role for the overall performance and stability of the device. [17, 27–34] The influence of the interfaces between the thin stacked films, which are prepared with different techniques e.g. lithography, physical vapor deposition (PVD), chemical vapor deposition (CVD), electrochemical deposition, evaporation, etching and further methods, need to be well understood. [35–40] At the same time, thinking of scale-up, the limitations of lithography are the boundary conditions concerning large-scale nanostructure fabrication and the production costs for real-world applications. Self-assembly is an alternative method to save money and time for the fabrication, and DBCs can help by their self-assembly ability for the preparation of specific structures e.g. for interface control in the organic layers. [2, 6, 11, 13, 41–46]

The fabrication of nanostructured electrodes and thin layers needs to be precise in the fabrication with minimal defects to reduce porous metal structures, foreign atoms from the manufacturing process or the surrounding atmosphere. [47] Therefore, the chemical interaction and morphological formation needs to be investigated for a better understand-

ing and control of the thin layers. Hence, the metal-polymer interface plays a crucial role for the optical and electrical properties of the prepared devices. [48]

The metal-polymer interface mostly depends on the surface tension differences between the metal and the polymer, and Vollmer-Weber growth is the dominating growth process for metal-polymer interfaces. [49] Thus, combined investigation of the growth morphology at the polymer-metal interface on the nanoscale and its correlation to the resulting optical and electronic properties during the metallization on the polymeric templates is necessary to prepare devices with defined properties. The preparation of nanostructured polymer thin films as templates for metallization can be used with microphase separated DBC with subsequent thermal or solvent-vapor annealing (SVA). [50–52] A common method to prepare the metallization is PVD, e.g. evaporation or sputter deposition, where sputter deposition reflects the morphology of the template and creates a high nanoparticle density on a macroscopic scale without a high amount of agglomerations and good adhesion properties with compact layers. [27] The self-assembly of the metals on the polymers can be influenced by the different metal and polymer types as e.g. Erb *et al.* have shown by creating a variety of uniform metal nanostructures with long-range order using sputter deposition. [5] The aim of this thesis is to develop a deeper understanding of the early metal growth on polymers, especially on DBC templates. The first DBC template for this thesis was chosen to be a model system for the metal growth on a well known DBC template and is called polystyrene-block-poly(methyl methacrylate) (PS-*b*-PMMA), applied as lamellar type DBC and with a domain spacing (D_L) of $D_L = 65$ nm. The second DBC template is poly(methyl methacrylate)-block-poly(3-hexylthiophene-2,5-diyl) (PMMA-*b*-P3HT) with a domain spacing of $D_L = 43$ nm. A hexagonal structure was used to investigate the metal cluster growth on a semicrystalline polymer as P3HT, which is a common polymer used for photovoltaics or organic electronics. The third DBC template is polylactide-block-poly(3-hexylthiophene-2,5-diyl) (PLA-*b*-P3HT). It has a biodegradable block PLA and is arranging in a lamellar type with a domain spacing of $D_L = 15$ nm and could be useful for photovoltaics applications as reported by the literature. [53]

Three different metals were used, namely Au, Ag and Al. The metal electrode formation with minimal material usage on application-oriented polymers is of high interest for industry and therefore requires deeper knowledge of the interactions with the polymers and the metal formation. Löhrer *et al.* followed *in situ* the Au electrode sputter deposition on low bandgap polymers used in OPV. [54] The use of Ag for organic electronics, sensors and photovoltaics as electrode material or for plasmonic effects is well established. [22, 26, 55–58] The chemical interaction of Ag with several molecular components, e.g. oxygen and sulfur, has been studied in the literature. [59, 60] However, the correlation between chemical interaction, topographic and optical changes is yet missing.

Al is a much cheaper material compared to Ag and Au and therefore a good candidate to replace them as an electrode material. [61, 62] The drawback is the high reactivity to molecular components of the polymers and the surrounding atmosphere. This interaction with the molecular components needs to be investigated in detail to better understand the Al interaction with the polymer. The better understanding could yield to an improved nanostructuring of the metal clusters and layers, which could improve the device performances of OPVs or organic electronics. The polymer metal interaction can lead to a different selective wetting of the metal on the different polymer domains on a DBC template. The selective wetting describes the visible metal content on one of the polymer domains compared to the other domain of the DBC template. The embedding of the metal clusters on different polymer types can additionally influence the metal size evolution on the DBC template. In order to elaborate the selective wetting of a metal on the polymer domains, a comparison between Ag and Au is demonstrated. Au is a metal, which tends to be chemically more stable, inert and interacts less with the polymer compared to Ag or Al. [63, 64] In this study, I focus on the metal cluster to thin metal film formation and nanostructuring by self-assembly during metal sputter deposition on the above mentioned DBC templates both acting as model systems for the metal formation on common polymers and on application-oriented polymers. The influence of the chemical interaction and the diffusion coefficient of the metal clusters with and on the polymer leads to a specific formation and shape structure of the thin metal films and the interface between metal and polymer. These effects can change the optical, electrical and topological properties of the resulting device. Conductive polymers with a π conjugated system are used for OPV applications with a donor material and an acceptor material, which are then arranging in a bulk hetero-junction morphology. [65] A way to improve the OPV efficiency is to nanostructure the polymer domains in such a way that the domain size is close to the exciton diffusion length. Here, a more detailed understanding of the metal-polymer interface could improve the long term stability and performance. [66–68]

In this thesis several methods were used to obtain an improved picture of the metal growth on polymer templates by correlating the topographic, spectroscopic and scattering methods for distinct metal thicknesses: The correlation between the metal-polymer interface-morphology and its optical, electronic and chemical properties are investigated during the metal sputter deposition on different polymer thin films.

In detail, *in situ* measurements with different techniques e.g. grazing-incidence small-angle X-ray scattering (GISAXS), ultraviolet-visible spectroscopy (UV-vis), grazing-incidence wide-angle X-ray scattering (GIWAXS) and resistance measurements were correlated.

These correlations help to reveal more information of the metal decoration for different time stamps, yielding in different metal thickness, which is missing today. Additionally chemical interactions of the metal and the polymer were investigated with X-ray photoelectron spectroscopy (XPS) and Fourier-transform infrared spectroscopy (FTIR) and have shown high chemical interactions of the metal (Ag, Al) with the polymer compounds, especially the oxygen and sulfur interactions. This is further correlated to topological measurements with atomic force microscopy (AFM) and field emission scanning electron microscopy (FESEM), which supported the results from GISAXS, resistivity and XPS very well. Hence, in this thesis the direct correlation of morphological, chemical, electrical and optical properties of the metal formation on the DBC templates gives insights into the early metal-polymer chemical interaction and allows for understanding the formation and structure for large-scale fabrication of optical sensors and electrode materials for organic solar cells.

After the introductory part, the theoretical background about polymers and DBCs is explained, and fundamentals of sputter deposition and X-ray scattering are shown in Chapter 2. Chapters 3 and 4 describe the characterization methods and sample preparation with measurement techniques for thin film investigations, used materials and the thin film preparation. The scientific results are discussed in the Chapters 5 to 8. All obtained findings are summarized in Chapter 9 and are answering the questions of the introduction about the early cluster growth and the template effect of the polymers.

In more detail, chapter 5 investigates the model system PS-*b*-PMMA for DBC templates, which is decorated with Ag by sputter deposition. Especially, the decoration of the Ag on the individual polymer domains for different Ag thicknesses is investigated. In Chapter 6 and 7 the DBC template PMMA-*b*-P3HT is decorated with Ag and Al. Clear differences between these metal interactions with the DBC template are shown. In Chapter 8 the interactions of Au and Ag is compared on PLA-*b*-P3HT and indicates a high selective decoration of Ag on the DBC template compared to Au. In general for Chapters 5 to 7, the growth models were developed for the two DBC templates (PS-*b*-PMMA, PMMA-*b*-P3HT) and the two metals (Ag, Al). For thicknesses $\delta_{Ag,Al} = 0$ nm to 20 nm the *in situ* deposition was measured, and the models describe the growth regimes for these metal thicknesses. The metal cluster formation on the polymer and chemical interaction of the metal with the polymer occurs mostly between $\delta_{Ag,Al} = 0$ nm to 10 nm. After 10 nm grain growth is dominant. Figure 1.1 schematically presents the metal growth models on the DBC templates for the individual scientific projects in this thesis. Figure 1.1a shows the sample preparation with spin-coating and the resulting DBC thin films with AFM measurements. Figure 1.1b represents the sputter deposition process

for the thin film metallization on the DBC thin films and PS-*b*-PMMA as the model system to describe the metal cluster growth. Figure 1.1c displays the difference in the metal growth on the same PMMA-*b*-P3HT DBC template. The growth regimes on the DBC templates are described as follows: The zero region (0) describes the pristine polymer without metal deposited. The first region (I) describes the nucleation and embedding process, where metal clusters start to nucleate and embed on and in the polymer domains. The second region (II) shows the diffusion-mediated cluster growth via coalescence and selective wetting of metal on the polymer domain. The third region (III) can be described as the reduced-selective adsorption-mediated growth, where the selective metal growth is decreased and is mostly dominated by the immobilized cluster growth with absorbing adatoms. The fourth region (IV) describes the percolation of the metal on one domain of the DBC template. For Al, region III and IV are combined to region III because of the specific Al growth, which will be shown in chapter 7. In the last region (V), (P), or IV for Al, the metal clusters start to percolate on the whole DBC template.

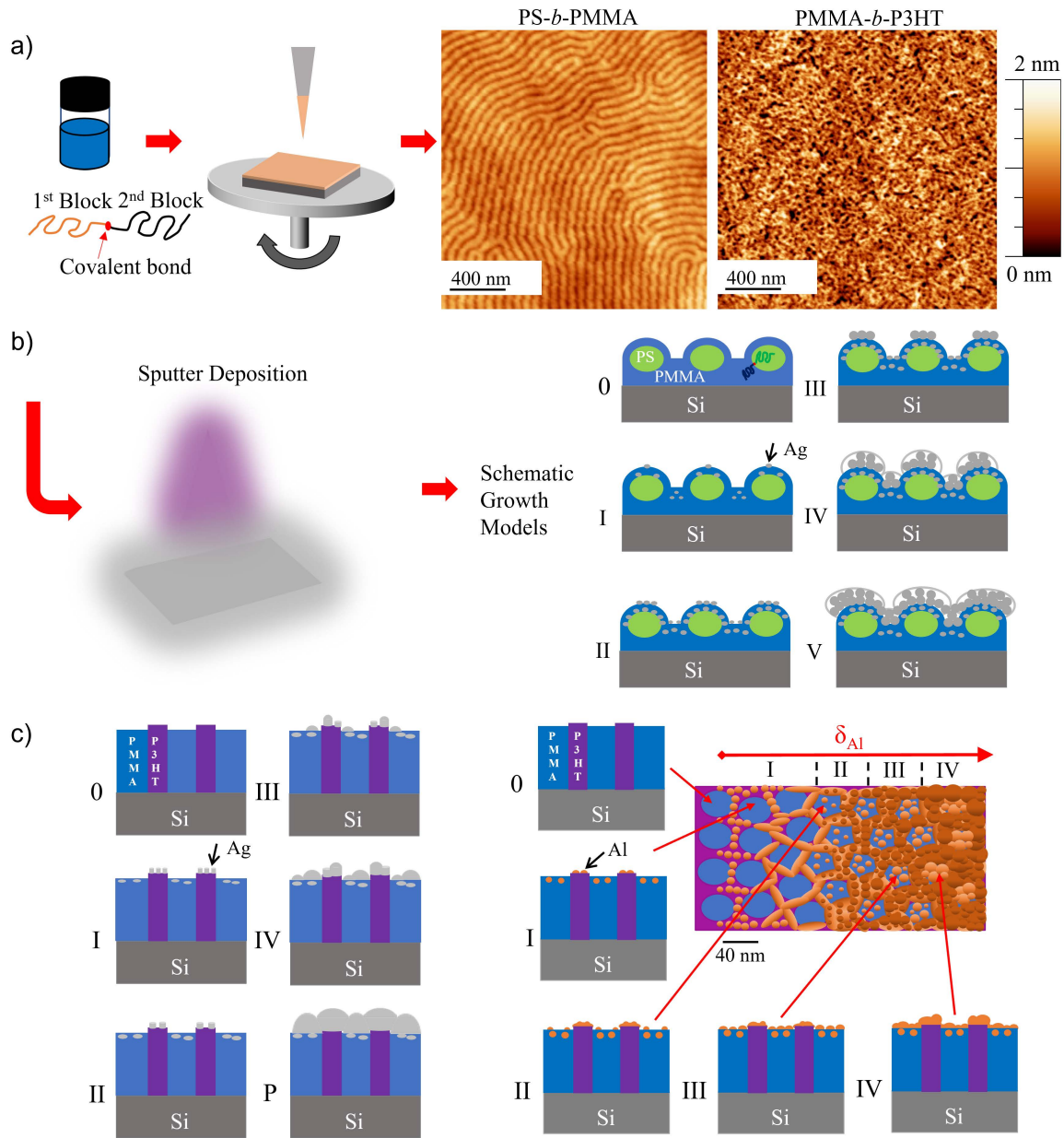


Figure 1.1.: a) Schematic description of the DBC thin film preparation with spin-coating and exemplary images of the resulting DBC nanostructure from the pristine PS-*b*-PMMA and PMMA-*b*-P3HT copolymers. b) Schematic description of the metal sputter deposition on the DBC templates and the Ag growth model on PS-*b*-PMMA (Chapter 5). Reprinted with permission from [69]. Copyright 2019 American Chemical Society. c) Ag and Al growth models on PMMA-*b*-P3HT (Chapter 6 and 7). Reprinted with permission from [70, 71]. Copyright 2021 American Chemical Society.

2. Theoretical aspects

A short summary of the basics of polymer physics for the work in this thesis is presented in this chapter. The chapter introduces the general physics of polymers and is followed by the more complex diblock copolymer templates. The principles of phase separation is explained, and conjugated polymer systems are further presented. The fundamentals of sputter deposition are shown in this thesis. The theoretical chapter is closing with the X-ray scattering basics for the investigation of the surface, and interface morphology of thin film systems.

2.1. Polymer Fundamentals

A more detailed understanding of the polymer basics can be found in the book by Strobl *et al.* [72] Large molecules with one or more identical units are known as polymers, where the subunits are covalently bond to form a macromolecule with a repeating structure to create a backbone. The subunits are known as monomers.

2.1.1. Polymer Principles

The polymers in this thesis can be classified as homopolymers and copolymers. [72] The homopolymers have only one repeating monomer species, and the copolymers have different monomers covalently bonded. A schematic overview of a homopolymer and copolymer is shown in Figure 2.1. [72] The different monomer types are presented in the Figure in blue and green and the polymer backbone in black. The copolymers can have different arrangement of the monomer species, and therefore different types of copolymers exist. The most common types of copolymers are statistical copolymers, alternating copolymers or diblock copolymers. In the framework of this thesis, different diblock copolymers (PS-*b*-PMMA, PMMA-*b*-P3HT and PLA-*b*-P3HT) and their corresponding homopolymers (PMMA, PS and P3HT) are investigated. The polymers are polydisperse, since during polymerization different chain lengths form. To characterize a polymer, the number of total monomer units (N) is given. The different polymer chain lengths are described with an index i , where each component consists of specific mol of chains with the degree of

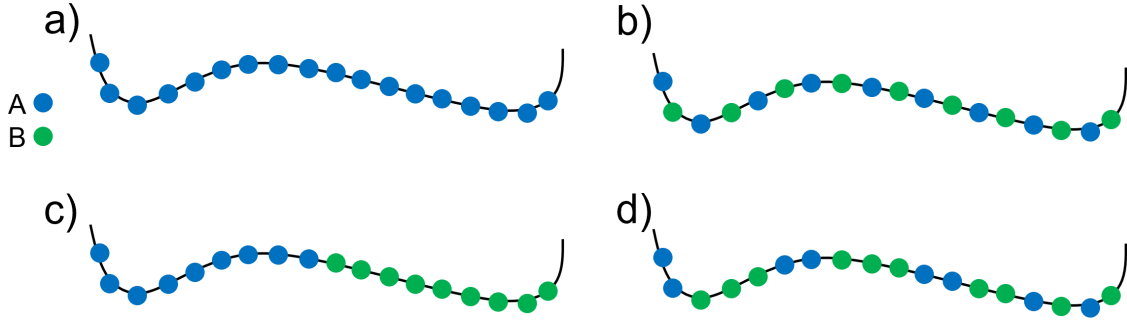


Figure 2.1.: Different types of polymers with two types of monomers presented in blue and green and the polymer backbone in black: a) homopolymer, b) alternating copolymer, c) block copolymer, d) statistical copolymer.

polymerization N_i . N_i describes the number of monomers of molar mass M_i in a chain of component. The total number of chains in this set is given by N . The number average molar mass of such a polymer is defined as

$$M_N = \frac{\sum_i n_i M_i}{\sum_i n_i}, \quad (2.1)$$

where n_i defines the amount of substance i . The number average molar mass or the weight average molar mass M_W is given by

$$M_W = \frac{\sum_i n_i M_i^2}{\sum_i n_i M_i} \quad (2.2)$$

A further important characteristic of a polymer is its polydispersity index (PDI) which provides a measure for the distribution width

$$PDI = \frac{M_W}{M_N} = 1 + U \quad (2.3)$$

with the inconsistency coefficient U which provides a measure of the distribution width. A monodisperse polymer is described with a polydispersity $PDI = 1$, whereas higher values correspond to a larger distribution.

2.1.2. Phase Separation

The Gibbs free energy describes the mixture of the polymers and therefore the phase separation for mean field theory

$$\Delta G = \Delta G_{AB} - \Delta G_A - \Delta G_B, \quad (2.4)$$

where ΔG_{AB} is the free energy of the mixture and ΔG_A and ΔG_B are the free energy of the components A and B. The phase separation can be assumed with the minimization of the free energy for the whole system. The Gibbs free energy of mixing for two polymers is described by the Flory-Huggins theory [72]

$$\Delta G = nk_bT \left(\frac{\phi_A}{N_A} \ln(\phi_A) + \frac{\phi_B}{N_B} \ln(\phi_B) + \chi \phi_A \phi_B \right), \quad (2.5)$$

where $\phi_{A,B}$ is the volume fraction, $N_{A,B}$ the degree of polymerization, which describes the number of monomers connected together to a polymer chain, T the temperature, n the number of molecules of the polymers in the mean field theory, k_b the Boltzmann constant and χ the Flory-Huggins interaction parameter, which can be written as

$$\chi = \chi_S + \frac{\chi_H}{T} \quad (2.6)$$

The two constants χ_H and χ_S , are related to the entropic and enthalpic contributions. The enthalpy term χ_H has a dependence on the temperature, while the empiric corrections are included in the entropic parameter χ_S . χ includes information about the mixing of the polymers and the repulsion of the polymers. For $\chi < 0$, mixing of the polymers is favoured. With a value of $\chi > 0$, polymer mixing is reduced, and the polymers separate from each other. However, for DBC systems the phase separation is more complex due to the covalent bond and additional theoretical assumptions as e.g. the weak and strong segregation need to be considered, which will be shown in the next section.

2.1.3. Diblock Copolymers

Diblock copolymers are two polymers covalently bond to each other. The covalent bond is shown in the abbreviation of the diblock copolymer as A-*b*-B, where A and B corresponds to the different homopolymers and *b* to the block for the covalent bond. The degree of polymerization for the homopolymers (N_A and N_B) determine the thin morphology. The block asymmetry of each block can be defined by a block ratio f_A and f_B as follows [72,73]

$$f_A = \frac{N_A}{N_A + N_B}, \quad (2.7)$$

where f_A describes the ratio of polymerization compared to the block of the B homopolymer. It defines further the ratio for the block of the B homopolymer

$$f_B = \frac{N_B}{N_A + N_B} = 1 - f_A \quad (2.8)$$

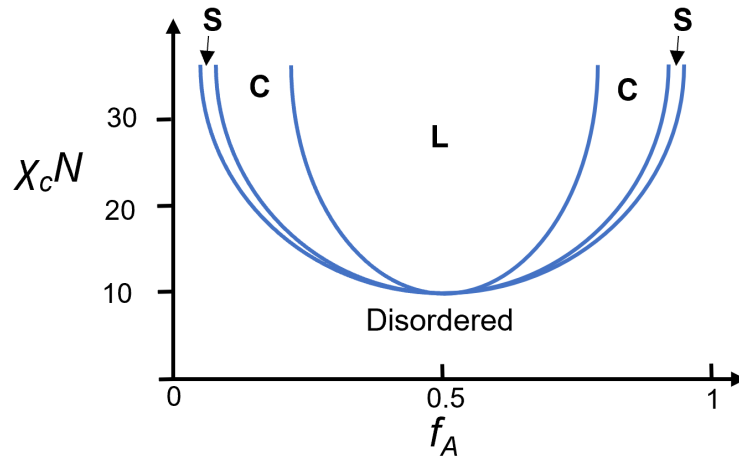


Figure 2.2.: Schematic mean-field phase diagram for a DBC template. The ordered phases are labeled as lamellar (L), cylindrical (C) and spherical (S). Below a critical $\chi_c N$ value the phase is disordered. [74]

The incompatibility of the two blocks leads to a phase separation on the nanoscale. Macro-phase separation is inhibited and instead a micro-phase separation takes place for the block copolymers. The reason for the self-assembly process is the covalent bond between the polymer blocks, which directs them in a nanostructure phase separation. The resulting nanostructure highly depends on the fraction of the two blocks, the temperature of the solvent and the solubility of the copolymer in the solvent or solvents as can be seen in Figure 2.2. The fraction f_A is the most important factor and defines the overall structure in the copolymer, e.g. lamella, cylinder, sphere or gyroid. [75] The temperature and solvent determine the order and disorder of the blocks in the solution. The copolymer solution can be deposited with different techniques to create a thin film, e.g. spin-coating, spray deposition, slot-die coating, or dip coating. [76–82] In this thesis, only spin-coating is used to prepare smooth and homogeneous copolymer thin films and the film thickness can be controlled very precisely with spin-coating. The film thickness is a crucial factor for a diblock copolymer thin film, because the quality of the highest order of phase separation occurs mostly for distinct film thickness for copolymer systems. The phase separation of the copolymer thin film can be described by the Flory-Huggins parameter χ_c and the weak and strong segregation. The symmetry of the blocks leads to a critical value for

symmetric diblock copolymer systems $\chi_c N$ around 10.5. For $\chi_c N < 10.5$ separation is not reached. A mixed phase is established for low polymerization, when $\chi_c N$ is far below 10.5. [74] When $\chi_c N$ is 10.5, the weak segregation limit (WSL) is reached, and the repulsion between the two blocks is large enough to form the phase separation, which is characterized by the Flory-Huggins parameter χ_c . [83–87] When the weak segregation region is passed and the polymerization degree is high enough, the order-disorder phase transition (ODT) is reached. With increasing polymerization, the strong segregation limit (SSL) follows. The strong segregation leads to a high demixing. The interfaces of the two blocks are well separated from each other, which results in a highly ordered phase separation with a clear domain arrangement of the blocks. A schematic phase diagram of the copolymer systems is shown in Figure 2.2, depending on $\chi_c N$ and f_A . [73, 74] The real phase separation for copolymer systems is mostly more complicated. They often need to be studied experimentally for many parameters, which include the film thickness, different monomer structures, monomer properties, deposition technique, solution temperature, solvent to solve the copolymer, annealing procedure and others. [88–90] Examples for the film thickness dependence for the DBC phase separation were shown in previous publications and show a strong correlation to the domain spacing. [91, 92]

2.1.4. Semi-Conducting Polymers

The first highly semi-conductive polymer was discovered by Shirakawa, MacDiarmid and Heeger in 1977 with the doping of polyacetylene (PA), which was rewarded with the noble prize in chemistry in 2000. [93] The origin of the conductivity is based on the delocalization of electrons by the overlapping of the atomic orbitals, which enables the charge transport. [94] The orbitals can be described with quantum mechanics, where wave functions characterize the probability density of the electrons. The overlap of the orbitals form a bonding orbital interfere constructive or are anti-bonding for destructive interference. This is described by the linear combination of atomic orbitals (LCAO). [95–97] The delocalization of the electrons leads to a free movement of the electrons along the backbone of the polymer. The backbone of the polymer consists of alternating single and double bonds (conjugated double bonds). The changing formation of double bonds and single bonds yield to the formation of π - π bonds, which are the origin of the movement for the free electrons in the polymer. The π - π bonds result in the formation of anti-bonding (highest occupied molecular orbital (HOMO), similar to the valence band) π^* bands and bonding π - bands (lowest unoccupied molecular orbital (LUMO), similar to the conduction band). Figure 2.3 shows the HOMO and LUMO energy levels for a π conjugated energy band with a high number of coupled monomers n to form a band in contrary to distinct energy levels for a low number of monomers. [98, 99] Figure 2.3

shows the LCAO structure as a function of the size of the monomers with the resulting bandgap E_{gap} , first ionization energy E_i for an electron to be released from the HOMO to the vacuum energy E_{vac} and the electron affinity E_a , which describes the ability of a molecule or atom to take up an electron. In order to describe the band structure of

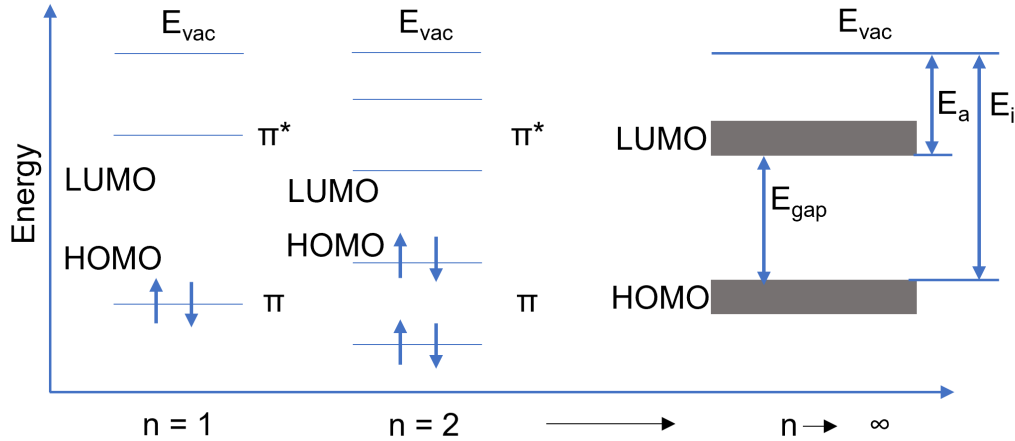


Figure 2.3.: Schematic description of the LCAO theory for molecules with conjugated π and π^* bonds to the energy band structure for large monomer n systems ($n \rightarrow \infty$). The band structure is defined by the bandgap E_{gap} , the ionization energy E_i for an electron to be released from the HOMO to the vacuum energy E_{vac} and the electron affinity E_a , which describes the ability of a molecule or atom to take up an electron.

these polymers with alternating single and double bonds, a model was assumed namely, the Peierls instability. [100] The model describes a one-dimensional (1D) metal chain, which is filled up to the Fermi energy, and the disturbance of the lattice is described by a flexible lattice, see Figure 2.4a. The black line in Figure 2.4a describes the polymer backbone, and the green spheres illustrate all the bonds in the polymer backbone with distance a between them. A dimerization takes place during the disturbance of the lattice and leads to a change in the band structure with a formation of a bandgap as can be seen in Figure 2.4b. The formation of the bandgap is corresponding to π bonds for the lower band and π^* bonds for the low band. The lower band is completely filled with electrons, while the upper band is empty. The Peierls instability for polymers changes the band gap much more than in a 1D metal. The concept of charge carriers in conducting polymers is different compared to metals or semiconductors. The quasiparticles include not only the charge, but also the lattice distortion which is described by δ , see Figure 2.4b. The lattice distortion is much higher compared to inorganic materials, because of the weaker

binding compared to inorganic materials. The bandgap can be influenced by the degree of polymerization, doping or the arrangement of the polymer backbones to each other in the polymer (crystallinity). [101–109] The quasiparticles for conductive polymers are

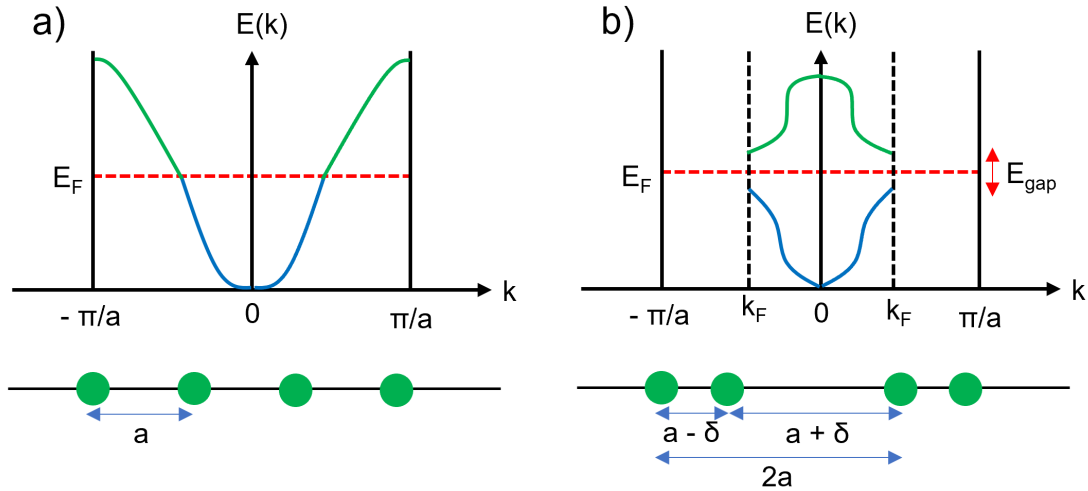


Figure 2.4.: Schematic band structure of Peierls instability is shown a) for an one-dimensional chain. b) The band structure in one Brioullin zone is shown after the dimerization. [100]

e.g. solitons, polarons, and bipolarons. A schematic description of the quasiparticles can be seen in Figure 2.5 and a description is shown by Su *et al.*, where solitons in PA are explained with the quasiparticles located between the upper and lower band in the bandgap. [110] A difference between electrons and quasiparticles is for example the spin of the particles: While for electrons or holes the spin is $1/2$, the spin for the before mentioned quasiparticles can be different. In Figure 2.5 the quasiparticles as the solitons can be neutral S^0 , positive S^+ or negative S^- . The S^0 state is allowed due to the change of the bondings from single to double bond leading to an unpaired electron. The charged solitons S^+ and S^- can be created by either chemical doping or induced light, but carry no spin. The polarons in turn have a spin $1/2$ from the unpaired electron and a charge, which can be positive P^+ or negative P^- . The bipolarons are again spin-less, but have doubled the charged compared to polarons with B^+ and B^- . The combination of solitons can lead to a polaron and can further be combined to bipolarons, but they can also annihilate each other.

P3HT is used in this thesis as a conductive polymer. Doping of the polymer can be achieved by reduction or oxidation with a dopant and increase the number of bipolarons in the polymer. The P3HT with regioregularity was used. The regioregularity describes the probability with which a single monomer within the chain is oriented. The polymer therefore forms highly crystalline P3HT arrangements.

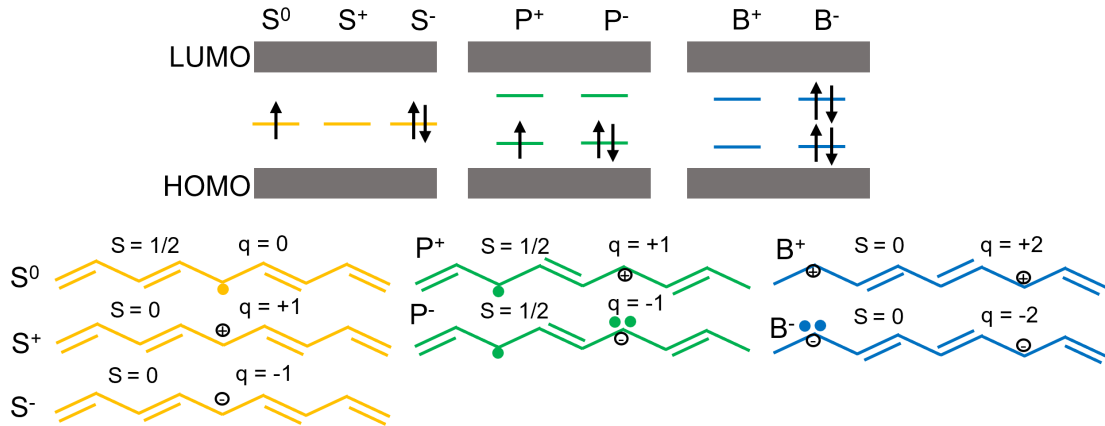


Figure 2.5.: Schematic description of quasiparticles (QP) in conductive polymers. Solitons (orange), polarons (green) and bipolarons (blue) define the state of the charge and spin of the QPs. [110] Solitons (orange) are neutral or charged QPs. Polarons (green) and bipolarons (blue) are charged QPs. The state of the QP is described by the charge and the spin "S". The HOMO (π^*) and LUMO (π) define the conduction and valence band. In between them the energy states of the QPs are located.

2.2. Sputter Deposition

Physical vapor deposition (PVD) techniques, such as sputter deposition, are common deposition techniques for metal or polymer coatings. In this work, the nanostructural evolution of metals on polymer templates is investigated. [111, 112] Thin metal films are prepared by radio frequency (RF) and non-reactive direct current (DC) magnetron sputtering from a pure metal target. In this section, the fundamental process of the sputter process is described, and a brief introduction to the resulting thin film morphology is given.

2.2.1. Fundamentals

The sputter process takes place in a vacuum chamber. For simplicity, DC sputtering is first explained. A high DC voltage is applied between the target (cathode), which is connected to the source gun at the top of the chamber and the grounded substrate (anode) located at the bottom of the chamber. This is schematically shown in Figure 2.6. The inert sputtering gas Argon (Ar) is led into the chamber with a gas valve. The sputter process is explained in three steps: 1.) ionization, 2.) interaction with the target, and 3.) released atoms from the target: [113]

- 1.) The high voltage leads to the partial ionization of Ar atoms. As a consequence, the Ar atoms release electrons. The free electrons collide with the neutral gas atoms if the energy is high enough and continue to ionize Ar atoms. After the collision with an Ar atom, an electron drifts to the anode (substrate). The electrons gain energy from the high electric field. This leads to further ionization of Ar atoms, if the energy is high enough when the electron collide with an Ar atom. For this process a high argon flux is needed to enhance the probability of a collision of an electron with an Ar atom. The plasma state is achieved when the ionization reaches an avalanche effect, where the electrons gain enough energy on their way to the anode from the electrical field to produce multiple electrons from the impact ionizations. If the energy is not high enough, different interactions can take place such as excitation, relaxation or recombination.
- 2.) The ionized Ar atoms bombard the target. Atoms from the target are ejected ("sputtered"). The interactions between the ion and the target material can lead to different effects: 1) Sputtering of target atoms, 2) secondary electrons can be generated, 3) Ar ions can be implanted in the target material, 4) Ar ions can be reflected by the target material, and 5) argon ions can lead to the displacement of the atoms from the target material by collision. These interactions are schematically shown in Figure 2.7. The sputtering yield defines the number of sputtered particles per incident ion of the target material. Target atoms will be sputtered, if the surface binding energy is reached by the kinetic energy of the atoms. In Figure 2.8 a schematic view of the sputter yield is shown for Au, Ag and Al. [114]
- 3.) The sputtered atoms from the target diffuse through the gas phase to the substrate. When the atoms move through the gas phase, they collide with each other and change their energetic and angular distribution. The sputtered atoms with enough energy and the right direction reach the substrate and start the nucleation, otherwise they will be lost by the walls of the chamber. The sputtered atoms can be adsorbed or reflected from the substrate. On the substrate surface, the atoms can diffuse and

the non-equilibrium sputtered atoms start the growth process, which will start the film formation depending e.g. on as the sputter conditions (e.g. sputter rate, target to sample distance, inert gas pressure), type of atoms and type of substrate material.

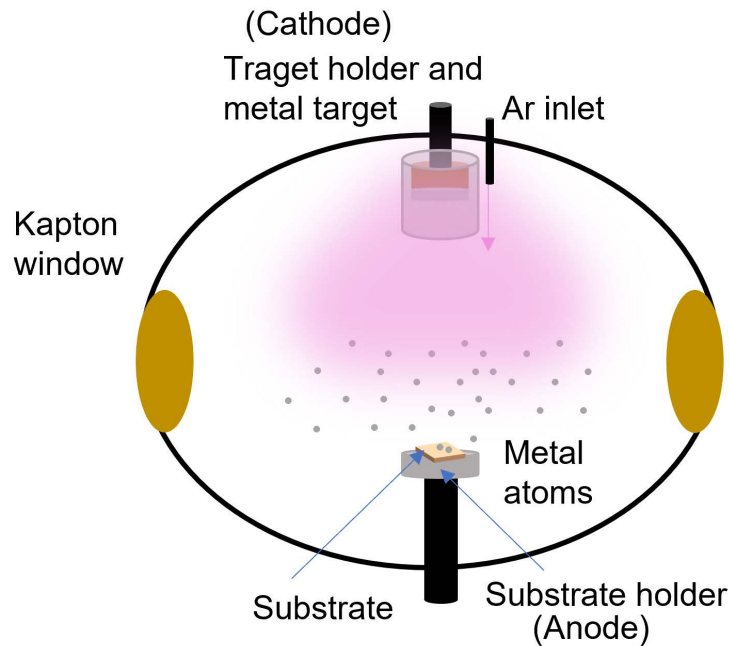


Figure 2.6.: Schematic drawing of sputter deposition. The inert gas (argon) will be let in the vacuum chamber and ignites the plasma. The argon ions hit the target and release target atoms, which travel to the substrate and start the nucleation process.

2.2.2. Radio frequency (RF) vs. Magnetron Sputtering

The two different sputter techniques, which are used in this thesis, are explained in more detail:

Radio frequency (RF)

The Ar ionization is limited by the loss of electrons for the ionization process for the DC sputter chamber. Therefore, the DC power supply can be replaced by an alternating-current radio frequency source. The alternating-current radio frequency device needs an

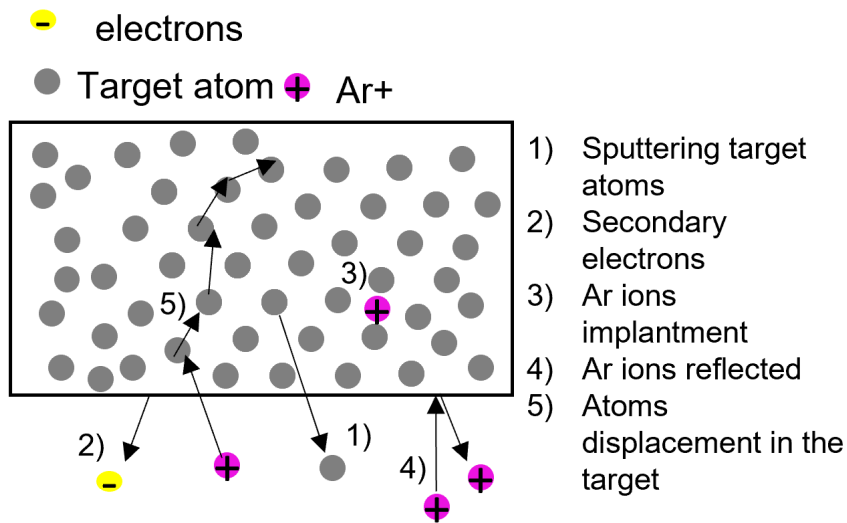


Figure 2.7.: Schematic drawing shows the possibilities of the interactions of the argon ions with the target. The possibilities can be implanting of the argon ions in the target, secondary electrons ejecting from the target, the surface geometry can be changed by the displacement of target atoms and ejecting of target atoms.

impedance-matching system to control the complex impedance. The general used radio frequency at the electrodes for a common RF sputter deposition device is 13.56 MHz, which relates to industrial, scientific and medical services and is not interfering with other services as telecommunications. The alternating RF power is adapted to the electron motion in the plasma. This leads to more collisional ionization, an increase of the plasma density, and longer electron lifetimes in the plasma. RF enables high density plasma for metals sputtering and further sputtering of insulating materials. [111,115,116]

Magnetron sputter deposition

Permanent magnets are positioned on the back side of the target. The ionization is enhanced due to secondary electrons, which are trapped in the magnetic field near the target position. Therefore, the high argon flow for the plasma ignition, can be reduced. The confinement of the electrons in the magnetic field leads to a track on the target material in the shape of a gauss function, where the material is sputtered. [117–119]

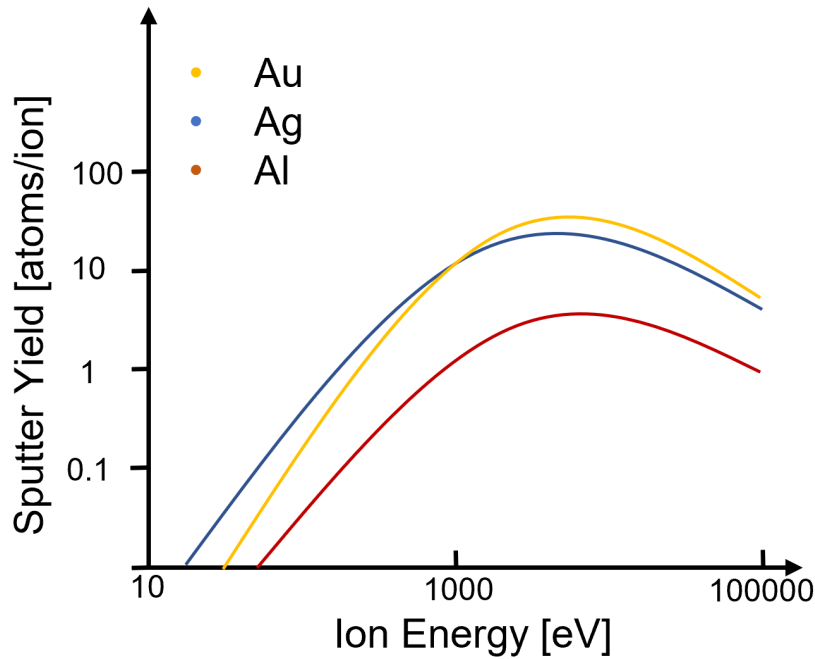


Figure 2.8.: Schematic representation of the sputter yield from Au, Ag and Al with Ar ions adopted from Yamamura *et al.* [114]

2.2.3. Thin Film Formation

The growth of thin films by sputter deposition can be described by a nucleation process, surface-diffusion-controlled growth and the formation of an overlapping network structure of the cluster-shaped structures to a closed film at the percolation threshold. For sputter deposition most of the atoms coming from the vapor phase to the substrate start with the nucleation process and diffusion and grow with incoming adatoms. The process takes place at thermodynamic non-equilibrium conditions for sputter deposition. For this the diffusion coefficient D can be described by [120, 121]

$$D = \frac{a^2}{4} \nu_0 \exp\left(\frac{-E_d}{k_B T}\right) \quad (2.9)$$

where a is the minimum adatom translational hopping distance on the substrate surface, ν_0 is the attempt frequency for adatom migration, E_d surface diffusion energy for adatoms against the potential barrier on the substrate surface, k_B the Boltzmann constant and T the absolute temperature. The sputtered atoms from the vapor phase condensate at the substrate surface, and different processes can be described for the atoms: 1) atoms

from the vapor phase to the substrate 2) diffusion, 3) clustering of atoms, 4) atoms can leave the cluster by dissociation, 5) the atoms can re-evaporate from the substrate, 6) direct adsorption of atoms from the vapor phase to growing clusters, 7) the atoms could also be captured by defects or jump on steps, 8) the atoms can also diffuse into the substrate and 9) atoms can do an inter-layer jump and then bind to a cluster. [122–126] The possible processes are illustrated in Figure 2.9. Thornton described the sputtering

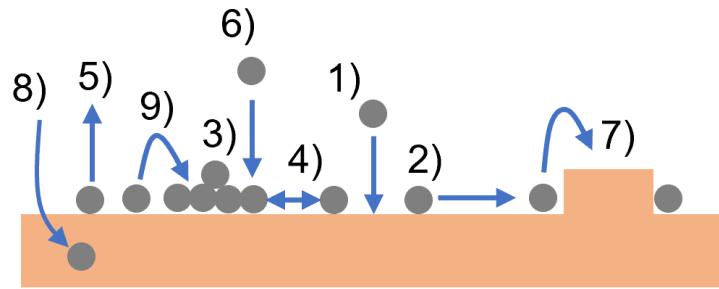


Figure 2.9.: Schematic description of the possible processes for sputtered atoms at the substrate surface e.g. 1) atoms arrive from the vapor phase to the substrate 2) diffusion, 3) clustering of atoms, 4) atoms can leave the cluster by dissociation, 5) atoms can re-evaporate from the substrate, 6) direct adsorption of atoms from the vapor phase to growing clusters, 7) atoms can also be captured by defects or jump on steps, 8) atoms can also diffuse into the substrate and 9) atoms can do an inter-layer jump and then bind to a cluster. [122–126]

process with a structure zone model, where the resulting microstructure is represented depending on the substrate temperature and the argon pressure. [127] The argon pressure represents the reference to the kinetic energy of the argon ions in the plasma. The zones characterize different growth regions of the crystallites. In zone 1 tapered crystallites are formed with many voids in between, which leads to a porous structure. Zone T contains densely packed fibrous grains, while for zone 2 columnar grains are formed and in zone 3 a recrystallized grain structure appears. The Thornton model is in good agreement with thick sputtered films, but thin films with only a few nanometers of the deposited material arrange in special growth types. The growth types can be described as island type (cluster formation of the target material), layer type or a mixed type depending on the material type, substrate type and their resulting interface energies. The growth types are shown in Figure 2.10, which are namely a) Frank-van der Merwe (layer type), b) Stranski-Krastanov (mixed type) and c) Volmer-Weber (island type). [120] The start of the island or layer like growth is by the adatoms, which are moving by Brownian motion on the surface and can be described by the diffusion of the adatoms and later of the islands. The adatoms

will be trapped at the beginning of the nucleation at a nucleation center, where the atoms stick to the substrate and form nuclei with increasing size, as more and more adatoms are absorbed to the nuclei. The type of growth is determined by the different surface and interfacial energies as the surface energy γ_M of thin metal films and the polymer substrates γ_P compared to the interfacial energy of the metal-polymer γ_{MP} . The Volmer-Weber growth is predominate if the surface energy of the metal is higher compared to the energy difference between the polymer substrate and the metal-polymer interfacial energy $\gamma_M > (\gamma_P - \gamma_{MP})$. The layer like growth appears to be dominate if the surface energy difference compared to the metal-polymer interfacial energy is higher as the surface energy of the metal $\gamma_M < (\gamma_P - \gamma_{MP})$. More details about the thin film formation of the target material (metals) from sputter deposition on polymer thin film substrates will be shown in the introductions of the respective chapters. The used model for describing the cluster growth is shown in the following section, where the scattering method is explained which is used to reveal the growth regimes from nucleation to percolation region. The metal-polymer introduction chapter 5 and the result chapters 6,7 will further investigate the chemical interactions and embedding of the metal clusters with the polymer substrates, which can influence the growth kinetics.

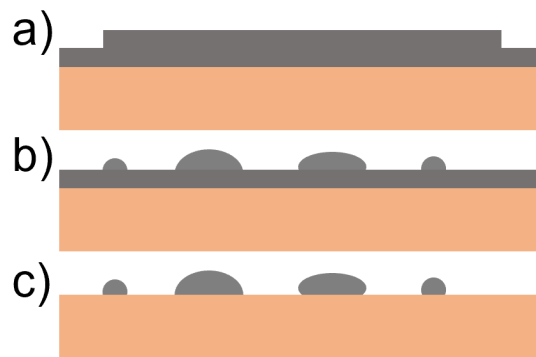


Figure 2.10.: Different growth mechanisms for the sputter deposition. Three possible growth types are a) Frank-van der Merwe b) Stranski-Krastanov and c) Volmer-Weber.

2.3. Scattering Basics

The general theoretical basics of X-ray scattering are explained in this section, followed by the basics of small-angle X-ray scattering for thin film investigation.

2.3.1. X-ray Introduction

A scattering event can be described by the scattered intensity I_{sc} , which is the number of scattered photons, which are recorded per second on a detector under a solid angle $\Delta\Omega$. The scattered intensity is further proportional to the number of particles in the sample N per unit area, the intensity of the incoming X-ray beam I_0 in photons per second and the differential cross section ($d\sigma/d\Omega$). When the sample is larger than the beam size, the scattering intensity is then given by the following equation [128]

$$I_{sc} = I_0 N \Delta\Omega \frac{d\sigma}{d\Omega}. \quad (2.10)$$

If the sample is smaller than the beam size the scattered intensity depends on the number of photons passing through the unit area per second, which is described by the flux of the incident beam Φ_0 . The differential cross-section measures the efficiency of the scattering process for the experiment with known flux and detector size. The differential scattering cross-section ($d\sigma/d\Omega$) is then defined by the formula [128]

$$\frac{d\sigma}{d\Omega} = \frac{I_{sc}}{\Phi_0 \Delta\Omega}. \quad (2.11)$$

The elastic scattering from an atom with Z electrons is depending on their electron distribution, which is given by a number density $\rho_e(\vec{r})$. The phase shift of the incident wave resulting from the scattering event of a volume element in the origin and in the distance \vec{r} is [128]

$$\Delta\phi(\vec{r}) = (\vec{k}_i - \vec{k}_f) \cdot \vec{r} = \vec{q} \cdot \vec{r} \quad (2.12)$$

where \vec{k}_i is the incident wave vector and \vec{k}_f the outgoing wave vector. $\vec{q} = \vec{k}_i - \vec{k}_f$ is the scattering vector. For a monochromatic X-ray beam assumed as plane wave, the scattering geometry in transmission is illustrated in Figure 2.11 with the scattering at two scattering center A and B in the sample. The distance between A and B is described by \vec{r} . For elastic scattering $|\vec{k}_i| = |\vec{k}_f|$, with the scattering is described by

$$\vec{q} = 2 |\vec{k}_i| \sin\theta = \frac{4\pi}{\lambda} \sin\theta, \quad (2.13)$$

where θ is the incident angle and λ the wavelength. The total scattering length $F(\vec{q})$ of the atom is then described by the volume element $d\vec{r}$ at distance \vec{r} with a contribution of $-r_e \rho_e(\vec{r}) d\vec{r}$ and a phase factor of $e^{i\vec{q}\cdot\vec{r}}$ with the equation [128]

$$F(\vec{q}) = -r_e f^0(\vec{q}) = -r_e \int_V \rho_e(\vec{r}) e^{i\vec{q}\cdot\vec{r}} d^3\vec{r} \quad (2.14)$$

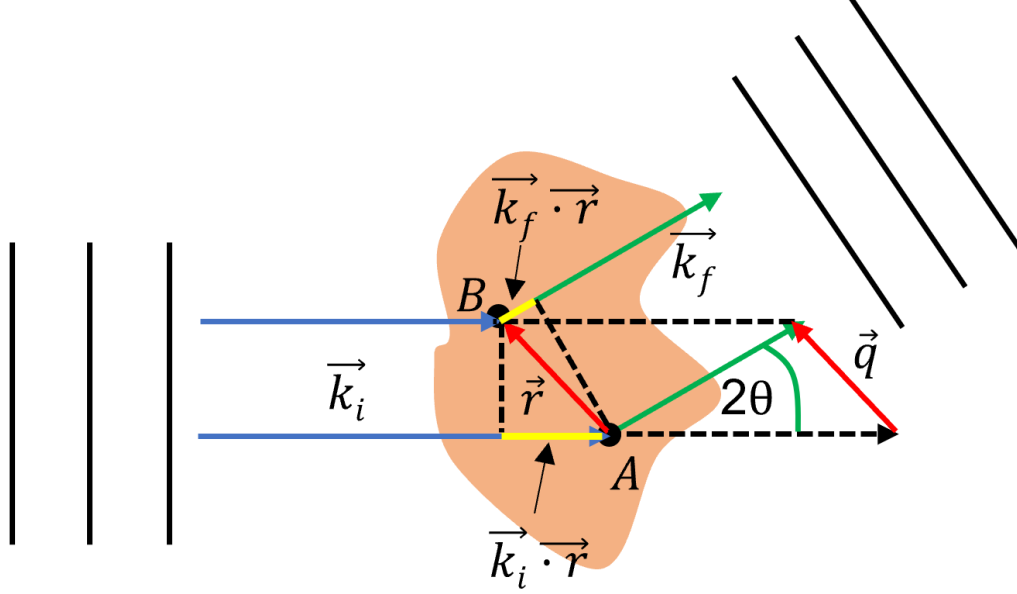


Figure 2.11.: Schematic description of the scattering process. The incident plane wave with a wave vector k_i is scattered at two scattering center in the sample A and B with an angle 2θ with a scattering wave vector k_f .

where $f^0(\vec{q})$ is the atomic form factor and r_e is the classical electron radius with $r_e = \frac{e^2}{4\pi\epsilon_0 mc^2}$, where ϵ_0 is the permittivity of the medium. The atomic form factor is depending on the scattering vector, so if $\vec{q} \rightarrow 0$, the volume elements scatter in phase and the atomic form factor would result as the number of electrons Z in the atom. In the other direction, so if $\vec{q} \rightarrow \infty$, the atomic form factor would result in 0, because the scattering from the volume elements are out of phase. The scattering length is described as shown in equation 2.14 as a Fourier transform from the distribution of the electrons in the sample. The scattering Intensity is further calculated with the equation 2.14 and their product with the complex conjugated to $|F(\vec{q})|^2$. The scattering intensity can be written as [129]

$$I(\vec{q}) \propto NP(\vec{q})S(\vec{q}) \quad (2.15)$$

where $I(\vec{q}) \propto |F(\vec{q})|^2 = |-r_e f^0(\vec{q})|^2$, $S(\vec{q})$ is the structure factor which is described by the electron density fluctuations of the particles to each other and thus their structural

arrangement, while the form factor $P(\vec{q})$ describes the shape of the particles e.g. spherical, cylindrical or hemispherical. The scattering length of an atom is moreover depending on quantum mechanics in specific, the interaction of the X-ray beam with the discrete energy levels of the electrons. The scattering length is therefore reduced by the interaction with the less tightly bounded electrons in the atom. This results in correction factors for the dispersion relation of the atomic form factor by f' for the real part and f'' for the imaginary part of the dispersion corrections. The dispersion corrections are energy dependent and the atomic form factor is written as follows [128]

$$f(\vec{q}, E) = f^0(\vec{q}) + f'(E) + f''(E) \quad (2.16)$$

The atomic scattering form factor $f(\vec{q}, E)$ is element specific and depends on the momentum transfer \vec{q} and the energy E . It can be divided into three parts, where $f^0(\vec{q})$ describes the in-phase superposition of the scattering amplitudes starting from the electron density $\rho(\mathbf{r})$ of the atom. The factors $f'(E)$ and $f''(E)$ describe corrections for the phase and magnitude to the form factor in the vicinity of absorption edges of the atom. The atomic factor $f(\vec{q}, E)$ depends on the wave vectors of the incident and exiting wave. If the energy is far away from absorption edges, the atomic form factors depends only on the first term $f^0(\vec{q})$ and the equations can be simplified as seen in the next section about the refractive index. The form factor for crystalline materials is defined by their periodic structure, which can be described by Bragg's law.

The Bragg equation describes the interference effect of either constructive or destructive interference depending on the incident angle of the X-ray beam. The beam path length difference ($d_{hkl} \sin \alpha_i$) lead to the interference phenomena of the scattered X-ray beam. The relation of the lattice spacing d_{hkl} , the incident angle α_i and the wavelength describe the Bragg conditions. The Bragg equation is defined as [128]

$$2d_{hkl} \sin \alpha_i = n\lambda \quad (2.17)$$

The construction of the interference can be described with Bragg's law, but the scattering intensity has to be identified as before with the scattering amplitude of the crystal structure. The crystalline structure can be investigated with X-ray diffraction, where a monochromatic X-ray beam is scattered at different lattice planes (hkl) of the sample as described by the theory of Bragg and Max van Laue. The periodic structure of the crystals in the sample leads to interference, when the wavelength is in the order of the lattice distance. If the reciprocal wave vector (\vec{G}) equals the scattered vector (\vec{q}) the Laue conditions are fulfilled, which will be shown below. The Bragg conditions are shown in Figure 2.12a. The conditions are visualized by the Ewald sphere for elastic scattering events with the conserved momentum, where the reciprocal wave vector is equivalent to

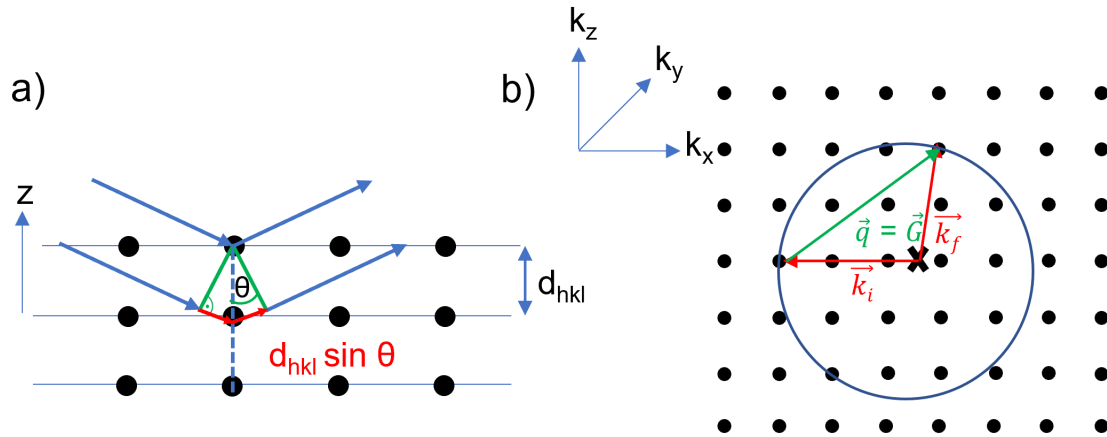


Figure 2.12.: a) Schematic description of the Bragg condition. The lattice planes are shown by the blue horizontal lines and defined by d_{hkl} . The X-ray beam is depicted by the blue arrows that impinge the lattice planes under an angle Θ . Constructive interference of the X-ray beams is accomplished, if the path length difference $d_{hkl}\sin\Theta$ is an integer multiple of the wavelength of the incident beam. b) The Ewald sphere shows the appearing constructive interference, if the momentum transfer corresponds to a reciprocal lattice vector. The radius of the sphere corresponds then to the wave vectors of the incident and the scattered X-ray beam. The observed Bragg peaks can give information about the crystal size, orientation and lattice spacing.

the scattered vector. Diffraction pattern are visible, if a reciprocal lattice point intersects the Ewald sphere as seen in Figure 2.12b.

The lattice points are defined for the crystal structure symmetry and the atoms are associated with each lattice site in a unit cell. The lattice vectors R_n represent the lattice and r_j the position of the atoms with respect to the lattice site. The position of any atom is then defines as $R_n + r_j$. The equation for the scattering amplitude for a crystal writes as follows [128]

$$F^{Crystal}(\vec{q}) = \sum_{j=1} f_j^0(\vec{q}) e^{i\vec{q}r_j} \sum_{n=1} e^{i\vec{q}R_n}, \quad (2.18)$$

where the first sum represents the units cell structure factor and the second term is the sum from all lattice sites. The terms in the lattice sum are phase factors, which are described by the complex plane. The lattice sum term can be described as follows [128]

$$\vec{q} \cdot \vec{R}_n = 2\pi N, \quad (2.19)$$

where N corresponds to the number of unit cells and the lattice vectors \vec{R}_n are defined as

$$\vec{R}_n = n_1\vec{a}_1 + n_2\vec{a}_2 + n_3\vec{a}_3, \quad (2.20)$$

where $\vec{a}_1, \vec{a}_2, \vec{a}_3$ are the basis vectors of the lattice and n_1, n_2, n_3 are the integers. The reciprocal lattice basis vectors are defined as

$$\vec{a}_1^* = 2\pi \frac{\vec{a}_2 \times \vec{a}_3}{\vec{a}_1(\vec{a}_2 \times \vec{a}_3)}, \vec{a}_2^* = 2\pi \frac{\vec{a}_3 \times \vec{a}_1}{\vec{a}_2(\vec{a}_3 \times \vec{a}_1)}, \vec{a}_3^* = 2\pi \frac{\vec{a}_1 \times \vec{a}_2}{\vec{a}_3(\vec{a}_1 \times \vec{a}_2)}, \quad (2.21)$$

which yields the lattice sites in the reciprocal space by

$$\vec{G} = h\vec{a}_1^* + k\vec{a}_2^* + l\vec{a}_3^*, \quad (2.22)$$

where h,k,l are integers. Hence the product of the lattice vector in real space \vec{R}_n and of the lattice vector in reciprocal space \vec{G} is

$$\vec{G} \cdot \vec{R}_n = 2\pi(hn_1 + kn_2 + ln_3) = 2\pi N, \quad (2.23)$$

if the a reciprocal lattice vector \vec{G} corresponds to the scattering vector \vec{q} , the scattering amplitude is not vanishing and the Laue conditions are fulfilled corresponding to Bragg's law in scattering. The scattering occurs for distinct regions in the reciprocal space, which are related to the crystalline structure. The use of this will be shown later in the GIWAXS section 2.3.2.

The discussion above only showed the interaction of X-ray photons with matter at the atomic level. The refraction behavior of the X-rays with the interfaces of different media is explained in this section. X-ray scattering can be described by an electromagnetic wave which interacts with matter by scattering or absorption. The electromagnetic wave interacts with the electrons in the sample medium, which is described by the refractive index $n(\vec{r})$. [130] The wave is assumed as monochromatic and plane wave, and when it scatters with the electron cloud in the medium, it results in a spherical wave, where the time dependence of the normal electromagnetic field vector can be neglected for plane waves. Therefore the electromagnetic wave can be described by a field vector [130]

$$\vec{E} = E_0 e^{i\vec{k}_i \cdot \vec{r}}, \quad (2.24)$$

E_0 is amplitude of the electromagnetic wave. The wave vector is described by \vec{k}_i and \vec{r} is the vector of the position. The relation of the wave vector \vec{k}_i to the wavenumber and wavelength can be outlined by the use of equation 2.13

$$|\vec{k}_i| = \frac{2\pi}{\lambda} \quad (2.25)$$

An electric field penetrating a medium can be described by the Helmholtz equation, which includes the refractive index n [130]

$$\Delta \vec{E}(\vec{r}) + k^2 n^2(\vec{r}) \vec{E}(\vec{r}) = 0 \quad (2.26)$$

The refractive index is given by the following equation

$$n(\vec{r}) = 1 - \delta(\vec{r}) + i\beta(\vec{r}), \quad (2.27)$$

where δ is the dispersion relation and β absorption relation. The dispersion relation is given by

$$\delta(\vec{r}) = \rho_e(\vec{r}) r_e \frac{\lambda^2}{2\pi} \sum_{j=1}^N \frac{f_j^0(\vec{q}) + f_j'(E)}{Z} = \rho_e r_e \frac{\lambda^2}{2\pi} \quad (2.28)$$

The absorption relation is described by

$$\beta(\vec{r}) = \rho_e(\vec{r}) r_e \frac{\lambda^2}{2\pi} \sum_{j=1}^N \frac{f_j''(E)}{Z} = \mu(\vec{r}) \frac{\lambda}{4\pi}, \quad (2.29)$$

where μ is the absorption coefficient. The grazing-incidence small-angle X-ray scattering uses for typical experiments a very shallow angle below $< 1^\circ$ with respect to the surface of the investigated sample, see Figure 2.13. The reflection mode in small-angle X-ray scattering has the advantage of a large footprint over the sample surface and improves the statistics of the scattering image, which is recorded with a 2D-detector. The recorded intensities corresponds to a wave vector in reciprocal space \vec{q} , defined by the incident angle \vec{k}_i of the incoming X-ray beam and the diffuse scattering \vec{k}_f at the sample surface, which describes the momentum transfer as described in equation 2.13 and seen in Figure 2.13a. [128]

The relation between the refractive index n , the incident angle α_i and the refracted grazing angle α' is described by Snell's Law.

$$\cos \alpha' = \frac{n_0}{n} \cos \alpha_i \quad (2.30)$$

With the assumption of $n_0 = 1$ for the refractive index of the air interface and the refracted angle $\alpha' = 0$. The relation of the critical angle can be described as follows for $\alpha_i = \alpha_c$

$$\alpha_c \approx \sqrt{2\delta} = \lambda \sqrt{\frac{\rho_e r_e}{\pi}} \quad (2.31)$$

The relation shows a roughly estimation for the critical angle and the proportionality to the dispersion of the material at a certain energy. The experiment from Yoneda was the first experiment to show the relation of the material specific diffuse scattering at the critical angle of the material. [131] The material scattering depth is depending on the incident angle of the X-ray beam. If the incident angle is below the critical angle $\alpha_i < \alpha_c$, total external reflection is appearing and leading to an evanescent wave, which is propagating parallel to the interface in the medium. If the incident angle is larger than the critical angle $\alpha_i > \alpha_c$ the scattering depth is in the micrometer scale. The scattering depth for which the scattered intensity is reduced by $1/e$ is described by Dosch *et al.* with the equation [132]

$$\Lambda = \frac{\lambda}{\sqrt{2\pi}(l_i + l_f)} \quad (2.32)$$

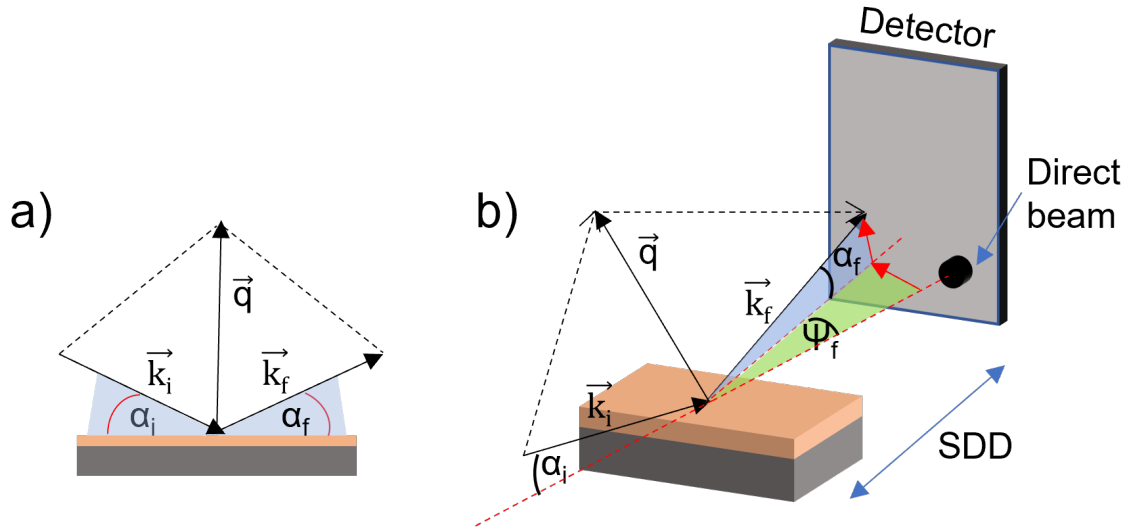


Figure 2.13.: Schematic description of the different scattering geometries. The descriptions show an incoming wave under an angle α_i , which is reflected at the sample surface. The in plane specular reflectance is shown in a) with the angle α_f . In b) the diffuse out of plane scattering is shown with the angle ψ_f .

where λ is the wavelength of the X-ray beam and with $l_{i,f}$ as follows

$$l_{i,f} = [(2\delta - \alpha_{i,f}^2) + \sqrt{(\alpha_{i,f}^2 - 2\delta)^2 + (2\beta)^2}]^{1/2}. \quad (2.33)$$

The equation for the scattering depth 2.32 shows the dependence for the critical angle α_c in the equation 2.33 with the use of equation 2.31. For $\alpha_i \ll \alpha_c$, the scattering depth is very small in the range of 1 nm or smaller. When the incident angle $\alpha_i = \alpha_c$ the scattering depth rises exponentially and the scattering depth can range from some nanometers to several micrometers. If the $\alpha_i \gg \alpha_c$ the scattering depth reaches a plateau of normally some micrometers, depending on the set X-ray energy. If the incident angle α_i is very close to the critical angle α_c the scattering depth can be set very precisely as mentioned before from some nanometers to several micrometers. The different regions for the scattering depth of the X-ray beam into the sample are illustrated in Figure 2.14 and are schematically presented and are adapted from the scattering depth examples from Tolan. [130]

2.3.2. Grazing-Incidence Small-Angle X-ray Scattering (GISAXS)

The position of the scattering on the 2D-detector (specific scattering pixel) can be attributed to a vertical α_f and horizontal ψ_f exit angle, corresponding to a fixed sample-

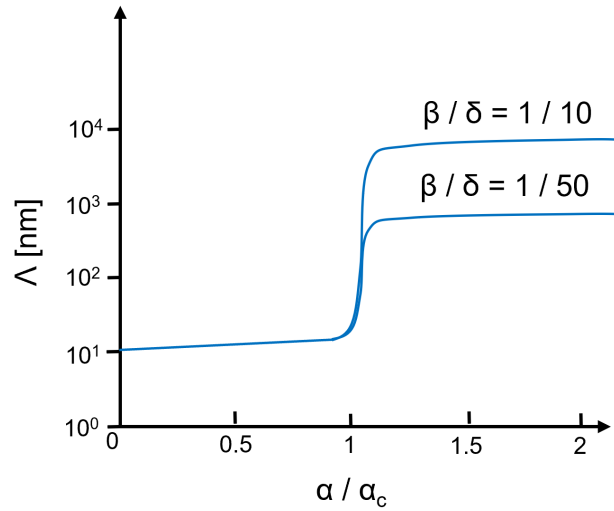


Figure 2.14.: The description shows schematically the relation between the incident angle α_i and the critical angle α_c on the scattering depth Λ of the X-ray beam ($\lambda = 0.154$ nm) into the sample (silicon). [130] Two different ratios ($\beta/\delta = 1/10$ and $\beta/\delta = 1/50$) between the absorption β and dispersion δ show the dependence on the scattering depth near and above the critical angle. [130]

detector distance (SDD), as seen in Figure 2.13b. The angles can be described by the following relation to the scattering vector \vec{q} [133–135]

$$\vec{q} = \frac{2\pi}{\lambda} \begin{pmatrix} q_x \\ q_y \\ q_z \end{pmatrix} = \frac{2\pi}{\lambda} \begin{pmatrix} \cos \alpha_f \cos \psi - \cos \alpha_i \\ \cos \alpha_i \sin \psi \\ \sin \alpha_i + \sin \alpha_f \end{pmatrix} \quad (2.34)$$

The scattering at small incident angles is investigated by grazing-incidence small-angle X-ray scattering (GISAXS), which is a powerful tool to investigate structures near surface at the nanoscale e.g. polymer colloids, nanoparticles, domains of DBC templates. The nanostructures can range up to several hundreds of nanometers. The method can be used to investigate thin film morphology with high statistics, where the X-ray beam is scattering in the vertical and horizontal scattering direction at the electron density of the thin films. The scattering geometry leads to reflection and scattering events at the surface of the thin film and the interfaces, depending on the scattering depth. These events are considered in the distorted wave Born approximation (DWBA) as a first order perturbation of an ideal system. [135] Figure 2.15 shows the possible first order DWBA events. The reflected and scattered waves interfere in the exiting wave. The DWBA can be analysed by simulation programs such as HipGISAXS, Bornagain and IsGISAXS, which

can simulate a complete 2D scattering patterns. [136–138] However, information about lateral and vertical structures can be analysed in the 2D-GISAXS data by the horizontal line-cuts at the Yoneda position and vertical line-cuts. The information gathered from the line-cuts of the GISAXS pattern with an appropriate model can give an average model of the lateral and vertical size distributions from the scattering objects. The differential cross section for diffuse scattering is given by [139, 140]

$$\frac{d\sigma}{d\Omega} = \frac{A\pi^2}{\lambda^4}(1 - n^2) |T_i|^2 |T_f|^2 P_{diff}(\vec{q}) \propto P_{diff}(\vec{q}) \quad (2.35)$$

with the Fresnel coefficients for the incident and outgoing beam for the transmission $T_{i,f}$, the area A which is illuminated and the diffuse scattering factor P_{diff} for the scattered intensity. The diffuse scattering factor P_{diff} for the horizontal line profiles is proportional to N identical objects of a certain spatial distribution and size. The size is given by a form factor F , where the form factor is the Fourier transform of the electron density distribution as described in the section before 2.15. [135, 140] The spatial distribution is set by an interference function, which is described by a structure factor S . [135, 141] The structure factor S is often described by a one-dimensional paracrystalline lattice. For disordered systems the form factor F includes the contributions of the DWBA. The diffuse scattering is then defined by [139]

$$P_{diff}(\vec{q}) \propto NS(\vec{q})F(\vec{q}) \quad (2.36)$$

Several form factors and their independent structure factors are used for the local monodisperse approximation (LMA). The LMA approximation includes only scattering with objects, which have the same form and structure factor and assumes that in the region of the nanoparticles, nanoparticles of the similar size arrange next to each other. [135, 141] The resulting intensity is then the sum of the intensities for each contributing with their respective form and structure factor. The model in this thesis uses a geometrical estimation to help to describe the metal growth on polymers, which is normally more complex modelled with the before mentioned form and structure factors but can be simplified with the geometrical estimation and yields good results, which are confirmed with electronic and topological measurement methods. [63, 69, 70, 142] The average distance between the clusters (D) can be calculated with the following equation

$$D = \frac{2\pi}{q_y^*}, \quad (2.37)$$

where q_y^* is the position of the maxima for the reciprocal space coordinates in lateral direction. The cluster radii and percolation threshold is calculated using the geometrical model, which was introduced by Schwartzkopf *et al.* [142] The geometrical model uses a

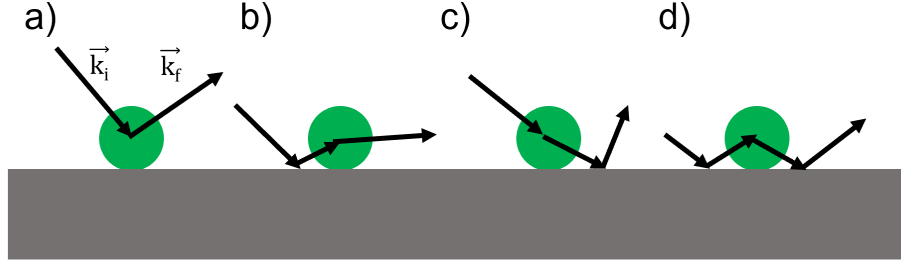


Figure 2.15.: The contributions of the DWBA are shown in the schematic description. a) The incoming beam is scattered directly to the outgoing wave. b) The incident wave is first reflected then scattered and then the wave is outgoing. c) The incoming beam is scattered and reflected before the wave is outgoing. d) Same as in b) followed by another reflection. [135]

volume relation between the volume of the triangle (A_{Δ}) and the volume of the intersecting metal cluster shape (e.g. hemisphere, full sphere, cylinder) to extract the radii of the clusters. In the example shown in Figure 2.16, a hemispherical cluster shape is assumed for the metal clusters showing the relations between the distance, radii and metal thickness ($\delta_{Met.}$). In this thesis we used hemispherical and cylindrical cluster shape to the data analysis of the metal growth. Therefore the following formulas were used

$$R_{Hemi.} = \left(3^{3/2}\pi \frac{\delta_{Met.}}{q_{y,max}^2}\right)^{1/3}, \quad (2.38)$$

$$R_{Cyl.} = \left(3^{1/2}2\pi \frac{\delta_{Met.}}{q_{y,max}^2}\right)^{1/3}, \quad (2.39)$$

where $R_{Hemi.}$ is the radii for hemispherical clusters and $R_{Cyl.}$ for cylindrical clusters.

2.3.3. Grazing-Incidence Wide-Angle X-ray Scattering (GIWAXS)

Grazing-incidence wide-angle X-ray scattering (GIWAXS) is used in this thesis to investigate the crystalline structure evolution in thin films. As for diffraction experiments the intensity in GIWAXS measurements corresponds to the same scattering origins, as described in the scattering section 2.3.1. GIWAXS measurements implies several corrections for the detector e.g. the sensitivity and polarization effects from the synchrotron radiation. The corrections are taken into account with the program used in this thesis GIXSGUI. [143] With GIWAXS thin films can be investigated, which are either crystalline, semi-crystalline or of amorphous nature. The molecular arrangement can be extracted by

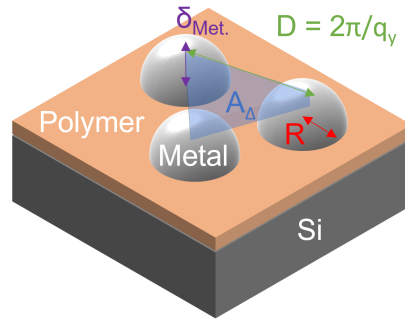


Figure 2.16.: Description of the geometrical model. The geometrical model shows three clusters in a triangle arrangement with a distinct cluster distance from each other (D) and a radii (R). The effective metal thickness is shown by $\delta_{Met.}$. The triangle area (blue) shows the volume relation between the three clusters and the triangle.

the diffraction peaks, as can be seen in Figure 2.17. [134] The amount of crystals relates to the amplitude of the peaks and the average distance of scattering planes to the position of the peaks. The lower limit of the crystallite size D_{hkl} can be described by the Scherrer equation [144]

$$D_{hkl} = \frac{K\lambda}{\Delta(2\Theta)\cos(\Theta_0)} \quad (2.40)$$

where λ is the wavelength of the X-rays and K the Scherrer constant, which value is most often of around 0.93 as derived from the original publication [144]

$$K = 2 \left(\frac{2\ln(2)}{\pi} \right)^{\frac{1}{2}} \approx 0.93 \quad (2.41)$$

$$D_{hkl} = \frac{2\pi K}{\Delta q_{hkl}} \quad (2.42)$$

The crystallite size calculated by the Scherrer equation is calculated in this thesis with the corrections for the peak broadening due to instrumental settings. It is therefore a good estimation of the lower limit of the crystal size.

The Bragg peaks can be further analysed with an extension of the Debye-Scherrer equation [144]

$$\Delta q = \frac{4\pi}{\lambda} \cos\Theta \frac{B}{2}, \quad (2.43)$$

$$B = \sqrt{W_{Exp}^2 - W_{Ins}^2}, \quad (2.44)$$

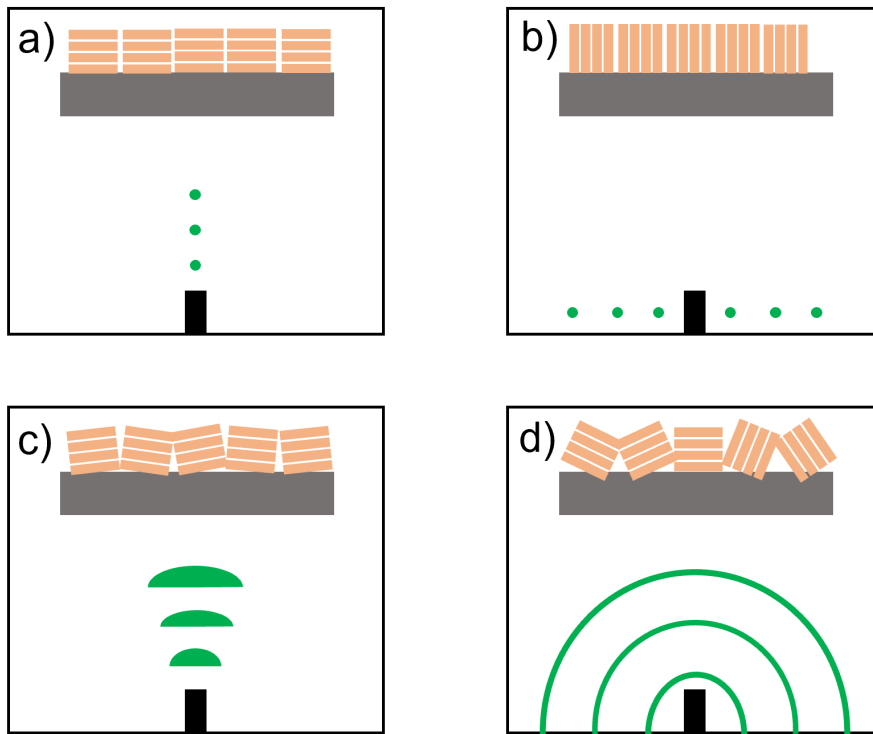


Figure 2.17.: Schematic crystal arrangement of the crystalline part of the polymers in GIWAXS geometry. The lamellae stacking of the polymer backbone is represented by the orange rectangles for a thin film. a) Bragg peaks in the q_z axis are measured, if the lamellae are well ordered in the vertical direction. b) Bragg peaks can be seen in the q_r axis, if the lamellae are ordered in the horizontal direction. c) A broadening of the Bragg peaks is measured, if the lamellae are stacked with rotational disorder. d) Scattering rings are seen, if a full rotational disorder is occurs. [134]

where B is the difference in FWHM in radians from the experiment W_{Exp} and the instrumental resolution W_{Ins} . λ is the wavelength and Θ the corresponding Bragg peak angle of the silver crystalline direction. Typically, in this thesis Bragg peaks in the (111)– and (200)–direction are analysed.

3. Characterization methods

In this chapter the characterization methods used in this thesis are described. Firstly, the imaging methods like atomic force microscopy (AFM) and field emission scanning electron microscopy (FESEM) are introduced followed by the chemical and electronic methods as X-ray photoelectron spectroscopy (XPS), Fourier-transform infrared spectroscopy (FTIR), ultraviolet-visible light spectroscopy and electronic resistance measurements. The scattering methods as grazing incidence small and wide angle X-ray scattering (GISAXS/GIWAXS) were used to correlate the findings from the topological, chemical and electronic measurements.

3.1. Imaging Methods

3.1.1. Atomic force microscopy (AFM)

Atomic force microscopy (AFM) images investigate the topography of sample surfaces e.g. polymers, molecules and thin metal films in the μm and nm range. The sample surface is scanned with a cantilever, which has a sharp tip at the end of the cantilever, see Figure 3.1. [145] A laser is focused at the back side on the cantilever, in order to follow the bending of the cantilever during scanning. The movement of the cantilever for scanning can be precisely controlled with piezo motors. The sample is raster scanned in defined areas line by line to produce a 2D and then 3D height image. The tip recognizes small changes with respect to the sample surface and the bending of the cantilever, which is monitored with the laser. The photodetector recognizes the small changes of the laser position. A computer program calculates the signal changes into a height profile for every measured line scan. The forces that describe the interaction between the tip and the sample surface are derived from the Lenard-Jones Potential, where the potential contains repulsive and attractive forces as the van der Waals force. [146–148] The AFM for this thesis was used in tapping mode, where the tip distance to the sample changes with the tip oscillations. The representative forces repulsive and attractive in tapping mode are both competing with the distance between the tip and the sample surface. The repulsive force function can be expressed as an exponential decay for this distance range

(tapping mode) from the tip to the sample surface, while the attractive force function has an exponential rise at this distance. The combination of both forces is expressed by a minima in the Lenard-Jones Potential. [149] For tapping mode, the attractive force is slightly more dominant compared to the repulsive force. The pristine polymer templates as well as the metal deposited samples were investigated by AFM. The AFM measurements were carried out in the semi-contact mode (tapping mode) with an NTEGRA probe Nano-Laboratory (Russia) using ETALON cantilevers with a tip radius of 10 nm and a resonant frequency of (120 ± 12) kHz (NT-MDT, Russia) for the PS-*b*-PMMA templates. For the measurements with the smaller domain period e.g. PMMA-*b*-P3HT and PLA-*b*-P3HT the NSG03 semi-contact (tapping mode) cantilevers were used. The tip radius for NSG03 is 6 nm and the resonant frequency (90 ± 8) kHz (NT-MDT, Russia). For each sample, surface topography images were taken at minimum three sample positions and using different scan sizes. The line-cuts have a resolution of one data point per 7.8 nm in the lateral direction. The sputtered samples for the AFM images were prepared by DC sputter deposition. The two-dimensional fast Fourier transformation (2D-FFT) of the phase images from AFM were performed with azimuthal integration to determine the domain period of the copolymer with the program Gwyddion (v2.53). [150] The program Gwyddion was used to analyze the AFM data, e.g. to extract the root mean square (rms) roughness values and domain period. The AFM images were visualized with WSxM (WSxM software v5.0). [151]

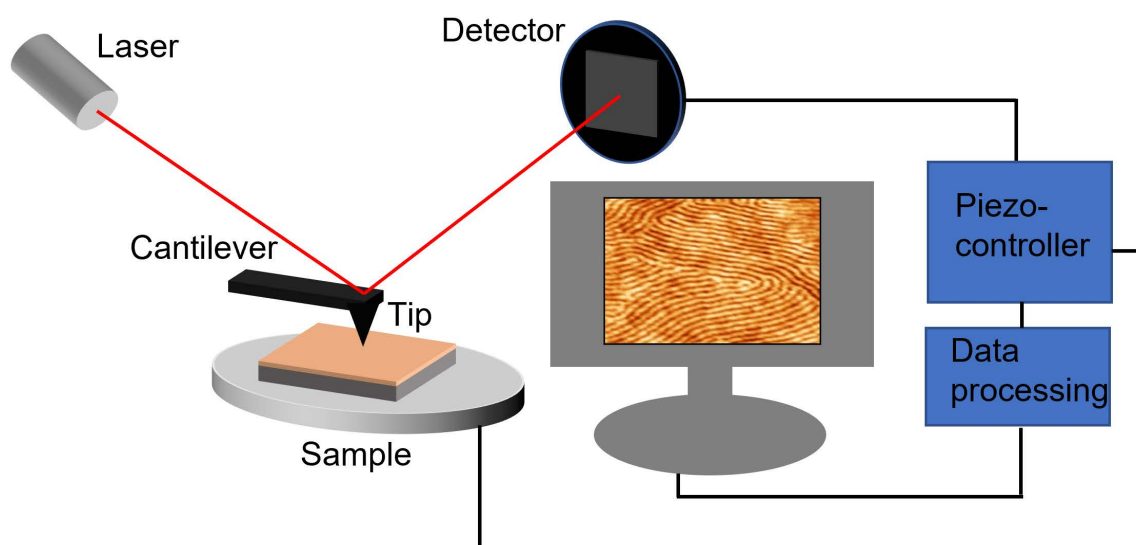


Figure 3.1.: Schematic description of an Atomic force microscopy (AFM). The sample is scanned with a very sharp tip mounted on a cantilever. The cantilever is vibrating with a resonance frequency, and a laser points on the cantilever and is reflected to a detector. If the tip experience force changes during the scanning over the sample, the cantilever will change its frequency. This frequency change is then detected by a deviation of the reflected laser beam on the cantilever and measured at the detector. The signal on the detector is then converted to a height profile. The example AFM height image shows a pristine PS-*b*-PMMA DBC template after solvent vapor annealing with a fingerprint lamella domain structure.

3.1.2. Scanning electron microscope (SEM)

The scanning electron microscope (SEM) is using focused electrons to measure the interaction between the sample and the incoming electrons, see Figure 3.2. Several interaction events occur depending on the incoming photoelectron energy: Auger electrons, secondary electrons, backscattering electrons, characteristic X-rays, continuum X-rays, Cathodo-luminescence, X-ray fluorescence, transmitted electrons, diffracted electrons and scattered electrons. For the measurements usually secondary (depicting the topography) or backscattered (depicting the composition) electrons are detected and used to reconstruct the sample surface depending on their different penetration depth. Backscattered electrons have higher energies (>50 eV) compared to secondary electrons (<50 eV). A SEM consists of an electron gun to produce the electron beam, condenser lenses to focus the electron beam, deflection coils to move the electron beam over the sample and high vacuum to reduce interactions of the electron beam with the atmosphere. The resolution

of a SEM is given by the minimum spot size, which can be reduced with a field emission gun.

For Ag, field emission scanning electron microscopy (FESEM) images were obtained with a Zeiss Gemini NVision 40 (Carl Zeiss SMT, Germany) at a low working distance of 3.1 mm with an accelerating voltage of 1.5 kV. A secondary electron in-lens detector was used to measure the secondary electron signal in beam direction without backscattering electrons.

For Al, FESEM images were obtained using a Zeiss Ultra Plus (Carl Zeiss SMT, Germany) at an aperture size of 10 μm with an accelerating voltage of 3 kV. The high voltage 3 kV is used for the aluminum coated samples to avoid accumulation of charges. A secondary electron in-lens detector was used to measure the secondary electron signal in beam direction without backscattering electrons.

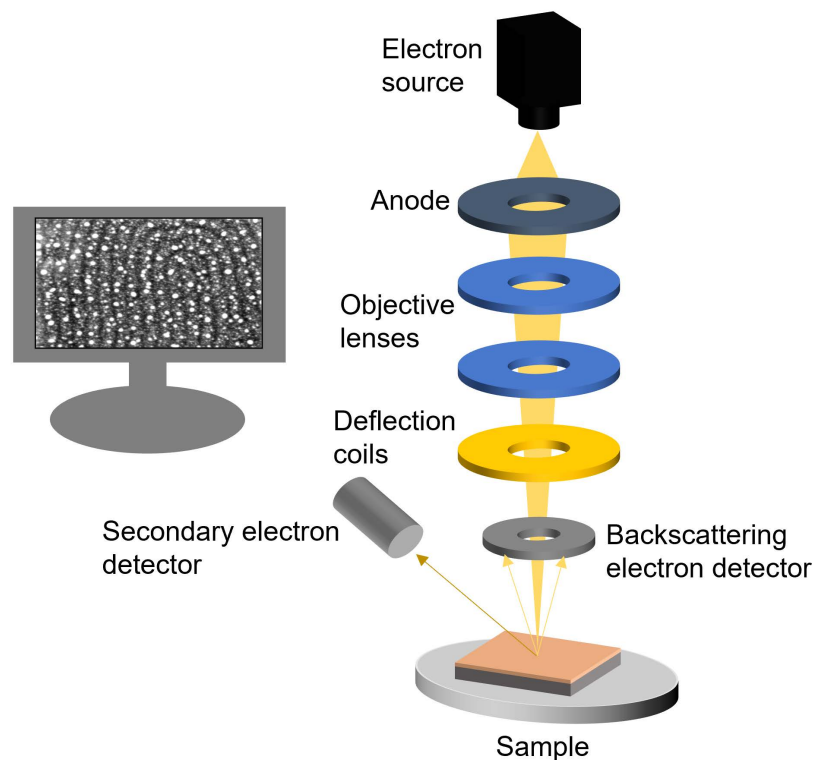


Figure 3.2.: Schematic description of an FESEM. An electron gun emits electrons, which are accelerated towards the anode and guided by an objective lenses system. Before the beam reaches the sample the beam is focused with deflection coils on the way to the sample. When the beam hits the sample surface, electrons can be ejected. The mostly detected electron are e.g. backscattered electrons or secondary electrons with their specific electron detector.

3.2. Spectroscopic Methods

3.2.1. X-ray photoelectron spectroscopy (XPS)

X-ray photoelectron spectroscopy (XPS) uses the photoelectric effect to reveal the chemistry of a material composition on a surface. [152] Typically Al $K\alpha$ or Mg $K\alpha$ sources are used to produce X-rays, which are irradiating the sample surface with sufficient energy to excite electrons from the core levels of the corresponding atoms in the materials, see Figure 3.3. The XPS spectrum is received by measuring the kinetic energy of the escaping electrons with an analyzer and calculate the binding energies with the use of the measured kinetic energy by the following formula

$$E_b = h\nu - E_{Kin} - \Phi_w, \quad (3.1)$$

where E_b is the binding energy of the electrons, $h\nu$ is the photon energy of the incoming X-rays, E_{Kin} is the measured kinetic energy of the electrons and Φ_w is the work function of a material. The distance between the analyzer and the sample is around 1 m, therefore a high vacuum system is needed for the XPS analysis to obtain enough electron counts during the measurement of the XPS spectra. XPS (Omicron Nano-Technology GmbH, Germany) was applied to investigate the chemical environment of Ag and Al clusters on the different polymer templates (PS, PMMA, PS-*b*-PMMA, P3HT and PMMA-*b*-P3HT) before and directly after 1nm Ag and Al sputter deposition. The DC sputter chamber was directly connected to the XPS device at the University of Kiel (CAU, Institut für Materialwissenschaft). The XPS was operated with an Al anode at a power of 240W and spectra were taken with a VSW 100 hemispherical analyser with pass energies of 100 eV (survey) and 30 eV (high-resolution spectra). CasaXPS (version 2.3.19, Casa Software Ltd) was used to charge reference the spectra using the carbon C 1s at 284.5 eV and the oxygen O 1s at 532 eV to quantify the amount and chemical shifts of carbonyl moieties before and after metal deposition.

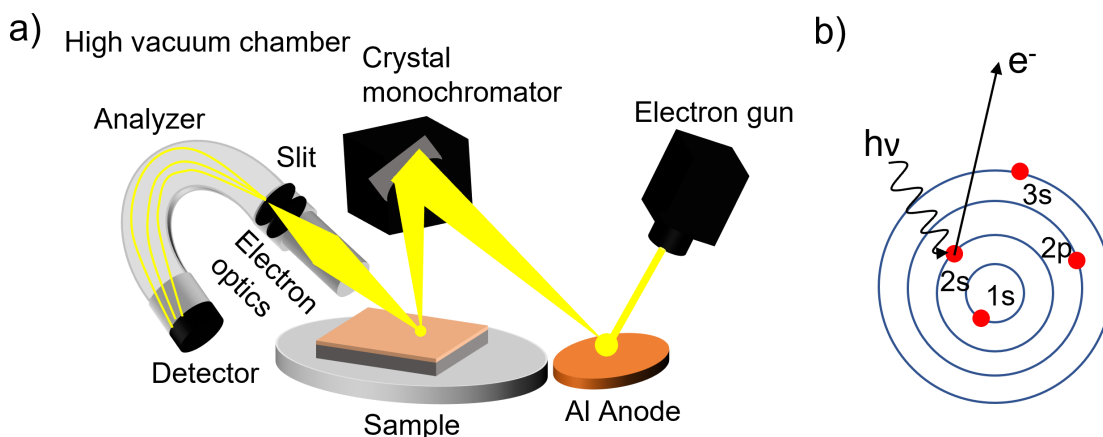


Figure 3.3.: Schematic description of a scanning electron microscope (XPS): a) An electron gun emits electrons, which reach an aluminium anode. Electrons with specific electron energies in the range around of 0.3 to 1.5 keV are produced and monochromatized with the help of a crystal monochromator. The electrons reaching the sample can kick out electrons from the atoms of the sample surface. The electrons in the analyzer are selected according to their kinetic energy and measured at the detector. b) Schematic drawing of the XPS process with high eV incoming X-ray beam (~ 1.5 keV) interacting with the core electrons of the surface atoms of the sample. Photoelectrons and Auger electrons can be measured with the hemispherical analyzer.

3.2.2. Fourier-transform infrared (FTIR) spectroscopy

The spectra of Fourier-transform infrared (FTIR) spectroscopy contain detailed information about the chemical environment of the molecular structure in the sample, e.g. the vibrational and rotational absorption bands of the molecules in the sample. [153] The IR light Fourier-transform infrared (FTIR) spectroscopy uses a broadband infrared source to guide IR light through an interferometer with a fixed mirror and a movable mirror. The IR light excite molecular vibrations and rotations in the molecule with a characteristic chemical structure for the functional groups. The movable mirror creates a pathway difference $\delta = 2x$ of the light compared to the fixed mirror, see Figure 3.4, which results in a interference signal and can be detected as the so called interferogram. The interferogram is the recorded signal over the pathway difference δ . The FTIR set-up is used as a Michelson interferometer, where the light beams split into two beams and one is reaching the fixed mirror and the other one is reaching the mirror with a pathway difference δ , the beams then transmit from the sample and reach the detector. A signal at the detector is created depending on the constructive inference of the beams depending on the molecular

vibrational and rotational states in the sample. For FTIR all frequencies are measured at the same time and the interferogram $I(x)$ is described by the superposition [154]

$$I(x) = I_0[1 + \cos(2\pi\nu x)] \quad (3.2)$$

The intensity is dependent on the optical path length δ with

$$I(\delta) = \int_{-\infty}^{+\infty} I(\nu)\cos(2\pi\nu\delta)d\nu \quad (3.3)$$

Then the complex Fourier-transformation can be written as

$$I(\nu) = \int_{-\infty}^{+\infty} I(\delta)D(\nu)e^{i(2\pi\nu\delta)}d\delta \quad (3.4)$$

where $I(\nu)$ is the intensity of the light source with a frequency ν . The measured interferogram uses a Fourier transformation to convert the spectra into a spectra as a function of the inverse wavelength. The spectra is then converted into an absorption spectrum

$$A(\nu) = -\log(I(\nu)/I_0) \quad (3.5)$$

The spectral data has a high resolution over a wide spectral range, due to the measured frequencies at the same time. The absorption spectra peaks represent the corresponding molecular vibration and rotation states from the sample. The spectra is then specific of the sample composition: The functional groups from polymers in the sample and the spectra can be compared to literature values to identify the specific functional groups. Fourier-transform infrared (FTIR) spectroscopy was performed on pristine polymer thin films (PS, PMMA, PS-*b*-PMMA) on silicon substrates and sputter coated with 1 and 2 nm effective deposited Ag. Further thin DBC films (PMMA-*b*-P3HT) on silicon substrates at selected thickness of Ag ($\delta_{Ag} = 1, 2$ and 8 nm) were measured. The frequency range from 800 to 4000 cm^{-1} was measured using an Equinox 55 spectrometer (Bruker Optik GmbH, Germany) with a resolution of 2 cm^{-1} and the signal averaging was done over 256 scans. A custom made copper sample holder was used to place the specimen in transmission in the setup. The FTIR instrument is purged with dry air and CO_2 filtered air stream, throughout all measurement for minimization of the concentration of IR active molecules.

3.2.3. Ultraviolet–visible (UV-vis) spectroscopy

Ultraviolet–visible (UV-vis) spectroscopy measures the absorption or reflection of a sample in the ultraviolet and visible wavelength regions. A schematic description of the used UV-vis setup can be seen in Figure 3.5a. The incident light can interact with the sample

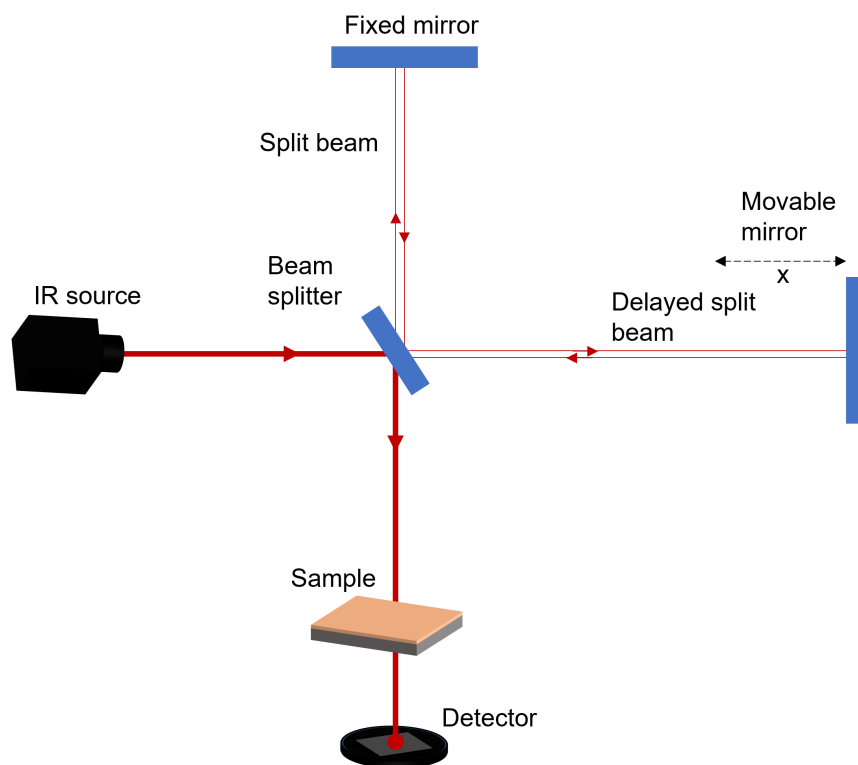


Figure 3.4.: Schematic description of FTIR. A light source produces IR light and is guided through a Michelson interferometer. The beam is split into two beams and a movable mirror produces different interference pattern. The pattern are hitting the sample and interact with the samples molecular structure. The outgoing beam is measured by a detector and using a Fourier Transformation the signal is calculated over the inverse frequency.

and endures to absorption effects of the atoms, molecules or clusters. Absorption effects can be electronic transitions of the electrons from the ground state to the excited state, e.g. in polymers, or plasmon absorption effects of metal nanoparticles or thin metal films. Surface plasmon resonance of thin metal layers on top of a dielectric film and localized plasmon resonance (LSPR) from metal clusters can be detected with UV-vis. The principle of the LSPR effect is described in Figure 3.5b. The LSPR effect is caused by incident light shining on a metal nanoparticle, which leads to coherent oscillations of the conduction band electrons inside the metal nanoparticles. The oscillation induces a high electric field at the particles surface and causes an absorption at the plasmon frequency. Therefore, the sizes of the metal clusters must be smaller than the wavelength of the incoming light. [22, 23]

For PS-*b*-PMMA, time-resolved UV-Vis measurements were performed in reflection mode at 55° incident angle due to geometric constraints of the sputter chamber. The wavelength range from 300-800 nm from a 75W Xenon lamp (LOT-Oriel, Germany) was guided by fiber optics and focused by lenses (Thorlabs, USA) onto the center of the sample surface. The focused spot size was (0.5×0.5) mm². The reflected spectra were collected by lenses and transmitted by a fiber optic to a Glacier X spectrometer (B&W TEK, USA) with an acquisition time of 5 ms and averaged over 100 spectra in a period of 2 s. The binning of the spectra for statistical improvement was done with a median over 5 data points.

For PMMA-*b*-P3HT, time-resolved UV-Vis measurements were performed in the reflection mode at a 55° incident angle. An Ocean insight DH-2000a (Ocean Optics, USA) was guided by fiber optics and onto the center of the sample surface. The focused spot size was (0.5×0.5) mm². The reflected spectra were collected and transmitted by a fiber optic to an Ocean Optics spectrometer (STS-UV) for wavelength range from 250 to 650 nm with an integration time of 200 ms and average over 5 measurements.

The relative reflectance change was recorded by the ratio between the background subtracted measured reflectance signal during the metal growth on the polymer sample and the signal of the pristine polymer template. The formula for the measured specular reflectance (SR) is given by the recorded spectra during sputter deposition (R_{sd}) reduced by the dark spectra (R_d) and divided by the pristine polymer spectra (R_p) reduced by the dark spectra (R_d) as follows

$$SR = \frac{(R_{sd} - R_d)}{(R_p - R_d)} \times 100\% \quad (3.6)$$

Due to technical restrictions of the sputter chambers, it was only possible to measure the reflectivity change from the metal on the polymer compared to the pristine polymer. This results in a relative reflectivity change starting at 100% for the bare polymer template and then increasing reflectivity due to the metal deposition.

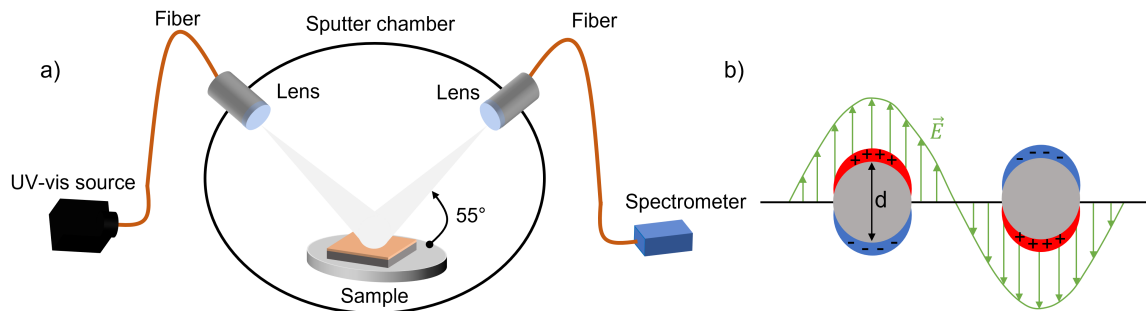


Figure 3.5.: a) Schematic description of UV-vis. A white light source produces light in the visible and ultraviolet range. The light is guided with optical fibers and focused with lenses on the sample surface. The reflected beam from the sample is collected again by an optical fiber and reaches a spectrometer. b) Schematic description of the oscillation from conduction band electrons inside metal nanoparticles caused by incident light.

3.3. Electronic Methods

3.3.1. Resistance Measurements

During the sputter deposition experiment the surface resistance was measured *in situ* with an acquisition time of 270 ms using a multimeter Keithley 2000 (Tektronix, Germany) and a LabVIEW based software shown in Figure 3.6. The two-wire resistance measurement setup consists of two coaxial cables insulated by shrinking tube separately fixed at the sample holder, seen in Figure 3.7a. The sample substrate is insulated with 125 μm Kapton foil (GoodFellow, U.S.A.) to the sample holder. Prior to evacuation the cables are connected with 10 μL silver conductive lacquer (Silver DAG 1415, Plano GmbH, Germany) onto the edges in 8 mm distance. The four-point resistance measurement setup consists of four coaxial cables separately fixed and insulated at the sample holder, seen in Figure 3.7b. Prior to evacuation the cables were connected with gold pins on the contacts (3×15) mm^2 , which were placed onto the sample in 3 mm distance by applying Ag conductive lacquer (Silver DAG 1415, Plano GmbH, Germany). For determination of the insulator-to-metal transition (IMT), the *in situ* resistance curve was partially fitted with a Boltzmann sigmoidal function using the program Igor Pro 6.37. [155] A current is applied to the outer pins and the inner pins are measuring the resulting voltage. The

sheet resistance R_{sh} is calculated by the measured resistance of the multimeter R and the geometrical factors as the length from the sample (L) and the width of the sample (W):

$$R_{sh} = \frac{RW}{L} \quad (3.7)$$

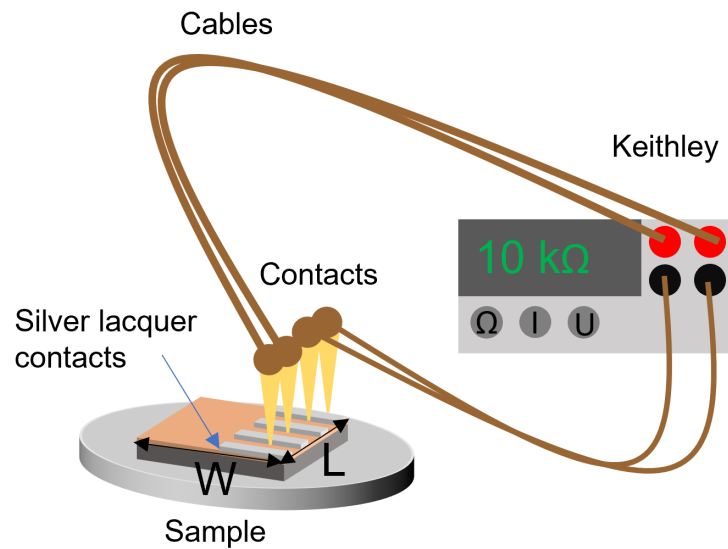


Figure 3.6.: Schematic description of how to measure the resistance of thin films. The sheet resistance of a thin film is measured using a multimeter. The four-point measurement is taken with four gold pin contacts on silver lacquer contacts in the same distance from each other. The gold pin contacts are connected with coaxial cables to the multimeter to measure the four-point sheet resistance.

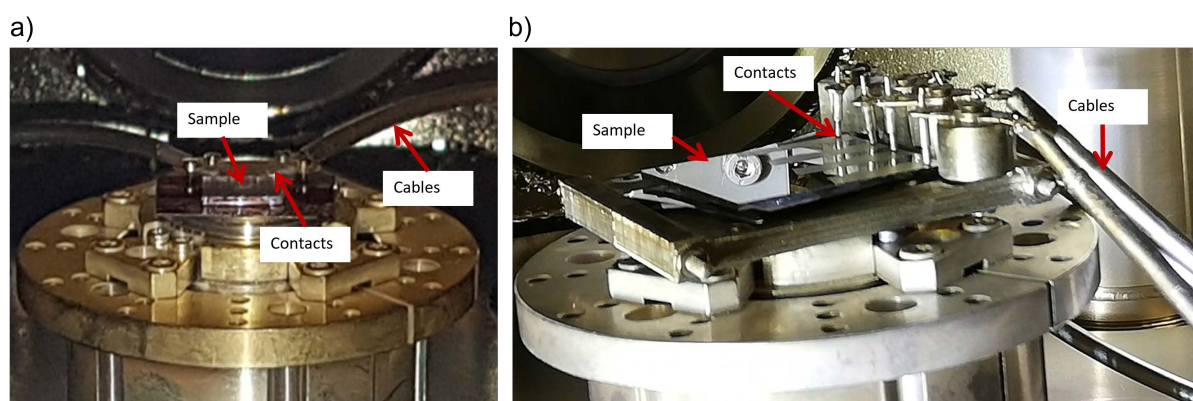


Figure 3.7.: Schematic description of 2- and 4-point resistance measurements. a) 2-point *in situ* measurement setup used for the Ag on PS-*b*-PMMA *in situ* samples. Reprinted with permission from [69]. Copyright 2019 American Chemical Society. b) 4-point *in situ* measurement setup used for the Ag on PMMA-*b*-P3HT *in situ* samples. Reprinted with permission from [70]. Copyright 2021 American Chemical Society.

3.4. Scattering Methods

In this section the data analysis of the small angle scattering methods used in this thesis are shown and explained using the example of the PMMA-*b*-P3HT DBC template with Ag sputter deposition on the template.

3.4.1. GISAXS

To reveal the average morphology evolution of the metal clusters on the polymer templates grazing incidence small angle scattering (GISAXS) is a powerful tool, due to the enlarged footprint and high statistical information. The typical beam size of around $20 \times 20 \mu\text{m}^2$ increases the gained information compared to local area methods such as AFM or SEM. In Figure 3.8, a schematic description of the GISAXS setup is shown. In Figure 3.9 the GISAXS data treatment for the analysis of the distances, radii for the metal clusters on the polymers is shown, how it was performed in the framework of this thesis. The corresponding line-cuts to analyse the specific regions of interests are marked in the 2D GISAXS data. The GISAXS data in Figure 3.9a shows the DBC template PMMA-*b*-P3HT and 1.5 nm of Ag sputtered on the DBC template. The Ag clusters can be seen by the broad cluster peak on the left side of the GISAXS pattern in a light blue color. The maximum of intensity can be seen around the Yoneda region of the metal and polymer. During the metal deposition the Yoneda region shifts from the polymer region (lower critical angle) to the metal region (higher critical angle), due to the change from lower

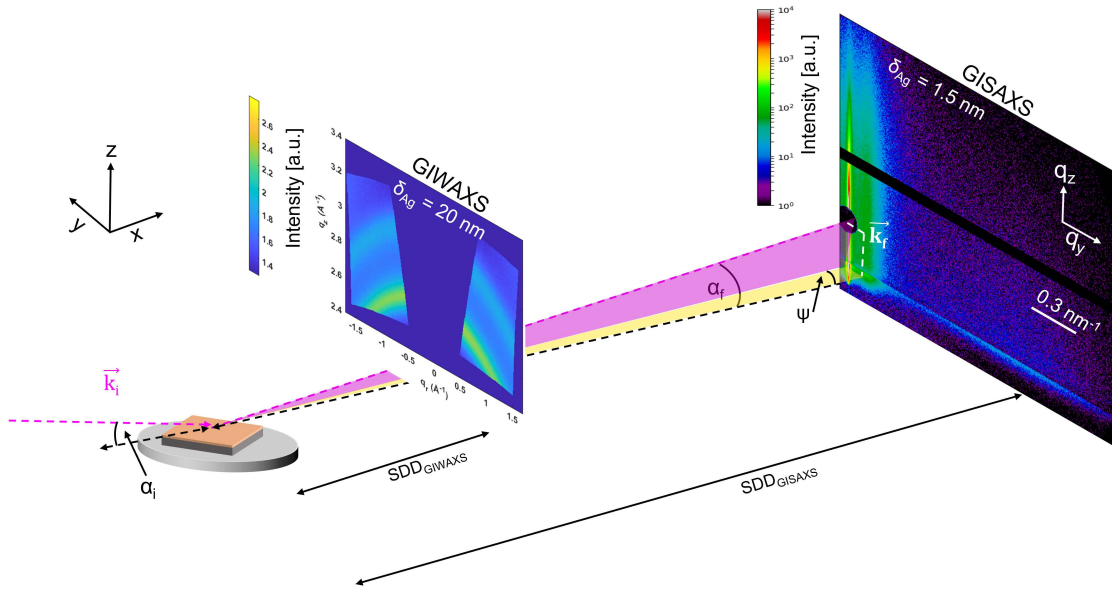


Figure 3.8.: Description of the setup for simultaneous grazing incidence small and wide angle scattering. The incoming X-ray beam (pink dashed line) encounters at a very small angle of incidence on the sample surface (typically $\alpha_i < 1^\circ$). The exit angle α_f (pink dashed line) defines the angle for the specular beam in vertical direction and ψ (orange area) the angle for the lateral direction. The scattering vectors k_f shows the outgoing scattering event e.g. domain spacing for the DBC template, average cluster distance or the metal crystal lattice. Two 2D-detector records the scattered intensity for wide and small angle scattering in a sample to detector distance (SDD) between $SDD_{GIWAXS} \approx 100\text{-}300$ mm and $SDD_{GISAXS} \approx 2000\text{-}4000$ mm.

electron density (polymer) to higher electron density (metal) $\alpha_i = \sqrt{2\delta} \propto \sqrt{\rho}$. The red box marks the Yoneda region for the lateral line-cut to analyse the morphology evolution of the metal cluster peak and the DBC domain peak. At $\delta_{Ag} = 1.5$ nm the domain peak is shown by a broad pseudo Bragg peak in green color at a higher q value compared to the Ag clusters. The domain peak yields information about the lateral ordering of the DBC template (FWHM of the domain peak) and the average distance between the domains. The yellow box shows the vertical line-cut at $q_y = 0 \text{ nm}^{-1}$ and gives information about the vertical arrangement (film thickness) of the polymer or metal-polymer compound. In Figure 3.9b the lateral line-cut of the GISAXS data is shown with the characteristic domain peak of the DBC template and the broad cluster peak. The data (black data points) in Figure 3.9b was analysed using the DPDAK software package with fitting three Lorentz functions (red line) for the polymer region at $q_y = 0 \text{ nm}^{-1}$, for the domain peak region at around $q_y = 0.15 \text{ nm}^{-1}$ and the dynamic cluster region with changing q_y

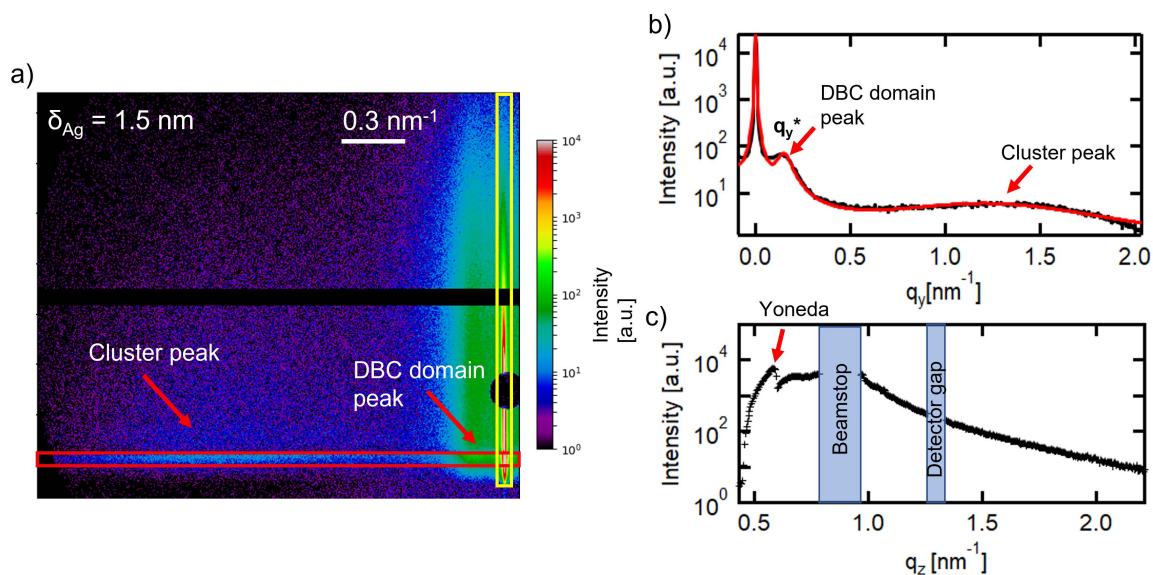


Figure 3.9.: Description of the GISAXS analysis. a) 2D-GISAXS data of $\delta_{Ag} = 1.5$ nm Ag sputter deposition with distinct scattering features (metal cluster peak, DBC pseudo Bragg domain peak and polymer scattering in the yellow box). b) Lateral line-cut (Yoneda cut) with the scattering features in the lateral direction. The features are fitted with three Lorentzian functions. c) Vertical line-cut shows the Yoneda region going from the polymer Yoneda to the metal Yoneda region during sputter deposition. From the bottom, the first gap is corresponding to the beamstop to cover the specular beam and the second gap is corresponding to the gap of the detector for the electronics.

value during the deposition. [156] The vertical cut at $q_y = 0 \text{ nm}^{-1}$ is shown in Figure 3.9c with the Yoneda peak, which is changing from the Yoneda peak position originating from the polymer to the Yoneda peak position corresponding to Ag. The vertical cut is used to calculate the final metal film thickness at the end of the deposition and to compare it with the measured quartz crystal microbalance (QCM) value. [157] The film thickness for all samples were in good agreement with the findings of the QCM values.

3.4.2. GIWAXS

In order to follow the crystallization of the metal clusters growing to thin metal films GIWAXS is performed. GIWAXS was performed at the same time as the GISAXS measurements and therefore can be correlated to the morphology evolution. In Figure 3.10 an example is shown how the typical metal rings of the fcc crystalline arrangement are measured with GIWAXS. Figure 3.10a shows a measured GIWAXS pattern for $\delta_{Ag} = 20$ nm

with the corresponding rings for the (111) and (200)-direction of the crystalline fcc lattice. In Figure 3.10b the azimuthal cuts are shown and reveal the evolution of the (111)- and (200)-direction of Ag during sputter deposition. The data was analysed with the GIXS-GUI software to transform the GIWAXS data in the right format in q-space. [143] The *in situ* samples were measured with a frame rate of 2 Hz and selective GIWAXS pattern at $\delta_{Ag} = 1, 2, 3, 5, 8, 10$ and 12 nm were chosen to investigate the crystalline size evolution with GIXSGUI. The scattered wave vector not only contains the q_z -component but also contributions from q_x or q_y , which cannot be neglected for small-angles in GIWAXS geometry. For $q_y = 0$ in the specular plane as it can be seen in Figure 2.12b, the scattering cannot be investigated by one scattering vector and has therefore a q_x and q_z -component. This leads to a problem for 2D detectors, which show a projection of the allowed Bragg reflexes of the Ewald sphere, where a certain scattering area cannot be represented. This area is shown in Figure 3.10a with a reshaped 2D GIWAXS image and is called missing wedge ($q_x \neq 0$).

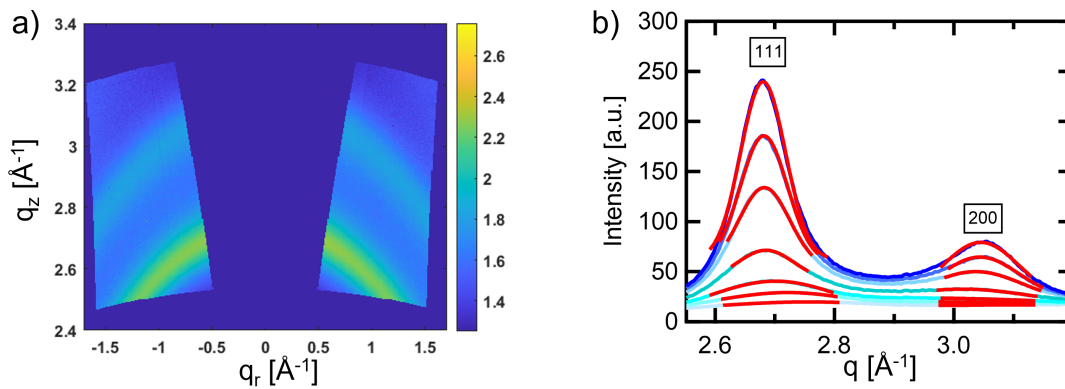


Figure 3.10.: Description of the GIWAXS analysis. a) 2D-GIWAXS data showing the Ag crystalline peaks of the (111) and (200) direction. b) The azimuthal integration shows the evolution of the crystalline peak during the Ag deposition to the Ag bulk values with the data in blue (from light to dark blue with increasing Ag thickness) and the fits for the (111) and (200) direction in red. Reprinted with permission from [70]. Copyright 2021 American Chemical Society.

4. Sample preparation

In this chapter the materials and the thin film preparation is shown. The materials are divided into three sections: The substrate material, the polymers on the substrate and the metal, which is decorating the polymer thin films. In the thin film section the substrate cleaning process is explained and the polymer deposition with the spin-coating parameters is shown. For PS-*b*-PMMA and PLA-*b*-P3HT the solvent vapor annealing technique is demonstrated. The last section explains the sputter deposition onto the polymer templates with the different metal materials silver (Ag), aluminium (Al) and gold (Au).

4.1. Materials

In this section the different materials are shown, which are used during the thesis project: substrates, polymers and metals.

4.1.1. Substrate Materials

Glass

Microscope glass slides (Carl Roth GmbH, Germany) $76 \times 26 \text{ mm}^2$ were cut into (sample size $20 \times 15 \text{ mm}^2$) pieces and used as substrates for the PS-*b*-PMMA templates. Microscope glass slides (Carl Roth GmbH, Germany) were used as substrates for 4-point resistivity measurements (sample size $25 \times 30 \text{ mm}^2$) for the PMMA-*b*-P3HT templates. The substrates are cleaned for 30 minutes in acetone using an ultrasonic bath and subsequently rinsed with acetone, isopropanol and ultra-clean water (ELGA Purelab Ultra, $18.2 \text{ M}\Omega\text{cm}$) in order to remove all organic residuals, followed by the acid cleaning as explained in the section 4.2.

Silicon

The substrates are cleaned for 30 minutes in acetone using an ultrasonic bath and subsequently rinsed with acetone, isopropanol and ultra-clean water (ELGA Purelab Ultra, $18.2 \text{ M}\Omega\text{cm}$) in order to remove all organic residuals, followed by the acid cleaning as explained

in the section 4.2. One-side polished boron-doped silicon (100) (Si-Mat, Germany) were used as substrates (sample size $12 \times 15 \text{ mm}^2$).

4.1.2. Polymers

The polymers were dissolved in a toluene solution (purity $\geq 99.5 \%$, Carl Roth GmbH, Germany). The concentration of the polymers was chosen in such a way that the resulting thin films have a film thickness of $(55 \pm 4) \text{ nm}$ for PS-*b*-PMMA and the corresponding homopolymers (PS and PMMA). For PMMA-*b*-P3HT the film thickness of $(20 \pm 5) \text{ nm}$ was used, same for the homopolymers P3HT and PMMA with the corresponding molecular weight. For PLA-*b*-P3HT the film thickness of $(137 \pm 7) \text{ nm}$ was used. The thickness of the polymers were determined with AFM measurements. First a cut was done as seen in Figure A.1a, followed by line-cuts as in Figure A.1b (e.g. blue line) over the two areas to see the homogeneity of the two areas. Then the black box was used to define an area which counts the height values in this area. The results show two distinct peaks for the two areas. The distance between the areas defines the thickness of the polymer films with a higher statistics compared to several line-cuts. The results for the line-cuts are seen in Figure A.2 and Gaussian fits are used to determine the peaks. The polymers used are shown in Figure 4.1.

Polystyrene (PS)

Polystyrene is a commonly used polymer and is applied in different applications such as packaging, insulating material, automotive and more [158–160]. The polymer is nowadays further used in nanotechnology such as a flat polymer template, which is mostly chemical inert compared to other polymers with the use for polymer composites [63, 161]. Here PS with a molecular weight of $M_n = 68 \text{ kg/mol}$, $M_w = 71 \text{ kg/mol}$ and $\text{PDI} = 1.04$ is used for the comparison of the first DBC template (Polymer Source Inc., Canada). The molecular weight was chosen to be comparable with the molecular weight of the DBC template.

Polymethylmethacrylate (PMMA)

Polymethylmethacrylate is another common used polymer, which is often used e.g. in prosthodontic and denture-based applications or as acrylic glass [162, 163]. In nanotechnology it is for e.g. used in polymer transistor devices, THz technology and photocatalysis applications [164–167]. Here PMMA with a molecular weight of $M_n = 70 \text{ kg/mol}$, $M_w = 75 \text{ kg/mol}$ and $\text{PDI} = 1.07$ is used for the comparison of the first DBC template. The second molecular weight was $M_n = 17 \text{ kg/mol}$, $M_w = 22 \text{ kg/mol}$ and $\text{PDI} = 1.29$ (Poly-

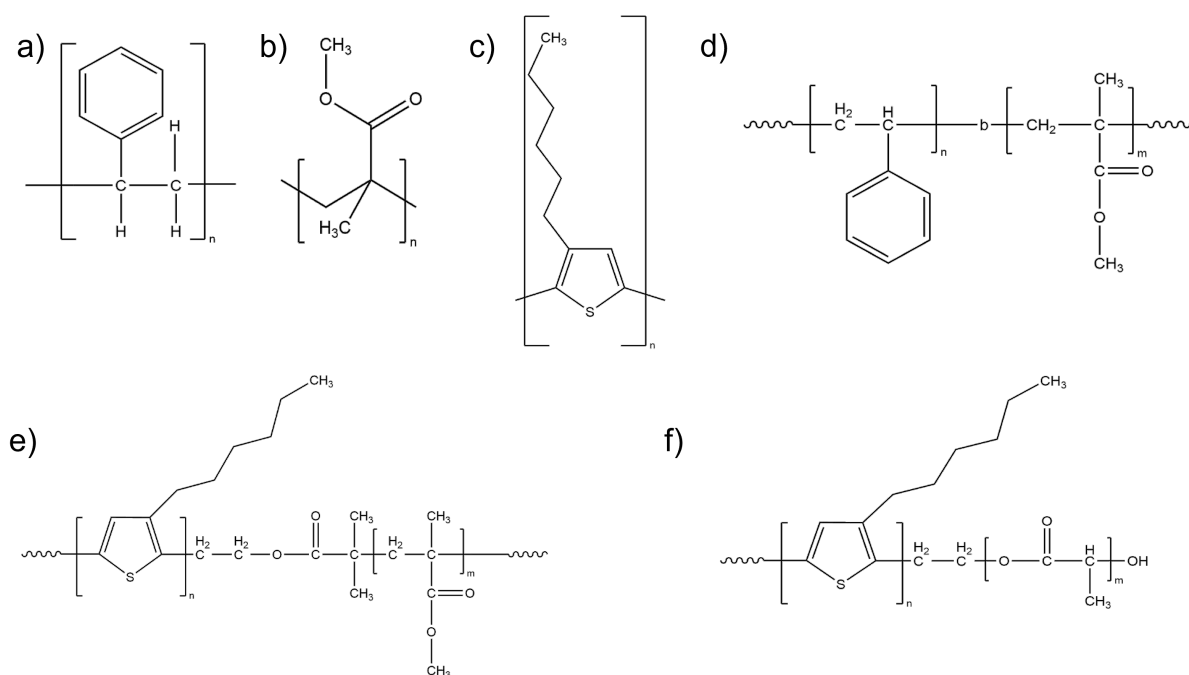


Figure 4.1.: Chemical structure of the used polymers. a) polystyrene (PS), b) polymethylmethacrylate (PMMA), c) poly(3-hexylthiophen-2,5-diyl) (P3HT), d) PS-*b*-PMMA, e) PMMA-*b*-P3HT, f) PLA-*b*-P3HT

mer Source Inc., Canada). The molecular weights were chosen to be comparable with the molecular weights of the DBC's templates.

PS-*b*-PMMA copolymer

The diblock PS-*b*-PMMA is used as a model system to investigate the Ag formation on DBC templates with different measurement techniques at the same time e.g. UV-vis, GISAXS and resistance. The fabrication of nanostructures on macroscopic scale with desired properties are of huge interest in science and industry for the production of sensors and circuit boards in the nanoscale. The deposition of thin metal layers on microphase-separated polystyrene-*b*-polymethylmethacrylate (PS-*b*-PMMA) thin films is one important example of using nanostructured polymer-templates to guide the metal growth. [4, 5, 64] This so-called selective wetting describes the preferred growth of metal particles on one polymer block, which can be due to different surface energies (mobility of the clusters) on the polymer, embedding or chemical interaction, as three prominent driving forces. [69, 168] The understanding of the nanostructure self-assembly could be useful for thin film applications in organic photovoltaics and organic electronics. [53, 169, 170] PS-*b*-PMMA is used with a molecular weight of $M_n = 66$ - b - 67 kg/mol and a polydispersity

index of PDI = 1.1 with $M_w = 70.5$ kg/mol and PDI = 1.07 for the PS block (Polymer Source Inc., Canada).

Poly(3-hexylthiophen-2,5-diyl) (P3HT)

P3HT is a conjugated polymer which is used e.g. in organic photovoltaics and transistor technology. Similar to semiconductors P3HT can be used to generate a current under illumination. If the energy is higher than the band gap of the material, similar to semiconductors, charges can be generated and travel along the polymer interfaces until recombination or charge collection at the current collector (electrode), for this acceptor and donor material is needed and P3HT is commonly used as the donor material. P3HT is the working horse of the conjugated polymers, because it is investigated in a lot of scientific studies for many applications such as OPV, organic transistor, organic electronics, photocatalytic devices, organic light emitting diodes (OLEDs) and many more. [171–177] P3HT with a molecular weight of $M_n = 13.5$ kg/mol, $M_w = 17$ kg/mol is used with a polydispersity index of PDI = 1.25 and a regioregularity of 90% (H-T) (Polymer Source Inc., Canada).

PMMA-*b*-P3HT copolymer

A conjugated polymer as P3HT can be used in various applications in organic photovoltaics and organic electronics as described above and the diblock can be used to nanostructure the P3HT domain. The diblock copolymer yields the possibility to easily nanostructure the P3HT. The PMMA can remain in the P3HT nanostructured network or can be removed by e.g. acetic acid treatment and UV-light exposure. [178, 179] The diblock PMMA-*b*-P3HT was used with $M_n = 22$ - b - 15 kg/mol and PDI = 2.3 with $M_w = 17.2$ kg/mol and PDI = 1.15 for the P3HT block and a regioregularity of 90% (H-T) (Polymer Source Inc., Canada).

PLA-*b*-P3HT copolymer

PLA is a biocompatible polymer, which can be removed easily from the DBC template by UV light and a green solvent such as water or ethanol. [53] Therefore PLA-*b*-P3HT can be used to create free standing nanostructure of the P3HT polymer domain by removing the PLA domain. The free standing nanostructure can be used for nanoelectronic devices or organic photovoltaics. The diblock PLA-*b*-P3HT was used with $M_n = 4.2$ - b - 4 kg/mol, PDI = 1.45 $M_w = 5$ kg/mol and PDI = 1.2 for the P3HT block and a regioregularity of 90% (H-T) (Polymer Source Inc., Canada).

4.1.3. Metals

Silver (Ag)

For sputter deposition a 1- and 2-inch Ag target, which was plasma-cleaned (99.999 %) from Kurt J. Lesker (USA) was used. Ag is a noble metal such as gold but has a higher electrical conductivity and therefore is often used as an electrode material or as functional material. [17, 58, 180–185] Silver is further often used in medical applications because of its antibacterial and disinfection functionality. [186, 187] The selective decoration for Ag on DBC templates was shown by Lopes *et al.* in previous publications and is therefore a good model system to investigate the chemical and topological properties of thin Ag films. [4]

Aluminium (Al)

For sputter deposition a 2-inch Al target, which was plasma-cleaned (99.999 %) from Kurt J. Lesker (USA) was used. Al is used for many applications such as electrode materials, ultraviolet absorption sensors or light weight metal compounds. [188–190] The advantage of Al compared to Au or Ag is the better availability and lower price. The oxidation of Al is used often used as a protective layer for oxidation in applications. [191] The drawback Al oxidation, if its used as a conductive material for a lot of applications, is therefore of high interest to investigate the chemical properties and formation of thin Al films. [192]

Gold (Au)

For sputter deposition a 2-inch Au target, which was plasma-cleaned (99.999 %) from Kurt J. Lesker (USA) was used. Au is a noble metal and is often used as an electrode material because it is chemically inert compared to other metals and therefore does not interact with the polymer template as Ag or Al. The Au metal growth was shown for example by Roth & Schwartzkopf *et al.* [63, 193, 194] Löhner *et al.* have shown a slight difference in the Au growth on different functional polymers, but the chemical interaction is much lower compared to Ag or Al. [54] Here, it is used on PLA-*b*-P3HT to compare the selective wetting differences of an inert metal on the DBC template to Ag.

4.2. Thin Film Preparation

In this section the thin film preparation is explained with substrate cleaning, spin-coating, solvent vapor annealing and the metal sputter deposition. All organic solvents are purchased by Carl Roth GmbH, Germany.

4.2.1. Substrate Cleaning

The substrates were cleaned for 15 minutes at 70°C in acid solution containing 190 mL sulfuric acid (96%), 87.5 mL hydrogen peroxide (30%) and 37.5 mL ultra-clean water (ELGA Purelab Ultra, 18.2 MΩcm) as it is shown in Figure 4.2 in order to remove all in-/organic residuals. [195]

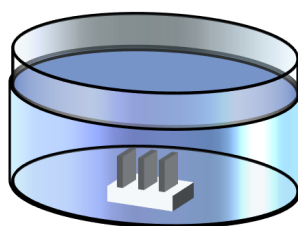


Figure 4.2.: Schematic drawing for acid cleaning of the wafers. A teflon sample holder (white) with the upright standing samples (grey) was placed in a glass vessel with the acid solution (blue) for 15 min. Afterwards the samples were rinsed in ultra-clean water and stored in ultra-clean water.

4.2.2. Spin-Coating

Spin-coating is a common method to prepare smooth homogeneous polymer thin films on substrate materials, which were e.g. silicon or glass substrates. [196,197] A schematic drawing of the spin-coating technique is shown in Figure 4.3. A polymer solution of about 70 μL was used to cover the whole surface of a silicon substrate ($12 \times 15 \text{ mm}^2$ sample size) and around 100 μL for a glass substrate ($20 \times 15 \text{ mm}^2$) or around 150 μL for a glass substrate ($25 \times 30 \text{ mm}^2$). The spin-coating parameters were chosen to prepare thin polymer films with a thickness of around $\delta_t \sim (55 \pm 3) \text{ nm}$ for PS-*b*-PMMA and their corresponding homopolymers and $\delta_t \sim (20 \pm 3) \text{ nm}$ for PMMA-*b*-P3HT and their corresponding homopolymers. For PLA-*b*-P3HT a thickness of $\delta_t \sim (137 \pm 5) \text{ nm}$ was used. This thickness of the DBC films revealed the best possible phase-separation for this kind of DBC films after spin-coating. The spin-coater 6-RC from SÜSS Micro Tec Lithography was used for spin-coating. The parameters for the PS-*b*-PMMA solution (c

= 12 mg/mL) and their corresponding homopolymers were rotations per minute (rpm) rpm = 3000, ramp = 9 and time = 30 s. The homopolymer coatings showed smooth continuous thin film morphology. The diblock copolymer thin film templates already show microphase-separation with a reduced long-range order directly after spin-coating. The parameters for the PMMA-*b*-P3HT solution ($c = 5$ mg/mL) and their corresponding homopolymers were rpm = 3000, ramp = 1, time = 30 s. The PMMA homopolymer coatings showed smooth continuous thin film morphology and the P3HT homopolymer thin films showed randomly orientated fibers along the thin film. The PMMA-*b*-P3HT thin film templates showed a good microphase-separation directly after spin-coating and yielded no improvement with solvent vapor annealing. The parameters for the PLA-*b*-P3HT solution ($c = 20$ mg/mL) were rpm = 3000, ramp = 1, time = 30 s. The diblock copolymer thin film templates showed no microphase-separation directly after spin-coating but a smooth homogeneous thin film, which revealed a very good phase-separation after solvent vapor annealing.

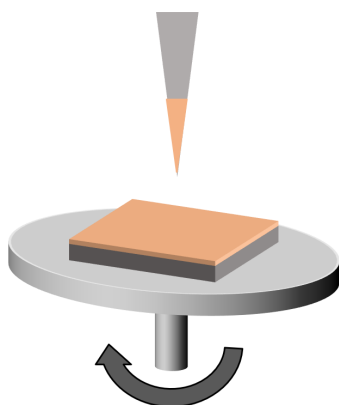


Figure 4.3.: Schematic drawing of the spin-coating technique. The substrate (Si or glass) is placed on the rotational stage and the spin-coating parameters are set e.g. rotational speed, ramp and spinning time. The polymer solution is deposited with an Eppendorf pipette on the substrate and the spin-coating process is started. The solution is accelerated to the outside and most of the solution is evaporating during the spinning process, the residual solution is forming a smooth homogeneous thin polymer film on the substrate material.

4.2.3. Solvent Vapor Annealing

Solvent-vapor annealing (SVA) is used to change the polymer film morphology after deposition e.g. spin-coating on substrate materials. [52, 198–203] A schematic drawing of the solvent vapor annealing technique is shown in Figure 4.4. This technique is often used for DBC templates in order to selectively affect one domain of the copolymer. The solvent swells the film and attracts primarily one of the blocks. Thus, the solvent increases the chain mobility more than for the other block, which in turn induces a rearrangement of the thin film morphology due to energy minimization. The parameter which describes the morphology of copolymers depending on the physicochemical properties of polymer and environment is the Flory-Huggins parameter χ . The morphology depends on the coupling between the blocks, the surface energies of the substrate-to-polymer interface and the polymer-to-air interface. This can lead to different morphologies of the polymer thin film, whereby only lamellar arranged polymer blocks were considered as templates in this work for PS-*b*-PMMA. The long-range order was increased by SVA on a sample stage in a closed vessel, where the sample (PS-*b*-PMMA) was exposed for 2.5 hours to 50 mg/ml acetone (Carl Roth GmbH, Germany) in a desiccator with solvent vapor, being a selective solvent for the PMMA domains. The PLA-*b*-P3HT copolymer was solvent-vapor annealed with 50 mg/ml chloroform (Carl Roth GmbH, Germany) in a desiccator for 45 minutes. The difference between acetone annealing was the vapor pressure of chloroform. Here, it is really important to have the right pressure in the desiccator. For acetone directly after was put into the vessel the pressure of the vapor was enough to swell the film. For chloroform the solvent was put in the desiccator, and waiting for 2 hours was performed to have the right solvent-vapor pressure in the desiccator. The PLA-*b*-P3HT thin film with initial blue color is then changing to a yellow color indicating the swelling of the film. For solvent-vapor annealing a DURAN-Glas desiccator (DN 150, volume: 2.4 l, diameter inside: 172 mm, diameter outside: 215 mm, height: 154 mm) was used with a desiccator plate as the sample stage (porcelain, diameter: 140 mm).

4.2.4. Metal Sputter Deposition

Two sputter chambers were used during this thesis. The first one is a dedicated chamber for RF sputter deposition and has three sputter guns which can be used to sputter at different angles and allows for sputtering of alloys. [204] The chamber was upgraded during in the framework of this thesis with a 4-point resistance measurement set up. The set up was built to measure the resistance change during sputter deposition and can reveal the insulator-to-metal transition (IMT) for a specific target material and the used template. The chamber setup can be seen in Figure 4.5. The first chamber was

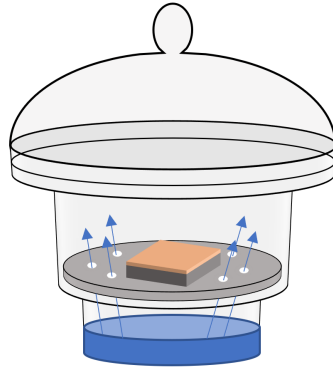


Figure 4.4.: Schematic drawing of the solvent vapor annealing technique. A solution of selective solvent is placed on the bottom of the desiccator. Above the solvent a plate with holes is placed as the sample stage. The holes allow the evaporating solution to spread in the desiccator and form a uniform solvent vapor. The polymer film is swelling with the solvent and the polymer self-assembly process is starting.

further integrated in the beamline P03 at PETRA III to observe the IMT during *in situ* morphology investigations with GISAXS. The second chamber is a DC magnetron chamber developed in a framework of a Deutsche Forschungsgemeinschaft (DFG) project with collaborators from Kiel university for high throughput *in situ* experiments at the beamline. [205] The second chamber setup can be seen in Figure 4.6. For the first chamber for sputter deposition, a plasma-cleaned 1 inch Ag target with of purity of 99.999 % (Kurt J. Lesker, USA) was used. For the XPS measurements a similar 2 inch target in a dedicated chamber was used. Sputter deposition experiments in the RF chamber with Ag on polymer templates was performed at an Ar working pressure of $p_{Ar} = 2.5 \times 10^{-2}$ mbar, power $P = 100$ W, voltage $U = 1200$ V, deposition rate $J = (0.42 \pm 0.01)$ nm/min and the base pressure $p_b \approx 5 \times 10^{-6}$ mbar. The sputter parameters for the *in situ* experiment as well as for samples prepared with selected Ag film thicknesses used for FTIR, AFM and FESEM were the same. The effective metal thickness of the sample was calculated by using a quartz crystal micro balance (QCM, Inficon, Switzerland), which can be positioned above the sample before and after the deposition, thus acting as a shutter system. For the second chamber for sputter deposition, a plasma-cleaned 2 inch Ag, Al and Au target with a purity of 99.999 % (Kurt J. Lesker, USA) was used. Sputter deposition parameters for the experiments in the DC magnetron chamber with Ag on polymer templates was performed at a power $P = 5$ W, voltage $U = 276$ V, deposition rate $J = (0.066 \pm 0.002)$ nm/s and

Ar flow of $p_{Ar} = 10$ sccm. For the x-ray photoelectron spectroscopy (XPS) measurements, the DC sputter source and QCM system the same equipment were connected to the XPS chamber (Kiel university), yielding the same pressure and sputter conditions as for the *in situ* measurements. Sputter deposition parameters for the experiments in the DC magnetron chamber with Al on polymer templates was performed at a power $P = 110$ W, voltage $U = 286$ V, deposition rate $J = (0.22 \pm 0.02)$ nm/s and Ar flow of $p_{Ar} = 10$ sccm. The sputter parameters for the Al deposition were chosen to sputter metallic Al. Sputter deposition parameters for the experiments in the DC magnetron chamber with Au on polymer templates was performed at a power $P = 7$ W, voltage $U = 334$ V, deposition rate $J = (0.22 \pm 0.02)$ nm/s and Ar flow of $p = 10$ sccm. The sputter rates are confirmed with AFM measurements of Au, Ag and Al on silicon and for the DC magnetron sputtered targets further with vertical cuts from the last analysed GISAXS image. The results are shown in Figure A.3 and A.4. The AFM images are analysed the same way as explained in the polymer section. The GISAXS vertical cuts use the following equation to determine the thickness of the metal film

$$t = \frac{2\pi}{\Delta q_z} \quad (4.1)$$

The metal layer thickness (t) is determined by the distance between the maxima Δq_z . The first maxima and the third maxima are fitted with Gaussian and used to define the thickness, because the second maxima lies in the detector gap. The vertical cuts for Al did not show any height profile and rely therefore on the QCM values and AFM measurements. The results for the metal thicknesses are shown in table A.1 and confirm the rates measured by QCM very well.

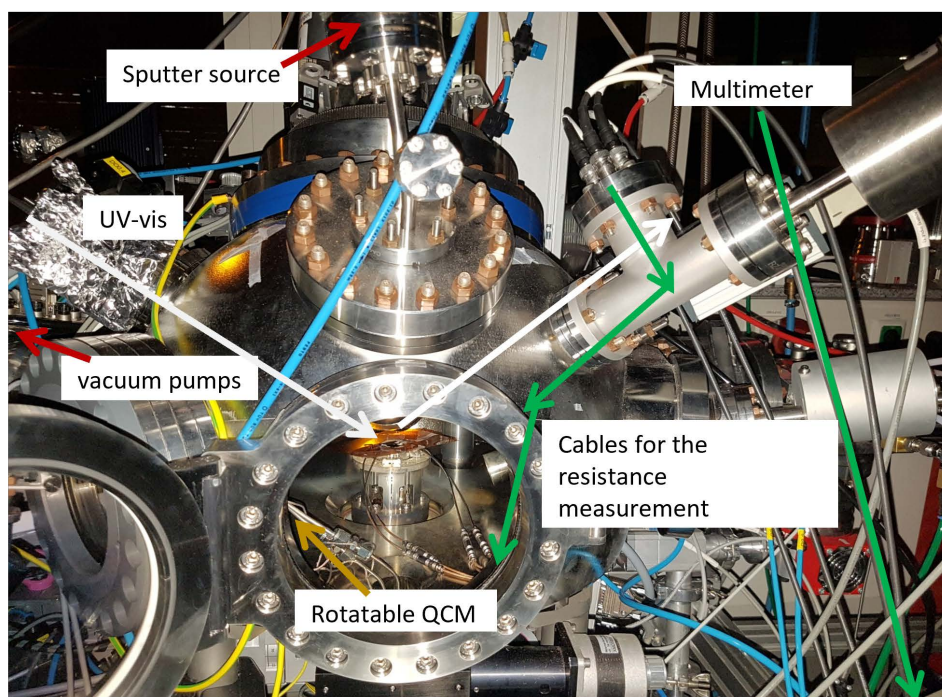


Figure 4.5.: DESY sputter chamber. Photograph of the RF sputter chamber equipped with a UV-Vis setup in reflection mode (white), the rotatable QCM (brown), a resistance measurement device (green) and the sputter source (red). Reprinted with permission from [69]. Copyright 2019 American Chemical Society.

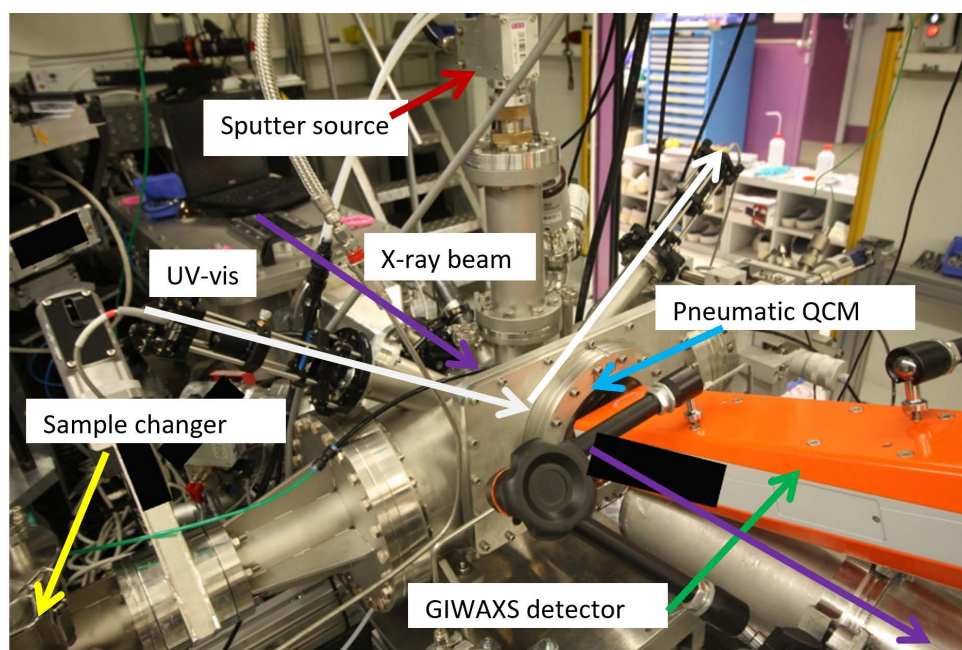


Figure 4.6.: Kiel sputter chamber. Photograph of the DC sputter chamber equipped with a pneumatic QCM (blue, inside the chamber, not visible), a UV-Vis setup in reflection mode (white), a sputter source (red), sample changer (yellow). The X-ray beam path trough the chamber is shown (violet) and the GIWAXS detector (green). Reprinted with permission from [70]. Copyright 2021 American Chemical Society.

5. Sputter Deposition of Nanogranular Ag Layers during on PS-*b*-PMMA

In this chapter GISAXS, AFM, resistivity and *in situ* UV-Vis measurements for this sample type were adopted from my master thesis at the University of Hamburg. [206] The detailed analysis was done in this PhD thesis for the *in situ* UV-Vis and GISAXS data, the other measurement methods which were done in the framework of the PhD thesis are XPS, FTIR and FESEM measurements. The chapter introduces the selective metal growth on DBC templates and the therefore useful methods, in order to reveal the selective decoration in the following results chapters 6,7,8.

Most parts of the results shown in section 5 were published in the article: *Correlating Nanostructure, Optical and Electronic Properties of Nanogranular Silver Layers during Polymer-Template-Assisted Sputter Deposition* [69] (M. Gensch *et al.*, *ACS Appl. Mater. Interfaces* 2019, 11, 32, 29416–29426, DOI: 10.1021/acsami.9b08594)

The design of optical and electronic devices with dimensions in the nanoscale is determined by the metal-polymer interface, as the electrical and optical properties are governed by the polymer-metal interface morphology. Therefore, a combined investigation of growth morphology at the polymer-metal interface on the nanoscale and its correlation to the resulting optical and electronic properties during the metallization of polymeric templates is necessary. Nanostructured polymer thin films as templates for metallization can be prepared by the microphase separation of diblock copolymers with subsequent thermal or solvent vapor annealing (SVA). Lithography is a well-established fabrication method to produce devices with improved control on the nanoscale. [207] However, the limitations of lithography methods will be reached in the coming years, and other methods for the improvement of nanostructure arrangement have to be developed. [208] Bottom-up routines to fabricate nanostructures on macroscopic scale with desired properties are of huge interest in science and industry. [16, 209–211] Self-assembled polymer-metal-nanocomposites offer an excellent perspective by combining the wealth of polymer materials and morphologies with the size- and shape-dependent optical and electronic properties of metals.

Correlating the nanostructure, the optical and electronic properties of thin metal layers during sputter deposition on homopolymer and DBC templates leads to a deeper understanding of the early metal formation for polymer-metal-composites. [27] Depending on the physicochemical properties of the materials involved, morphologies on different length scales can be addressed. [203, 212–214] The metal growth can be guided by the types of polymers of the microphase-separated DBC thin films and can create unique nanostructured templates. [1, 4, 5, 215, 216] Polymer-template assisted sputter deposition of metal on PS containing homopolymer and diblock copolymer thin film templates were investigated *in situ* during sputter deposition, allowing for observing in real time the nanoparticle growth on such complex templates. [63, 205, 217, 218] A preferential accumulation of metal on PS was reported and primarily attributed to the differences in surface interaction and mobility of the metal adatoms with the PS domains. [4, 214] Furthermore, directional hierarchically nanostructures with optical anisotropy were fabricated via glancing angle sputter deposition on thermally annealed PS-*b*-PMMA templates. [64] Alternatively to physical vapor deposition (PVD), diblock copolymer thin films can serve as a scaffold to guide nanoparticles or metal precursors prior to synthesis to obtain mesoporous metal nanostructures. [3, 219–221] However, comprehensive studies to unravel the origin of selective wetting behavior and its impact on the optical and electronic properties are still missing to date.

In order to preserve the template morphology and obtain high nanoparticle density on a macroscopic scale without excessive agglomerations and better adhesion properties, the metallization using PVD, e.g. evaporation or sputter deposition, is favorable.

In this chapter the correlation between the metal-polymer interface-morphology and its optical and electronic properties are investigated during Ag sputter deposition on different polymer thin films. Ag itself is a widely used metal in organic electronics, sensors and photovoltaics. The focus is especially on the lamellar-type diblock copolymer PS-*b*-PMMA thin films with improved long-range order by SVA for exploiting the selective wetting of Ag on one of the polymer blocks. In order to unravel the fundamentals of the wetting behavior, Ag growth on the respective homopolymer films is investigated. In section 5.1 the topography of the DBC template and the resulting Ag nanostructure is investigated with AFM, FESEM and *ex-situ* GISAXS measurements. In section 5.2 the chemical interaction of Ag with the polymer template is revealed with XPS and FTIR measurements. In section 5.3 the *in situ* GISAXS measurements are evaluated and the correlation between the GISAXS measurements and the electronic properties is shown. In section 5.4 the *in situ* UV-Vis measurements are correlated to the morphological findings of the previous sections. Further the results from the master thesis, which showed the correlation of the IMT to the morphology evolution are correlated in more detail to the Ag

growth with the findings of the AFM, SEM, XPS and FTIR measurements. Correlating all these measurements, a detailed model of the Ag growth on the polymer domains is given in this thesis.

5.1. Microscopic analysis of polymer-template assisted Ag growth

In this section the topography of the diblock copolymer template PS-*b*-PMMA and the Ag cluster decoration on this diblock is shown. The results of the Ag metal formation on PS-*b*-PMMA is compared with the formation on the homopolymers to identify differences in the Ag cluster growth. For this different techniques were used: AFM, FESEM and GISAXS. [4]

5.1.1. AFM, FESEM and *ex-situ* GISAXS analysis

The AFM height image in Figure 5.1a shows the as spun pristine PS-*b*-PMMA thin film, which shows the typical randomly orientated DBC template after spin-coating. In Figure 5.1b the solvent vapor annealed PS-*b*-PMMA is shown with curved lamellar diblock morphology (finger-print morphology). The thin film was annealed with acetone vapor for 2.5 hours in a closed vessel. The green circle marks the end of a lying cylinder of a PS domain. In Figure 5.1c an AFM height image is shown with a solvent vapor annealed PS-*b*-PMMA template after sputter deposition with an effective silver layer thickness of $\delta_{Ag} = (2.0 \pm 0.1)$ nm. In Figure 5.1a,b,c the inset of the power spectral densities (PSD) of a 2D-FFT is shown, where symmetries of the sample surface can be seen as rings for this DBC template. The 2D-FFT shows the evolving rings for the non annealed sample compared to the annealed sample and the influence of the Ag decoration for this effective thickness. The distribution with increasing parallel lamellar ordering results in a crescent-type pattern with a second order maximum for the 2D-FFT. The peak width of the distribution decreases with increasing lamellar order. Thus, the improvement of the long-range order is quantified by the change in the FWHM from the as-spun (see also Figure 5.1a) polymer thin film ($\text{FWHM} = (10 \pm 2) \text{ nm}^{-1}$, black line in Figure 5.2a) to the solvent annealed template ($\text{FWHM} = (5 \pm 1) \text{ nm}^{-1}$, blue line in Figure 5.2a) which is decreasing by a factor of 2 and thus corresponds to the improved long range order of the lamellar structure. The average lamellar distance for the as-spun sample is (55 ± 10) nm, smaller than for the solvent annealed and subsequent Ag sputtered sample (65 ± 2) nm. The domains of the DBC template show a different formation of the Ag on the surface. The difference in the Ag cluster formation leads to a selectivity of the Ag growth and to

a so-called selective wetting on one of the polymer domains of the DBC.

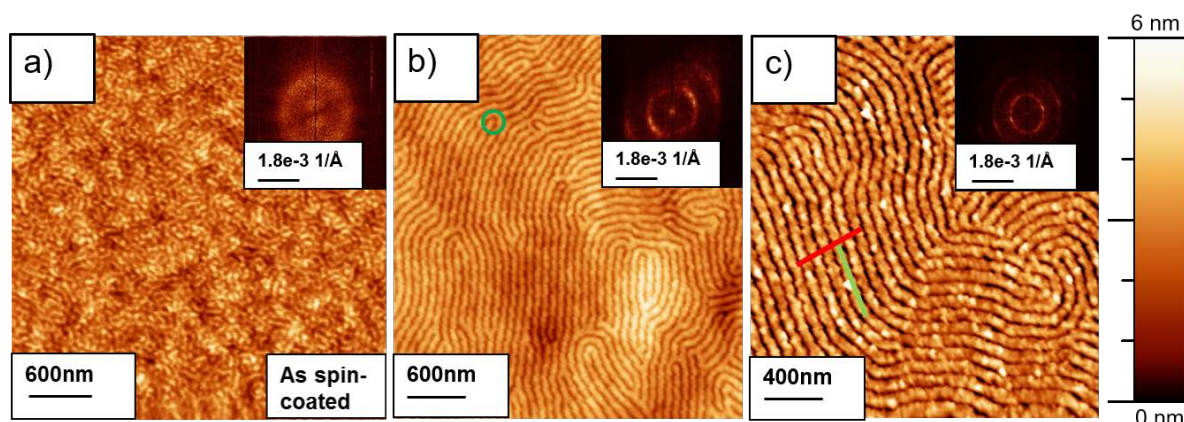


Figure 5.1.: a,b) AFM image of the PS-*b*-PMMA film before and after solvent vapor annealing with acetone for 2.5 hours in a closed vessel. The green circle marks an ending of a PS block having an ultrathin PMMA overlayer and hereafter denominated as “PMMA/PS”. c) Acetone solvent annealed PS-*b*-PMMA copolymer thin film after Ag sputter deposition of $\delta_{Ag} = (2.0 \pm 0.1)$ nm. The AFM image shows small clusters predominantly wetted on the protrusions, i.e. the PMMA/PS domains of the copolymer thin film. The red line shows a line-cut over the lamella structures, while the green line is a line-cut on the lamella. The Power spectral density (PSD) is shown in the insets. The AFM data was adopted from the Master thesis [206], the detailed analysis was done in the PhD thesis. Reprinted with permission from [69]. Copyright 2019 American Chemical Society.

In order to quantify this, two line-cuts are performed in the AFM topography images. The line-cuts are indicated in Figure 5.1c by a red line for the perpendicular line-cuts and green for the line-cuts on the PS domain of the DBC. The perpendicular line-cut is done for 3 lamellae for $\delta_{Ag} = 0, 2$ and 4 nm to have a higher statistic relevance to show the relative domain height differences induced by selective metal decoration of the different polymer domains (Figure 5.1c). The line-cuts on the lamellae show the Ag cluster growth behaviour on the domain for different δ_{Ag} thickness, for this 3 line-cuts were taken for each Ag thickness to have a reasonable statistic relevance. The perpendicular line-cuts can give a tendency of the decoration of Ag clusters on the different polymer type domains with the change of the peak-to-valley distance (D_{ptv}). For the SVA DBC thin films the AFM height images show a uniform peak-to-valley distance of $D_{ptv} = (1.3 \pm 0.3)$ nm between the two blocks. Zhang *et al.* described these distances between the polymer domains as the height of protrusions resulting from the selective SVA process. [200]

As PS-*b*-PMMA is one of the most common DBC templates and mostly investigated DBCs, e.g. Xuan *et al.* showed for these templates that a few PMMA chains form an

ultrathin overlayer covering the PS domains, I refer to this here in the chapter as the PMMA/PS domain. [201] The PMMA/PS domain can be seen in a later section for the growth model in Figure 5.11 for $\delta_{Ag} = 0$ nm with a thin PMMA overlayer on the PS domains.

Figure 5.2a reveals the change of lateral order of the DBC formation from the as-spun

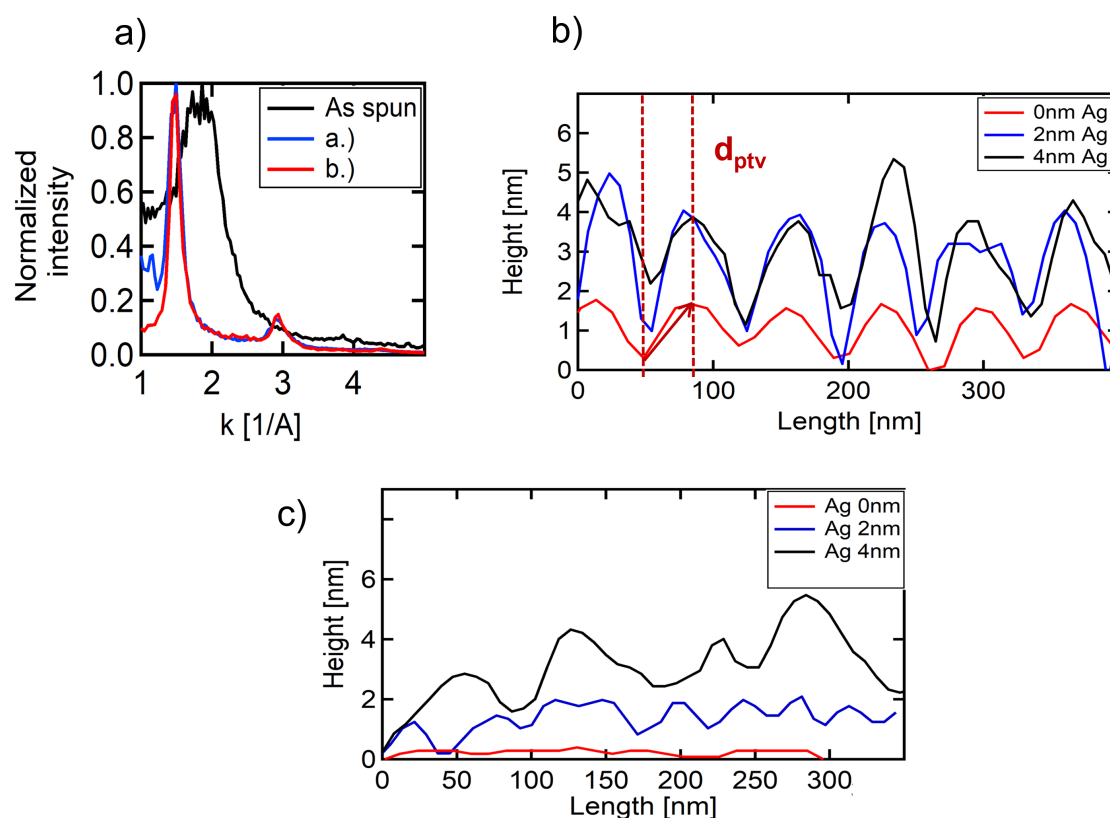


Figure 5.2.: a) Power spectral density (PSD) from the Figures 5.1a-c) for pristine PS-*b*-PMMA (black), SVA PS-*b*-PMMA (blue) and with $\delta_{Ag} = 2$ nm (red) b) Comparison of AFM line-cuts perpendicular across 5 lamellas (red line in Figure 5.1c) from pristine PS-*b*-PMMA film without silver sputtered (red), and sputter-coated with 2 nm (blue) and 4 nm of silver (black). The peak-to-valley distance (D_{ptv}) increases with silver thickness. c) Comparison of AFM line-cuts along one PMMA/PS lamella (green line in Figure 5.1c) of the pristine PS-*b*-PMMA (red), and sputter-coated with 2 nm (blue) and 4 nm Ag (black). The AFM data was adopted from the Master thesis [206], the detailed analysis was done in the PhD thesis. Reprinted with permission from [69]. Copyright 2019 American Chemical Society.

PS-*b*-PMMA template to the annealed template. The massive decreased FWHM in the power spectral density shows the change from the solvent vapor annealing and stays constant after sputter deposition of $\delta_{Ag} = 2$ nm on the DBC template, which means the

metal is replicating the surface of the DBC template for the first nanometers. Figure 5.2b shows the selective wetting behavior by the before mentioned D_{ptv} with a deposited Ag thickness of 2 nm, the D_{ptv} is increased by 1.7 nm to $D_{ptv} = (3 \pm 0.3)$ nm compared to the pristine SVA DBC. Figure 5.2b shows the evolution of the selective wetting of Ag on the PS/PMMA domain with different amount of Ag. The D_{ptv} increases drastically for $\delta_{Ag} = 2$ nm and then reduces slowly and remains nearly constant during the further deposition of Ag, as seen in Figure 5.2b. Figure 5.2c shows the Ag deposition on the lamellae for different Ag thickness $\delta_{Ag} = 0, 2$ and 4 nm and reveals the homogeneous growth of Ag clusters on the domain at the beginning of Ag cluster growth until $\delta_{Ag} = 2$ nm. After $\delta_{Ag} = 2$ nm the Ag clusters seem to growth not only on the PS/PMMA domain preferential but also on the Ag clusters itself. This leads to an inhomogeneous Ag cluster height formation for the further Ag deposition. The result also shows an initial preferential Ag cluster growth on top of the PMMA/PS blocks due to surface energy respectively mobility differences of the metal adatoms and clusters on the polymer domains: A difference in diffusion coefficients of sputtered gold on PS and PMMA was reported by Ruffino *et al.*, and Lopes *et al.* modelled a mobility difference of Ag on PS-*b*-PMMA. [4, 214, 215] The diffusion coefficient can be one explanation for the different Ag growth on PS and PMMA and therefore a selective growth of Ag on the different domains of the diblock copolymer with Ag preferring the PMMA/PS block. Another explanation could be a decoration effect, but here this plays a minor role because of the vertical position of the sputter source compared to the polymer surface. [64] Figure 5.2b shows the peak-to-valley distance for a deposited Ag thickness of 0, 2 and 4 nm; a decoration effect would change the peak-to-valley distance leading to an asymmetric Ag decoration on the boundaries of the polymer domains. The selective wetting will be further shown in more detail for different Ag thickness in the X-ray section. The AFM analysis will focus on the embedding of Ag into the polymer films, which will be further demonstrated by the analysis of the Ag deposition on the homopolymer thin films.

Ag	PS			PMMA		
$\delta_{Ag} / [\text{nm}]$	$\sigma_{rms} / [\text{nm}]$	D / [nm]	R / [nm]	$\sigma_{rms} / [\text{nm}]$	D / [nm]	R / [nm]
0	0.23 ± 0.05	-	-	0.25 ± 0.05	-	-
1.0 ± 0.1	0.47 ± 0.05	17.7 ± 0.4	5.1 ± 0.2	0.27 ± 0.05	3.4 ± 1.0	1.7 ± 1.0
4.0 ± 0.1	0.79 ± 0.05	19.5 ± 0.6	8.6 ± 0.3	0.62 ± 0.05	17.7 ± 0.03	8.0 ± 0.2

Table 5.1.: Root mean square value of the surface roughness σ_{rms} , the average Ag cluster radii R and the average distances D on PS and PMMA homopolymer thin films with different amount of sputtered Ag thickness.

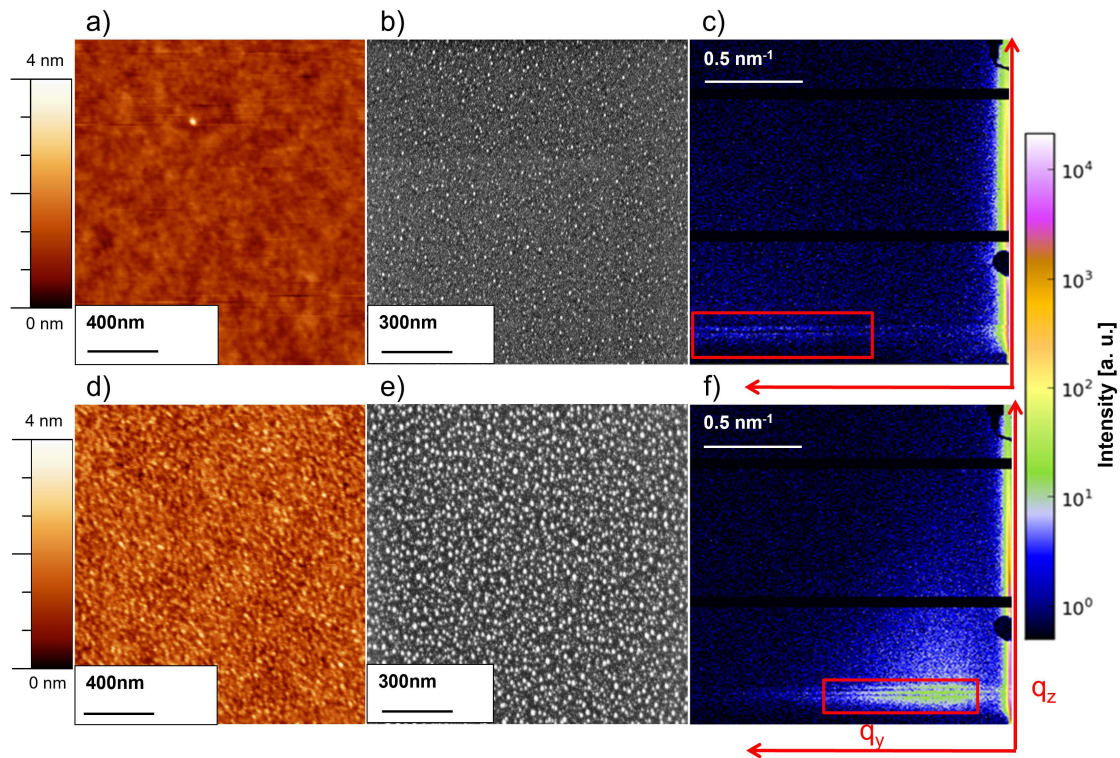


Figure 5.3.: Comparison of 1 nm Ag-coated PMMA (a-c) and PS (d-f) homopolymer thin films using a) AFM, b) FESEM and c) *ex-situ* GISAXS. The different cluster growth morphologies are indicated by the out-of-plane scattering intensity distribution (red boxes). The AFM and GISAXS data was adopted from the Master thesis [206], the correlation between AFM, GISAXS and FESEM was done in the framework of the PhD thesis. Reprinted with permission from [69]. Copyright 2019 American Chemical Society.

The peak-to-valley distance D_{ptv} is increasing fast as described in Figure 5.2b after Ag deposition ($\delta_{Ag} = 2$ nm) and seems to appear constant until $\delta_{Ag} = 4$ nm, this indicates a strong influence from embedding and subsurface growth of Ag in the investigated polymers. In Figure 5.3a comparison of the homopolymers of the DBC template are shown. Three techniques (AFM, FESEM, GISAXS) reveal the differences of the Ag growth on the homopolymer templates, due to the influences of surface diffusion, embedding and sub-surface growth of adatoms and clusters at the different polymer domains. Figure 5.3 a and d show AFM height images of deposited Ag with a thickness of 1 nm on PMMA and PS. The Ag clusters cannot be seen on the surface of the PMMA film but are clearly visible on the PS template, which is a first indication of a different growth on the templates. Further, the comparison of the roughness in Table 5.1 of the pristine PMMA and PS templates to the Ag decorated ones, reveals a different roughness value for PS but a similar

value for PMMA, indicating that the Ag clusters grow differently due to e.g. different chemical interactions and embedding. The AFM images of the pristine homopolymer thin films have similar roughness. A clear difference resulting from the higher embedding and subsurface growth in the PMMA film are the smaller and darker Ag clusters compared to the Ag clusters on PS with the same Ag material content. This is shown in the FESEM measurements in Figure 5.3 b and e for PMMA and PS thin films with $\delta_{Ag} = 1$ nm. The same amount of Ag material proportion is sputtered on PMMA and PS thin films but the contrast on PMMA is much lower, which suggests a higher embedding and much smaller Ag cluster sizes on PMMA. The same tendency was shown by Ruffino *et al.* for embedding with thermal annealing of the films. Here the Ag and Au clusters embed more in the PMMA compared to PS thin films. [168] In order to identify the cluster size differences between Ag on PMMA and PS homopolymer thin films, GISAXS was used to determine the radii and the average center-to-center distance of the Ag clusters. *Ex-situ* GISAXS was performed with samples covered with $\delta_{Ag} = 1$ nm and $\delta_{Ag} = 4$ nm on PMMA and PS, which can be seen in Figure B.1c,f as an example for $\delta_{Ag} = 1$ nm. *Ex-situ* GISAXS here means that the samples were sputtered for the specific δ_{Ag} thickness at the same time in the HASE sputter chamber (PMMA and PS with $\delta_{Ag} = 1,4$ nm) and one day later measured with GISAXS. Both sample types (PMMA and PS with $\delta_{Ag} = 1,4$ nm) age for the same time to ensure the same conditions for the metal-polymer samples. The out-of-plane peak position marked with the red boxes in Figure B.1c,f can be considered as a Pseudo-Bragg peak, which is correlated to the average interparticle distance D of the clusters arrangement. Schwartzkopf *et al.* have shown to calculate the clusters radii R from the effective metal layer thickness and the interparticle distance, which is used here to calculate the radii of PMMA and PS for 1 and 4 nm Ag thicknesses, following the local monodisperse hemispherical model approach. [142] The results shown in Table 5.1 confirm the tendency of increased Ag sub-surface cluster growth and embedding in the PMMA thin film compared to the PS thin films. The lower cluster radius R on PMMA can be correlated to σ_{rms} . The changes of the root mean square roughness rms values from the homopolymer samples at different Ag thicknesses (Table 5.1) quantify the ratio between Ag surface and sub-surface cluster growth. With a pronounced Ag embedding and sub-surface cluster growth the roughness will be less affected at identical deposited thicknesses δ_{Ag} . The roughness analysis from the AFM images indicates for $\delta_{Ag} = 0$ nm and 1 nm no significant change on the PMMA film, whereas the rms on PS is twice as large.

Regarding the growth of Ag on PS-*b*-PMMA templates, apparently the clusters grow in the beginning preferentially on the PMMA/PS domains as they are more embedded and separated in the pure PMMA domains, thus the diffusion of the Ag metal atoms seems

to be higher on the PS domain. This explains the difference of the R values of Ag on PS and PMMA.

The *ex-situ* GISAXS measurements in Figure B.1 showed similar growth behaviour of Ag with smaller clusters for the first nanometers on PMMA as the AFM and FESEM measurements. With further deposition the Ag cluster size distribution on PMMA adjusts to the growth of Ag clusters on PS ($\delta_{Ag} = 4$ nm). The radii of the Ag clusters in Figure B.1 is calculated with the before mentioned geometrical model, assuming a hemispherical cluster shape. [142] When the film thickness of Ag is around $\delta_{Ag} = 4$ nm, the differences of the Ag cluster sizes and distances on PMMA and PS thin films is not seen any more. The results of the homopolymer investigations show a higher tendency of Ag adatoms to migrate into the sub-surface regime of PMMA in the early stages due to differences in chemical and mechanical properties of the macromolecular thin film, e.g. differences in the mobility of the Ag clusters. [214] The target-to-sample distance is considerably large in the utilized HASE sputter chamber (10 cm). Therefore the sticking coefficient for sputter deposition is nearly one and the amount of Ag on the polymer templates is the same. [222–224] In order to investigate the chemical interaction of Ag with the molecular components of the polymers, chemical measurements will be shown in the next section. The embedding of Ag in PMMA and therefore the mechanical properties on the sample surface were revealed with AFM and GISAXS measurements. The as-spun DBC template in Figure 5.4a show the fingerprint like morphology of the DBC template as seen also by the AFM measurements with the PS/PMMA domain (lighter lamella region) and the PMMA domain (darker lamella region). Additional FESEM with $\delta_{Ag} = 1$ nm measurements seen in Figure 5.4b show similar Ag formation on the corresponding domains of the DBC, where bigger Ag clusters arrange on the PS/PMMA domain (lighter lamella region) and smaller clusters on the PMMA domain (darker lamella region). The Ag clusters follow this fingerprint morphology, which shows the selective decoration of the Ag clusters on the different polymer domains on the DBC. A higher Ag thickness on the homopolymers thin films ($\delta_{Ag} = 2$ nm) in Figure 5.5 confirms the still smaller clusters on the PMMA thin films, but show also the size increase and reduced embedding for ongoing Ag deposition on PMMA.

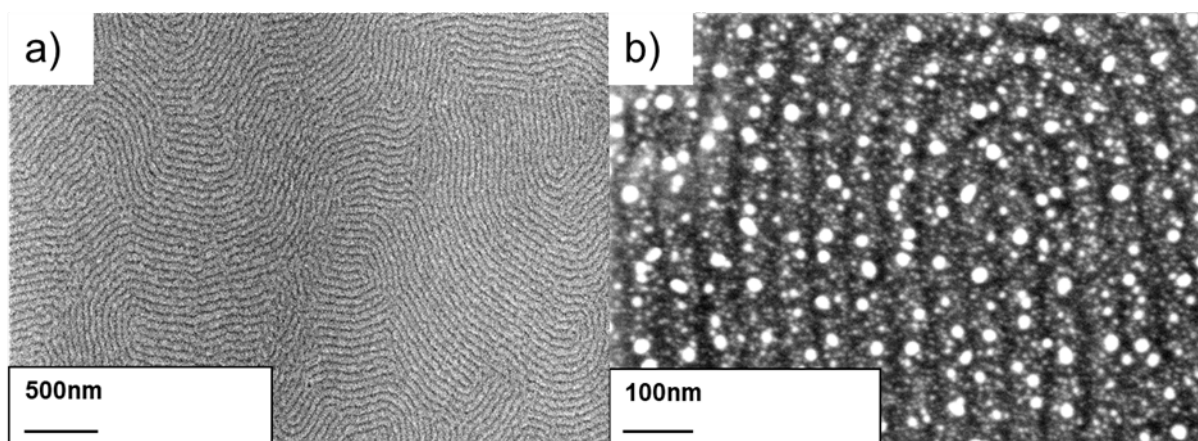


Figure 5.4.: FESEM of a) pristine PS-*b*-PMMA and with b) $\delta_{Ag} = 1\text{nm}$. Reprinted with permission from [69]. Copyright 2019 American Chemical Society.

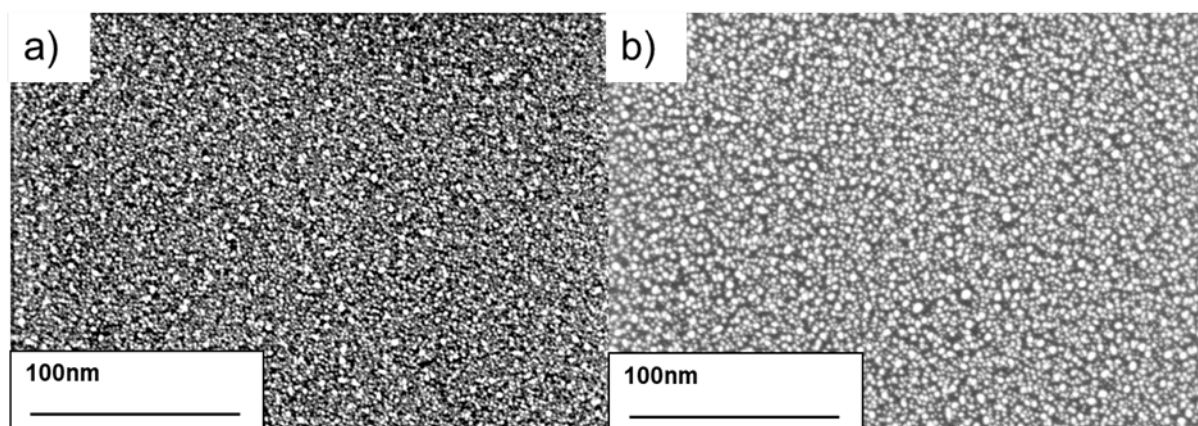


Figure 5.5.: FESEM comparison of a) PMMA and b) PS with $\delta_{Ag} = 2\text{nm}$. Reprinted with permission from [69]. Copyright 2019 American Chemical Society.

5.2. Chemical interaction of the metal with the polymer

5.2.1. XPS and FTIR analysis

The difference in Ag cluster growth on PMMA and PS can be explained with different interactions such as the mobilities, embedding and chemical interaction. Here, the chemical interaction is investigated for the early cluster growth in order to reveal the Ag interaction differences between PMMA and PS. XPS is therefore one of the most useful methods because it shows the binding of the metal with the molecules of the polymer. In Figure 5.6a an XPS spectra of the C 1s peak from the pristine PS-*b*-PMMA is shown. The spectra reveals different bonding components of carbon e.g. C-C, C-H, C-O and C=O. The

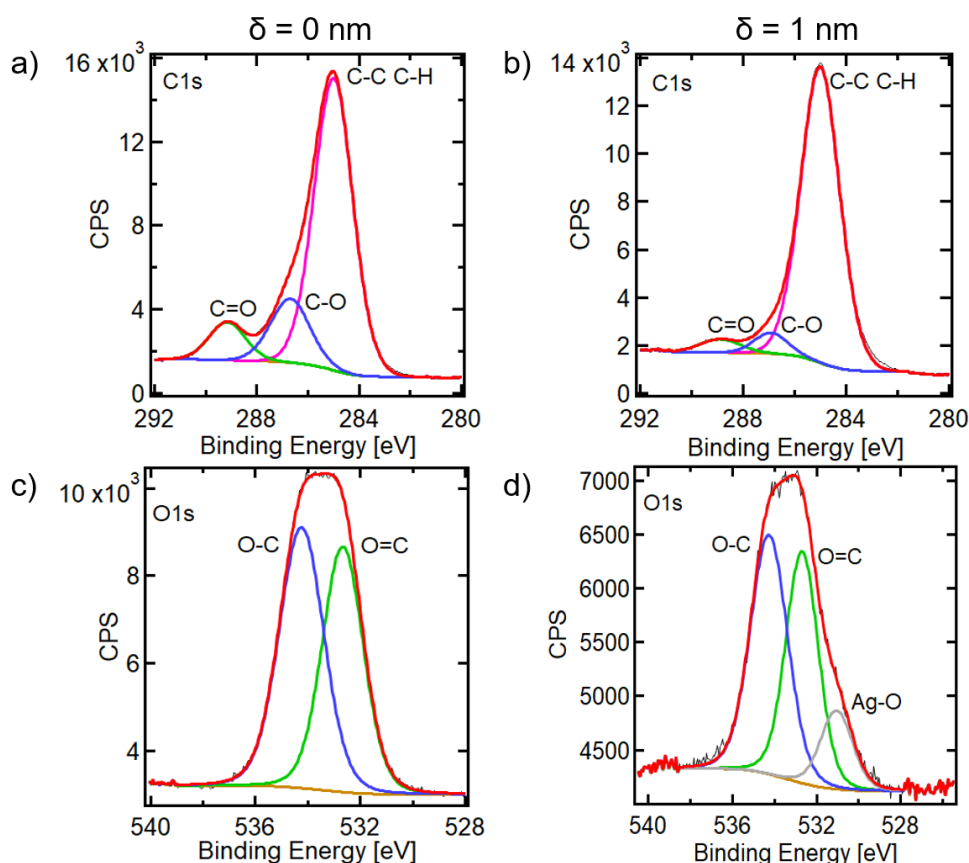


Figure 5.6.: XPS spectra at C 1s edge of pristine PS-*b*-PMMA ($\delta_{Ag} = 0$ nm) and b) of sputter-coated PS-*b*-PMMA with $\delta_{Ag} = 1$ nm. c) XPS spectra at O 1s edge of pristine PS-*b*-PMMA ($\delta_{Ag} = 0$ nm) and d) of sputter-coated PS-*b*-PMMA with $\delta_{Ag} = 1$ nm. C-O bonding (blue), C=O bonding (green), C-C and C-H bonding (pink), Ag-O (grey), the envelope (red) and the background (brown) are shown in the XPS spectra. The intensity of C=O, C-O and O=C, O-C bonds is decreasing after sputtering of 1 nm Ag for the C 1s and O 1s electrons in PS-*b*-PMMA. Furthermore, an AgO bonding is arising with Ag deposition for PS-*b*-PMMA. Reprinted with permission from [69]. Copyright 2019 American Chemical Society.

bindings after coating with $\delta_{Ag} = 1$ nm can be affected by the chemical metal-polymer interaction such as the reduction of the component proportions, due to breaking or establishment of bondings. The reduction of the component proportions can be seen in Figure 5.6b, especially for the C-O and C=O components. This is a first indication of a high bonding of Ag clusters to the PMMA domain and also to the small layer of PMMA on the PS domain (PS/PMMA domain in the DBC template). On PMMA, the Ag adatoms might move to the carbonyl moieties of acrylate side chains and thus not contribute to Ag cluster coalescence and growth. The phenyl side chains of PS are more chemical inert to Ag, leading to a more pronounced surface cluster growth via diffusion-mediated coales-

cence. This could be one explanation for the above mentioned morphological differences of the Ag layer on the two homopolymer thin films. In Figure 5.6c,d the O 1s peak with $\delta_{Ag} = 0$ nm and $\delta_{Ag} = 1$ nm is shown. The shape of the O 1s peak changes after Ag deposition and an additional Ag-O contribution appearing at around 531 eV in the O 1s spectra. Ag seems to chemically interact with oxygen of the acrylate side chains for the PMMA and the PS-*b*-PMMA template in the early stages of sputter deposition. Figure 5.7a-d show the same tendency as the DBC template for PMMA. The intensity of the C=O and C-O bonds are shrinking for PMMA and PS-*b*-PMMA, which implies that the acrylate side chain interacts with the Ag clusters. For the PS template in Figure 5.7e,f the spectra of the C 1s and O 1s peak are remaining the same after sputtering, due to the chemically inert phenyl side chains.

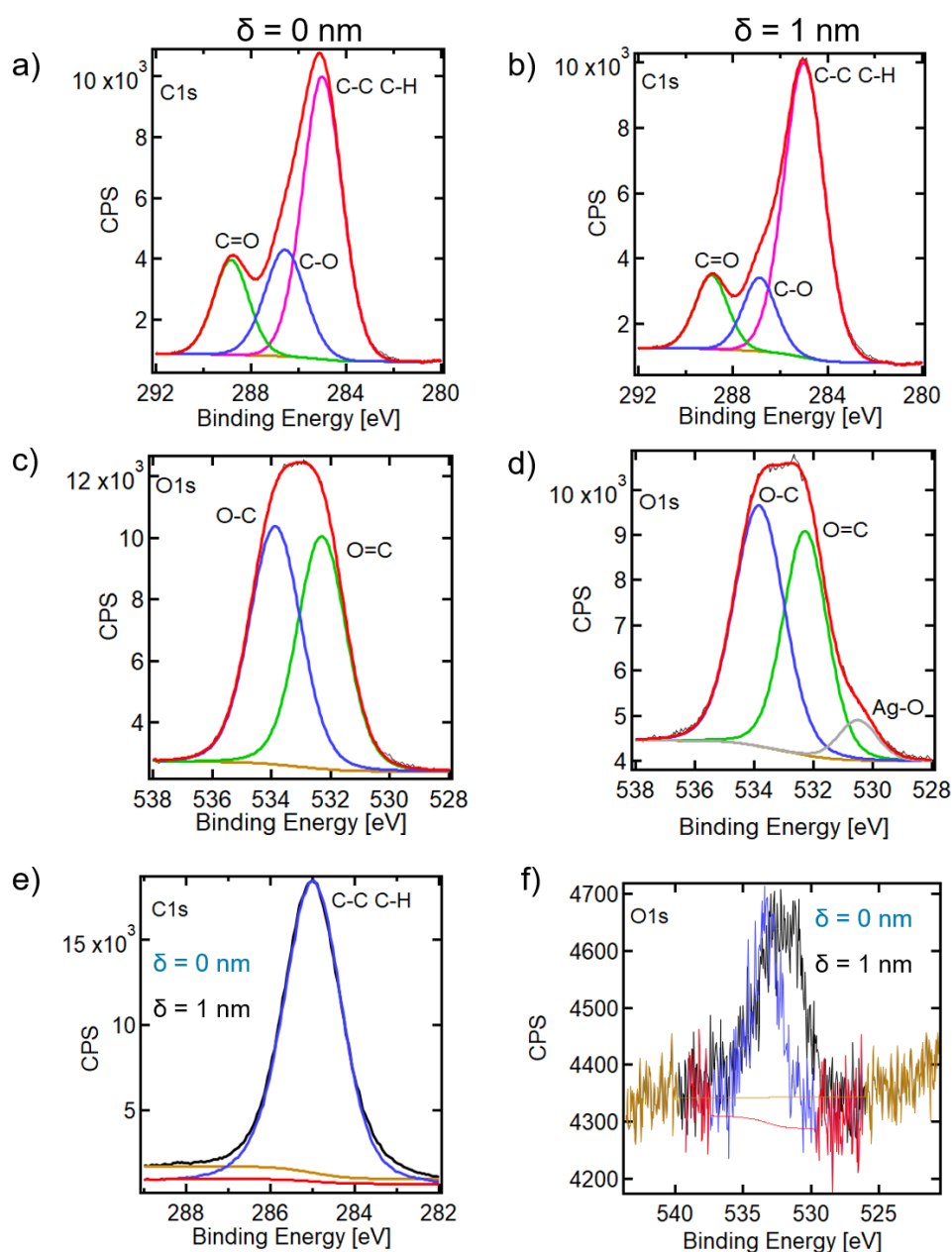


Figure 5.7.: a) XPS spectra at C 1s edge of pristine PMMA ($\delta_{Ag} = 0$ nm) and b) of sputter-coated PMMA with $\delta_{Ag} = 1$ nm. c) XPS spectra at O 1s edge of pristine PMMA ($\delta_{Ag} = 0$ nm) and d) of sputter-coated PMMA with $\delta_{Ag} = 1$ nm. C-O bonding (blue), C=O bonding (green), C-C and C-H bonding (pink), Ag-O (grey), the envelope (red) and the background (brown) are shown in the XPS spectra. The intensity of C=O, C-O and O=C, O-C bonds is decreasing after sputtering of 1 nm Ag for the C 1s and O 1s electrons in PMMA. Furthermore, an AgO bonding is arising with Ag deposition for PMMA. e) XPS spectra at C 1S edge of pristine PS (blue) and of sputter-coated PS (black) show no significant changes and with the background in yellow and red. f) XPS spectra at O 1S edge of pristine PS (blue) and of sputter-coated PS (black) with negligible changes and with the background in yellow and red. Reprinted with permission from [69]. Copyright 2019 American Chemical Society.

The acrylate side chain of the PMMA seems to be the potential interaction point with the Ag atoms, therefore further investigations with FTIR measurements were done to reveal the oxygen interaction at this bonding. [225] The spectra in Figure 5.8 show the presence of the C=O carbonyl stretching vibrations at a wavenumber of around 1735 cm^{-1} for the pristine PMMA (turquoise) and PS-*b*-PMMA (red) thin film. The PS (light green) thin film does not show a peak at a wavenumber of around 1735 cm^{-1} . When the films are covered with $\delta_{Ag} = 1\text{ nm}$ the peak related to carbonyl stretching vibrations is strongly reduced for PMMA (blue) and PS-*b*-PMMA (orange) and for PS (green) still nothing is changing. With further deposition $\delta_{Ag} = 2\text{ nm}$ the peak at PS-*b*-PMMA (brown) is vanishing and for PMMA (dark blue) the peak is highly reduced, while for PS (dark green) no change appears. These results supports the strong interaction of the acrylate side chain with the sputter deposited Ag.

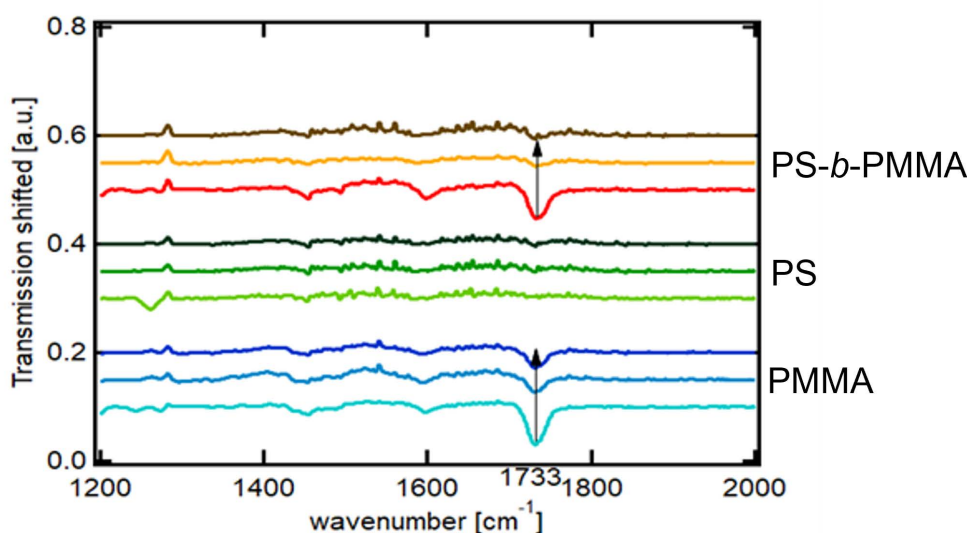


Figure 5.8.: FTIR spectra of pristine PS-*b*-PMMA (red), PS (light green), PMMA (light blue) and sputter-coated with 1 nm Ag PS-*b*-PMMA (orange), PS (dark green) and PMMA (dark blue) and 2 nm Ag PS-*b*-PMMA (brown), PS (darkest green) and PMMA (darkest blue). The intensity of C=O carbonyl stretching vibrations at a wavelength of 1733 cm^{-1} changes for all templates from 0 nm to 2 nm Ag. Reprinted with permission from [69]. Copyright 2019 American Chemical Society.

5.3. *In situ* GISAXS and resistivity measurements on different polymer templates

AFM and FESEM measurements showed first indications how the Ag growth on the PMMA and PS homopolymer thin films and the corresponding DBC template takes place. In order to get a more detailed understanding of the Ag growth on the polymer templates, combined *in situ* measurements are performed with GISAXS, resistance and UV-Vis. A sputter deposition chamber Figure 4.5 was integrated in a GISAXS set-up at the P03/MiNaXS beamline of the PETRA III storage ring at DESY (Hamburg, Germany). [204] An incident photon energy of 13 keV was used with a beam size of $(31 \times 24) \mu\text{m}^2$ at the sample position. The sample-to-detector distance was set at $SDD_1 = (4163 \pm 2)$ mm for *in situ* GISAXS using a Pilatus 1M (Dectris Ltd., Switzerland; pixel size of $172 \mu\text{m}$) and $SDD_2 = (3410 \pm 2)$ mm using a Pilatus 300K (Dectris Ltd., Switzerland; pixel size of $172 \mu\text{m}$) for *ex-situ* measurements in two experimental runs at the beamline P03. The direct and specular beams were both shielded by two separate beam stops to avoid saturation or damage to the detector. In order to achieve a good separation between the polymer and Ag Yoneda peaks, an incident angle of $\alpha_i = 0.45^\circ$ was selected during the *in situ* experiments and an incident angle of $\alpha_i = 0.36^\circ$ was selected for the *ex-situ* experiments. In order to prove macroscopic homogeneity of the nanoscale morphology and to avoid possible X-ray beam effects during the *in situ* GISAXS experiments, the sample was laterally moved over several millimeter distances during the experiment. [57] Meanwhile, the scattering patterns were continuously recorded at a frame rate of 5 images per second. The GISAXS data were analyzed using the DPDAK software package. [156] In the first part of this section the GISAXS measurements are discussed, which are then followed by the *in situ* resistance measurements and their correlation to the morphological data. In the next section, the *in situ* UV-Vis data is discussed in relation to the found results. In Figure 5.9 typical 2D-GISAXS data are shown, which contain lateral and vertical information of the thin film and metal layer, depending on the sample-to-detector distance and the incident angle. A closer look to Figure 5.9 with $\delta_{Ag} = 0.5$ nm shows out-of-plane intensity corresponding to Ag cluster formation and pseudo Bragg rods, which are related to lateral symmetries on the sample surface. The lateral symmetries describe the distance of the domain peaks, which was also shown before by AFM measurements. More than one pseudo Bragg rod is seen in this GISAXS data, which is an indication for a very good long range ordering of the domain peaks to each other. The selection in Figure 5.9 shows the sputter deposition of Ag with increasing thickness $\delta_{Ag} = [0.5; 1; 2; 3; 4; 8; 10; 13; 15; 20]$ nm. For the analysis of the sequence of GISAXS data, horizontal line integrations (Yoneda cuts, red box) are made along an integrated q_z region ($q_z = 0.5\text{-}0.6$

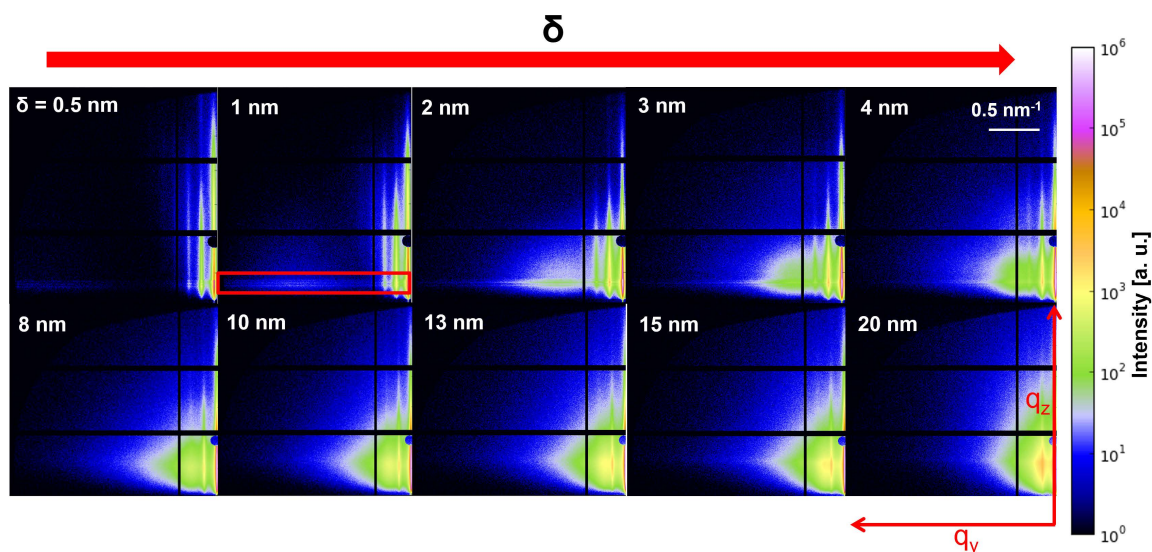


Figure 5.9.: Evolution of selected *in situ* 2D GISAXS data with increasing Ag thickness deposited on PS-*b*-PMMA ($\delta_{Ag} = 0.5, 1, 2, 3, 4, 8, 10, 13, 15$ and 20 nm). The GISAXS data was adopted from the Master thesis [206], the interpretation was done in the PhD thesis. Reprinted with permission from [69]. Copyright 2019 American Chemical Society.

nm^{-1}), near to the critical angle of the polymer. This horizontal line integrations allow to identify and follow the peak positions of the Ag cluster peak and the DBC domain peak during the sputter deposition. The position can be used to calculate the average distance between the Ag clusters and the radii with the before described geometrical model in the theory chapter 2.3.2. Further the DBC domain peak position can be correlated to the domain spacing found by AFM and to follow the intensity changes of the domain peak during Ag deposition. From $\delta_{Ag} = 0.5$ nm to 20 nm the cluster peak position is shifting to lower q_y values indicating the Ag cluster growth on the DBC template. At the same time the domain peak intensity is changing related to the selective Ag cluster decoration on the lamellae domains of the DBC template, with the domain peak position remaining constant. At around $\delta_{Ag} = 13$ nm the cluster peak is overlapping with the domain peak, seen by the increasing domain peak intensity in Figure 5.9. Higher order peaks of the domain peak are arising in the beginning of the Ag deposition by the selective wetting and gradually disappear the more both domains are decorated with Ag.

The analysis of the evolution of the Ag cluster formation and DBC domain peak from the 2D-GISAXS data is shown in a contour plot with lateral cuts at the Yoneda region of the polymer types with increasing Ag thickness. The contour plot is shown in Figure 5.10a as a function of effective Ag thickness. The clear changes of the key features e.g. Ag cluster peak (black dashed arrow in Figure 5.10a) and DBC domain peak (marked by

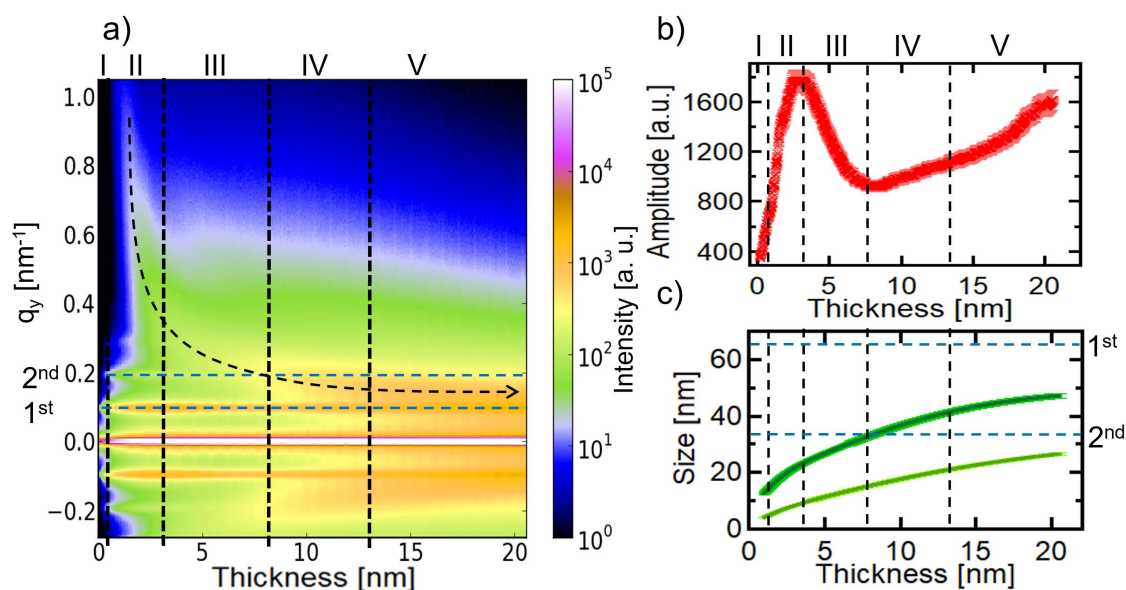


Figure 5.10.: a) Contour plot of Yoneda cuts from the *in situ* GISAXS data during sputter deposition on PS-*b*-PMMA as a function of effective deposited Ag thickness. The cluster peak (black dashed arrow) and the lamellar 1st and 2nd order peak (blue dashed lines) at $q_y = 0.096 \text{ nm}^{-1}$ (1st) and $q_y = 0.192 \text{ nm}^{-1}$ (2nd) change due to the Ag deposition. The black dashed vertical lines indicate different growth regions: Nucleation and embedding (I), selective diffusion-mediated cluster growth via coalescence (II), non-selective adsorption-mediated growth (III), partially interconnection between the domains (IV), and percolated regime (V). b) Evolution of the amplitude of the domain peak of PS-*b*-PMMA during the Ag sputter deposition. The black dashed vertical lines mark the as before mentioned growth regions; the intensity contrast in regions (I) and (II) is increasing due to the selective wetting and decreasing in region (III) due to the limited embedding of Ag clusters in the polymer and the sub-surface growth. c) Evolution of the mean interparticle distance (D, dark green) and the cluster radius (R, bright green) in the different growth regions. The GISAXS data was adopted from the Master thesis [206], the interpretation was done in the PhD thesis. Reprinted with permission from [69]. Copyright 2019 American Chemical Society.

1st and 2nd in Figure 5.10a for the first and second order domain peak) can be identified in this contour plot. Further five general growth regimes (I-V) are marked and separated with black dashed line in the contour plot, the origin of the growth regions will be explained later in detail. In the contour plot the strong intensity peak located at $q_y = 0 \text{ nm}^{-1}$ (Yoneda peak) is caused by unresolved large scale structures in the sample. [131] The additional equidistant peaks at higher q_y values originate from the microphase separation in the PS-*b*-PMMA template and represent the average interdomain distances of

the lamella (domain spacing, blue dashed lines, at $q_y = 0.096 \text{ nm}^{-1}$ (1st) and $q_y = 0.192 \text{ nm}^{-1}$ (2nd) order). [135, 140, 216] From the contour plot the change of the intensity of the interdomain distance during Ag sputter deposition can be clearly seen and will be later analysed in more detail. The Ag cluster peak is appearing after around $\delta_{Ag} = 0.4 \text{ nm}$ of Ag deposition, the broad side peak (dashed black arrow) in Figure 5.10a primary originates from the interference of the growing Ag clusters assembly and appears at high q_y values. A delayed appearance of the cluster peak was already observed for Al sputter deposition on Alq3 and related to embedding and chemical interaction between metal and template. [226] The region until $\delta_{Ag} = 0.4 \text{ nm}$ marks the first region, where nucleation and embedding starts and defining regime I. The selective embedding is consistent with the findings of Ruffino *et al.* and the analysis of the AFM image. [168] In Figure 5.10b the intensity of the domain peak is shown for ongoing Ag deposition. The selective wetting of Ag clusters on the different domains is followed *in situ* by the evolution of the amplitude of the domain peak and can be correlated to peak-to-valley distances from the *ex situ* AFM analysis and can be used to identify different growth regimes. The change of the amplitude of the domain peak is a result of the change in selective wetting, due to the changing electron contrast on the domains by the selective Ag deposition and therefore an indicator how the Ag growth takes place on the DBC template. With the onset of Ag deposition, the amplitude increases and higher orders of the peak turn visible, which can be seen in Figure 5.10a by the appearing 2nd and 3rd domain peak in the contour plot at around $q_y = 0.192 \text{ nm}^{-1}$ (2nd) and at around $q_y = 0.29 \text{ nm}^{-1}$. The domain peak of the copolymer is not shifting in q_y -position during deposition, meaning that the deposition process does not change the periodicity nor the morphology of the DBC template. The so-called cluster peak in Figure 5.10a is shifting from high q_y values at around $q_y = 1 \text{ nm}^{-1}$ to smaller q_y values during sputter deposition indicating a simultaneous increase of average interparticle distance and size consistent with a coalescence-driven cluster growth. The coalescence-driven cluster growth can be correlated to the intensity of the lamella peak, which is enhancing up to $\delta_{Ag} = 2.9 \text{ nm}$, due to an increase of the electron density contrast in the near surface regime, as the scattered intensity is roughly proportional to the square of the density difference of the two differently coated blocks. The second regime is defined up to $\delta_{Ag} = 2.9 \text{ nm}$ by the coalescence and the therefore selective wetting on the polymer domains indicated by the domain intensity. The embedding and sub-surface growth of Ag clusters in the PMMA domains can explain this behaviour, when at the same time the Ag cluster grow takes place on top of the PS/PMMA lamellas. This growth difference on the polymer domains clearly indicates the initial selective wetting in the early stages. The electron density contrast between surface-coated PMMA/PS-domains and sub-surface implanted pure PMMA domains can be explained by this growth differences.

In regime II the selective diffusion-mediated cluster growth via coalescence is the main growth mechanism. After $\delta_{Ag} = 2.9$ nm, the intensity signal of the domain peak starts to decrease, indicating that the electron density contrast between the domains is reduced, which can be seen in Figure 5.10b. At this point the embedding and sub-surface growth at the pure PMMA lamellae is saturated, and the Ag clusters grow on top of both domains introducing the end of the selective wetting behaviour. After $\delta_{Ag} = 2.9$ nm the clusters now grow arbitrarily on both domains and the growth is described now by a non-selective adsorption-mediated growth (regime III). This can be seen by e.g. the homopolymer GISAXS measurements, where at $\delta_{Ag} = 4$ nm deposition, the Ag cluster radii are similar (see Table 5.1 and Figure B.1). The adsorption-mediated growth can be followed by the domain peak intensity in Figure 5.10b until $\delta_{Ag} = 7.8$ nm. The 1st order lamella peak intensity starts to increase again at $\delta_{Ag} = 7.8$ nm, while the intensity of the 2nd order is shadowed by the overlapping of the shifting cluster peak. This means that the average interparticle distance of the Ag clusters reaches half of the interdomain distance of the polymer template (Figure 5.10c). Now the limit is reached, where the polymer-assisted sputter deposition of the Ag clusters grown on the different domains tend to partially interconnect and defining regime IV. With ongoing deposition, the average cluster distance approaches the interdomain distance, leading to an independent Ag cluster growth. The shift of the cluster peak significantly decreases at an effective thickness of $\delta_{Ag} = 13$ nm, this is related interconnection of the Ag clusters between the domains and the percolation of the metal layer resulting in a layer growth (regime V). In Figure 5.10c the interparticle distance and the radii of the Ag clusters is shown in detail and correlated to the orders of the lamella peak and the growth regimes. The slope of the interparticle distance curve and the radii curve is changing through the evolution of the Ag deposition, when reaching another growth regime. This is indicated by a slow down of the size growth speed for the interparticle distance and the radii and mostly pronounced by regime II to III for reduction the selective wetting.

A schematic model of the Ag cluster growth morphology on PS-*b*-PMMA DBC template is sketched in Figure 5.11 showing a visualization of the five growth regimes. The growth of Ag clusters on PS thin films and especially on PS-*b*-PMMA DBC shows distinct differences compared to gold clusters on PS templates during sputter deposition, as it was described by Kaune and Schwartzkopf *et al.* in previous publications. [48, 63] The Au growth on PS homopolymer thin films showed four distinct growth regions: nucleation, diffusion-mediated growth until a partial cluster coalescence, adsorption-mediated growth with cluster branching and layer growth after percolation. The DBC template assisted sputter deposition revealed a different metal-polymer interaction and the interface morphology disturbs the growth regimes as described with Au and alter their thresholds. [48, 63] The

Ag clusters start to grow on top of the PMMA/PS block (green) and sub-surface growth preferentially on the pure PMMA block (yellow). Schematically, two polymer chains are shown at $\delta_{Ag} = 0$ nm (PS in green, PMMA in brown). Then the clusters start to grow mostly on the lamella block as height differences. At first, the nucleation and selective embedding (I) is the predominant process for $\delta_{Ag} < 0.4$ nm. Afterwards, a selective diffusion-mediated cluster growth via coalescence (II) sets in. At a thickness of around $\delta_{Ag} = 2.9$ nm, a non-selective adsorption-driven growth of immobilized clusters on both diblock copolymer domains occurs (III). After $\delta_{Ag} = 7.8$ nm, a partially interconnection of Ag clusters in between the domains occurs (IV). After $\delta_{Ag} = 13$ nm a fully percolated metal film grows (V). The clusters in IV and V are merged to big cluster aggregates on the domains (grey circle), which visualize the interconnection between the domains. Figure B.2 shows the results of the measured radii and interparticle distance of Ag on PS-*b*-PMMA compared to their corresponding homopolymers PMMA and PS. The Ag cluster growth on the DBC template in the beginning until around $\delta_{Ag} = 7-8$ nm seem to grow with the same size as Ag on the PS thin film. This is a further indication of the selective growth on the PS/PMMA domain in the early Ag growth and the therefore similar growth compared to the PS polymer template. The growth is dominated by the larger Ag clusters on the PS/PMMA domain, which the FESEM image in Figure 5.4 confirmed. Below $\delta_{Ag} = 7-8$ nm, the embedding and sub-surface growth is dominant on the PMMA domain. The Ag cluster growth on the surface of the PMMA domain just started and is then rapidly reaching the Ag cluster sizes as on PS. Afterwards the Ag cluster growth on the DBC template follows the Ag cluster growth on the PMMA thin film and shows even bigger cluster sizes. This might originate from the higher roughness on the DBC template compared to the smooth PMMA homopolymer thin films and the therefore reduced mobility. The correlation of the Ag morphology evolution on the polymer templates compared to their measured electronic properties of the *in situ* experiment results are shown in Figure B.3. Figure B.3a shows the ratio of the average diameter $2R$ of the clusters compared to the interparticle distance D between the clusters. The aforementioned geometrical model was used to determine the radii and the interparticle distance of the Ag clusters. [142] The ratio $2R/D$ with the geometrical model can give a theoretical value for the percolation, which means that the metal clusters start to interconnect. The majority of clusters starts to interconnect, when the ratio $2R/D$ equals one. When the clusters start to interconnect, the percolation threshold is reached, which is depending on specific parameter related to sputter deposition conditions (e.g. sputter rate, argon pressure, target to sample distance) and the target material. At percolation ($2R/D = 1$) the metal clusters start to form a conductive pathway over a macroscopic sample area. In Figure B.3a three curves are shown from the different polymer tem-

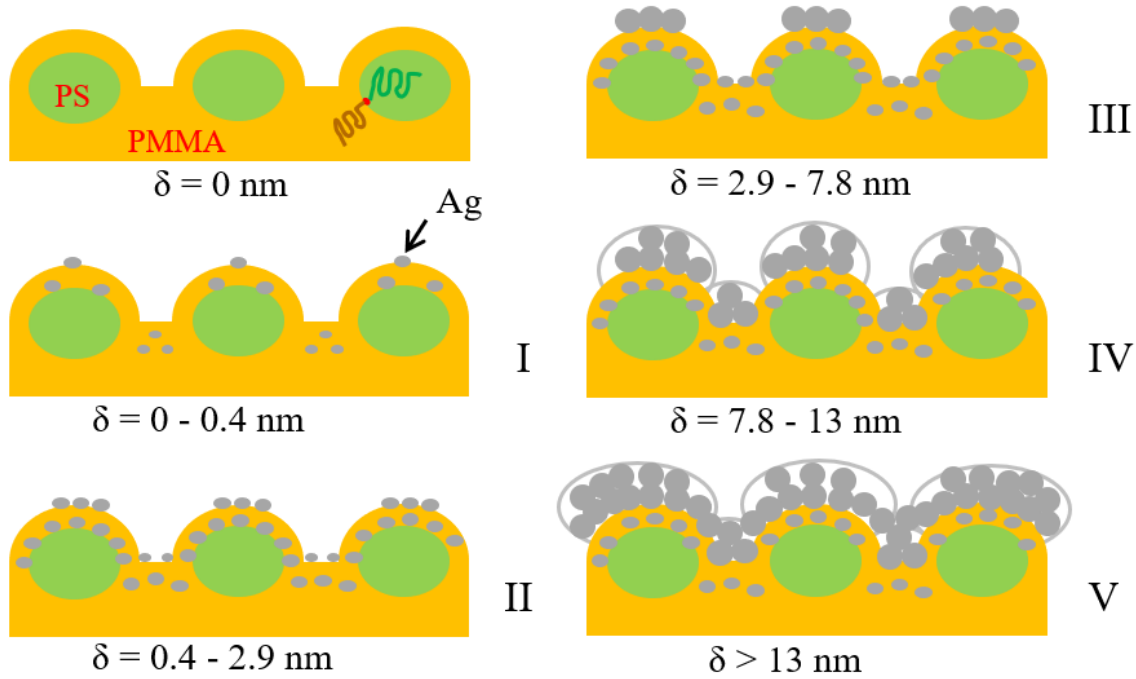


Figure 5.11.: General growth of Ag on PS-*b*-PMMA copolymer templates. The Ag clusters start to grow on top of the PMMA/PS block (green) and sub-surface growth preferentially on the pure PMMA block. Schematically, two polymer chains are shown at $\delta_{Ag} = 0$ nm (PS in green, PMMA in brown). Then the clusters start to grow mostly on the lamellar block as height differences. Growth regions: Nucleation and selective embedding (I) for $\delta_{Ag} < 0.4$ nm. Selective diffusion-mediated cluster growth via coalescence (II) between $\delta_{Ag} > 0.4$ nm and $\delta_{Ag} < 2.9$ nm. Non-selective adsorption-driven growth of immobilized clusters on both diblock copolymer domains (III) at $\delta_{Ag} = 2.9$ nm. Partially interconnection of Ag clusters in between the domains occurs (IV) after $\delta_{Ag} = 7.8$ nm. Fully percolated metal film grows (V) after $\delta_{Ag} = 13$ nm. The clusters in IV and V are merged to big cluster aggregates on the domains (grey circle), which visualize the interconnection between the domains. Reprinted with permission from [69]. Copyright 2019 American Chemical Society.

plates and the percolation threshold is compared to determine their differences. PMMA can be seen by the black crosses and seems to percolate at first (less points are shown here for PMMA, to include only data of the center of the sample and to neglect sample inhomogeneity and sample edge effects for the *in situ* experiment of PMMA). PMMA is followed by PS with the blue crosses, and at last PS-*b*-PMMA is percolating. The shape of the $2R/D$ curve is different compared to before shown results with Au on PS thin films. [63] The Ag cluster growth on PS homopolymer thin films, showed no distinct partial coalescence, which would result in a local maximum in the curve $2R/D$ as

a function of δ_{Ag} , as it was shown by the previous study. The shape of the $2R/D$ curve indicates different coalescence kinetics and reduced cluster branching by the protrusions and the finite lamellar size of the PS-*b*-PMMA template. It seems the Ag clusters tend to grow in size and distance along one lamella without pronounced branching. For deposition on PMMA, the Ag clusters seem to percolate at smaller deposited Ag thickness (approximately 1 nm smaller) than on PS and PS-*b*-PMMA. The percolation threshold of the Ag layer grown on PS-*b*-PMMA occurs at much higher film thicknesses than for the homopolymer templates. This behavior can be related to the finite lamella length of the polymer, as it can be seen by the green circle in Figure 5.1. The results presented here show that a variation of the polymer surface at constant sputtering conditions is affecting this threshold, as well. In order to correlate the Ag layer growth morphology with the resulting electronic properties, *in situ* GISAXS is combined with *in situ* two point resistivity measurements, simultaneously during sputter deposition on PS-*b*-PMMA and compared to the deposition on the corresponding homopolymer thin films. The *in situ* resistance measurements directly confirm the growth behaviour derived from Figure B.3a the *in situ* GISAXS measurements. In Figure B.3b the Ag layers on all polymers expose high electrical sheet resistance up to 8 nm effective layer thickness. Then, a steep decrease of the sheet resistance by more than 4 orders of magnitude occurs, which is attributed to the insulator-to-metal transition (IMT). The first small decrease in resistivity occurs for every polymer thin film before the IMT. This could be a hint for electron tunneling effects. The percolation thresholds extracted from the *in situ* GISAXS measurements and resistance measurements are in good agreement, seen in Figure B.3c. The effective Ag thicknesses for IMT: $\delta_{IMT,PMMA} = (10.6 \pm 0.5) \text{ nm} < \delta_{IMT,PS} = (11.6 \pm 0.4) \text{ nm} < \delta_{IMT,PS-b-PMMA} = (12.7 \pm 0.4) \text{ nm}$. The percolation thresholds determined by GISAXS: $\delta_{p,PMMA} = (10.5 \pm 0.5) \text{ nm} < \delta_{p,PS} = (11.2 \pm 0.5) \text{ nm} < \delta_{p,PS-b-PMMA} = (13 \pm 0.5) \text{ nm}$. Thus, the more pronounced embedding and sub-surface growth on PMMA thin films in the early stages directly affects the metal layer percolation and therefore the IMT in the later stages. This observation is in good agreement with the formation of smaller clusters in smaller distances due to the stronger interaction of deposited Ag with the oxygen in PMMA and thus an earlier percolation. In general, a shift of percolation thresholds to larger values is directly connected to faster cluster surface diffusion and coalescence kinetics.

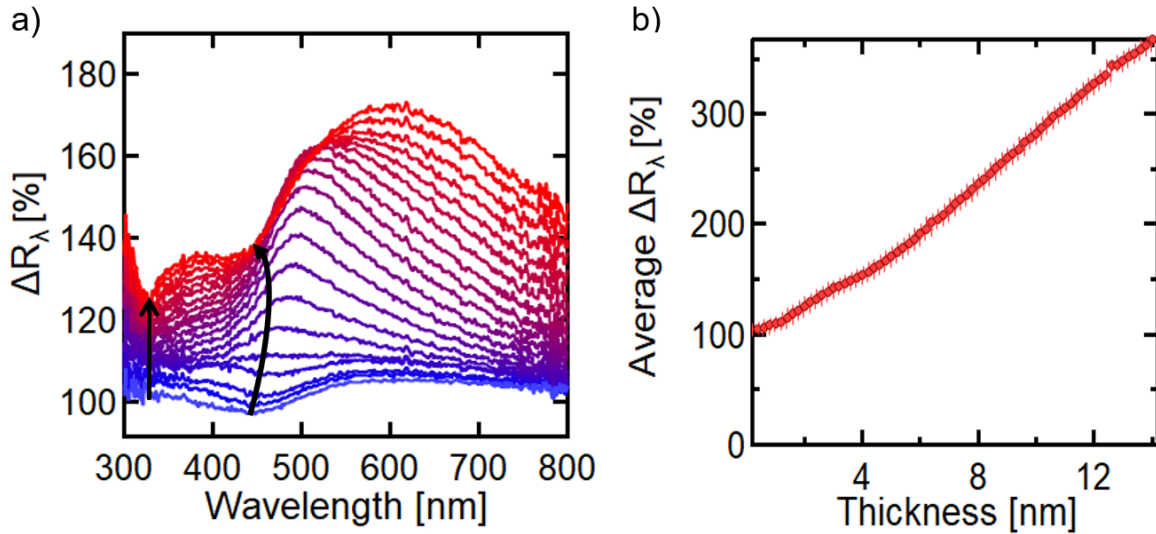


Figure 5.12.: a) Selection of UV-Vis spectra, where the appearing minima is related to the LSPR of Ag clusters on PS-*b*-PMMA template for $0.1 \text{ nm} \leq \delta_{Ag} \leq 4.1 \text{ nm}$. The first minimum is at around 320 nm (3.87 eV) and the second minimum around 444 nm (2.79 eV). The second minimum shows a small red shift with the first few nm Ag deposition and then changes to a small blue shift until it stays constant around $\delta_{Ag} = 4 \text{ nm}$. b) Average reflectance of the whole spectrum for $0.1 \text{ nm} \leq \delta_{Ag} \leq 14 \text{ nm}$. The UV-Vis data was adopted from the Master thesis [206], the interpretation was done in the PhD thesis. Reprinted with permission from [69]. Copyright 2019 American Chemical Society.

5.4. Correlation of the optical relative reflectance change and Ag growth on PS-*b*-PMMA

The Ag morphology evolution on the PS-*b*-PMMA DBC template during the Ag sputter deposition is correlated to the electronic properties and further correlated to *in situ* UV-Vis surface differential reflectance spectroscopy, which are measured at the same time. A part of the results of the *in situ* measured spectra can be seen in Figure 5.12a from 0.1 nm δ_{Ag} to 4.1 nm δ_{Ag} . Here, the relative reflectance change during the growth of Ag clusters on the DBC template is shown for the early cluster growth. The first black arrow indicates a first minimum at around 320 nm (3.87 eV), which might origin from the transverse polarized LSPR of Ag clusters on the polymer template. On the other hand, the optical dielectric function of silver (bulk) has an interband transition near to the observed minimum. The second LSPR minimum (longitudinal polarization) appears at around 444 nm (2.79 eV) and shows a small red shift with the first few nm Ag deposition

and then changing to a very small blue shift until it stays constant around $\delta_{Ag} = 4$ nm. Similar UV-Vis spectra were found by Grachev *et al.*, where they showed the appearing LSPR during Ag sputter deposition on a sapphire substrate. [227] The lamellae structure forces the clusters into elongated cluster arrays, which might result in this polarization effect. Only the relative specular reflectance is measured here, which could result in a different position of the minima in the reflectance spectra compared to the position of the LSPR absorption spectra, but it can be regarded as an indicator for the presence of LSPR. Figure 5.12b shows the integral relative reflectance change, which increases gradually. A slight bump is observed in between $2 \text{ nm} < \delta_{Ag} < 4 \text{ nm}$, which might be an indication of the embedding of Ag in PMMA. Afterwards the reflectance increases linearly indicating the formation of a metal film. The increasing reflectance after $\lambda = 500 \text{ nm}$, goes in the direction of the Ag bulk value with ongoing Ag deposition.

5.5. Summary

A detailed GISAXS analysis of the data taken in the master thesis was based on the model in this thesis. The polymer-template assisted growth of sputter-deposited Ag clusters on PS, PMMA, and PS-*b*-PMMA was demonstrated. The early metal cluster growth on the individual blocks determines the later stages and strongly influences the resulting nanogranular metal layer. The above results show that both, the difference in surface energy (mobility) of the clusters on the domains as well as the specific chemical interaction play a major role in the growth of the clusters on the polymers. Correlating the *in situ* relative reflectance change to the IMT and the embedding, which showed at these Ag thicknesses a higher increase in the optical response. This hints to the fact, that only electrons confined to the clusters contribute to localized plasmon activity. Once the clusters are interconnected, electrons can move freely through the film and can no more contribute to the localized plasmon absorption phenomena. Thus, the study enables a deeper understanding of the origin of the selective wetting behavior in template-assisted sputter deposition. The localized plasmon activity is important for sensor applications, whereas the electrical conductivity is important for electrodes and electronic devices. The electrical conductivity can be adjusted by the polymer template and the metal layer thickness. The embedding is beneficial for tailoring metal contacts for an enhanced extraction of charge carriers in conductive polymers.

6. Selective Ag Nanocluster Metallization on Partially Conjugated PMMA-*b*-P3HT Templates

The most parts of the results shown in chapter 6 were published in the article: *Selective Silver Nanocluster Metallization on Conjugated Diblock Copolymer Templates for Sensing and Photovoltaic Applications* [70] (M. Gensch et al., *ACS Appl. Nano Mater.* 2021, 4, 4, 4245–4255, DOI: 10.1021/acsanm.1c00829)

In this chapter the topography and chemical interaction of the diblock copolymer template PMMA-*b*-P3HT with a Ag cluster decoration is shown. The results of the Ag cluster formation on PMMA-*b*-P3HT is compared with the formation on the corresponding homopolymers to identify differences in Ag cluster growth. To reach this goal different techniques were used such as e.g. AFM, FESEM, GISAXS, GIWAXS, FTIR and XPS.

Functional polymers are becoming more and more interesting for industrial applications such as photovoltaics, organics electronics, transistor and medical applications. [228–234] Electronic and optical performances of functional polymers can be improved by adding nanoparticles in the polymer solution or by the embedding of metals in the polymer matrix. The structure formation of the metal component in the composites at the interface needs a better understanding for the future to influence the metal formation and therefore the optical and electronic properties to tune the metal-polymer composite for applications. [19, 26, 59, 207, 235–237] The metal electrode formation with minimal material usage on application-oriented polymers is of huge interest for nowadays sensors, batteries and photovoltaics industry to a faster transformation in a more sustainable industry. [54, 238, 239] The deposition of metal clusters on polymer surfaces is a common method to prepare electrodes, contacts or multilayer structures. Several studies investigated nanoparticle-polymer compounds in this regard. For example Löhner *et al.* followed

in situ the gold electrode sputter deposition on low bandgap polymers used in OPV. [54] Growth regimes were discovered for example by Kaune *et al.* with Au on such polymer types. [48] In this study, I focus on the cluster formation by self-assembly during metal sputter deposition on application-oriented polymers. The self-assembly process of the metal clusters can be guided by diblock copolymer (DBC) templates to make use of the nanostructure for nanoelectronics or sensing applications. [4, 169, 170] The advantage is the easy tuning ability towards the application by creating hierarchical materials by exploiting the phase-separated polymer structure and the nanocluster length scales. [57, 64] In general, many OPV applications use conductive polymers as a donor material and arrange donor and acceptor in a so-called bulk hetero-junction morphology. [65] The OPV efficiency can be improved with nanostructured polymer domains if the domain size is close to the exciton diffusion length. [66–68] The growth behavior and so-called selective wetting for model systems Ag on PS-*b*-PMMA is described in the previous chapter and other DBC systems with different metal materials is further known from literature. [4, 5, 64] The growth of metals on more complex polymers e.g. semi-crystalline polymers is still not fully understood and therefore is important for the understanding of e.g. electrodes, organic electronics and photovoltaics.

In this chapter the selective Ag wetting is shown on microphase separated polymer domains with an application-oriented polymer as a template. One polymer component of the DBC used for this templating is PMMA. PMMA is chosen as it can be dissolved easily from the surface with acetic acid rinsing. This can be used for further processing. For the second block of the DBC, I selected the model polymer from the field of OPVs, poly(3-hexylthiophen-2,5-diyl) (P3HT). P3HT is semi-crystalline and a widely used p-type organic semiconductor material. In the first section 6.1 the AFM, SAXS, WAXS and static GISAXS measurements are shown, revealing the Ag formation on the polymer domains and the DBC properties. Further FESEM measurements reveal the selective Ag growth on the polymer domains. In the second section 6.2 the chemical interaction is investigated with XPS and FTIR. In the third section 6.3 the *in situ* GISAXS and GIWAXS measurements reveal the dynamics of Ag growth on the DBC template and are correlated with the electronic behaviour, which was measured with resistance measurements. The wetting of Ag on the conjugated DBC films shows different growth behavior than previous studies on amorphous DBCs. The direct correlation measuring electrical, morphological, and chemical properties of the Ag formation on the DBC and the corresponding homopolymer thin films yields to a more detailed understanding of the metal-polymer interaction and formation towards the fabrication of electrode materials for sensors and organic solar cells.

6.1. Topography characterization

In this section the topography of the diblock copolymer template PMMA-*b*-P3HT and the Ag cluster decoration on this diblock is shown. The results of the Ag metal formation on PMMA-*b*-P3HT is compared with the formation on the homopolymers to identify differences in the Ag cluster growth. For this, AFM and FESEM were used.

6.1.1. AFM, SAXS, WAXS and static GISAXS analysis

The pristine PMMA-*b*-P3HT film is shown in Figure 6.1a with an AFM height image of the surface. The topography shows a locally pronounced hexagonal cylindrical DBC structure from an as-spun sample, as it was seen with this DBC type from Zenossi *et al.* in previous publications. [240] The local hexagonal structure is shown in Figure 6.1a by a zoom in (yellow box). The lighter color of the DBC matrix corresponds to the P3HT domain and the darker color wells to the PMMA domain. This will be shown later by the acetic acid treatment. A nanostructure with this DBC template is already accomplished after spin-coating with this polymer thickness without further annealing. The DBC thin films after spin-coating often have to be solvent vapor annealed in order to establish their nanostructure. The solvent vapor annealing is normally done with the use of harmful solvents depending on the polymer domain types. This makes the used DBC template more environmentally friendly for the use of nanostructuring, even though it has to be solved in toluene. Figure 6.1b shows a schematic drawing of the microphase separated structure of the DBC, which we can assume from the acetic acid treatment results shown later. Orange corresponds to the P3HT matrix as shown in 6.1a and black corresponds to the PMMA domains in a local hexagonal arrangement. In the schematic drawing the local hexagonal structure is replicated from the AFM height images. The green line marks an example of a line-cut to determine the height variations from the AFM images and to show the peak-to-valley distance D_{ptv} of the pristine DBC template compared to the Ag decorated DBC template. The corresponding line-cuts in Figure 6.1c show the pristine DBC with a peak-to-valley distance of about $D_{ptv} = (0.6 \pm 0.2)$ nm. Figure 6.1d shows an exemplary schematic side view of the pristine PMMA-*b*-P3HT with a green line describing an exemplary line-cut. In order to identify the corresponding domains of the DBC in the AFM image (P3HT or PMMA), the DBC was immersed in an acetic acid bath for 10 or 15 min (see Figure 6.2a,b), as acetic acid dissolves preferentially the PMMA domain from the DBC. The acetic acid does not break the covalent bonds of the DBC but partially dissolves the PMMA from the valleys, and PMMA migrates to the surface on the P3HT domains. Acetic acid treatment is not applied for the samples used for the sputter deposition and

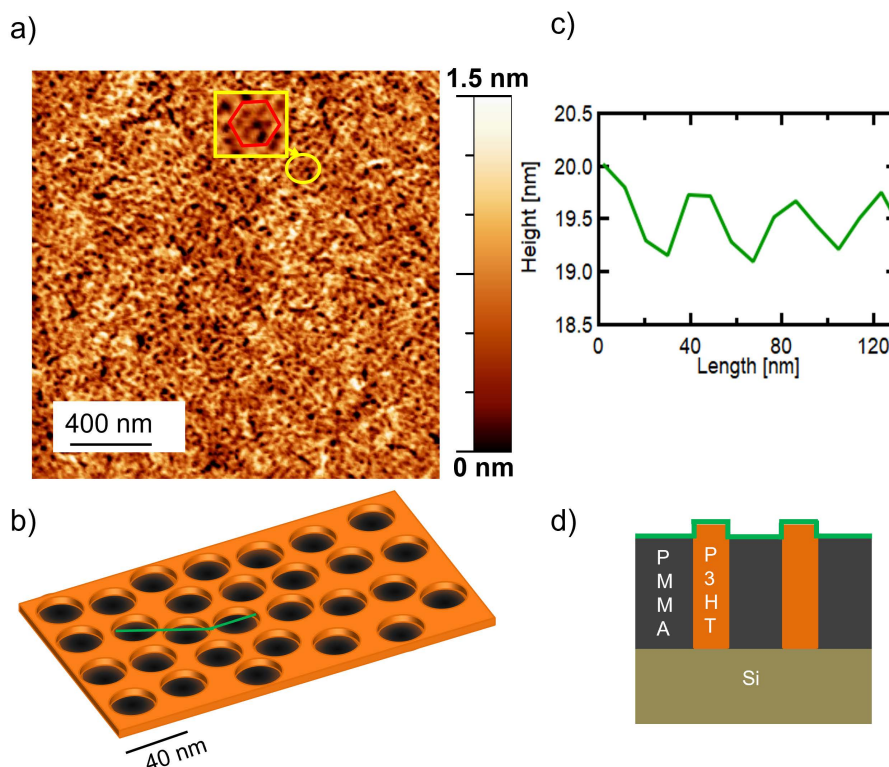


Figure 6.1.: a) AFM topography of the pristine PMMA-*b*-P3HT DBC thin film. The yellow circle shows an example of the local hexagonal cylindrical DBC morphology (marked in red) with a zoom-in. b) Schematic model of the pristine PMMA-*b*-P3HT film with PMMA (black) and P3HT (orange) regions and an exemplary AFM line-cut (green line). c) Height profiles extracted from the AFM images of the pristine PMMA-*b*-P3HT (green line) DBC thin film. d) Schematic side view of pristine PMMA-*b*-P3HT. Reprinted with permission from [70]. Copyright 2021 American Chemical Society.

was only used to identify the specific domains on the DBC template. Acetic acid (100 % , Carl Roth GmbH, Germany) was used to dissolve the PMMA from the diblock copolymer PMMA-*b*-P3HT. The samples were placed vertically in a sample holder and immersed in an acetic acid bath for 10 and 15 minutes. Afterwards the samples were cleaned in an ultra-clean water bath (ELGA Purelab Ultra, 18.2 M Ω cm) for 10 minutes. After cleaning the samples were dried on a hotplate at 40 °C for 1 minute. The AFM height images in Figure 6.2a,b show the DBC rinsed for 10 min and 15 min, respectively, with the partially dissolved PMMA in the wells. Figure 6.2c shows that the acetic acid rinsing increases the well depth of the surface structure, resulting in a higher peak-to-valley distance D_{ptv} ($D_{ptv}(10 \text{ min}) = (8.9 \pm 0.3) \text{ nm}$, $D_{ptv}(15 \text{ min}) = (17.6 \pm 0.5) \text{ nm}$). These results show that the PMMA domains are selectively dissolved from the wells to the surface of the polymer

template. The reconstruction of the PMMA from acetic acid rinsing was already shown by Gharbi *et al.* and Xu *et al.* in previous studies. [178, 179] The polymer domains have

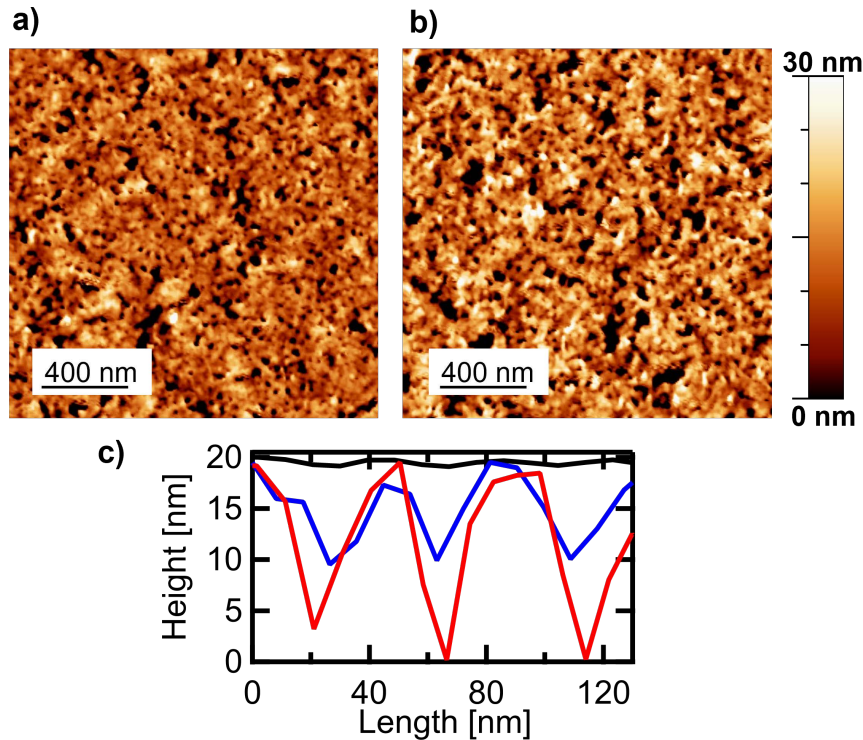


Figure 6.2.: a) AFM height image for 10 min acetic acid rinsing. b) AFM height image for 15 min acetic acid rinsing. c) Line-cuts for pristine PMMA-*b*-P3HT (black), 10 min acetic acid rinsing (blue) and 15 min acetic acid rinsing (red). Reprinted with permission from [70]. Copyright 2021 American Chemical Society.

been identified with the acetic acid treatment and can be now used to follow the selective Ag growth on the specific domains of the DBC template. In Figure 6.3a,b line-cuts are shown for different Ag thickness to determine the peak-to-valley distance (D_{ptv}). Further the domain peak distance L_D can be seen by the pristine sample and followed for different Ag thickness. Figure 6.3c shows the power spectral density (PSD) of the AFM images for different Ag thickness. The PSD can follow the evolution of the domain peak and give us information about the change of the selective wetting. Figure 6.3d-f shows AFM height images for $\delta_{Ag} = 1, 4$ and 10 nm, with different Ag decoration on the DBC template, which will be shown later as different growth regimes. The measured PSD is shown as an inset in Figure 6.3c-f.

Figure 6.4a shows an AFM height image of the DBC template, which is coated with

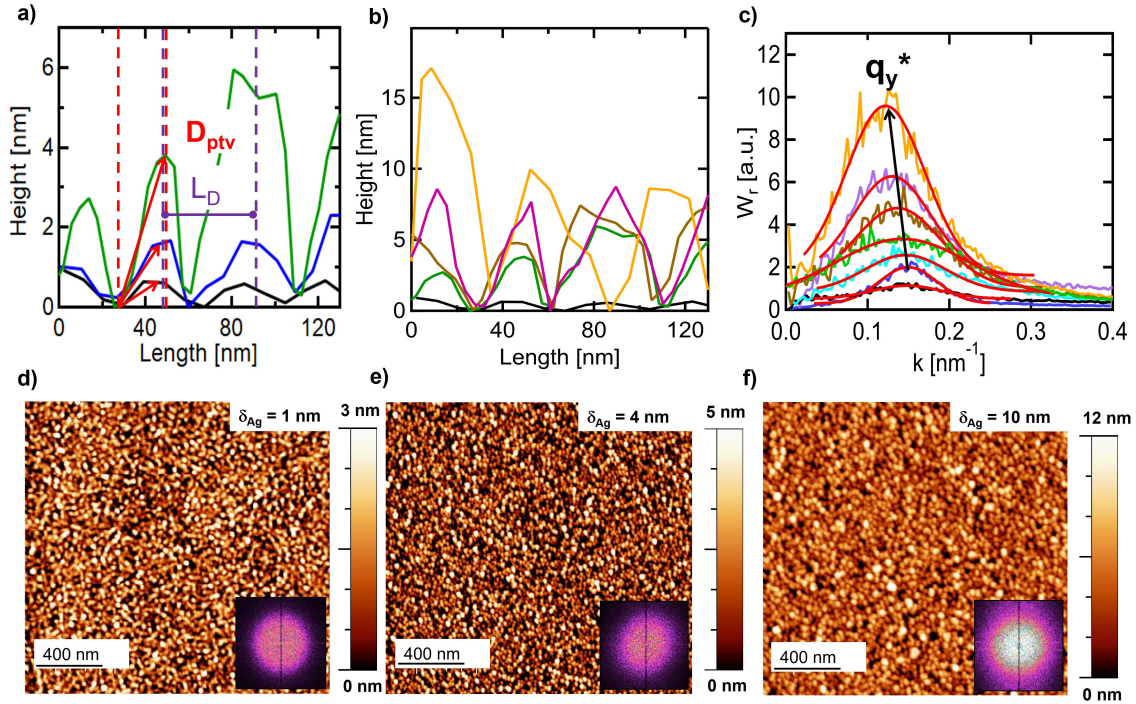


Figure 6.3.: a), b) AFM height profiles of PMMA-*b*-P3HT with $\delta_{Ag} = 0$ nm (black), $\delta_{Ag} = 1$ nm (blue), $\delta_{Ag} = 4$ nm (green), $\delta_{Ag} = 8$ nm (brown), $\delta_{Ag} = 10$ nm (violet) and $\delta_{Ag} = 14$ nm (yellow) nm Ag thickness showing increasing peak-to-valley distance up to 10 nm. c) Power spectral density (PSD) functions calculated from AFM images of Ag thickness of $\delta_{Ag} = 0$ nm (black), 1 nm (blue), 2 nm (light blue), 4 nm (green), 8 nm (brown), 10 nm (violet) and 14 nm (yellow) on PMMA-*b*-P3HT, obtained by azimuthally integrating the Fourier transformed images to enhance the statistical information. LD shows the domain period of the copolymer structure. AFM topography of the PMMA-*b*-P3HT film sputter coated with an Ag thickness of d) $\delta_{Ag} = 1$ nm, e) 4 nm and f) 10 nm, respectively. The insets show the Fourier transform (FT) of the corresponding AFM images with the scale bar corresponding to 0.3 nm^{-1} . Reprinted with permission from [70]. Copyright 2021 American Chemical Society.

an effective Ag thickness of $\delta_{Ag} = 1$ nm. The local hexagonal arrangement is still visible and more pronounced compared to the pristine sample. Ag clusters selectively decorate the P3HT matrix of the DBC template in Figure 6.4a, seen by the small white clusters on the matrix. The selective wetting of the Ag clusters on the P3HT matrix was further derived by line-cuts for different effective Ag thickness (δ_{Ag}) shown in Figure 6.4b. Here, the peak-to-valley (D_{ptv}) value is followed with AFM measurements to reveal the selective wetting. In Figure 6.4b the increase of the D_{ptv} between $1 \text{ nm} \leq \delta_{Ag} \leq 14 \text{ nm}$ is shown.

The D_{ptv} would indicate here a selective wetting of Ag on the P3HT domains on the DBC film until $\delta_{Ag} = 14$ nm.

However, the growth modes are more complex and need additional input to analyse the selective wetting. In Figure 6.4b for $\delta_{Ag} \leq 4$ nm, the increase of the peak-to-valley distance follows a linear growth. The decoration until $\delta_{Ag} = 4$ nm could be regarded as selective wetting of the Ag clusters on P3HT. After $\delta_{Ag} = 4$ nm, the growth phase is changing indicating by a slowing-down of the D_{ptv} until $\delta_{Ag} = 8$ nm. At $\delta_{Ag} > 8$ nm the linear increase starts again with a different slope of the D_{ptv} . The slowing-down compares well to the AFM images seen in Figure 6.3f: More and more of the PMMA is covered with Ag clusters, filling the PMMA wells. This can be seen in Figure 6.3d-f, by the reduction of the black wells. The further increase for $\delta_{Ag} > 8$ nm could be related to the different Ag cluster growth stages on both polymers, which will be shown later by GISAXS and FESEM measurements. Reasons for this could be the previous embedding of Ag in PMMA, different Ag cluster shapes and different Ag formation on the polymer domains on the DBC. In addition, I analyzed in Figure 6.4c the power spectral density (PSD) of the AFM images. Details about the PSD analysis can be found in Figure 6.3c. The PSD function indicating a domain period of $L_D = (43 \pm 5)$ nm for the pristine PMMA-*b*-P3HT thin film, with ongoing Ag decoration the domain period slightly changes until $\delta_{Ag} = 4$ nm, which can be also seen as nearly constant in Figure 6.4c and indicates a selective wetting until $\delta_{Ag} = 4$ nm. Above $\delta_{Ag} = 4$ nm, the periodic structure does not follow the domain period of the DBC anymore, as shown in Figure 6.4c by a linear increase of the domain period. At the same time, the peak-to-valley distance increase significantly, but the increase of the domain period is indicating the loss of correlation of the lateral structure between the DBC structure and the growing Ag layer.

Figure 6.5 presents AFM images of the surface of the pristine PMMA and P3HT homopolymer thin films. PMMA shows a smooth amorphous surface, while the surface of the P3HT thin film is rougher due to the semi-crystalline fiber arrangement. The crystallinity of the P3HT domain of the DBC template needs to be further understood compared to the P3HT homopolymer. The surface morphology of the DBC is investigated with GISAXS and the crystallinity with GIWAXS (Figure 6.6).

The size of the domain period of the pristine PMMA-*b*-P3HT was calculated from the GISAXS data in Figure 6.6a. The domain peak is seen by the pseudo Bragg peak in the out-of-plane direction in the GISAXS data. The peak is not as pronounced compared to the PS-*b*-PMMA peak, because of the less-developed long range ordering compared to the amorphous DBC. The domain period is $L_D = (42 \pm 4)$ nm and in good agreement with the findings of the AFM measurements above. In Figure 6.6b the semi-crystalline

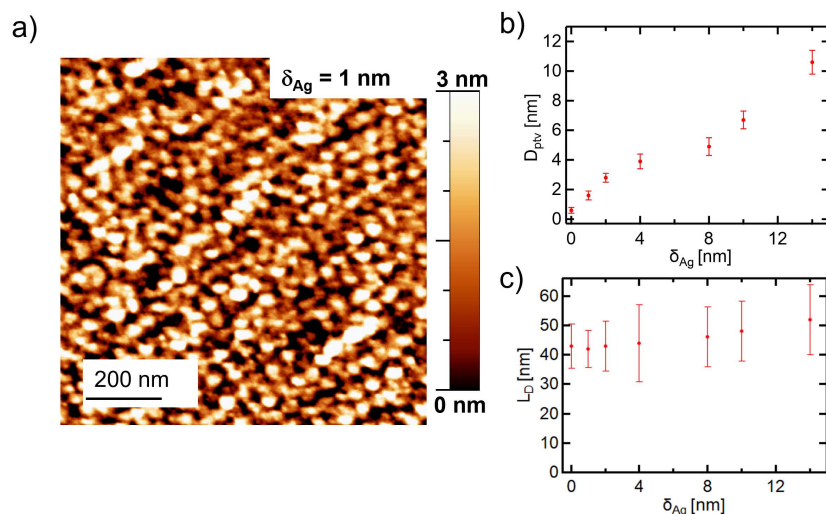


Figure 6.4.: AFM topography of the PMMA-*b*-P3HT film sputter coated with an Ag thickness of a) $\delta_{Ag} = 1$ nm. b) Peak-to-valley distance (D_{ptv}) derived from the line-cuts seen in Figure 6.3. c) PMMA-*b*-P3HT DBC domain period (L_D) derived from the power spectral density (PSD) functions calculated from AFM images seen in Figure 6.3. Reprinted with permission from [70]. Copyright 2021 American Chemical Society.

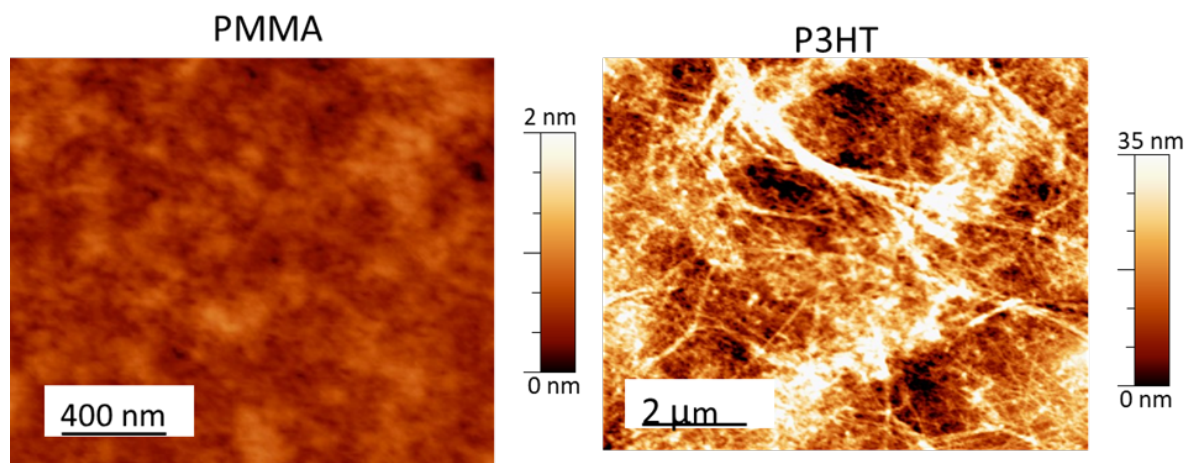


Figure 6.5.: A comparison of AFM topography of the pristine homopolymer thin films: PMMA and P3HT. Reprinted with permission from [70]. Copyright 2021 American Chemical Society.

structure of the PMMA-*b*-P3HT template is shown in comparison to their corresponding homopolymer P3HT. The DBC template shows a less pronounced crystallinity compared to P3HT but still has a some crystalline arrangement, seen by the fitted red bump for the

100 direction of the blue curve.

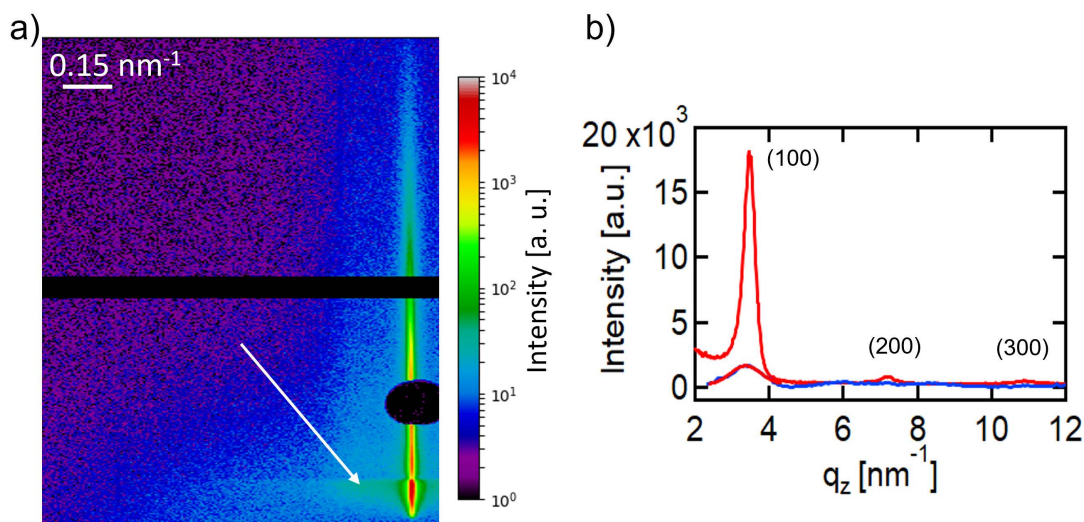


Figure 6.6.: a) 2D-GISAXS data of a PMMA-*b*-P3HT thin film with a pseudo Bragg peak (white arrow) at around $L_D = (42 \pm 4)$ nm for the domain peak. b) GIWAXS line-cuts from PMMA-*b*-P3HT (blue line) with a fit for only the (100) peak (2nd red line) and P3HT (red line) thin films with 20 nm thickness showing three Bragg peaks. The characteristic P3HT peaks (100), (200) and (300) are shown for the 20 nm P3HT thin film. For the PMMA-*b*-P3HT thin film with a thickness of 20 nm only the (100) peak is seen and a small bump of the amorphous PMMA-*b*-P3HT peak. Reprinted with permission from [70]. Copyright 2021 American Chemical Society.

SAXS and WAXS was applied to a thick PMMA-*b*-P3HT film of around $2 \mu\text{m}$ to investigate the thermal stability of the crystallinity and DBC ordering. For the SAXS and WAXS measurements a Pilatus 300k was used. The SDD for SAXS measurements was SDD: 1051.35 mm and for WAXS: 101.35 mm. The wavelength was $\lambda = 0.15418$ nm. In addition the morphology of the DBC template is investigated during heating and cooling with SAXS in Figure 6.7. The DBC template is heated from $T = 25^\circ\text{C}$ to 250°C to see changes of the domain peak during the heating. The temperatures were chosen to see changes near to the glass temperature of PMMA (around $T = 100^\circ\text{C}$) and P3HT (around $T = 200^\circ\text{C}$). The domain peak (L_D) improved slightly for $T = 100^\circ\text{C}$ and $T = 110^\circ\text{C}$ but after $T = 160^\circ\text{C}$ the domain peak is clearly reduced. After $T = 250^\circ\text{C}$ the domain peak is vanishing, which results in the loss of the DBC nanostructure. The cooling did not result in a reversible process, the domain peak did not reappear. In Figure 6.8 the

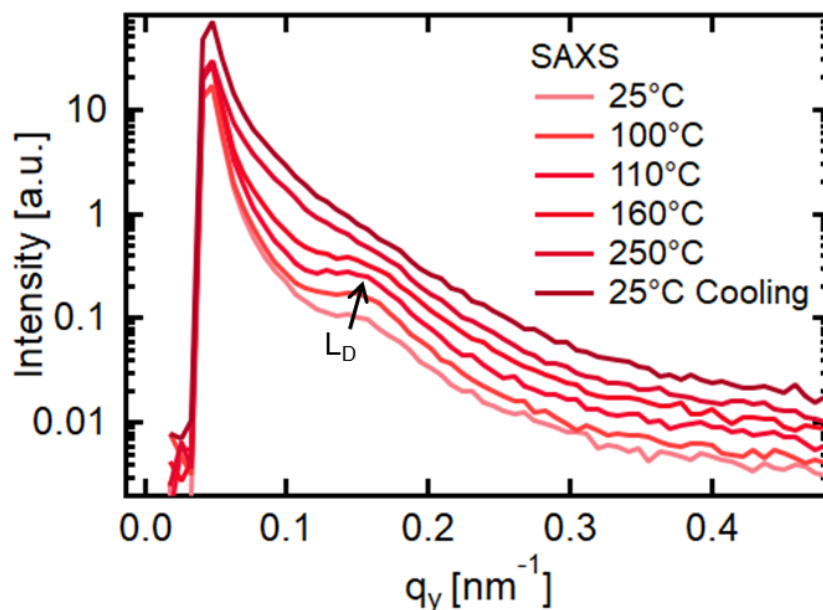


Figure 6.7.: SAXS line-cuts from a thick PMMA-*b*-P3HT polymer film treated with different temperatures (25°C, 100°C, 110°C, 160°C, 250°C and cooled down again to 25°C). The domain peak L_D is increasing which results in a more arranged structure but with reaching the 160°C the arrangement gets irreversible destroyed. Cooling down does not result in the previous structure. A domain period of $L_D = (41 \pm 5)$ nm was obtained for 25°C. Reprinted with permission from [70]. Copyright 2021 American Chemical Society.

crystallinity of the DBC template is shown for heating from $T = 25^\circ\text{C}$ to 250°C . The typical (100) peak of P3HT can be seen. The crystallinity of the DBC template is shown to be improved during heating still until $T = 250^\circ\text{C}$. This is also seen by the (010) peak of P3HT, which has a small appearance for $T = 25^\circ\text{C}$ and is slightly improving until $T = 250^\circ\text{C}$. Due to the DBC template an amorphous region between the (100) and (010) peak is visible, which is growing during the heating process. The heating can improve the crystallinity but the loss of the nanostructure between $T = 110^\circ\text{C}$ and $T = 160^\circ\text{C}$ leads to a diffuse orientation of the DBC nanostructure.

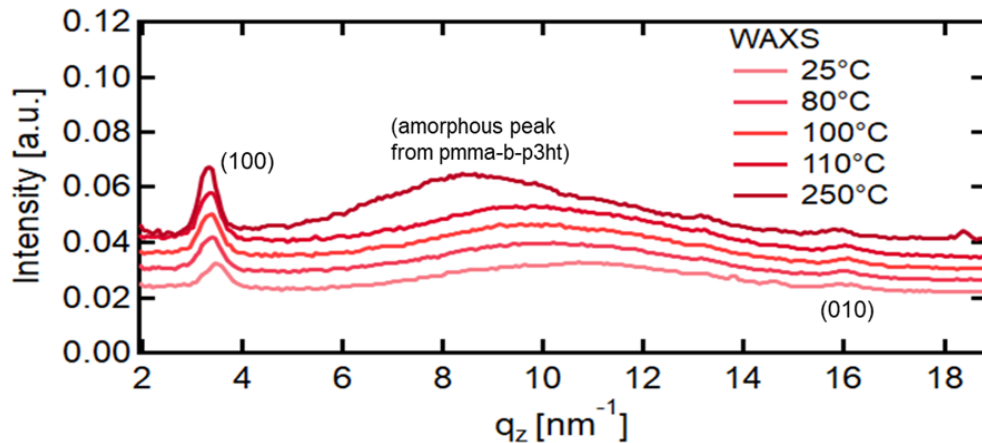


Figure 6.8.: WAXS line-cuts from a thick PMMA-*b*-P3HT polymer film treated with different temperatures (25°C, 80°C, 100°C, 110°C, 250°C). The typical P3HT crystalline structure with the 100 direction is seen with an amorphous PMMA-*b*-P3HT peak overlapping the 200 and 300 peak of the P3HT. A face on (010) orientation can be seen at around 16 nm⁻¹. Reprinted with permission from [70]. Copyright 2021 American Chemical Society.

6.1.2. FESEM analysis

The early cluster growth on the DBC is further investigated by FESEM. The influence of the semi-crystalline part of the P3HT can be seen especially for the early cluster stages. The Ag clusters seem to arrange on the crystalline part of the ordered P3HT domain and form small regions of cluster aggregation, see Figure 6.9a. The cluster aggregation regions were identified with the program ImageJ, shown in Figure 6.9b by the red marked aggregates. [241] The threshold (red) was set such as to match the cluster aggregation regions with very little deviation to the original image in Figure 6.9a. The cluster aggregation regions are clearly replicated by the threshold marked in red. In Figure 6.9c the outlines of the cluster aggregation regions are then shown, which were found by the threshold from Figure 6.9b. The contrast for analysis was guided by the contrast of the clusters similar in Roth et al. in previous publication. [194] The size of these average cluster aggregation regions is calculated by the histogram in Figure 6.9d as (46 ± 13) nm. The ongoing Ag growth on the DBC template is further investigated with FESEM measurements, shown in Figure 6.10. The FESEM images show the PMMA-*b*-P3HT templates with different Ag thicknesses. In Figure 6.10a, for $\delta_{Ag} = 1$ nm the before mentioned formation of clusters on the crystalline parts of the P3HT can be seen. In the red triangle, the estimated model of Schwartzkopf *et al.* with three adjacent local monodisperse equidistant clusters can be observed. [142] With ongoing deposition, it is observed that until an effective Ag thickness

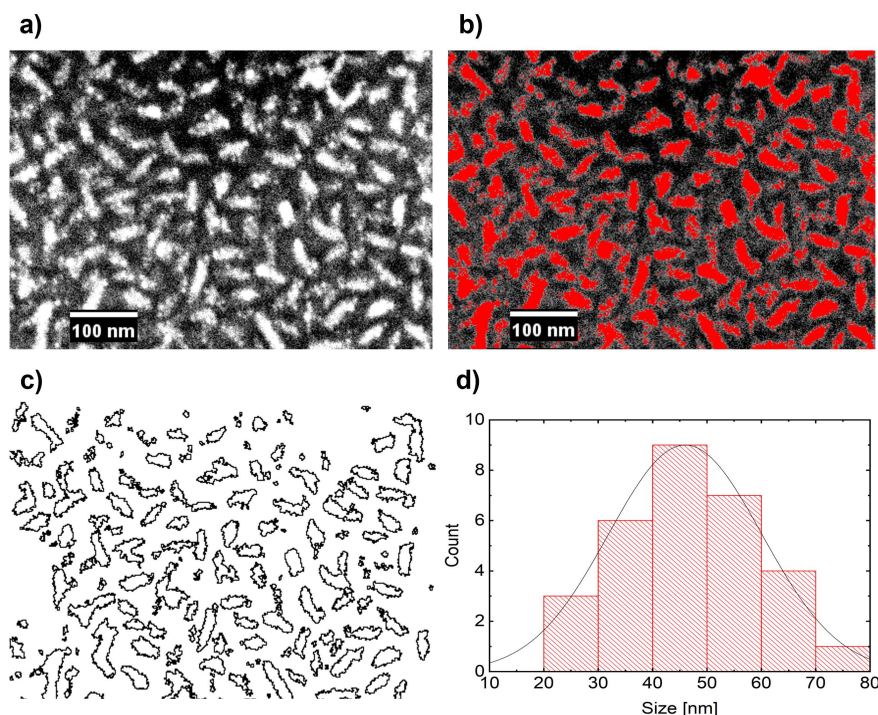


Figure 6.9.: a) A FESEM image of PMMA-*b*-P3HT with Ag thickness $\delta_{Ag} = 1$ nm. b) FESEM edited with ImageJ (v1.51k) to mark the regions with parts of crystalline P3HT (red). c) A result of the analyzed image in b) using ImageJ. One example of a line-cut for the image in c) shows the size of one region with Ag cluster aggregation. In these regions individual clusters are visible which stick to the crystalline part of the P3HT. The line-cuts indicate an average size (length) of these regions of (46 ± 13) nm. d) A histogram image of the average size obtained from the line-cuts as shown in c). Reprinted with permission from [70]. Copyright 2021 American Chemical Society.

of 10 nm the clusters did not form a percolated network, see Figure 6.10a-c. The first connected pathway can be found for $\delta_{Ag} = 10$ nm in Figure 6.10d. In Figure 6.10e for $\delta_{Ag} = 12$ nm, even multiple connected pathways can be observed, the film seems to be electrically conductive from that point on. In Figure 6.10f at $\delta_{Ag} = 14$ nm, the metal film is nearly covering the whole polymer template and a fully connected metal film can be seen. Eventually, in Figure 6.10f a nanostructured electrode layer can be found for around $\delta_{Ag} = 14$ nm. The Ag cluster growth on the corresponding homopolymer thin films is shown in Figure 6.11. The Ag growth on PMMA shows a more fractal like cluster growth compared to more separated cylinders of Ag on P3HT, seen in Figure 6.11b,c for PMMA and Figure 6.11e,f for P3HT. The cylindrical shape of Ag clusters on P3HT will be shown

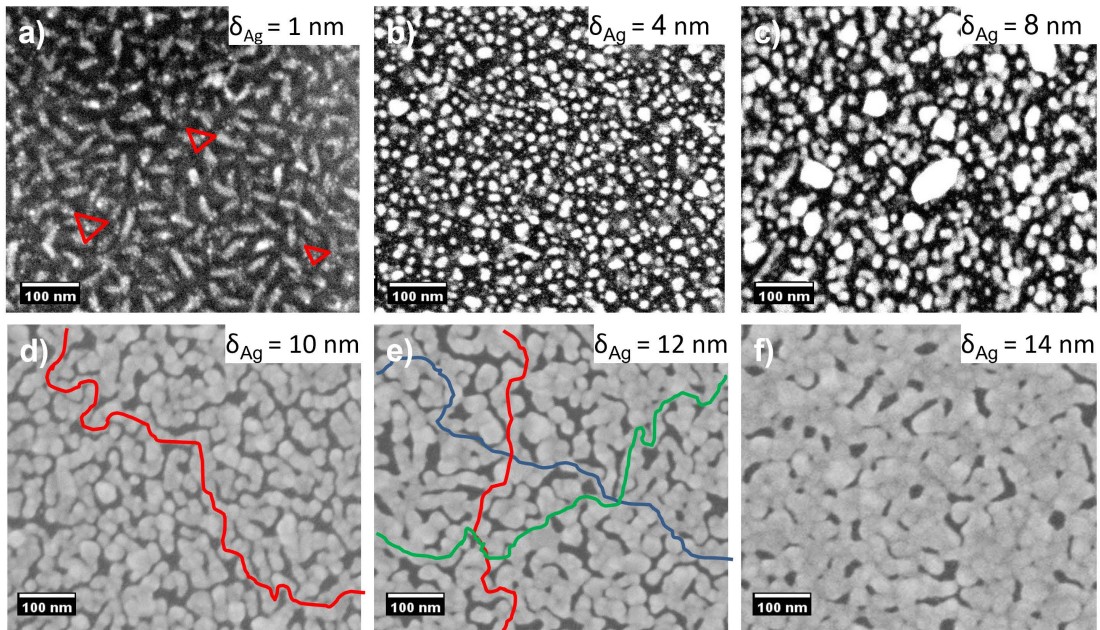


Figure 6.10.: FESEM images with different sputter-deposited Ag thickness δ_{Ag} : a) $\delta_{Ag} = 1$ nm shows Ag cluster formation on the crystalline part of the P3HT domain. The clusters often locally arrange in a triangular structure as described in the model of Schwartzkopf et al.. b), c) $\delta_{Ag} = 4$ nm and 8 nm continuous cluster grow. d) $\delta_{Ag} = 10$ nm a possible single conductive pathway arises (indicated as red line). e) $\delta_{Ag} = 12$ nm multiple conductive pathways arise (indicated with red, blue, and green lines). f) $\delta_{Ag} = 14$ nm the metal film starts to completely percolate the DBC surface. Reprinted with permission from [70]. Copyright 2021 American Chemical Society.

later by the X-ray scattering results. From Figure 6.11e with $\delta_{Ag} = 4$ nm on P3HT, it is not expected to percolate earlier than Ag on PMMA. But due to the crystalline fibers, the Ag growth is directed on the fibers and leads to percolation on these fibers. This can be seen very nicely in Figure 6.11f, where already a percolated pathway is visible for $\delta_{Ag} = 8$ nm, while for PMMA in Figure 6.11c separated islands are visible.

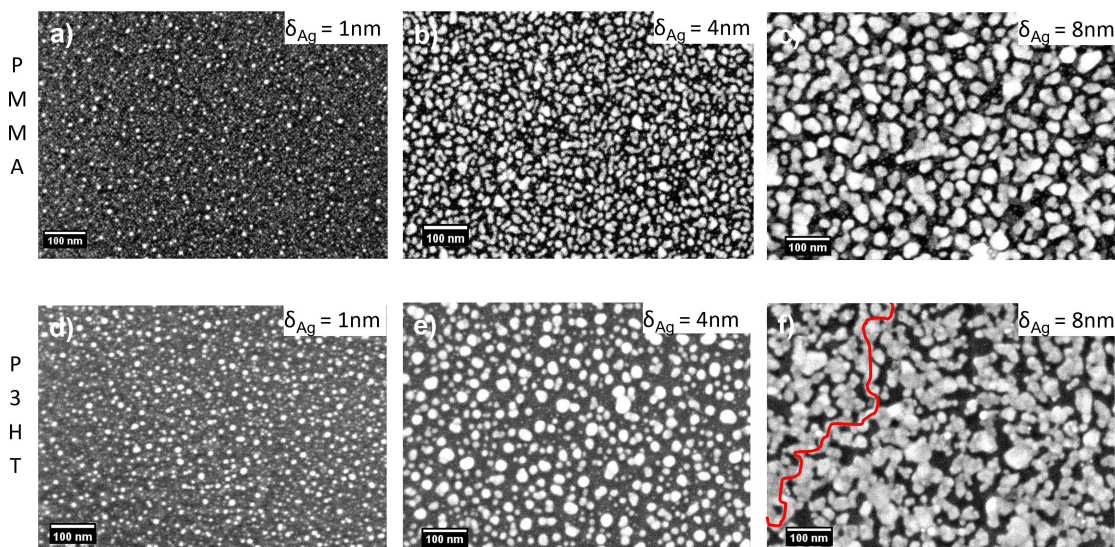


Figure 6.11.: a-c) FESEM images of PMMA with Ag thickness $\delta_{Ag} = 1, 4$ and 8 nm. d-f) P3HT with Ag thickness $\delta_{Ag} = 1, 4$ and 8 nm. The red line shows a potential conductive pathway for P3HT with $\delta_{Ag} = 8$ nm. Reprinted with permission from [70]. Copyright 2021 American Chemical Society.

6.2. Surface chemistry characterization

6.2.1. XPS and FTIR analysis

In this section the interaction of the metal with the polymers is investigated in more detail to reveal the selective wetting in the early stages of cluster growth. In Figure 6.12 the XPS data of the pristine ($\delta_{Ag} = 0$ nm) PMMA-*b*-P3HT film is compared to the Ag decorated PMMA-*b*-P3HT film with $\delta_{Ag} = 1$ nm. The interaction between the Ag and the polymer domains is seen by the oxygen and sulfur components of the polymers. Therefore the S 2p and O 1s peak in the XPS spectra are investigated. Figure 6.12a shows the S 2p electron peak for sulfur in P3HT of the PMMA-*b*-P3HT DBC for $\delta_{Ag} = 0$ nm with two bonding types (C-S-C, S-H). After $\delta_{Ag} = 1$ nm deposition a bump is appearing at 161.5 eV in Figure 6.12b. The bump is identified as chemical bonding of Ag with sulfur to Ag sulfide. Figure 6.12c shows the pie chart of the atomic percentage relations of the different bonds in the S 2p peak with $\delta_{Ag} = 1$ nm. After deposition of only $\delta_{Ag} = 1$ nm, the proportion of Ag sulfide is already very high, which shows the high interaction of Ag with P3HT in the early Ag growth. The same behavior is observed at the O 1s spectra, indicating a bonding of Ag with the oxygen in the PMMA block to silver oxide (Figure 6.12d,e). Figure 6.12f shows the pie chart of the atomic percentage relations of

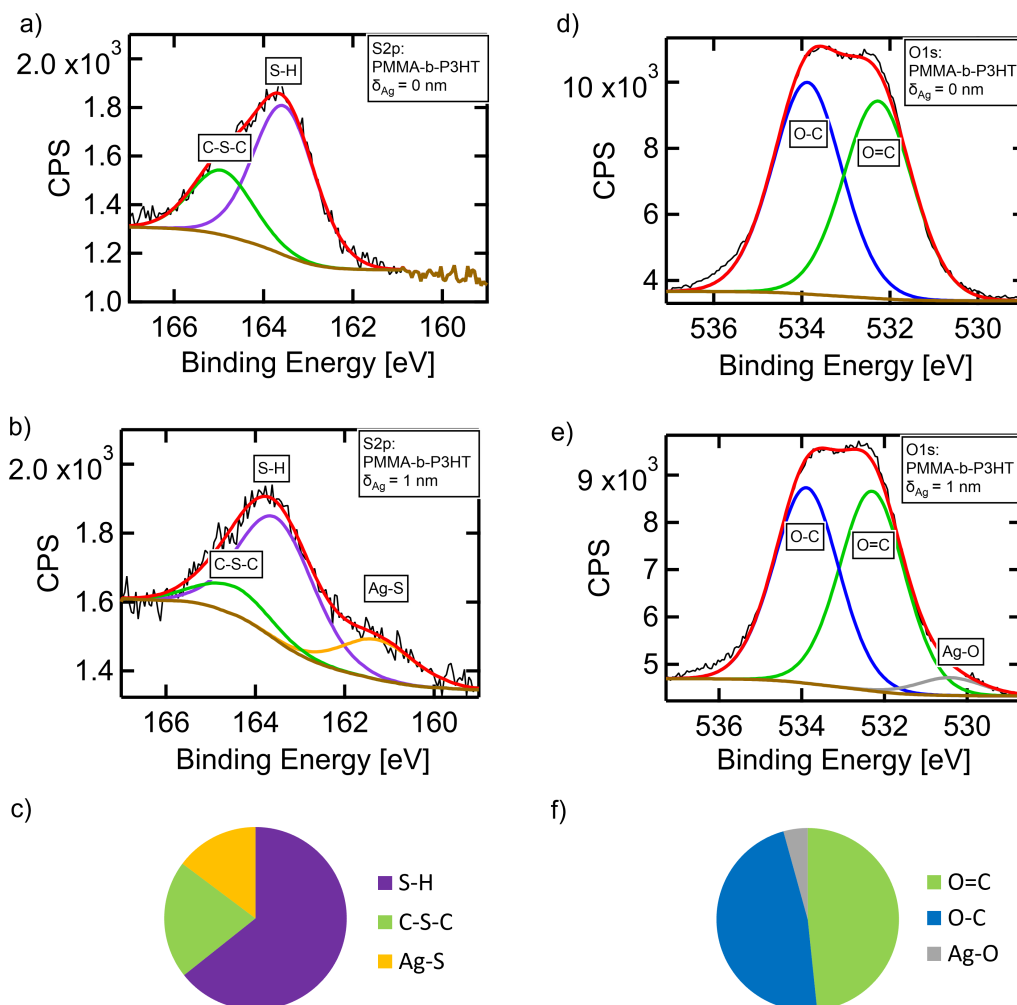


Figure 6.12.: a) XPS spectra at S 2p edge of pristine PMMA-*b*-P3HT ($\delta_{Ag} = 0$ nm) and b) sputter-coated PMMA-*b*-P3HT with $\delta_{Ag} = 1$ nm. c) Atomic percentage relation in the S 2p peak on the bonds for PMMA-*b*-P3HT with $\delta_{Ag} = 1$ nm. d) XPS spectra at O 1s edge of pristine PMMA-*b*-P3HT ($\delta_{Ag} = 0$ nm) and e) sputter-coated PMMA-*b*-P3HT with $\delta_{Ag} = 1$ nm. f) Atomic percentage relation in the O 1s peak on the bonds for PMMA-*b*-P3HT with $\delta_{Ag} = 1$ nm. Reprinted with permission from [70]. Copyright 2021 American Chemical Society.

the different bonds in the O 1s peak at $\delta_{Ag} = 1$ nm. The exact values for the atomic relations can be seen in Figure 6.13. The analysis of the O 1s and S 2p peak reveals that the affinity of Ag to sulfur seems to be higher compared to oxygen (Ag-S: 20% compared to Ag-O: 5%). The pie charts reveal a different chemical reaction of the Ag atoms with the polymer domains. Ag binds at the components of the polymer domains and acts as a

nucleation site during the metal growth. The XPS results for the C 1s peak of the DBC can be seen in Figure 6.14 and confirm the lower interaction of the Ag with C=O bonds compared to the results of Ag with PS-*b*-PMMA in the previous chapter.

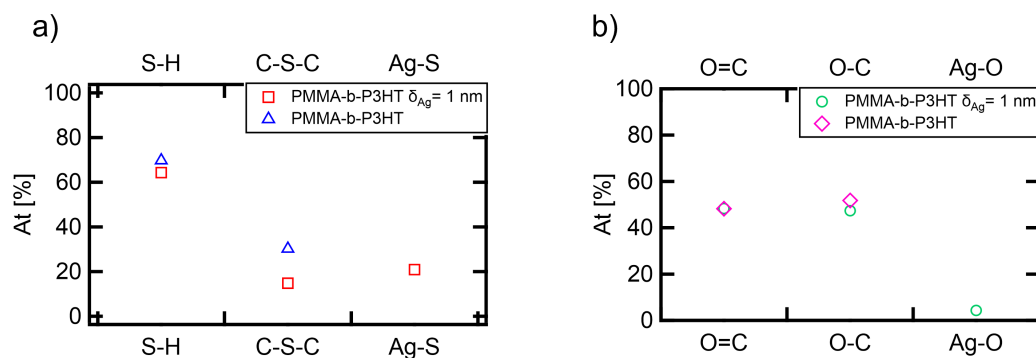


Figure 6.13.: a) Atomic percentage relation (At) in the S 2p peak on the bindings for PMMA-*b*-P3HT with $\delta_{Ag} = 0$ nm and with $\delta_{Ag} = 1$ nm. b) Atomic percentage relation (At) in the O 1s peak on the bindings for PMMA-*b*-P3HT with $\delta_{Ag} = 0$ nm and with $\delta_{Ag} = 1$ nm. Reprinted with permission from [70]. Copyright 2021 American Chemical Society.

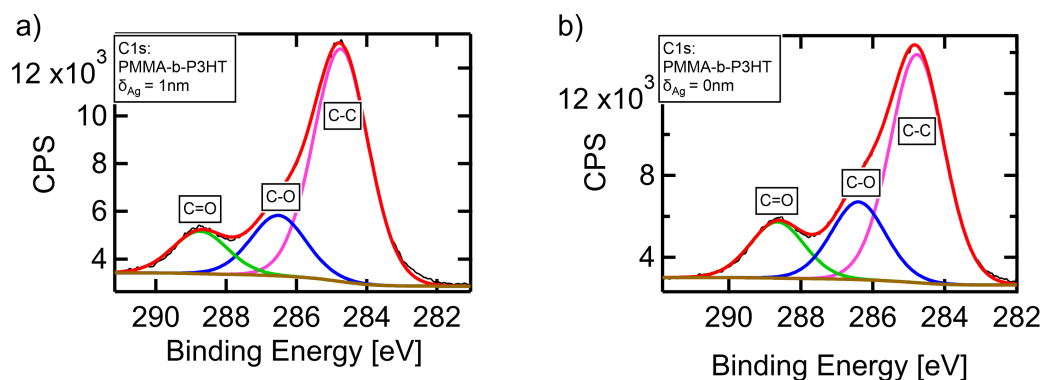


Figure 6.14.: XPS spectra at C 1s edge of a) sputter-coated PMMA-*b*-P3HT ($\delta_{Ag} = 1$ nm) and b) pristine PMMA-*b*-P3HT with $\delta_{Ag} = 0$ nm. Reprinted with permission from [70]. Copyright 2021 American Chemical Society.

The XPS results for the homopolymer films can be seen in Figure 6.15 and Figure 6.16. The metal growth depends on the polymer environment and influences the different

cluster morphologies. As described in the previous chapter, the Ag growth on PMMA starts with embedding and subsurface growth. For Ag growth on the P3HT domain, this does not seem to be the case. As it was seen in Figure 6.9 by the FESEM measurements with the Ag clusters arranging on the P3HT crystalline structures. In Figure 6.17 the XPS results for the homopolymer thin films show the same trend as the DBC template for the affinity of Ag to sulfur and similar ratio for the components before and after Ag deposition.

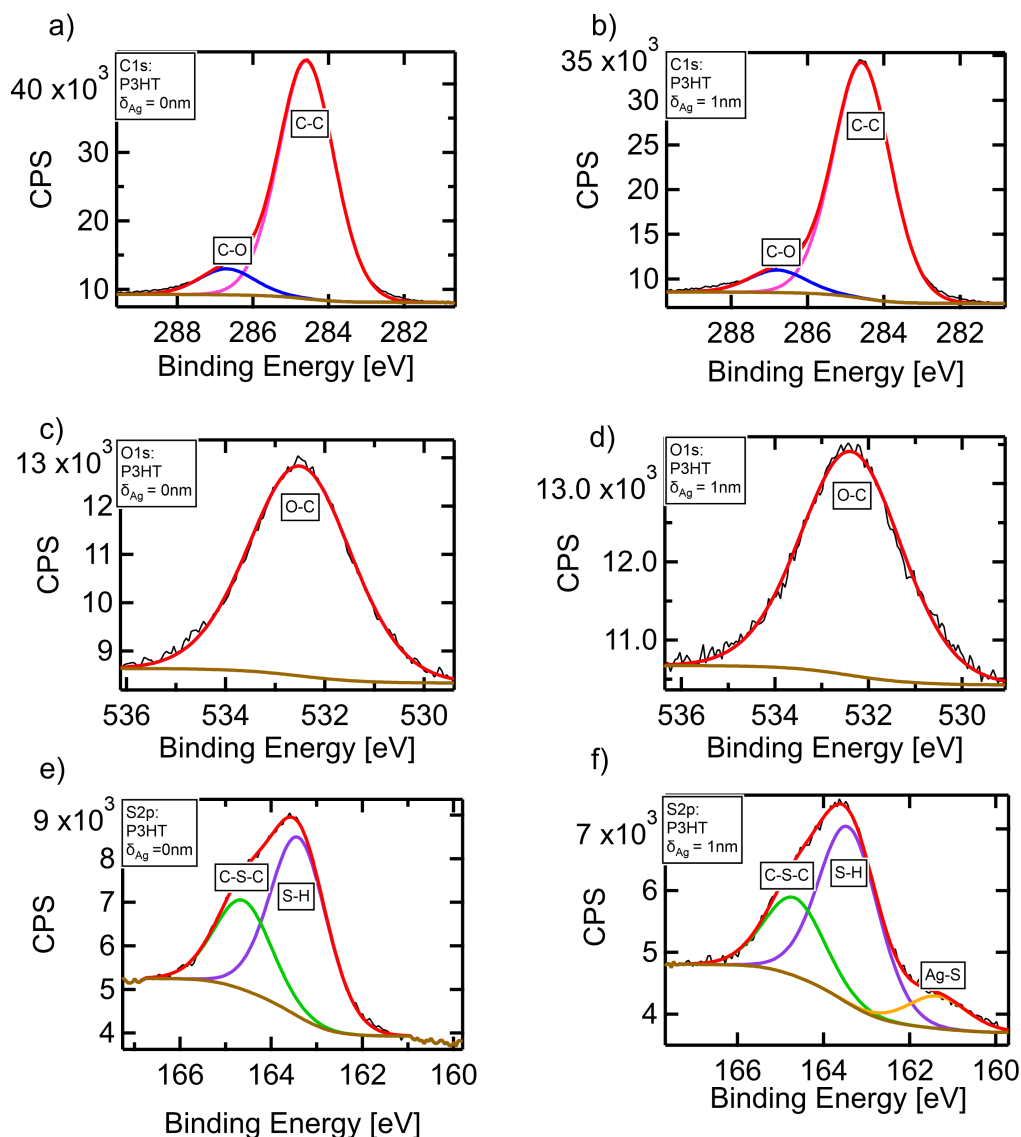


Figure 6.15.: XPS spectra at C 1s edge of a) pristine P3HT ($\delta_{Ag} = 0$ nm) and b) sputter-coated P3HT with $\delta_{Ag} = 1$ nm. XPS spectra at O 1s edge of c) pristine P3HT ($\delta_{Ag} = 0$ nm) and d) sputter-coated P3HT with $\delta_{Ag} = 1$ nm. XPS spectra at S 2p edge of e) pristine P3HT ($\delta_{Ag} = 0$ nm) and f) sputter-coated P3HT with $\delta_{Ag} = 1$ nm. Reprinted with permission from [70]. Copyright 2021 American Chemical Society.

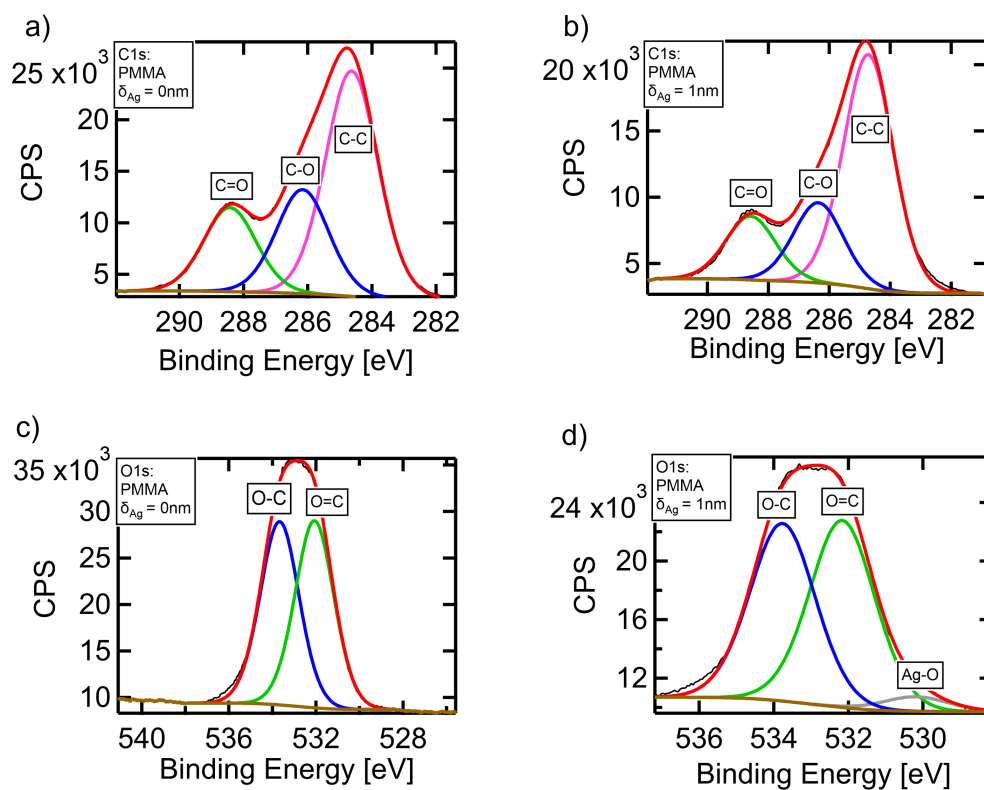


Figure 6.16.: XPS spectra at C 1s edge of a) pristine PMMA ($\delta_{Ag} = 0$ nm) and b) sputter-coated PMMA with $\delta_{Ag} = 1$ nm. XPS spectra at O 1s edge of c) pristine PMMA ($\delta_{Ag} = 0$ nm) and d) sputter-coated PMMA with $\delta_{Ag} = 1$ nm. Reprinted with permission from [70]. Copyright 2021 American Chemical Society.

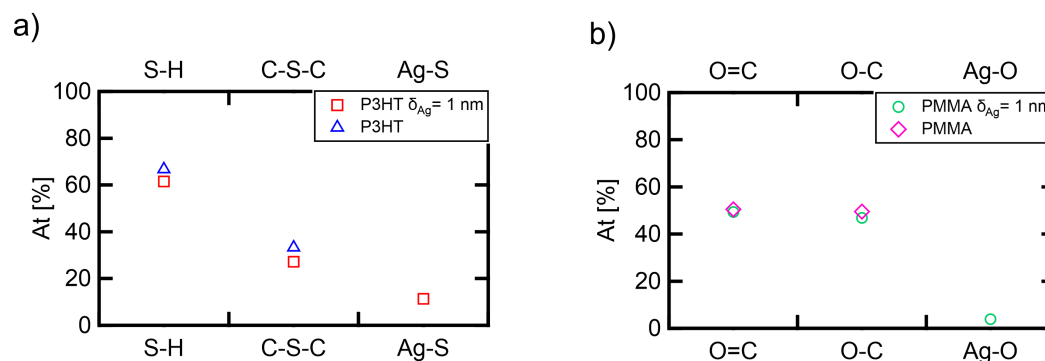


Figure 6.17.: a) Atomic percentage relation (At) in the S 2p peak on the bindings for P3HT with $\delta_{Ag} = 0$ nm and with $\delta_{Ag} = 1$ nm. b) Atomic percentage relation (At) in the O 1s peak on the bindings for PMMA with $\delta_{Ag} = 0$ nm and with $\delta_{Ag} = 1$ nm. Reprinted with permission from [70]. Copyright 2021 American Chemical Society.

The FTIR measurements in Figure 6.18 show the spectra of $\delta_{Ag} = 1$ nm, $\delta_{Ag} = 2$ nm and $\delta_{Ag} = 8$ nm on PMMA-*b*-P3HT. The intensity of the C=O carbonyl stretching vibrations at a wavenumber of 1733 cm^{-1} decreases to 0% from $\delta_{Ag} = 1$ to $\delta_{Ag} = 8$ nm Ag. The intensity of C-S stretching vibrations at a wavenumber of 1108 cm^{-1} decreases from $\delta_{Ag} = 1$ to $\delta_{Ag} = 8$ nm Ag, as well. In addition, the higher Ag-S peak is consistent with the finding from FESEM: Ag seems to interact first with the crystalline part of the semi-crystalline P3HT domain during the nucleation stage. Later, Ag will reach the amorphous part of P3HT. This in turn could increase the chemical interaction of Ag and sulfur of the P3HT domain. The high decrease of the C=O carbonyl stretching vibrations shows the fast Ag decoration of the PMMA wells on the surface after Ag embedding in PMMA. From the peak-to-valley distance and the cluster aggregation analysis from the FESEM image, I deduce that Ag seems to grow preferentially on the crystalline part of the P3HT surface. The linear increase up to $\delta_{Ag} = 4$ nm of D_{ptv} from AFM measurements indicates reduced embedding of Ag inside the P3HT polymer domain. The FTIR measurements in Figure 6.18 show a trend for the Ag reaction with oxygen and sulfur for even higher Ag thicknesses.

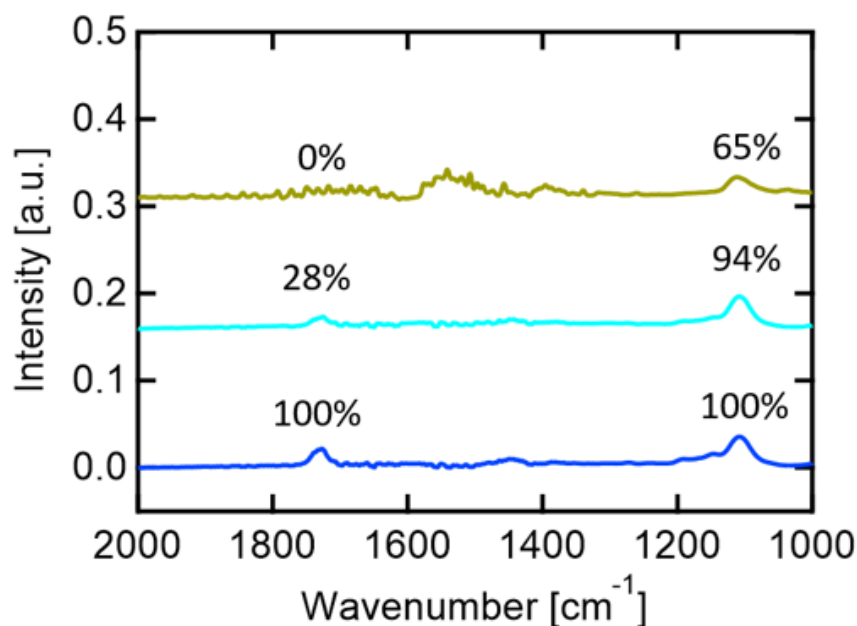


Figure 6.18.: FTIR spectra of 1 nm Ag on PMMA-*b*-P3HT (blue), 2 nm Ag on PMMA-*b*-P3HT (light blue) and 8 nm Ag on PMMA-*b*-P3HT (dark yellow). The spectra are shifted along the y-axis for clarity. The intensity of C=O carbonyl stretching vibrations at a wavenumber of 1733 cm^{-1} changes for all templates from 1 nm to 8 nm Ag (100 % to 0 %). The intensity of C-S stretching vibrations at a wavenumber of 1108 cm^{-1} changes for all templates from 1 nm to 8 nm Ag (100 % to 65 %). Reprinted with permission from [70]. Copyright 2021 American Chemical Society.

6.3. *In situ* GISAXS on different polymer templates

In this section the *in situ* morphological data is shown for GISAXS and GIWAXS and is compared to resistance and simulations. The results are collected and a model is derived, for Ag growth on the PMMA-*b*-P3HT DBC template. A sputter deposition chamber (Figure 4.6) was integrated in a GISAXS set up at the P03/MiNaXS beamline of the PETRA III storage ring at DESY (Hamburg, Germany). An incident photon energy of 13 keV was used with a beam size of $(31 \times 24)\mu\text{m}^2$ at the sample position. The sample-to-detector distance was set at $SDD_3 = (2462 \pm 2)\text{ mm}$ for *in situ* GISAXS using a Pilatus 300K (Dectris Ltd., Switzerland; pixel size of $172\ \mu\text{m}$) at the beamline P03. The sample-to-detector distance for *in situ* GIWAXS was set at $SDD_4 = (178 \pm 3)\text{ mm}$ using a LAMBDA 750k detector (X-Spectrum GmbH, Germany; pixel size of $(55 \times 55)\ \mu\text{m}^2$) at the beamline P03. The direct and specular beams were both shielded by two separate beam stops to avoid saturation or damage to the detector. In order to achieve a good

separation between the polymer and Ag Yoneda peaks, an incident angle of $\alpha_i = 0.39^\circ$ was selected during the *in situ* experiments. In order to prove macroscopic homogeneity of the nanoscale morphology and to avoid possible X-ray beam effects during the *in situ* GISAXS experiments, the sample was laterally moved several millimeter distances during the experiment. Meanwhile, the scattering data were continuously recorded at a frame rate of 20 images per second for GISAXS and at a frame rate of 2 images per second for GIWAXS. The GISAXS data were analyzed using the DPDAK software package. [156]

The Ag growth on the DBC template with partly semi-crystalline domains is compared to the Ag growth on the corresponding homopolymers and investigated with GISAXS. In Figure 6.19a-d 2D-GISAXS data of the DBC template are shown from $\delta_{Ag} = 1$ to 10 nm Ag thickness. The characteristic cluster peak, as well as the DBC domain peak, are both depicted by red arrows in Figure 6.19a. The domain peak for $\delta_{Ag} = 1$ nm directly shows the selective wetting of Ag on the P3HT network by its increasing intensity due to the electron contrast enhancement. The pseudo Bragg peak supports the before mentioned assumption of the hexagonal structure of the DBC template. The shape and the length of the Bragg rod are an indication for vertical arrangement of cylinders (PMMA) in a matrix (P3HT). This is comparable to the results of Lupi and Li *et al.* shown in previous publications. [80, 242] With ongoing sputter deposition, the cluster peak migrates to smaller q_y values corresponding to higher distances between the clusters and growing radii. At $\delta_{Ag} = 5$ nm and $\delta_{Ag} = 10$ nm in Figure 6.19c,d height oscillations are visible and have a certain shape, which indicate a cylindrical cluster growth. The shape of the height oscillations are more uniform and separated (not smeared out) compared to for example half-spheres or spheres. [135, 194] In Figure 6.19e-h and 6.19i-l the Ag growth on the corresponding homopolymers P3HT and PMMA is shown. The comparison to the DBC template shows no pseudo Bragg peak for the homopolymers due to the missing arranged nanostructure. The evolution of the Ag cluster peak shows a similar growth on P3HT with the DBC template and a different growth on PMMA. The cluster peak position is very similar for the DBC and P3HT, while for PMMA the position is at smaller q_y values for the same δ_{Ag} (see in Figure 6.19a,e,i). From the AFM results in Figure 6.4 as well as from the XPS and FTIR results in Figure 6.12 and 6.18, the selective growth of Ag on the P3HT domain was already shown. The XPS results showed for the first nanometer a clear interaction of the Ag and sulfur of the P3HT domain, which leads to selective wetting. Additionally, the GISAXS data of PMMA-*b*-P3HT and P3HT on the one hand and PMMA on the other hand show distinct differences in the cluster shapes. PMMA shows a more hemispherical cluster shape by the out-of-plane scattering intensity, which is a fingerprint of the clusters form factor as explained before for the cylindrical shape. [135, 194] It can be seen very

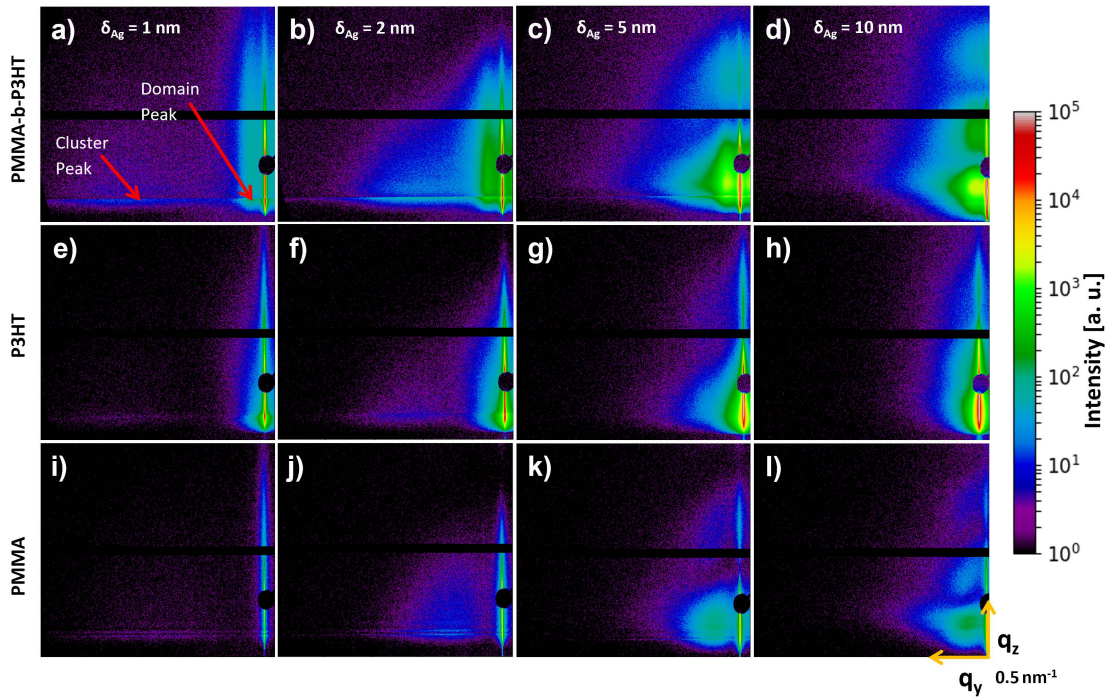


Figure 6.19.: Selected 2D GISAXS data of Ag cluster growth on a-d) PMMA-*b*-P3HT, e-h) P3HT, and i-l) PMMA for Ag thicknesses of $\delta_{Ag} = 1, 2, 5$ and 10 nm, respectively. The domain peak and cluster peak are highlighted. The scattering data indicates a hemispherical shape of the cluster for the PMMA and a more cylindrical shape for PMMA-*b*-P3HT and P3HT. Reprinted with permission from [70]. Copyright 2021 American Chemical Society.

clearly for $\delta_{Ag} = 5$ and 10 nm of the 2D-GISAXS data in Figure 6.19 with a more tilted and smeared out shape of the height oscillations. Following Schwartzkopf *et al.*, I can assume a cylindrical Ag cluster growth on PMMA-*b*-P3HT and P3HT compared to a hemispherical Ag cluster growth on PMMA. [142]

The contour plot in Figure 6.20a shows the summarized results of all lateral cuts at the Yoneda region (integrated q_z region of $q_z = 0.5-0.7 \text{ nm}^{-1}$, around the Yoneda peak) from $\delta_{Ag} = 0$ to 12 nm. This map indicates four different growth regimes, which can be seen in more detail in the schematic drawing in Figure 6.25. The first region describes the nucleation and embedding process (I), where clusters of Ag start to nucleate at the P3HT surface and embed in the P3HT and PMMA polymer domains. No out-of-plane scattering is visible at large q_y values, except for the DBC domain peak. The second region shows the diffusion-mediated cluster growth via coalescence and selective wetting of Ag on P3HT (II). The clusters start to form bigger aggregates on the P3HT, whereas an enhanced Ag

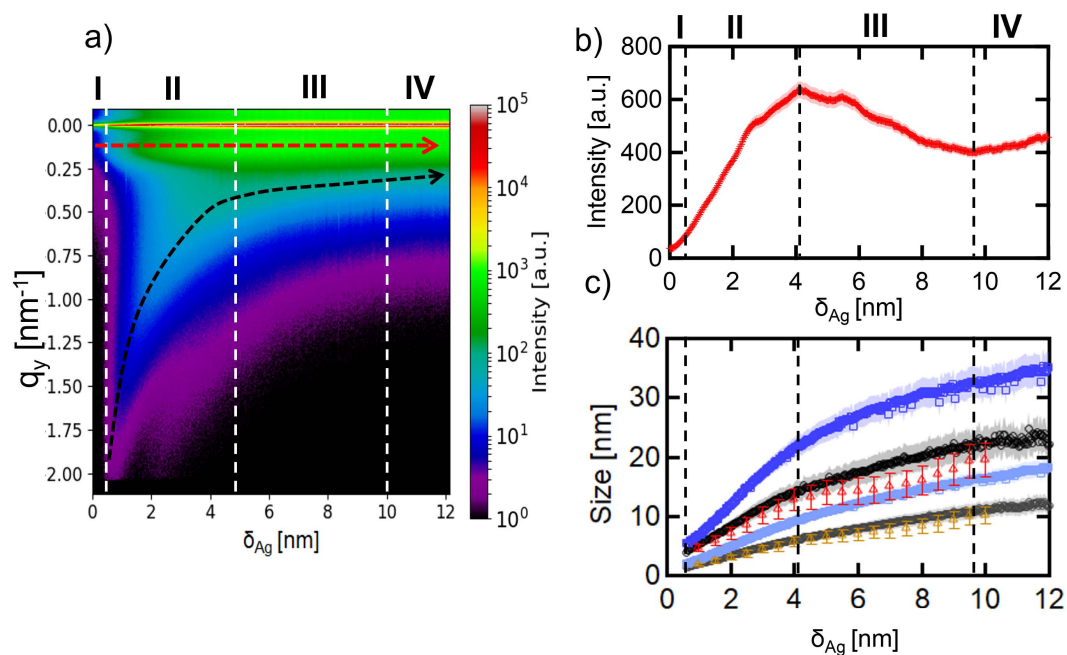


Figure 6.20.: a) Contour plot of Yoneda cuts from the *in situ* GISAXS data during sputter deposition on PMMA-*b*-P3HT as a function of effective Ag thickness δ_{Ag} . The cluster peak (black dashed arrow) and the 1st order domain peak (red dashed line) at $q_y = 0.15 \text{ nm}^{-1}$ change due to the Ag deposition. The white dashed vertical lines indicate different growth regions: (I) Nucleation and embedding, (II) selective diffusion-mediated cluster growth via coalescence, (III) reduced-selective adsorption-mediated growth and (IV) percolated regime on the P3HT domain. b) Evolution of the amplitude of the domain peak of PMMA-*b*-P3HT during the Ag sputter deposition. The black dashed vertical lines mark the before-mentioned growth regions; the intensity contrast in region (II) is increasing due to the selective wetting and decreasing in region (III) due to the limited selective growth. c) Evolution of the average interparticle distance on PMMA (D_{PMMA} , blue), PMMA-*b*-P3HT ($D_{PMMA-b-P3HT}$, black), P3HT (D_{P3HT} , red), and the corresponding cluster radii (R_{PMMA} (bright blue), $R_{PMMA-b-P3HT}$ (grey), R_{P3HT} (orange) in the different growth regions. Reprinted with permission from [70]. Copyright 2021 American Chemical Society.

sub-surface growth take place on PMMA domains. Region III can be described as the reduced-selective adsorption-mediated growth. Here, the clusters on the P3HT domain become more immobile and mainly grow by adsorbing adatoms. Furthermore, the growth of Ag on the surface of PMMA decreases the scattering contrast between the two blocks (see Figure 6.20b). In region IV – starting around $\delta_{Ag} = 9.5 \text{ nm}$ – the Ag metal clusters

start to percolate on the P3HT network and form a conductive pathway, see also FESEM images in the section above in Figure 6.10. In this region the Ag clusters still grow on the PMMA until the whole film percolates. The clusters on the P3HT and PMMA region start to touch each other and form a complete thin metal film on the DBC template. The different growth of Ag on the homopolymer films can be seen in the FESEM images in Figure 6.11. The four regions can be correlated with the amplitude of the domain peak intensity in Figure 6.20b. The evolution of the amplitude of the domain peak (dashed red line in Figure 6.20a) of PMMA-*b*-P3HT during the Ag sputter deposition is shown in order to follow the selective Ag growth on the polymer domains. The black dashed vertical lines mark the before-mentioned growth regions. Region (I), the nucleation regime, does not show significant out-of-plane scattering. The intensity contrast in region (II) increases due to the selective wetting and decreases in region (III) due to the limited selective growth on the P3HT domain. In this region, the domain peak overlaps with the cluster peak, whose amplitude increases with ongoing Ag deposition. The difference in cluster size (see Figure 6.20c) and shape (see Figure 6.19) indicate the different growth behaviour of Ag on PMMA and P3HT.

At the same time as *in situ* GISAXS measurements, *in situ* GIWAXS measurements were taken to investigate the crystalline arrangement of Ag on the DBC template. In Figure 6.21a the reference measurement can be seen with LaB₆ to determine the instrumental resolution with the FWHM of the LaB₆ rings. In Figure 6.21b-d the evolution of the typical Ag rings can be seen for the (111) and (200) Bragg peaks. With ongoing Ag deposition the intensity of the rings increases and the FWHM is shrinking. For $\delta_{Ag} = 1$ nm in Figure 6.21b only a slight intensity of the (111) peak can be seen. For $\delta_{Ag} = 5$ nm in Figure 6.21c the (111) peak is much more pronounced, and the (200) peak is appearing. At $\delta_{Ag} = 12$ nm the (200) peak is now clearly visible.

Further, the height of the Ag clusters will be investigated with the help of vertical cuts of the GISAXS data and simulations. The crystalline size which is measured with the GIWAXS measurements and compared to the height of the Ag clusters from GISAXS. The height of the Ag clusters is firstly analysed in Figure 6.22a, which shows the off-centered vertical line-cuts of the Ag sputter deposition on PMMA-*b*-P3HT obtained by *in situ* GISAXS for different Ag thickness. The line-cuts are taken at a position related to the cluster peak without the influence of the polymer template (polymer peak at $q_y = 0 \text{ nm}^{-1}$) e.g. without the domain peak region (domain peak at $q_y = 0.15 \text{ nm}^{-1}$). Figure 6.22b shows the respective *in situ* GIWAXS data as shown before in Figure 6.21 with the corresponding (111) and (200) Bragg peaks of Ag derived with the software GIXSGUI. The crystallite size is calculated using the modified Debye-Scherrer equation (see equations 2.43, 2.44) and the instrumental resolution (Figure 6.21a). In order to receive the full information of the

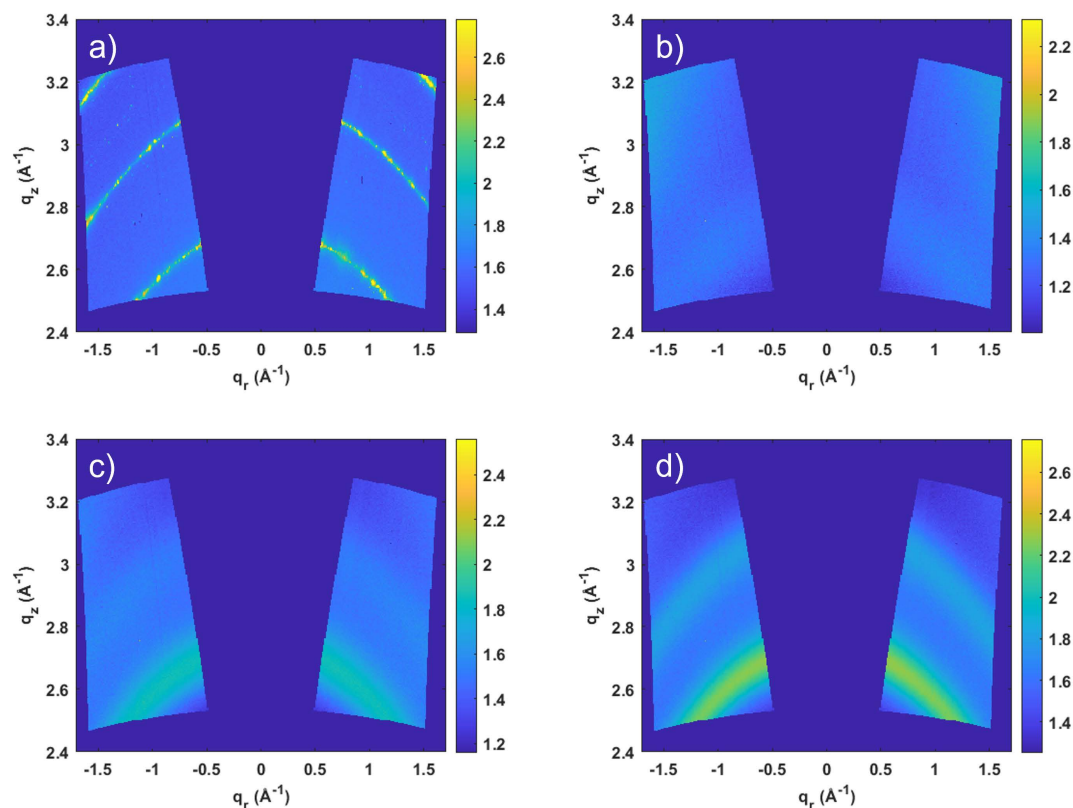


Figure 6.21.: Examples of the reshaped 2D-GIWAXS data by GIXSGUI. a) LaB6 for instrumental resolution. b) GIWAXS data of PMMA-*b*-P3HT for $\delta_{Ag} = 1$ nm. c) GIWAXS data of PMMA-*b*-P3HT for $\delta_{Ag} = 5$ nm. d) GIWAXS data of PMMA-*b*-P3HT for $\delta_{Ag} = 12$ nm. Reprinted with permission from [70]. Copyright 2021 American Chemical Society.

Ag crystallite growth, the values from Figure 6.22b are interpolated in Figure 6.22c, seen by the lines between the points. For comparison, Figure 6.22c shows also the temporal evolution of the cluster height (green squares) as deduced from minima in the vertical line-cuts. The detailed analysis of the height calculation is shown below in Figure 6.23. Furthermore, the diameter of the clusters $2R_{PMMA-b-P3HT}$ (black) is shown in Figure 6.22c. In Figure 6.22c the crystallite size evolution for the (111) peak and the (200) peak is following nearly continuous linear growth laws during Ag sputter deposition. For the (111) peak the size of crystallites increases between $1 \leq \delta_{Ag} \leq 3$ nm linear with first a high slope, before it levels off. The crystalline size of the Ag clusters shows an isotropic distribution over the whole sample with no preferred crystallite orientation, seen in the Figure 6.21b-d. The height of the clusters is calculated from the off vertical cut. Off vertical cut denotes the whole q_y region without the region around $q_y = 0-0.15 \text{ nm}^{-1}$ in the GISAXS data. Here,

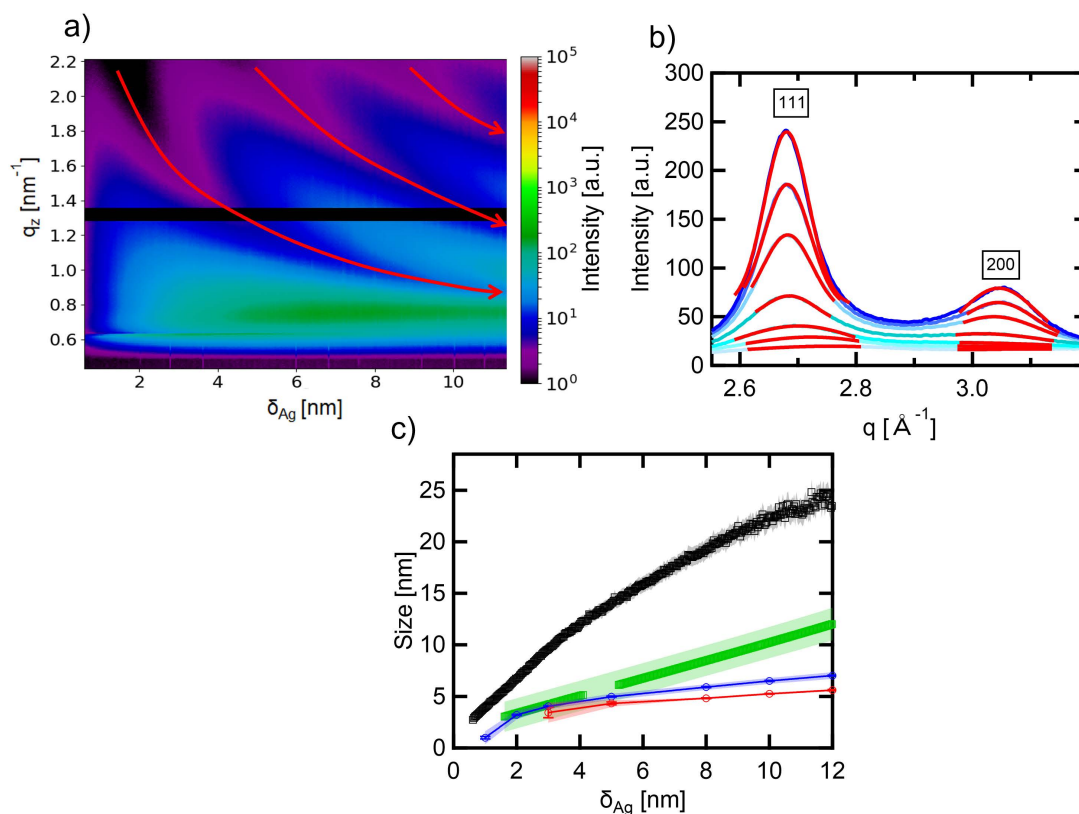


Figure 6.22.: Sputter deposition of Ag on PMMA-*b*-P3HT followed *in situ* with GISAXS and GIWAXS. a) Contour plot of off-center vertical line-cuts of the 2D GISAXS data plotted as a function of the effective deposited Ag thickness δ_{Ag} . The red arrows show the position of minima between the height oscillations. b) Integrated 2D GIWAXS data (blue) with fits (red). The (111) and (200) Bragg peak of Ag are illustrated. c) Comparison of the diameter of the clusters $2R_{PMMA-b-P3HT}$ (black), the height of the clusters (green) and the crystallite size in 111 direction (blue) and in 200 direction (red). Reprinted with permission from [70]. Copyright 2021 American Chemical Society.

the vertical electron density distribution is independent of the polymer template thickness increase oscillations. Figure 6.23 shows the position of q_z minima of the experimental data and the simulations with IsGISAXS. [138] The simulations take into account the distorted wave born approximation (DWBA). With the relation between the minima of the experimental data and the simulation Schwartzkopf *et al.* offers a possibility to calculate the average cluster height from the minima relation. [63] For the simulations the same parameters as for the experiment were considered and for the diblock copolymer: A 50 % mixed scattering length density was used for PMMA and P3HT in order to simulate

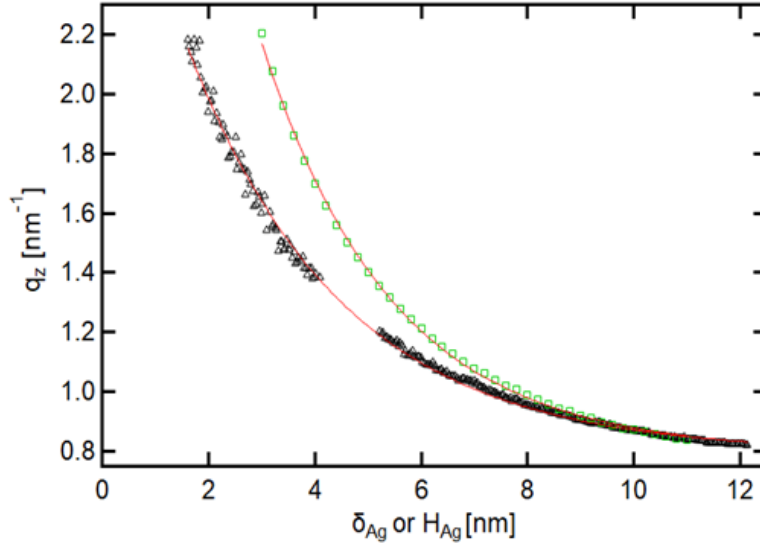


Figure 6.23.: First minima in q_z for the experiment (black) and for the simulations (green), fitted with an exponential function. Reprinted with permission from [70]. Copyright 2021 American Chemical Society.

the diblock copolymer. For the simulation a percolated film ($2R/D = 1$) of Ag clusters was considered for simplification. The resulting exponential functions from Figure 6.23 for the experiment and the simulations are

$$q_{zmin,sim}(H) = 0.79808 + 4.6247exp(-0.40509H) \quad (6.1)$$

$$q_{zmin,exp}(\delta_{Ag}) = 0.79492 + 2.3641exp(-0.3428\delta_{Ag}) \quad (6.2)$$

$$H(\delta_{Ag}) = \frac{\ln(-0.00316 + 2.3641exp(\frac{-0.3428\delta_{Ag}}{4.6247}))}{-0.40509} \quad (6.3)$$

The calculated height is shown in Figure 6.22c in green with a linear increase over the Ag thickness.

Figure 6.24a shows the determined percolation threshold, obtained from *in situ* GISAXS measurements. Therefore the lateral line-cuts enable the possibility to calculate the ratio between the radii and the average cluster center-to-center distance. The percolation of the metal network starts when the clusters start to touch each other. This is indicated by the point, where the cluster diameter ($2R$) reaches the average cluster center-to-center distance (D). This does not essentially predict that the entire metal network is macro-

scopically high electrically conductive, but it is a hint when the metallic network begins to be electrically conductive.

These morphological results are now correlated with the electrical properties. From the resistance measurements shown in Figure 6.24b I obtained the insulator-to-metal transition (IMT). The results for the percolation obtained by GISAXS are PMMA-*b*-P3HT $\delta_{Ag} = (10.2 \pm 0.5)$ nm, PMMA $\delta_{Ag} = (9.9 \pm 0.5)$ nm, P3HT $\delta_{Ag} = (7.8 \pm 1.0)$ nm and for the IMT are PMMA-*b*-P3HT $\delta_{Ag} = (10.8 \pm 0.6)$ nm, PMMA $\delta_{Ag} = (10.5 \pm 0.5)$ nm and P3HT $\delta_{Ag} = (8.3 \pm 0.6)$ nm. Figure 6.24a,b show agreement between geometrical determined percolation threshold and measured onset of conductivity. Further the 4-point resistance measurements confirmed the above estimated cylindrical Ag cluster growth on the P3HT domain of the DBC PMMA-*b*-P3HT, while the models for hemispherical or spherical clusters would lead to a later percolation. The result for the homopolymers support the percolation found by the above shown FESEM measurements in Figure 6.11. The FESEM results for the DBC template are in good agreement with the previously found percolation threshold and IMT. The general growth model of Ag on PMMA-*b*-P3HT DBC templates is shown in Figure 6.25. The first model shows a side view of the pristine PMMA-*b*-P3HT DBC thin film with the two polymer blocks P3HT (orange) and PMMA (black) (0). At first, the nucleation and selective embedding (I) is the predominant process for $\delta_{Ag} < 1$ nm. Afterwards, a selective diffusion-mediated cluster growth via coalescence (II) sets in. The Ag clusters (grey) start to grow cylindrically on top of the P3HT block (orange) (II). A sub-surface growth preferentially on the pure PMMA block starts (hemispheres) (II). At a thickness of around $\delta_{Ag} = 4.8$ nm, a reduced-selective adsorption-driven growth of immobilized clusters on the P3HT DBC domain occurs (III). Around $\delta_{Ag} = 10$ nm a fully percolated network of metal film is grown on the nanostructured P3HT film (IV). After $\delta_{Ag} = 10$ nm the whole polymer film starts to percolate (P).

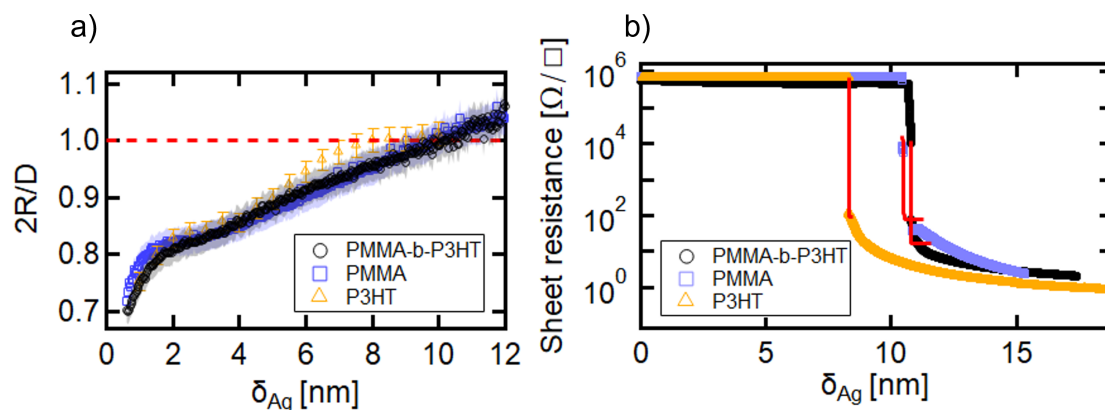


Figure 6.24.: a) Evolution of the average cluster diameter ($2R$) over the mean interparticle distance (D) ratio for PMMA (blue), PMMA-*b*-P3HT (black), and P3HT (orange). When $2R/D$ equals one (red line) the majority of clusters tend to touch each other, which can result in a macroscopic conductive path. b) *In situ* 4-point resistance measurements during sputter deposition of Ag on PMMA-*b*-P3HT (black), PMMA (blue), and P3HT (orange) thin films. The red line is a fit using the Boltzmann sigmoidal fit function in order to determine the insulator-to-metal transition for all samples. Reprinted with permission from [70]. Copyright 2021 American Chemical Society.

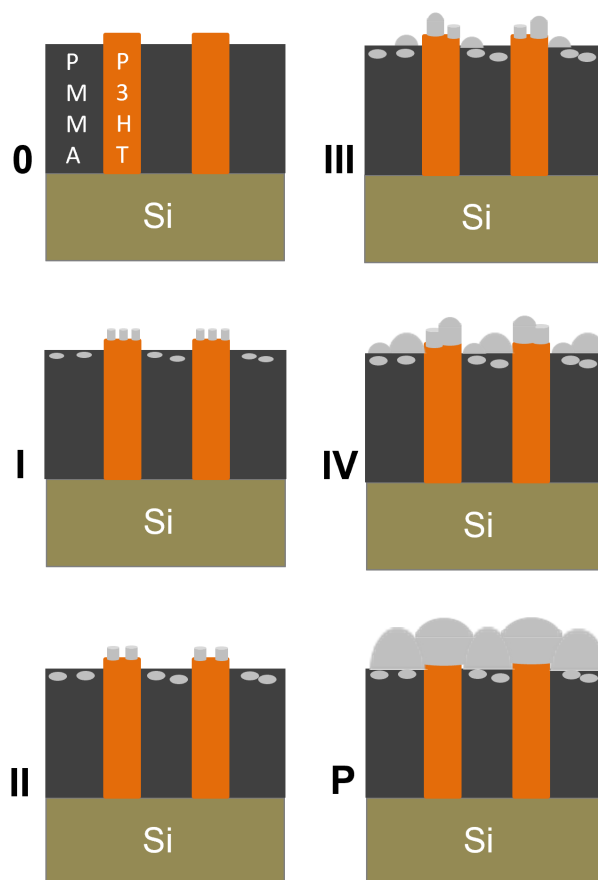


Figure 6.25.: Sketch of the general growth model of Ag on PMMA-*b*-P3HT DBC templates. Growth regimes: 0: initial state I: $\delta_{Ag} < 1$ nm, II: $1 \text{ nm} < \delta_{Ag} < 4.8$ nm, III: $4.8 \text{ nm} < \delta_{Ag} < 10$ nm, IV: $\delta_{Ag} > 10$ nm, P: after percolation state. Reprinted with permission from [70]. Copyright 2021 American Chemical Society.

6.4. Summary

The selective growth of Ag as a potential electrode was visualized on a conjugated DBC template during sputter deposition. Clear differences are found for early stages and late stages prior to the percolation threshold. During early growth stages Ag selectively wets the P3HT domain. In addition, a completely different growth of Ag clusters in size and shape on the corresponding P3HT and PMMA homopolymer thin films is found with a cylindrical Ag cluster growth on the P3HT domain and a hemispherical cluster growth on PMMA. This indicates a different growth behavior on the domains of the conjugated DBC. The influence of the chemical interactions of the impinging atoms revealed by XPS confirms an interaction of the Ag atoms with the sulfur and oxygen compounds of the different polymer domains. On the DBC template, Ag tends to grow preferentially on the P3HT domains at the beginning (low metal layer thickness) and to embed to a larger extent into the PMMA domain. The growth models agree well with the insulator-to-metal transition measurements. Direct observation of percolated pathways has been achieved with FESEM. The results demonstrate a possible method for template-directed nanogranular electrode preparation for sensing and photovoltaic applications by exploiting the selective Ag growth. One can envisage that the domain period and found morphology is suitable to produce an organic solar cell with the investigated DBC template. For predictive material science *ab initio*, molecular dynamics would help in rational material design for organic photovoltaics and electronics and by the correlation with experimental results presented here. This study shows that the choice of polymer and metal influences the wetting behavior and can be used to tailor the interface to the needs of future organic electronic devices, which can be used e.g. to extend lithography schemes to the 10 nm scale.

7. Aluminum Nanocluster Layers Growing on Partially Conjugated PMMA-*b*-P3HT Templates

Most parts of the results shown in chapter 7 were published in the article: *Correlating Optical Reflectance with the Topology of Aluminum Nanocluster Layers Growing on Partially Conjugated Diblock Copolymer Templates* [71] (M. Gensch et al., *ACS Appl. Nano Mater.* 2021, 13, 47, 56663–56673, DOI: 10.1021/acsami.1c18324)

In this chapter the morphology and chemical interaction of the diblock copolymer template PMMA-*b*-P3HT with Al cluster decoration is shown. The results of the Al metal formation on PMMA-*b*-P3HT are compared with the formation on the homopolymers to identify differences in the Al cluster growth. For this comparison different techniques were used such as e.g. AFM, FESEM, GISAXS, GIWAXS and XPS.

The optoelectronic properties of nanostructures such as Al clusters can be influenced by their self assembly and are of high interest for surface enhanced Raman scattering (SERS) type sensors due to the high absorption in the ultraviolet (UV) spectral range and lower material costs compared to, e.g., silver (Ag) or gold (Au). [188, 243–245] A broad range of Al plasmon absorption from various Al nanoparticles obtained by chemical synthesis or lithographic procedures were reported to be located in the UV-vis spectral region, depending on the size, shape, amount of oxygen, local arrangement, and surrounding medium. [243, 245–248] In addition Al is often used as an electrode material in organic electronics such as in organic photovoltaics (OPVs). [61, 249, 250] Therefore, a comprehensive investigation of tuning the morphology and collective optical reflectance of Al layers sputter-deposited on nanostructured DBC and homopolymer thin films are still missing. The intrinsic physicochemical and nonequilibrium processes during sputter deposition are complex, in particular, when using reactive metals such as Al. [251] A profound view on the interaction potentials of the Al with the template material on which sputter deposi-

tion takes place is of importance to tailor morphology and optoelectronic properties for OPV device fabrication. The tunability e.g. of plasmon resonance frequency in the ultraviolet visible (UV-vis) spectral range was shown by Knight *et al.* with the influence of the oxidation of the Al disks for plasmonic applications. [243] Al_2O_3 was further used as a buffer layer to increase the electrode stability in ambient air. [62, 252, 253] These studies show the influence of the chemical interaction from Al with the template and the need to be properly understood for the specific templates as for the used PMMA-*b*-P3HT DBC template, which could be used as a candidate for a part of the OPV active layer. In the previous chapter, I investigated the interaction of Ag on the same DBC template with GISAXS and XPS to reveal the topological changes and chemical interactions. The chemical interaction of noble metals such as Ag with several molecular components was proven, e.g., oxygen and sulfur. [69, 70] Ag was reacting with different molecular components of the polymer template (PMMA and P3HT), which lead to a cylindrical cluster growth on P3HT and a hemispherical cluster growth on PMMA. Less noble metals as Al, change the situation and become even more complex. In an earlier work, the Al formation on P3HT and Alq3 during sputtering in an atmosphere with a high oxygen content, demonstrating the complexity of Al growth on these different surfaces. [226, 254]

In the present chapter, the focus is on correlating topological changes with optical changes by combining *in situ* UV-vis spectroscopy and GISAXS during Al sputter deposition at the same time. The respective homopolymers PMMA and P3HT are studied for comparison as well. The specific DBC morphology offers the possibility to improve devices from OPVs and optical sensor applications. In section 7.1 I monitor the optical response by *in situ* surface differential reflectance spectroscopy (SDRS) in the specific UV spectral range in comparison to the topological development of the Al decoration characterized by AFM measurements. In section 7.2, XPS measurements are done at early deposition states to show the high affinity of the Al clusters to the molecular components of the DBC. In section 7.3, the *in situ* X-ray scattering data is showing the growth of Al on the DBC template and can be compared to the previous chapter with Ag on the same DBC template. In section 7.4, the growth of Al on the homopolymers is compared to the growth on the DBC template and reveals information distinct difference of the cluster arrangement. In section 7.5 a model of the Al decoration on the DBC template is derived from the correlated results of the different measurements techniques.

7.1. Optical reflectance and morphology change during sputter deposition

The Al layer growth on the DBC template leads to a relative change in the UV-vis reflectance spectra. The reflectance was measured at an incident angle of 55° , the pristine 20 nm PMMA-b P3HT thin film on a Si wafer was set as a reference to 100%. The surface differential spectra from these measurements show the change from the pristine polymer and Si wafer compared to the spectra of polymer, Si wafer and Al layer. Depending of the metal nanoparticle/cluster distribution, size, shape and metal type, distinct minima can be observed in these surface differential spectra for localized surface plasmon resonance (LSPR). The position in the reflectance spectra does not necessarily show the exact position of the LSPR but provides an indication of an existing plasmon activity as it was shown in my previous publications for Ag. [57,69] The correlation of the changing interface morphology from the Al growing layer on the DBC template and the changing optical spectra were simultaneously measured with UV-vis spectra and surface-sensitive X-ray scattering pattern (GISAXS). The results of the UV-vis spectra can be seen in Figure 7.1a-b, which are compared to AFM measurements with the corresponding Al thickness (Figure 7.1c-f). In Figure 7.1a the relative UV reflectivity is strongly reduced for $\delta_{Al} = 1$ to 6 nm, which is located in the spectral region of absorption from Al due to LSPRs. In order to understand the reflection behavior in more detail a sequential spectral simulation based on the complex matrix form of the Fresnel equations of a compact (nongranular and nonplasmonic) Al layer growing on top of a 20 nm PMMA/2 nm SiO₂/Si template was done with the help of Dr. Matthias Schwartzkopf (DESY) and can be seen in the appendix in Figure C.1a. The detailed UV-vis spectra can be seen in Figure C.1b and Figure C.1c in the appendix until $\delta_{Al} = 20$ nm. The simulation shows that the distinct reflection minima at approximately $\lambda_1 = (265 \pm 3)$ nm and $\lambda_2 = (365 \pm 2)$ nm become suppressed by the Al layers on the topmost interface, as it is also seen by the UV-vis measurements.

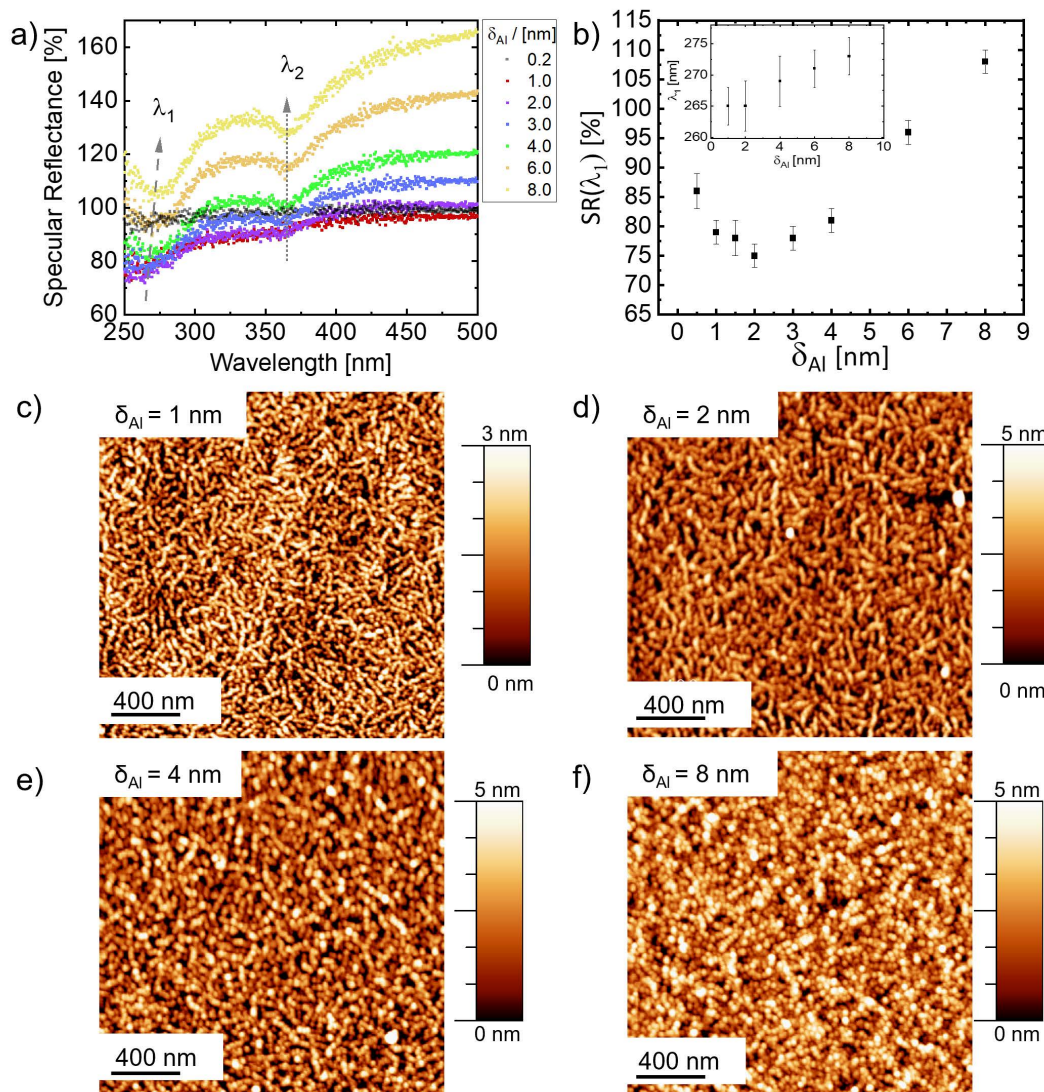


Figure 7.1.: a) *In situ* UV-vis surface differential specular reflectance data from Al sputter deposition on PMMA-*b*-P3HT, showing two peaks with antireflective behavior in the UV regime. The first local minimum at $\lambda_1 = 265$ nm (dashed gray arrow) and the second local minimum at $\lambda_2 = 365$ nm (dotted gray arrow) from template shadowing effects during Al layer growth are both located in the region of Al plasmonic contributions. b) Specular reflectance intensity changes at $\lambda_1 = 265$ nm as an indicator of plasmon activity at different effective Al thicknesses reveal a local minimum around $\delta_{Al} = 2$ nm. The inset shows the redshift in λ_1 minima position. AFM topography of the PMMA-*b*-P3HT film sputter-coated with an Al thickness of c) $\delta_{Al} = 1$ nm (wormlike Al layer), d) $\delta_{Al} = 2$ nm (wormlike Al layer), e) $\delta_{Al} = 4$ nm (nanogranular layer), and f) $\delta_{Al} = 8$ nm (nanogranular layer). Reprinted with permission from [71]. Copyright 2021 American Chemical Society.

However, the relative UV reflectivity below $\lambda = 400$ nm shows antireflective behavior until $\delta_{Al} = 6$ nm, this can not be covered by these simulations. This indicates the LSPR activity as an additional source of absorption. At around $\delta_{Al} = 6$ nm, the Al cluster layer seems to reach its percolation threshold, and the LSPR activity is drastically decreasing due to the more dense formation of the Al layer compared to the previous isolated Al clusters. The specular reflectance illustrates this high decrease in Figure 7.1b, where at $\delta_{Al} = 1$ nm the specular reflectance is reduced to around 78% of the original value of the pristine DBC. The reduction of the specular reflectance stays below 100% until around $\delta_{Al} = 6$ nm for the spectral region below $\lambda = 400$ nm. The change is as explained above due to gradual vanishing of the LSPR activity, the emerging normal surface plasmon absorption, and additional thin-film interference effects, which become more significant in the optical reflectance. The first minima of the plasmon activity is tracked and the change of position of the minima is demonstrated in the inset of Figure 7.1b during the increase of the Al thickness. The typical red-shift of the minima position is seen for the LSPR effect, as the particle size of the Al clusters is increasing with higher Al thickness. [243, 251] The use of sensors in applications is increasing from year to year, and the need of high and pronounced antireflective specular reflectance in the UV range is of high interest in this regard. The effective Al thicknesses shown here between $\delta_{Al} = 1$ nm and 4 nm could be interesting for further investigation of the optical properties by controlling the interface morphology, e.g. size, shape, and distance of the Al clusters on various templates depending on the sensor application. Bottom-up procedures for manufacturing thin Al formation by sputter deposition on different polymer templates to prepare highly dense and well-arranged Al nanostructures for high plasmonic active sensors is a major task for future distinct sensor applications.

The formation of the Al cluster layers on the used DBC template (PMMA-*b*-P3HT) surface was followed firstly by AFM measurements for selected Al thicknesses. The evolution of the Al layer formation is shown in Figure 7.1c-f with the AFM height images for different Al thicknesses (Al = 1, 2, 4, 8 nm). AFM images of thicker Al layers can be seen in the appendix in Figure C.2 until $\delta_{Al} = 20$ nm. A typical dense nanogranular Al layer for sputter deposition can be seen in the later stages of Al thickness at around $\delta_{Al} > 10$ nm. The difference compared to Ag growth on the similar DBC template is mostly in the beginning of the Al layer formation. An example for the different growth of Al on PMMA-*b*-P3HT compared to Ag on the DBC template is the shape of metal clusters on the P3HT domain. For Ag, cylindrically shaped Ag clusters on the P3HT domain of the DBC template are present, while for Al the shape of the clusters will be revealed with X-ray scattering measurements in a following section. In the early stages of Al sputter deposition for $\delta_{Al} = 1$ nm, Al forms small clusters on the P3HT domain, which are con-

necting very fast to wormlike Al nanostructures growing in size (see Figure 7.1c). Figure 7.1c shows wormlike nanostructures on the P3HT domain and small isolated clusters next to the P3HT domains. With increasing Al thickness in Figure 7.1d at around $\delta_{Al} = 2$ nm, the clusters on the P3HT domains are already merged to wormlike nanostructures of Al and cover the entire P3HT domains. At $\delta_{Al} = 2$ nm the Al clusters on the PMMA domains are still not appearing significantly. This results in a maximum of the selective Al growth induced by the DBC template, seen by the minima in Figure 7.1b. The wormlike Al growth on the DBC template continuous until around $\delta_{Al} = 2$ nm and slightly above as it can be seen in Figure 7.1d. In Figure 7.1e with ongoing Al deposition ($\delta_{Al} = 4$ nm), newly forming clusters start to grow on the wormlike structures on the P3HT domains. In Figure 7.1f for $\delta_{Al} = 8$ nm, the Al clusters seem to arrange on the complete surface of the DBC template. This means that the Al clusters also appear more and more on the PMMA domains, and nearly the whole DBC template is completely covered by a percolated Al layer.

7.2. Chemical interaction of Al with the polymer components

In order to understand the difference in the metal formation for Al compared to Ag on the same DBC template, the chemical interaction for the early metal formation on the polymer template has to be investigated. The chemical interaction could be a reason for the different Al cluster size and shape compared to Ag on the same DBC template. This assumption is verified by XPS measurements in Figure 7.2 for the DBC template and compared to the metal interaction on the corresponding homopolymer thin films. Figure 7.2a shows the C 1s peak of PMMA-*b*-P3HT after deposition of $\delta_{Al} = 1$ nm. A peak is appearing at around 282.5 eV, which is an indication of a C-Al-O compound. [255,256] A similar interaction with Ag to carbon was not seen for this DBC template in Figure 6.14 after Ag deposition. This indicates for an interaction of the Al with the carbon molecules of the polymer. The shape of the O 1s peak shows a clear change after deposition of $\delta_{Al} = 1$ nm in Figure 7.2b compared to the pristine DBC sample and to the Ag deposited sample in Figure 6.12d,e. The intensity ratio of the double peak did not change after Ag deposition compared to the pristine sample: For both the double peak stays, while for the $\delta_{Al} = 1$ nm deposited sample the shape changed completely. In Figure 7.2c the Al 2p peak is illustrated and shows a strong interaction of Al with the molecular components of the polymer domains by the peaks appearing at around 74.3 eV (Al_2O_3) and 72.9 eV (Al-O-C). A peak appearing at around 71.8 eV corresponds to the proportion of Al metal

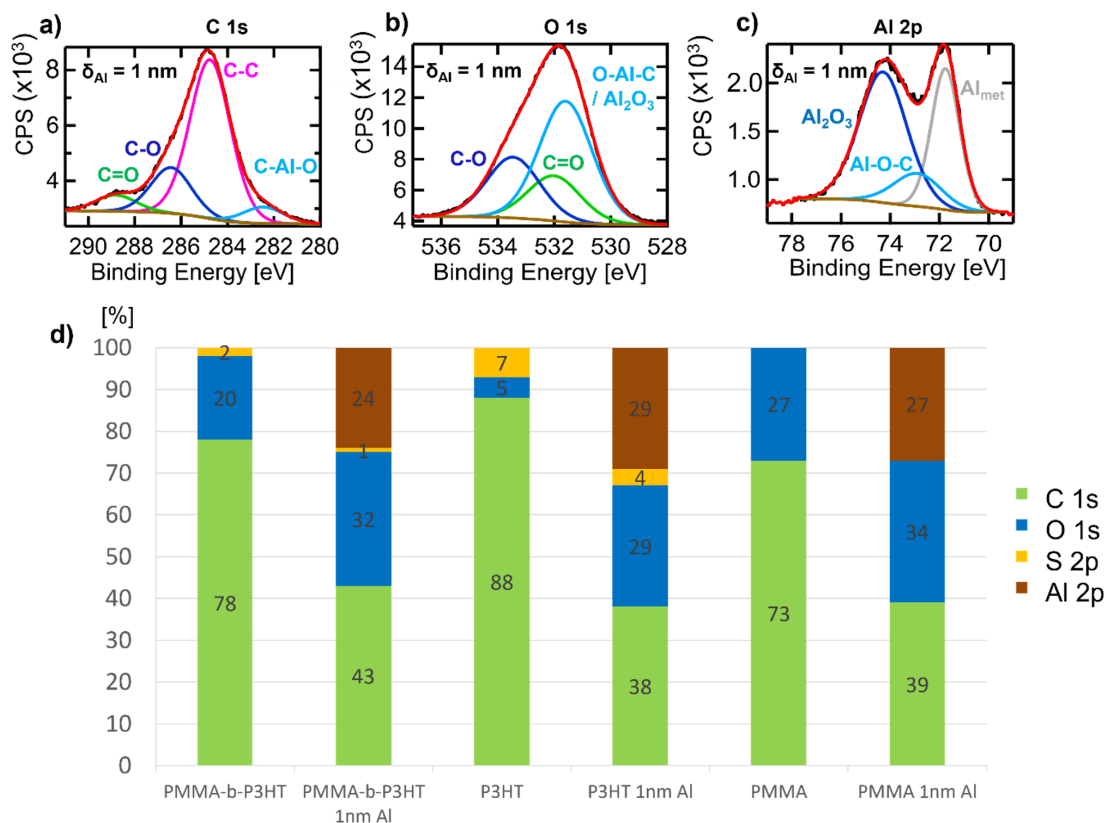


Figure 7.2.: XPS spectra of PMMA-*b*-P3HT with $\delta_{Al} = 1$ nm at a) C 1s, b) O 1s, and c) Al 2p edge. d) Elemental compositions as the atomic percentage of the corresponding polymer template for $\delta_{Al} = 0$ nm and $\delta_{Al} = 1$ nm derived from the C 1s, O 1s, S 2p, and Al 2p spectra, respectively. Reprinted with permission from [71]. Copyright 2021 American Chemical Society.

forming. The high proportion of the oxygen peak in Figure 7.2c for the Al 2p component (Al₂O₃ and Al-O-C) compared to the metallic component (Al_{met}) demonstrates the strong interaction at the early stages of Al cluster formation, which is highly influenced by the interaction of the Al with the molecular components of the polymer domains. The same tendency of the Al interaction can be seen by the homopolymers P3HT and PMMA in Figure 7.3 for the C 1s, O 1s and Al 2p peaks.

The strong interaction of Al with the molecular components of the polymers is supported by the formation of the wormlike shaped Al layer on the P3HT domains, which was shown by the AFM measurements. The Al and the polymer are forming a mixed Al/polymer compound, which tends to bound quickly together and to form the wormlike structure. Zhao *et al.* showed that for Al nanoparticles, an Al₂O₃ shell formed around the Al nanoparticles. [188] Such an oxide shell might be a reason for the fast formation

of a wormlike mixed Al/polymer layer because the flat Al clusters with an Al₂O₃ shell are connecting fast and interacting strongly with the molecular components of the P3HT domain for the first two nanometers of Al deposited. The forming Al₂O₃ compositions are seen in Figure 7.4 for the DBC template and the respective homopolymers P3HT and PMMA. The thin P3HT domains on the DBC template could guide the Al to the wormlike structure, while for the PMMA the embedding is strongly enhanced in the beginning as it can be seen in Figure 7.4 with 64% Al₂O₃ for PMMA and <60% Al₂O₃ for P3HT and the DBC. The embedding is further investigated and will be shown later in section 7.4. With increasing Al thickness the interaction of the Al with the polymer is strongly decreased as it was shown by Bou et al. [255] Here the metal peak, as seen in Figure 7.2c, increased with further Al deposition, whereas the oxygen peak in the Al 2p spectra was negligible for thicker Al thicknesses. Therefore, also the plasmon response increases quickly until the percolation threshold, which will be confirmed later in section 7.3 (GISAXS results). [255–257] Figure 7.2d compares the atomic proportions of the molecular components with $\delta_{Al} = 0$ nm to $\delta_{Al} = 1$ nm for PMMA-*b*-P3HT, PMMA and P3HT. For PMMA-*b*-P3HT after 1 nm Al deposition, the atomic proportions of the C 1s peak decreases significantly, while the O 1s peak increases and an Al 2p double peak appears for the metal and the metal oxide. The decrease for the C1s peak shows a high affinity of the Al to interact further with the carbon molecules of the polymer. The O 1s peak demonstrates the high interaction of the Al with oxygen in the beginning of the Al deposition. The atomic proportions for PMMA show similar chemical interactions. The P3HT atomic proportions in Figure 7.2d show an interesting increase in the O 1s peak after 1 nm Al deposition, which indicates the high chemical interaction with the surrounding oxygen from the atmosphere. Al seems to try to chemically interact with its environment. After Al deposition, the O 1s peak in the P3HT spectra indicates a high amount of Al₂O₃, which might result from the interactions with oxygen in the surrounding atmosphere as seen in Figure 7.3. The Al 2p spectra shows the high interaction potential of Al with the molecular components of the polymer and with oxygen by an appearing oxygen compound peak. The interaction of Al with the components is highly dependent on the oxygen content in the polymer, which is illustrated in Figure 7.5. The overall proportions in the spectra of the O 1s peak are increasing after Al deposition (light blue). This result can be explained by the appearance of the two components at the O-C peak position after Al deposition. The signals of the appearing Al₂O₃ and O-Al-C peak are overlapping with the O-C component. This demonstrates the high chemical interaction between the Al and the oxygen and carbon molecules of the polymer template. The relations between the Al metal peak and Al oxygen peak in the Al 2p spectra depend on the reactive molecules in the polymer template, which is clarified in Figure 7.4 for the

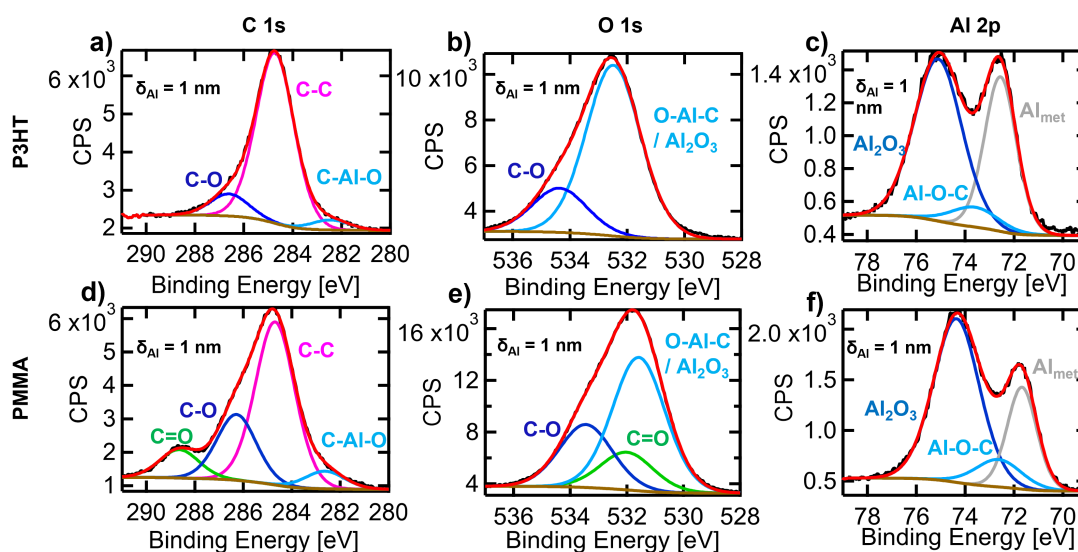


Figure 7.3.: XPS spectra of PMMA and P3HT with $\delta_{Al} = 1$ nm at a),d) C 1s, b),e) O 1s, and c),f) Al 2p edge. Reprinted with permission from [71]. Copyright 2021 American Chemical Society.

different templates. The detailed chemical interaction of Al is depending on the oxygen amount and molecular arrangement in the polymer. The appearance of the O-Al-C peak in the C 1s spectra in Figure 7.6 shows the bonding of Al with carbon molecules on the polymer template and is indicated by a decrease of the C=O peak. The spectra of the S 2p peak for sulfur did not indicate a significant change before and after Al deposition for the DBC and only intensity reduction after deposition (mostly at the S-H compound) for the P3HT homopolymer and the DBC, as shown in Figures C.3 and C.4. The intensity reduction can be an indication for the formation of the mixed Al/polymer layer for the DBC template. For Ag, the interaction at the S-H group with the sulfur to metal sulfide was shown but for Al no significant peak is seen after deposition. The results match with the chemistry of these two metals, where Ag has a high affinity to sulfur and a much smaller affinity to oxygen, while for Al the opposite holds and a strong bonding with oxygen is expected and a weak bonding to sulfur.

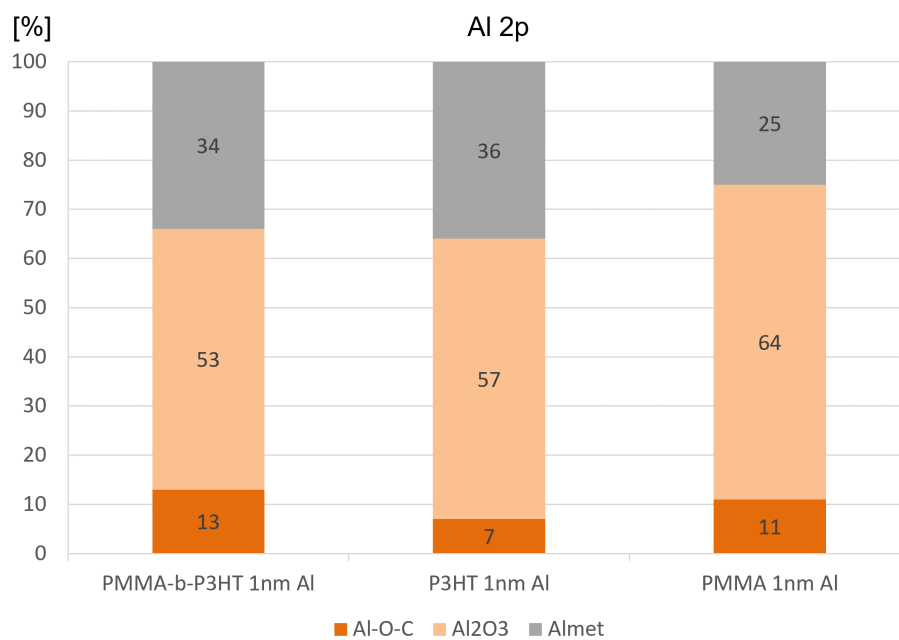


Figure 7.4.: XPS spectra of PMMA-*b*-P3HT with $\delta_{Al} = 1$ nm at a) Al 2p edge. Reprinted with permission from [71]. Copyright 2021 American Chemical Society.

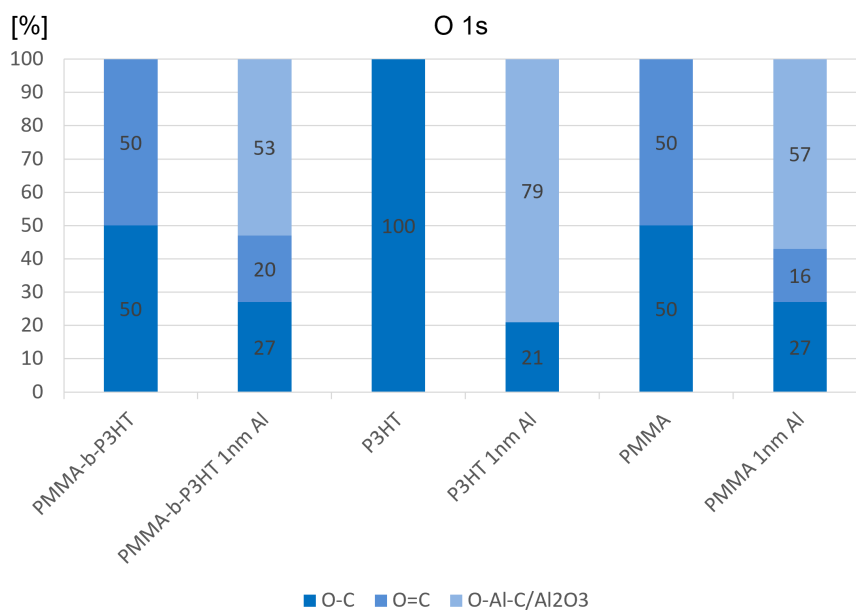


Figure 7.5.: XPS spectra of PMMA-*b*-P3HT with $\delta_{Al} = 1$ nm at a) O 1s edge. Reprinted with permission from [71]. Copyright 2021 American Chemical Society.

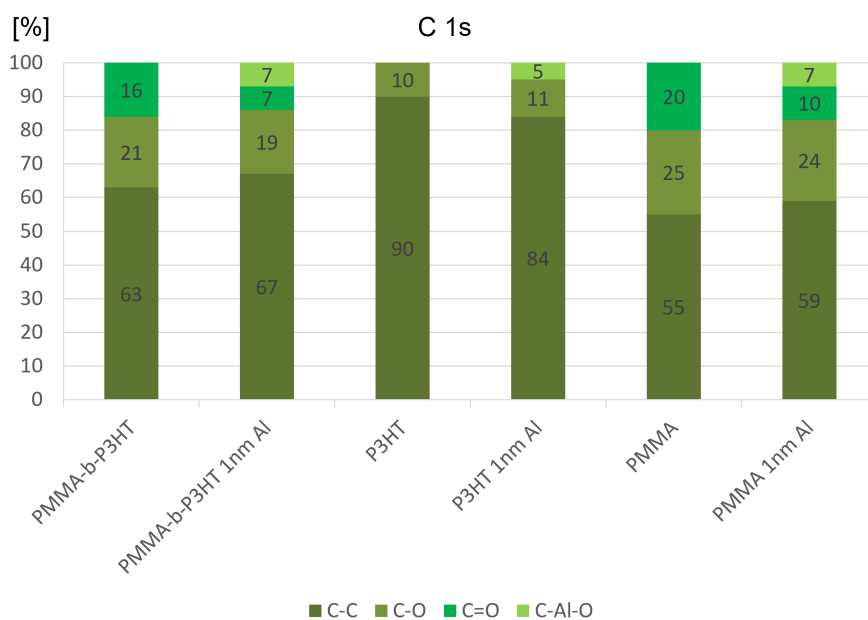


Figure 7.6.: XPS spectra of PMMA-*b*-P3HT with $\delta_{Al} = 1$ nm at a) C 1s edge. Reprinted with permission from [71]. Copyright 2021 American Chemical Society.

7.3. Scattering analysis

The same *in situ* GISAXS set up is used as in the previous chapter 6. 2D-GISAXS images in Figure 7.7 illustrate the evolution of the Al sputter deposition from $\delta_{Al} = 2$ to 14 nm on the DBC template and their corresponding homopolymers PMMA and P3HT. The typical features as the domain peak of the DBC and the metal cluster peak are marked with a white arrow in Figure 7.7a and the corresponding horizontal line-cuts are marked with a red box in Figure 7.7a,b. The growth of the cluster peak is quite similar for all three templates and will be analysed in more detail later in the section. On PMMA it seems that a second cluster peak is arising at around $\delta_{Al} = 5$ nm, which will be explained later by the AFM analysis of the homopolymers. From the shape difference of the Al cluster peak, seen in Figure 7.7b,c,d for $\delta_{Al} = 5, 10, 14$ nm compared to the Ag cluster peak on the same DBC template, a hemispherical cluster growth is assumed. [135, 194] The percolation threshold for cylindrical or spherical cluster would lead to a percolation threshold, which would not match with the later shown AFM and FESEM data, while for hemispherical clusters it matches well. In Figure 7.8a the contour plot of the horizontal line-cuts from the *in situ* GISAXS data at the Yoneda peak position, which was marked with the red box in Figure 7.7a. The Al cluster peak is marked in black and can be followed by the black arrow in Figure 7.8a and the DBC domain peak is indicated by a red arrow in Figure 7.8a. The different Al growth regimes on the DBC template are displayed by Roman numbers and are separated with white dashed lines: (I) nucleation, embedding, the point of first observation of the cluster peak and formation of the merged cluster layer on P3HT; (II) selective diffusion-mediated cluster growth via coalescence and cluster growth on the Al merged cluster layer; (III) reduced-selective adsorption-mediated growth and percolated regime on the P3HT domain; (IV) percolated layers on both polymer domains. In Figure 7.8b, the scattered intensity of the domain peak of the DBC is followed during the Al deposition and indicates a selective wetting by an increased scattering intensity at the domain peak of the DBC, which relates from the increased electron density contrast on one domain of the DBC. A selective decoration of Ag on the DBC template was shown in the previous chapter and seems to be present also for Al but with a different selectivity. The selective wetting for Al can be seen until around $\delta_{Al} = 2$ nm in Figure 7.8b, which then turns into a reduced selective wetting on the P3HT domain, seen by the change of the slope for the intensity of the domain peak. From this thickness on the Al clusters start to grow on the merged Al layer on the P3HT domain as it was shown by the AFM images in Figure 7.1d and the Al clusters start to appear on the surface of the PMMA domain. The maximum at $\delta_{Al} = 5.2$ nm indicates the end of the selective wetting. Now the Al clusters starts to cover more and more of the surface on both polymer domains of the DBC and the clusters tend to merge more

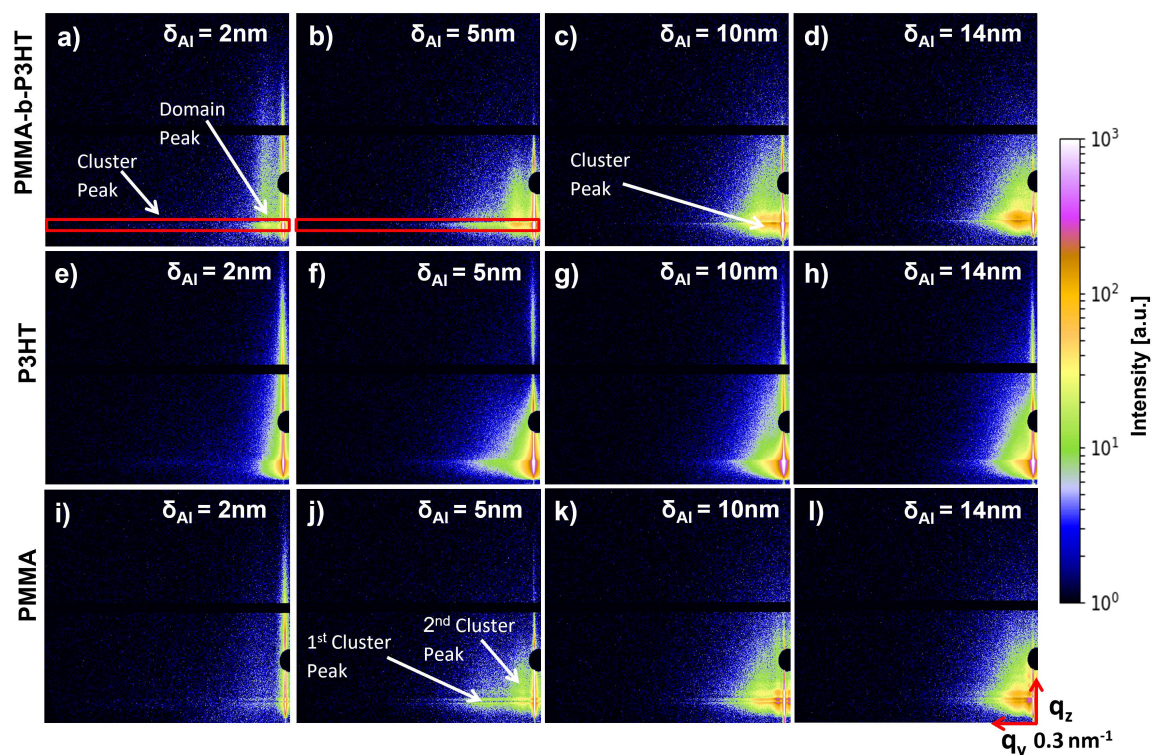


Figure 7.7.: Selected 2D GISAXS data of Al cluster growth on a-d) PMMA-*b*-P3HT, e-h) P3HT, and i-l) PMMA for Al thicknesses of $\delta_{Al} = 2$ nm, 5 nm, 10 nm and 14 nm, respectively. The red boxes show the Yoneda region for the lateral line cuts. The domain peak and cluster peaks are highlighted. The scattering pattern indicate a hemispherical shape of the Al nanostructures for all templates. Reprinted with permission from [71]. Copyright 2021 American Chemical Society.

often. At around $\delta_{Al} = 8$ nm, the Al cluster peak starts to overlap with the DBC domain peak, which leads to an increase in its intensity. This is indicative of the connecting network of the merged Al cluster layers on both polymer domains, starting to close the Al metal film on the DBC template. Figure 7.8c shows the average center-to-center distances (D) and the cluster radii (R) of Al on PMMA-*b*-P3HT (red), PMMA (blue), and P3HT (green). On all three polymer templates the Al growth seems to be homogeneous over the deposition, illustrated by the linear growth of D . The radii R are calculated from the geometrical model using the center-to-center distances and the film thickness on the assumption of a hemispherical cluster shape. The growth on all templates with a constant slope for R and D (in contrast, Ag showed different slopes in the different growth regions) appears to be a hint for the reduced diffusion of atoms on the polymer surface. This indicates a disturbed diffusion of the Al clusters/atoms on the DBC domains (PMMA and P3HT), which might be due to the chemical interaction of the Al with the molecular

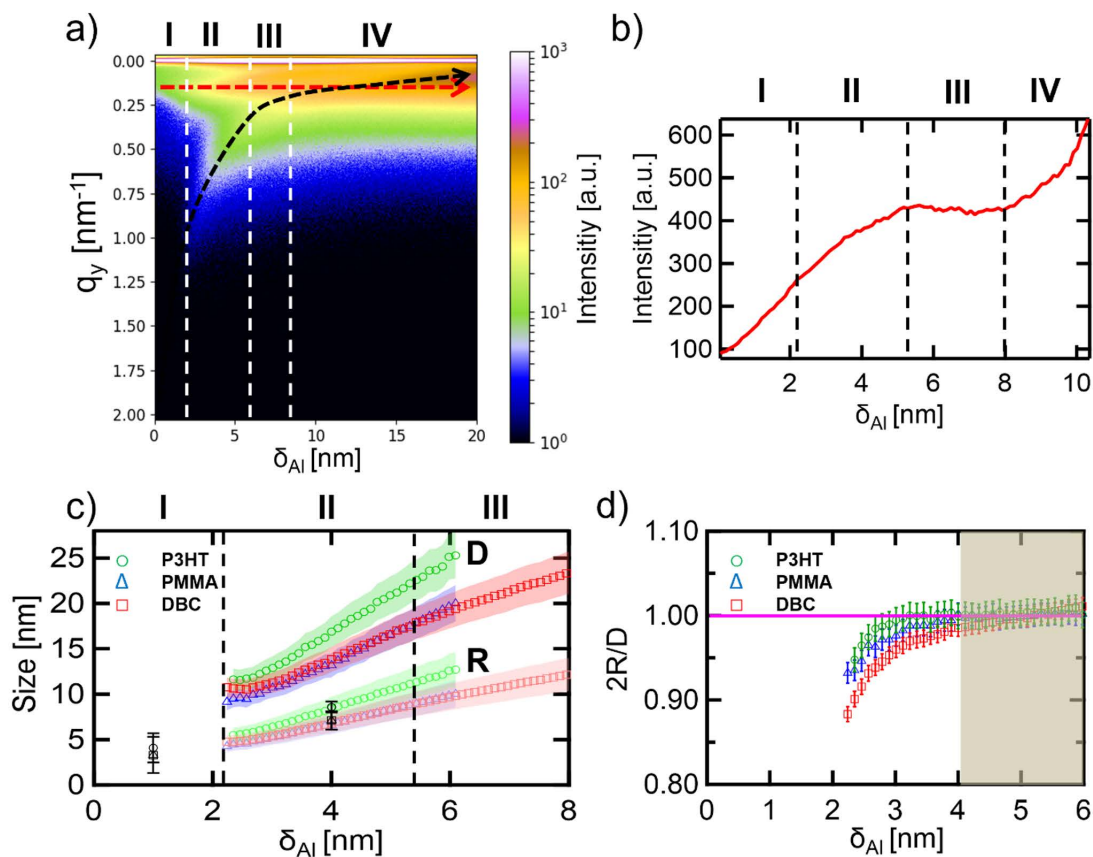


Figure 7.8.: a) Contour plot of horizontal line-cuts from the *in situ* GISAXS data measured during sputter deposition on PMMA-*b*-P3HT as a function of effective Al thickness δ_{Al} . The position of the cluster peak (black dashed arrow) is changing due to the Al deposition and the position of the first-order DBC domain peak (red dashed arrow) at $q_y = 0.15 \text{ nm}^{-1}$ is constant during Al deposition. The white dashed vertical lines indicate different growth regions as explained in the text. b) Amplitude of the domain peak of PMMA-*b*-P3HT during Al sputter deposition. c) Average Al interparticle distance on PMMA (D_{PMMA} , blue), PMMA-*b*-P3HT ($D_{PMMA-b-P3HT}$, red), P3HT (D_{P3HT} , green), and the corresponding cluster radii for the different polymer films R_{PMMA} (bright blue), $R_{PMMA-b-P3HT}$ (bright red), and R_{P3HT} (bright green). The radii calculated from FESEM images at $\delta_{Al} = 1$ and 4 nm are shown as black symbols. d) Ratio of the average cluster diameter (2R) and the average interparticle distance (D) ratio for PMMA (blue), PMMA-*b*-P3HT (red), and P3HT (green). When $2R/D = 1$ (magenta line), the clusters start to touch each other, resulting in a macroscopic conductive path. The brown box covers the region, in which the Al reaches the percolation on the three templates. Reprinted with permission from [71]. Copyright 2021 American Chemical Society.

components of the polymer domains. In comparison to the typical metal formation for Au or Ag on polymers, the interaction of Al with the polymer seems to be much stronger on these polymer thin films hindering the diffusion of Al atoms and clusters. The increased chemical interaction is demonstrated by the high interaction peak in the Al 2p spectra (Al_2O_3 and O-Al-C compounds). The bonding of Al with the molecular components of the polymers could be considered as defects on the polymer thin films and could hinder the diffusion of the metal atoms on the films. The sizes ($2R$) of the clusters measured with GISAXS are correlated with FESEM results in Figures 7.10c-e and 7.12a-c and can be seen as black markers in Figure 7.8c, which reveal nearly the same cluster radii for $\delta_{\text{Al}} = 4$ nm. A similar linear growth is found for the radii and center-to-center distances for both homopolymers P3HT and PMMA, as it is seen by the GISAXS measurements in Figure 7.8c. The size distribution on the three polymers types reveal larger Al cluster sizes on P3HT compared to PMMA and the DBC template, which is confirmed later by AFM and FESEM measurements. The Al growth on the DBC template shows further a slight difference compared to the growth on the homopolymers by a deviation in the slope from a linear growth from the center-to-center distances in Figure 7.8c), which could be related to the different Al growth on the polymer domains of the DBC and therefore resulting in a later percolation. This can be seen in the region from $\delta_{\text{Al}} = 5-6$ nm, where the linear increase for the center-to-center distances slows down, which indicates the transition from the selective diffusion-mediated cluster growth via coalescence on the merged cluster layer on P3HT to the reduced-selective adsorption-mediated growth and a percolated regime on the P3HT domain. The detailed percolation analysis is shown in Figure 7.8d, which is calculated from the geometrical model. The percolation threshold is not as clearly developed as for Ag on these templates. The brown box marks the region, which can be identified as the Al percolation region between $\delta_{\text{Al}} = 4-6$ nm, which is in excellent agreement with the FESEM data at the onset of percolation (Figures 7.12a-c). The Al decoration on the DBC template demonstrates a much smoother and more uniform growth due to a more controlled growth on the more ordered domains on the DBC template compared to the randomly oriented fibers of the P3HT homopolymer in Figure 7.14d and the uncontrolled embedding in the PMMA template with different cluster aggregation regions in Figure 7.14b. The DBC template has a sharper percolation transition between $\delta_{\text{Al}} = 5-6$ nm compared to the respective homopolymers, which would be advantageous for more controlled electrode deposition. The Al deposition on PMMA shows a second observable peak in the GISAXS data located at smaller q_y values for the aggregation regions in Figure 7.7j. This second peak is not considered in the calculations for the percolation and will be identified later by AFM images as the cluster aggregation regions. The identification of sputtering metallic Al is found in the GIWAXS measurements. The

ring-shaped intensity distribution (Figure 7.9) results from a powder texture of the Al grains. The position of the intensity rings corresponds to the (111) and (200) plane of metallic Al.

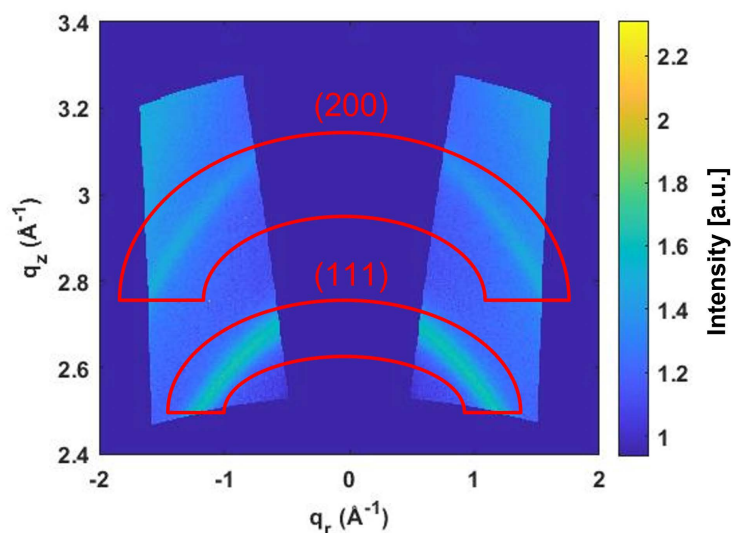


Figure 7.9.: Reshaped 2D GIWAXS data (using GIXSGUI) of PMMA-*b*-P3HT after sputter deposition of $\delta_{Al} = 20$ nm. The (111) and (200) planes of metallic Al are indicated with the red regions. Reprinted with permission from [71]. Copyright 2021 American Chemical Society.

7.4. Comparison of the Al decoration on the polymer types

The growth of Al on the DBC domains is studied *ex situ* in more detail in Figure 7.10 with AFM line-cuts over the polymer domains of the DBC template, the analysis of the rms roughness for different Al thicknesses and the comparison to the homopolymers. In Figure 7.10a the line-cuts from the AFM data for different Al thicknesses show the selective wetting of the Al merged cluster layer on the PMMA-*b*-P3HT template and reveal the Al cluster decoration on the merged cluster layer. The change in the average peak-to-valley distance (D_{ptv}) in comparison to the pristine substrate is an indicator for the selective wetting of the metal on one polymer domain, similar to Ag in Figure 6.3 and Figure 6.4. The maximum of the selective wetting for Al on the DBC template is

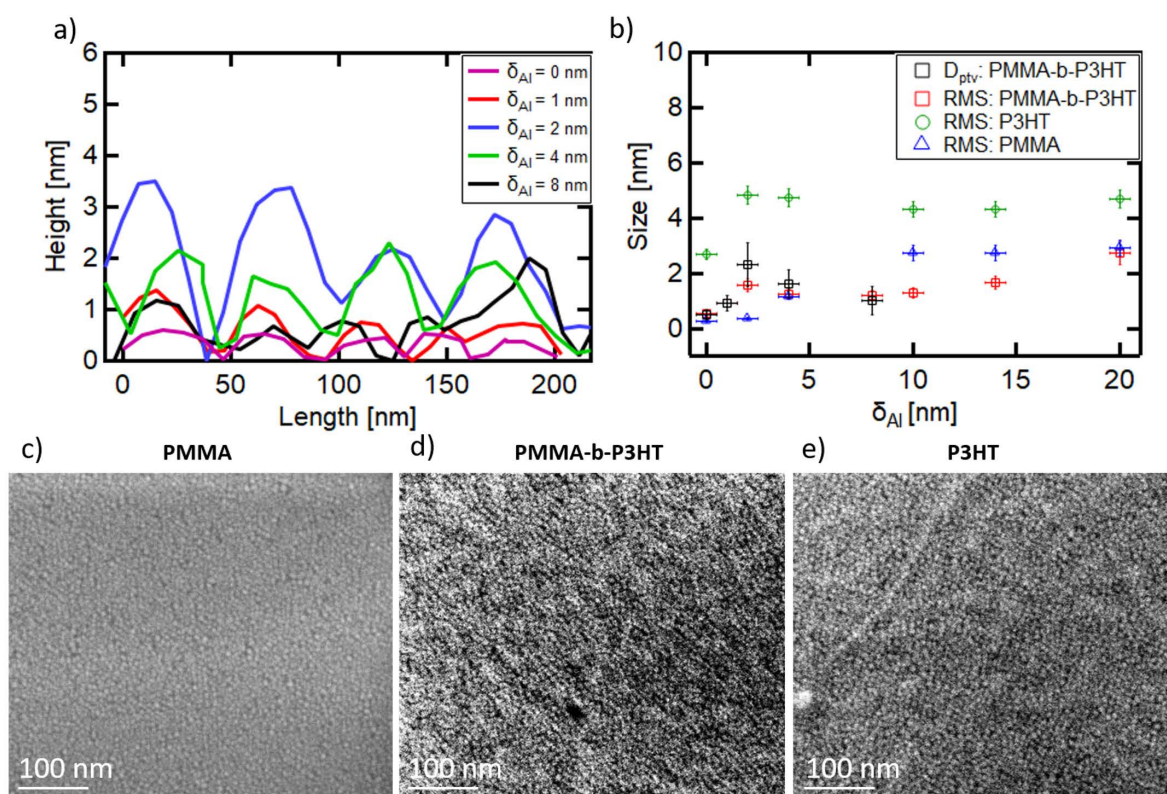


Figure 7.10.: a) Line-cut from AFM data of PMMA-*b*-P3HT films sputter-coated with a different Al thickness as indicated. b) Average peak-to-valley distance (D_{ptv}) and root-mean-square (rms) roughness measured with AFM for different Al thicknesses on PMMA-*b*-P3HT, PMMA, and P3HT. FESEM images for c) Al/PMMA, d) Al/PMMA-*b*-P3HT, and e) Al/P3HT with $\delta_{Al} = 1$ nm. A homogeneous Al cluster distribution is observed on all templates. Reprinted with permission from [71]. Copyright 2021 American Chemical Society.

illustrated in Figure 7.10b at around $\delta_{Al} = 2$ nm from the analysis of the D_{ptv} from the line-cuts. Compared to Ag, Al cluster are fastly forming a wormlike nanostructure of Al (merged cluster layer) demonstrated in Figure 7.1c,d. The merged cluster layer on the P3HT domain is already present at $\delta_{Al} = 1$ nm until $\delta_{Al} = 2$ nm and then changes to a cluster like growth on top of the wormlike nanostructure. On the PMMA domain the Al clusters seem to embed and start subsurface growth which is indicated in Figure 7.14a,b and demonstrated by the rms roughness value in Figure 7.10b: Compared to the rms roughness for DBC and P3HT, it is reduced for PMMA and increases later strongly due to the extended growth on the surface of PMMA. Ag in contrast tempts to self-assemble firstly on the crystalline part of the polymer domains as clusters without forming such a merged cluster layer. Above $\delta_{Al} = 2$ nm, the selective decoration of Al is still present

for Al clusters on the merged Al cluster layer until around $\delta_{Al} = 8$ nm but is reduced as demonstrated in Figure 7.10b by the reduction of the growth increase of the D_{ptv} for PMMA-*b*-P3HT. D_{ptv} is following the overall rms roughness trend of the DBC thin film and is visible until $\delta_{Al} = 8$ nm, which indicates the end of the selective wetting on the DBC template by the Al clusters. After $\delta_{Al} = 8$ nm, the Al clusters fill up the valleys of the PMMA domains and the value of D_{ptv} decreases significantly due to the closing metal layer, the D_{ptv} is then not measurable any more. In order to investigate the Al cluster growth on the P3HT domain, line-cuts on the P3HT domain similar to Figure 5.2c for Ag were done to investigate the evolution of the merged cluster layer formation and the Al cluster growth on the merged layer (Figure 7.11). The Al clusters and the merged cluster layer underneath do not show a change in the height distribution until $\delta_{Al} = 8$ nm: In Figure 7.11 the height distribution on the P3HT domain stays the same. This is an indication for the smooth merged cluster layer formation in the beginning, followed by a homogeneous cluster arrangement on the Al merged cluster layer. The

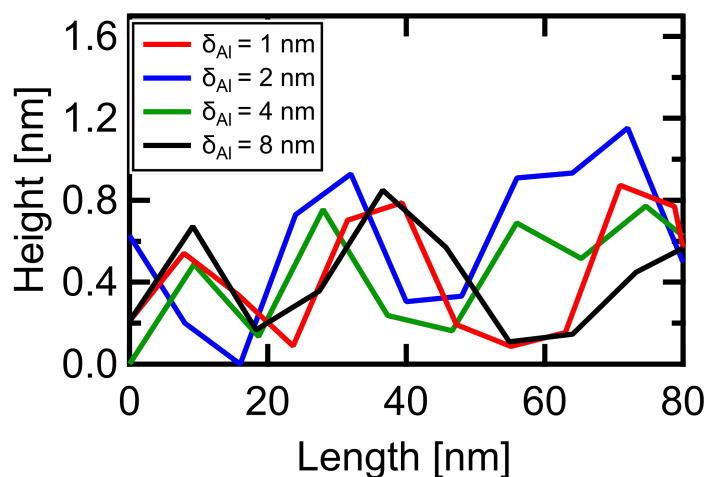


Figure 7.11.: Line-cut from AFM data on the P3HT domain of PMMA-*b*-P3HT films sputter coated with different Al thicknesses as indicated. Reprinted with permission from [71]. Copyright 2021 American Chemical Society.

smooth Al distribution on the DBC template is acknowledged in Figure 7.10b, where the rms roughness values of the Al growth on the DBC template is lower until $\delta_{Al} = 20$ nm compared to the homopolymers. The rms roughness value increases significantly after $\delta_{Al} = 8$ nm for the DBC and approaches the values of the homopolymers in the later stages of the sputter deposition indicating the loss of selectivity. Further FESEM images show the early Al cluster distribution on the DBC template compared to the homopolymers. The FESEM images in Figure 7.10c-e illustrate the uniform Al cluster growth independent

of the polymer template in the early stages of cluster formation. The contrast in Figure 7.10c is lower for PMMA compared to the DBC and P3HT in Figure 7.10d,e. The lower contrast hints at the embedding of the Al clusters inside the PMMA film, as it can be seen later by the AFM measurements in Figure 7.14a, and the rms roughness values for PMMA in Figure 7.10b). The merged cluster layer seems to arrange on the DBC template, which is demonstrated in Figure 7.10d. The Al clusters are merged and highlight the P3HT domain in white compared to the dark PMMA domain. This fits very well with the before shown AFM images in Figure 7.1c,d. On the pure P3HT thin film in Figure 7.10e, the Al clusters are homogeneously distributed and seem to be slightly larger compared to the other templates (DBC and PMMA), as also seen by the AFM measurements in Figure 7.14. The aforementioned uniform Al cluster distribution can be seen up to $\delta_{Al} = 4$ nm, illustrated in Figure 7.12a-c. Above $\delta_{Al} > 10$ nm, a uniformly distributed nanogranular cluster layer is observed in Figure 7.12d-l for all three templates.

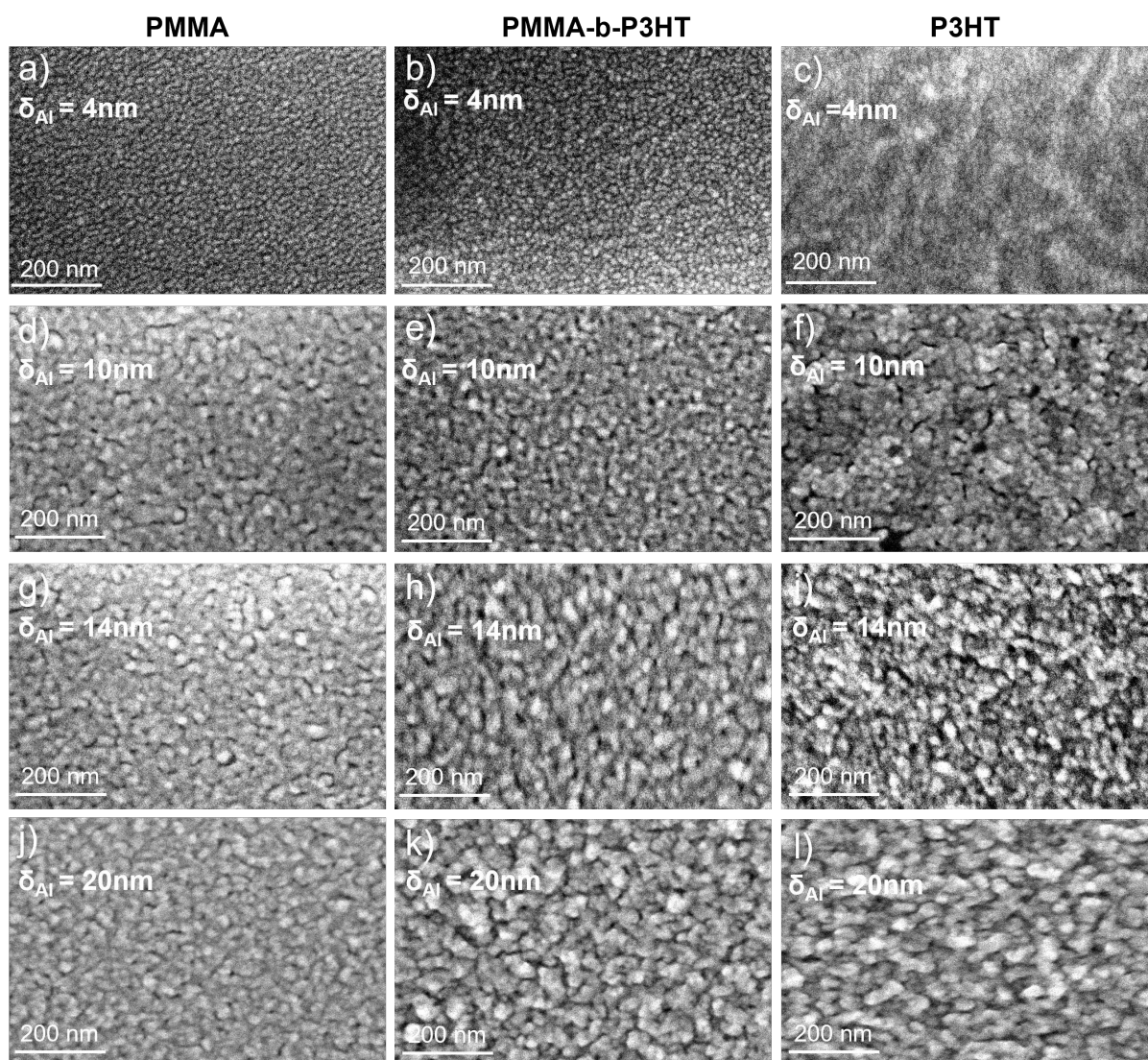


Figure 7.12.: FESEM images a,d,g,j) PMMA, b,e,h,k) PMMA-*b*-P3HT, and c,f,i,l) P3HT with $\delta_{Al} = 4\text{ nm}$, 10 nm , 14 nm and 20 nm . Reprinted with permission from [71]. Copyright 2021 American Chemical Society.

In Figure 7.13, a) PMMA (homogenous thin polymer film), b) the DBC template (P3HT domain around PMMA standing cylinders) and c) the pristine films of P3HT (fibers) can be seen prior to Al deposition. To enhance the understanding of the Al cluster formation on the DBC template, the Al growth on the corresponding homopolymers is analyzed in more detail with AFM. In Figure 7.14a-c, AFM height images of the Al growth on PMMA are shown at selected Al thicknesses. Al shows a similar embedding behavior as shown in a previous chapter for Ag on PMMA. The Al clusters embed and start a subsurface growth for the first 2 nm of deposited Al, as indicated by the low rms roughness value for

$\delta_{Al} = 2$ nm on PMMA in Figure 7.10b. In Figure 7.14b, Al clusters are visible together with some aggregation regions (*AR*, green circles). These regions can be seen in more detail at a larger Al film thickness, e.g., for $\delta_{Al} = 10$ nm in Figure 7.14c. The regions shown in Figure 7.10b,c agree with the appearing scattering peaks in Figure 7.7j,k for $\delta_{Al} = 5$ nm, 10 nm and increase from $AR \sim 100$ nm for $\delta_{Al} = 5$ nm to $AR \sim 200$ nm for $\delta_{Al} = 10$ nm. For the comparison to P3HT in Figure 7.14d-f AFM topography images of the Al growth on P3HT are shown. The Al merged cluster layer is also seen on the P3HT homopolymers in Figure 7.14d, replicating the homopolymer fiber structure of the pristine P3HT thin film. It seems that the Al atoms adsorbed from the vapor phase on the P3HT domain are chemically interacting directly with the P3HT domain and are forming clusters homogeneously arranged on the fibers as seen in Figure 7.14d. This can be further seen in Figure 7.14e,f, where the clusters continuously grow laterally on the fibers.

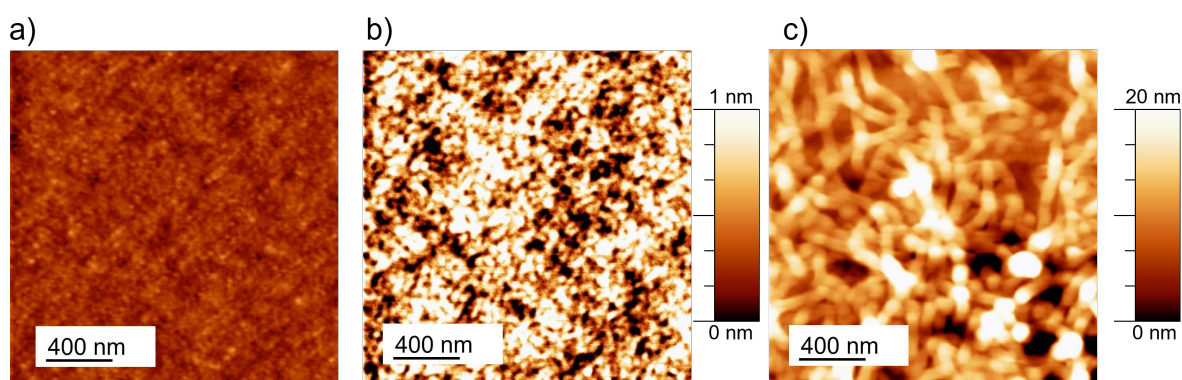


Figure 7.13.: AFM height images of the pristine a) PMMA, b) PMMA-*b*-P3HT and c) P3HT thin films. Reprinted with permission from [71]. Copyright 2021 American Chemical Society.

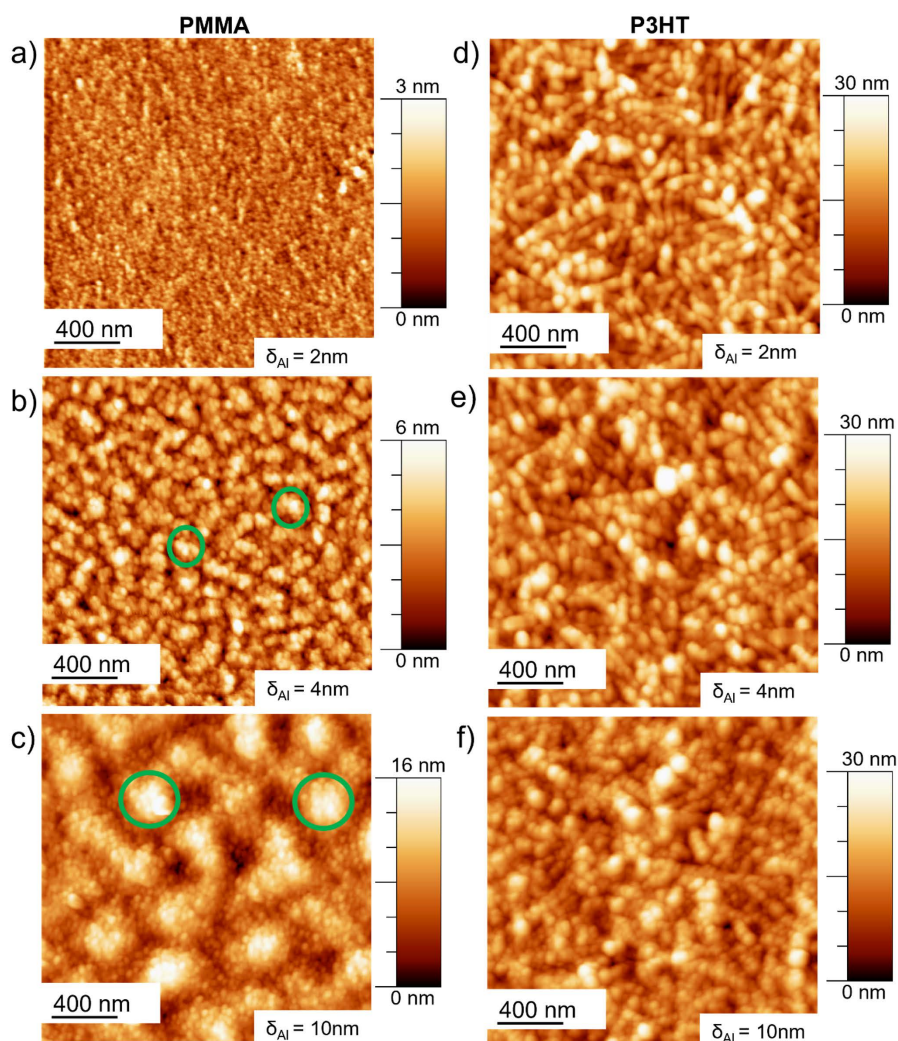


Figure 7.14.: AFM topography of a-c) PMMA and d-f) P3HT thin films sputter-coated with Al thicknesses of a, d) $\delta_{Al} = 2$ nm, b, e) $\delta_{Al} = 4$ nm, and c, f) $\delta_{Al} = 10$ nm. Green circles show the cluster aggregation regions of Al on PMMA. Reprinted with permission from [71]. Copyright 2021 American Chemical Society.

7.5. Growth model

The results of the Al sections are combined to derive a model for the different growth regimes of Al on the DBC template, as shown in Figure 7.15. The side view of the Al deposition and growth on the DBC template is shown in sketches in Figure 7.15a-e for the pristine and Al-deposited DBC morphology. The nucleation, embedding, and subsurface growth are shown in Figure 7.15b, regime (I). Figure 7.15c shows the selective diffusion-mediated cluster growth via coalescence on the merged cluster layer on P3HT,

which defines the next regime (II). The reduced-selective adsorption-mediated growth and percolated regime on the P3HT domains are shown in Figure 7.15d, regime (III). The percolated layers on both polymer domains are sketched in Figure 7.15e and mark the final regime (IV). A top view of all growth regimes is sketched in Figure 7.15f. Flat Al clusters are present on the P3HT domains at the beginning of deposition, which are then merged to the wormlike Al layers on the P3HT domains (merged cluster layer). Subsequently, newly adsorbed Al atoms form well ordered Al clusters on the merged Al layers (II). After embedding and subsurface growth on the PMMA domains (I), the Al atoms form continuously growing Al clusters on the PMMA surface (II and III). The Al clusters on the Al merged Al layer continuously grow in size, as seen also on the fibers of the P3HT homopolymer thin film, into a nanogranular Al layer (III).

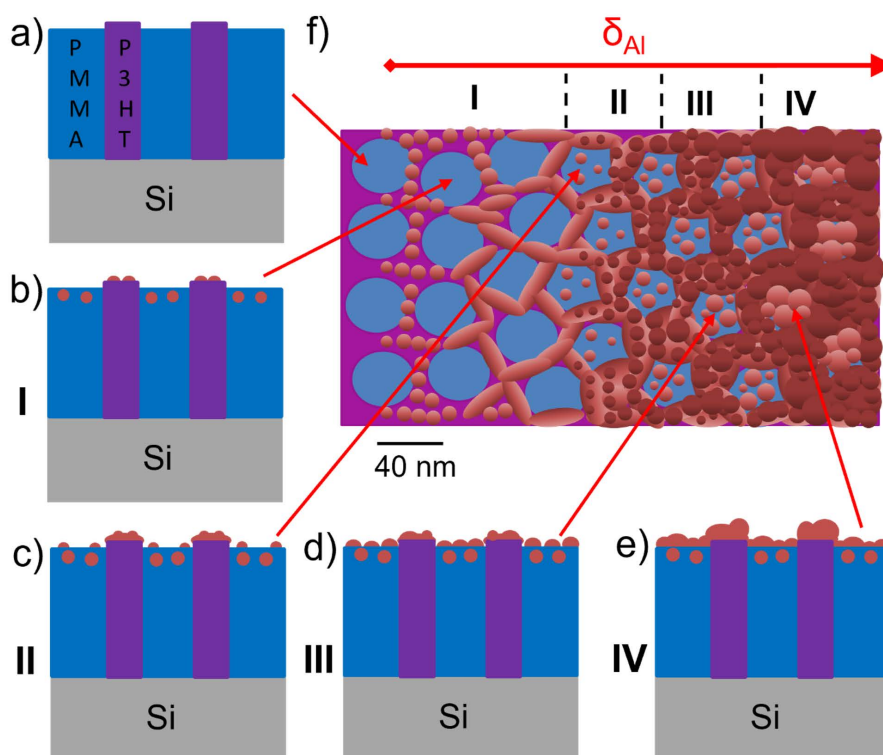


Figure 7.15.: Sketch of the growth model of Al (brown clusters) on the PMMA-*b*-P3HT DBC template in a-e) side view and f) from the top. Roman numbers I-IV indicate different growth regimes as described in the text. Reprinted with permission from [71]. Copyright 2021 American Chemical Society.

7.6. Summary

The growth of Al on PMMA-*b*-P3HT DBC template shows a clear difference compared to that of Ag on the same DBC template from the previous chapter. The XPS measurements show a clear tendency of the high chemical interaction of Al with the molecular components of the polymers. Even on the P3HT domain Al₂O₃ or Al-O-C compounds are formed in contrast to Ag. The optical properties and the complex growth of Al nanostructures were measured simultaneously with *in situ* methods and revealed four growth stages on PMMA-*b*-P3HT and plasmon activity for distinct Al thickness regions. The UV-vis *in situ* relative reflectance change of the pristine DBC template is correlated to the Al formation on the DBC template and yields an antireflective behavior in the UV regime for Al thicknesses below the percolation threshold, which can be attributed to Al plasmon resonance. The Al cluster arrangement on PMMA is found to be different compared to the other polymer templates P3HT and PMMA-*b*-P3HT. On PMMA, the Al clusters tend to embed in the polymer and then start to grow to a rough cluster layer. The early Al growth on P3HT follows a fast percolation of clusters to a merged cluster layer on the P3HT fibers and domains. A clear correlation between the morphology of nanogranular Al merged cluster layers to its optical and morphological properties is demonstrated by the change from its antireflective behavior in the reflectance spectra with the Al cluster size and distance evolution from GISAXS and AFM. The correlation of optical and morphological properties is of interest because of the increased high absorption of 20% for UV light and due to the achieved homogeneous Al cluster distribution. This could be used for large-scale sensor applications to fabricate such metal-polymer hybrid films. Future investigations of polymer-assisted sputter deposition will elucidate the tailoring of optically active metal merged cluster layers for sensors and could be also expanded to organic photovoltaic applications by controlling the size, distribution and chemical interaction of the metal clusters on the corresponding templates. The direct correlation of morphological, chemical, and optical properties of the Al formation on the DBC gives insight into the early Al polymer chemical interaction and allows for understanding the formation for large-scale fabrication of optical sensors and electrode materials for organic solar cells.

8. Selective Wetting of Au versus Ag on PLA-*b*-P3HT Templates

OPV devices need certain requirements to maximise the efficiency such as the thickness of the polymer thin film of around $t = 100$ nm for efficient absorption and the distance of the polymers of the bulk heterojunction (BHJ) should be in the range of the exciton diffusion length to reach the interface of polymer domains and unravel the exciton into an electron and a hole. Therefore I used a known DBC template system as reported by Bontiz *et al.*, where the domain distance is around the exciton diffusion length. [53] The aim of this chapter is to investigate the selective decoration behavior of Ag and Au on the P3HT polymer domain of the DBC template, which could be useful for the extraction of the electron from the donor material. In this chapter the topography and selective decoration of Ag and Au on the diblock copolymer template PLA-*b*-P3HT are compared with each other. The results of the AFM measurements in section 8.1 and GISAXS measurements in section 8.2 show the same behavior for the selective Ag decoration and a non selective growth of Au on the DBC template.

8.1. Morphological comparison of Au and Ag on PLA-*b*-P3HT with AFM

The copolymer used here is similar to the copolymer used in a previous publication [53]. Therefore, the copolymer structure in the thin film is well-defined. In Figure 8.1a the as-deposited copolymer film with a thickness of around $t = (137 \pm 5)$ nm can be seen in the AFM height image. The just spin-coated sample shows no phase separation. In order to improve the phase separation solvent vapor annealing was used for 45 min in a desiccator with chloroform. 50 mL of chloroform was used in the vessel to fully swell the copolymer thin film. During swelling the blue thin film of the copolymer changed color to yellow, which indicates the swelling of the thin film. The final solvent vapor annealed film after 45 min can be seen in Figure 8.1b with the oriented lamella structure.

The lamella structure is oriented parallel to each other in groups of lamellae next to each other and aggregations are visible in Figure 8.1c blue circle. The zoom-in region (green circle in Figure 8.1b) in Figure 8.1c shows the fine lamella structure agreeing well with the previous publication [53]. The lamella to lamella distance is around $D_L = (15 \pm 2)$ nm, seen in Figure 8.1c indicated by the red line. The fine lamella structure can be even better seen in the phase image in Figure 8.1d. From the previous publication I know that the lighter domain corresponds to the P3HT domain of the DBC template [53].

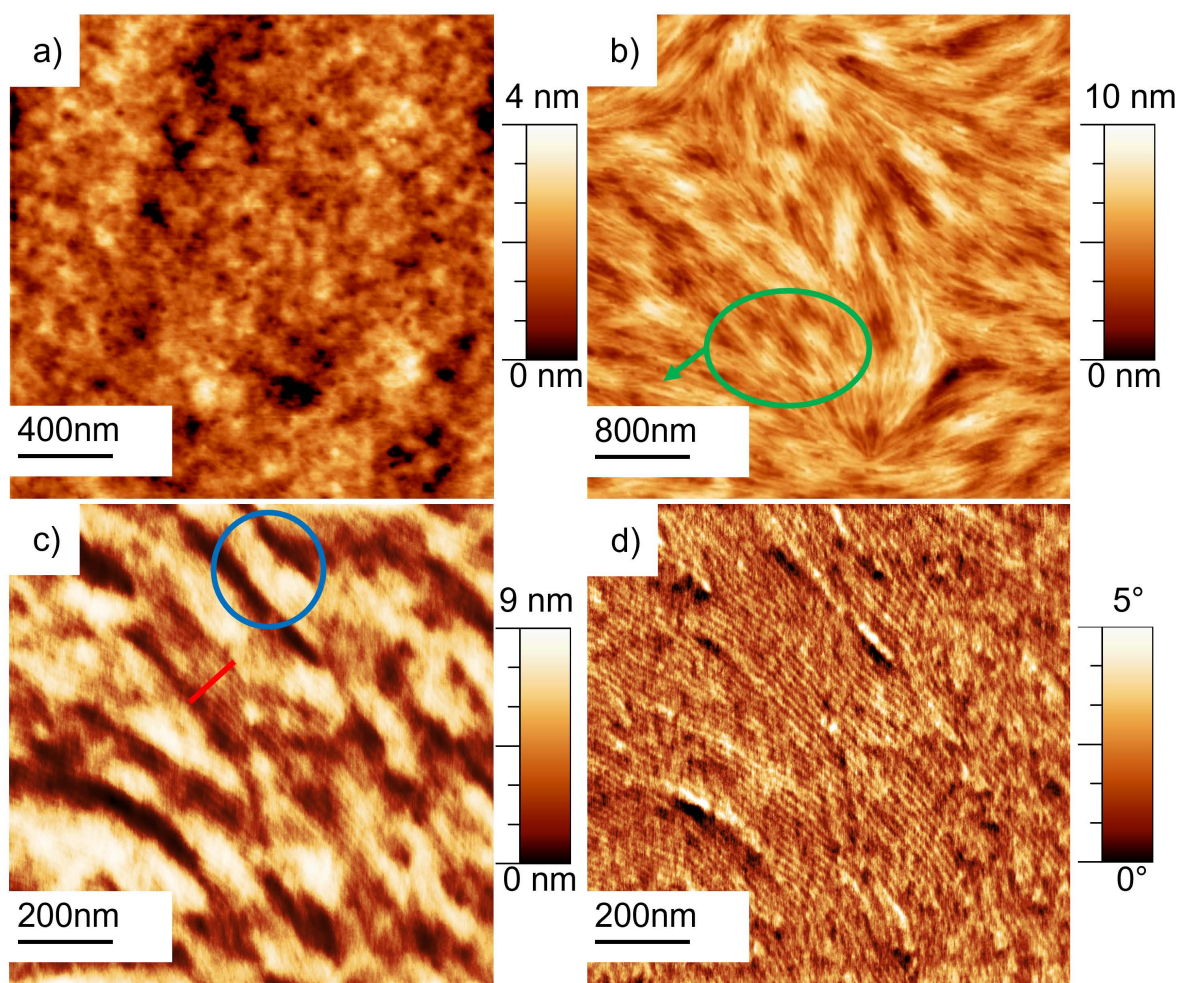


Figure 8.1.: a) AFM height image of pristine PLA-*b*-P3HT DBC template. b) AFM height image of solvent vapor annealed PLA-*b*-P3HT DBC template. c) Zoom-in of the solvent vapor annealed PLA-*b*-P3HT DBC template. d) AFM phase image of the zoom-in of the solvent vapor annealed PLA-*b*-P3HT DBC template.

The selective metal behavior was studied with two metal types namely Au and Ag. The results for $\delta_{Au,Ag} = 1$ nm can be seen in Figure 8.2a,b. The Au clusters in Figure 8.2a

seems to overlap with more than one lamella domain, while for Ag clusters in Figure 8.2b, the metallization seems to be selective to one lamella domain. This behavior can be seen very clearly by the AFM line-cuts (red line in Figure 8.2b is an exemplary line-cut) over several lamellae in Figure 8.2c. The line-cut for $\delta_{Ag} = 1$ nm (red line) nearly replicates the pristine DBC template (black line). The Au deposited sample (blue line) decorates more than one lamella. The selective Ag decoration can be seen very clearly by the AFM phase image in Figure 8.2d. For Ag some aggregation regions of Ag fractals can be seen in Figure 8.2b (blue circle), which could be resulting from the regions seen in Figure 8.1c.

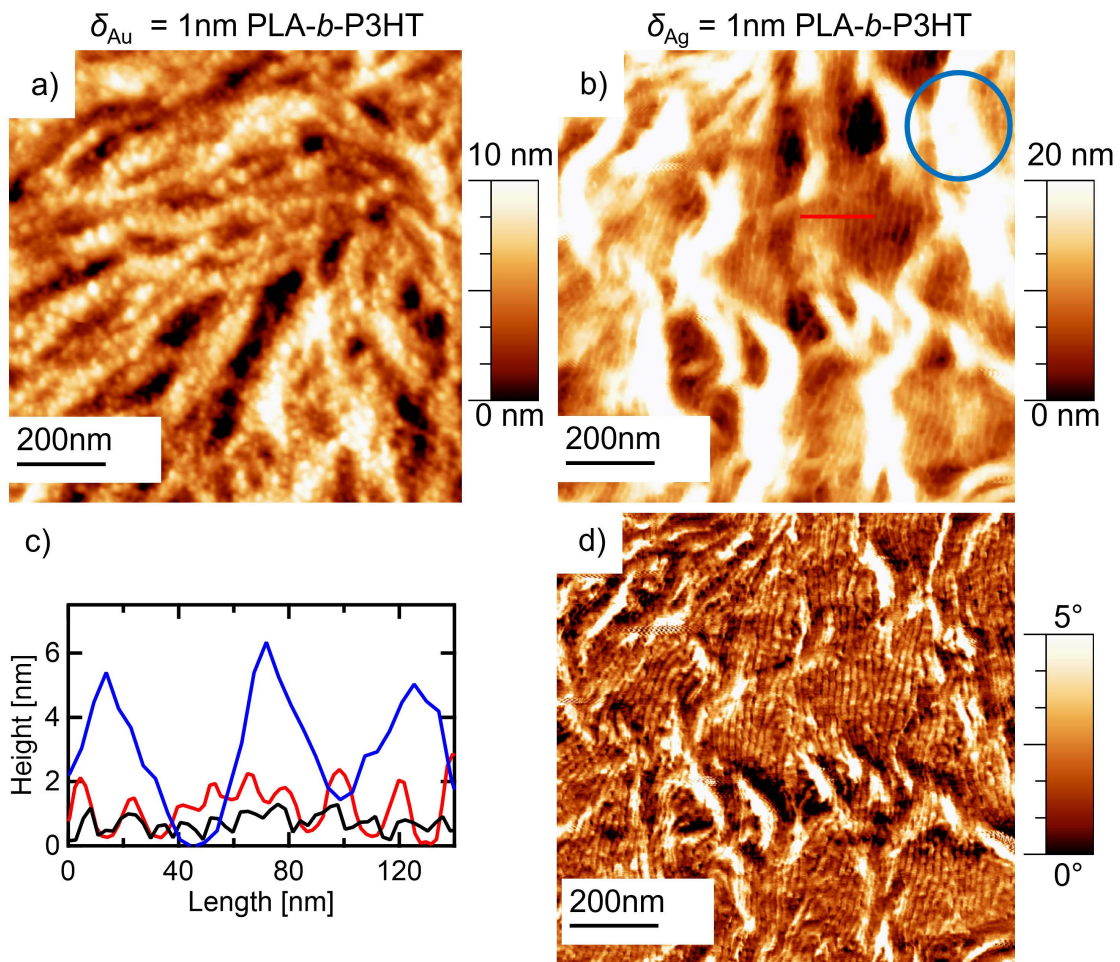


Figure 8.2.: a) AFM height image of $\delta_{Au} = 1$ nm on PLA-*b*-P3HT. b) AFM height image of $\delta_{Ag} = 1$ nm on PLA-*b*-P3HT. c) AFM height profiles of PLA-*b*-P3HT with δ_{Au} and $\delta_{Ag} = 1$ nm. d) AFM phase image of $\delta_{Ag} = 1$ nm on PLA-*b*-P3HT.

8.2. Morphological comparison of Au and Ag on PLA-b-P3HT with GISAXS

A sputter deposition chamber (Figure 4.6) was integrated in a GISAXS set-up at the P03/MiNaXS beamline of the PETRA III storage ring at DESY (Hamburg, Germany). An incident photon energy of 11.8 keV was used with a beam size of $(31 \times 24)\mu\text{m}^2$ at the sample position. The sample-to-detector distance was set at $SDD_5 = (2447 \pm 2)$ mm for *in situ* GISAXS using a Pilatus 300K (Dectris Ltd., Switzerland; pixel size of $172 \mu\text{m}$) at the beamline P03. The direct and specular beams were both shielded by two separate beam stops to avoid saturation or damage to the detector. In order to achieve a good separation between the polymer and the metals, an incident angle of $\alpha_i = 0.4^\circ$ was selected during the *in situ* experiments. The scattering patterns were continuously recorded at a frame rate of 20 images per second for GISAXS. The GISAXS data were analyzed using the DPDAK software package. [156]

In order to verify the selective wetting behavior and its dependence on different metal

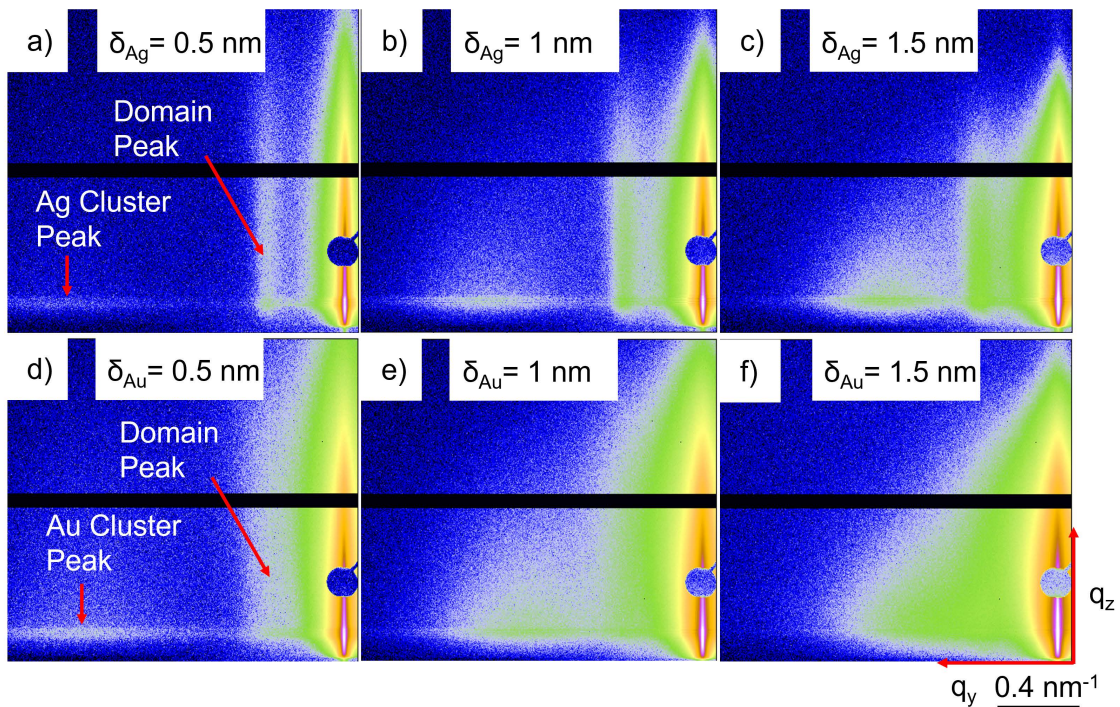


Figure 8.3.: Selected 2D GISAXS data of a-c) Ag cluster growth and d-f) Au cluster growth on PLA-b-P3HT for metal thickness $\delta = 0.5, 1$ and 1.5 nm, respectively.

thickness, GISAXS measurements during sputter deposition with Au and Ag are done.

The comparison of Au and Ag sputter deposition for different deposited metal thickness can be seen in Figure 8.3. The GISAXS data for the PLA-*b*-P3HT DBC template, revealed a domain period of $D_L = (15 \pm 0.5)$ nm. The selective wetting behavior holds only for thin Ag metal films. Therefore, I show the early metal cluster evolution in Figure 8.3 for metal thicknesses of $\delta = 0.5, 1$ and 1.5 nm. For Ag in Figure 8.3a-c a clear cluster peak is visible at all Ag thicknesses and further a clear pseudo-Bragg peak is visible for the domain peak. In Figure 8.3d-f for $\delta_{Au} = 0.5$ nm, the cluster peak is clearly visible. However, after $\delta_{Au} = 0.5$ nm for $\delta_{Au} = 1$ and 1.5 nm, the cluster peak overlaps with the domain peak and the peak intensities between the cluster peak and domain peak cannot be distinguished. This indicates the rapid loss of selective decoration for Au on PLA-*b*-P3HT. In Figure 8.4a,b the change of the horizontal line-cuts from the GISAXS images is

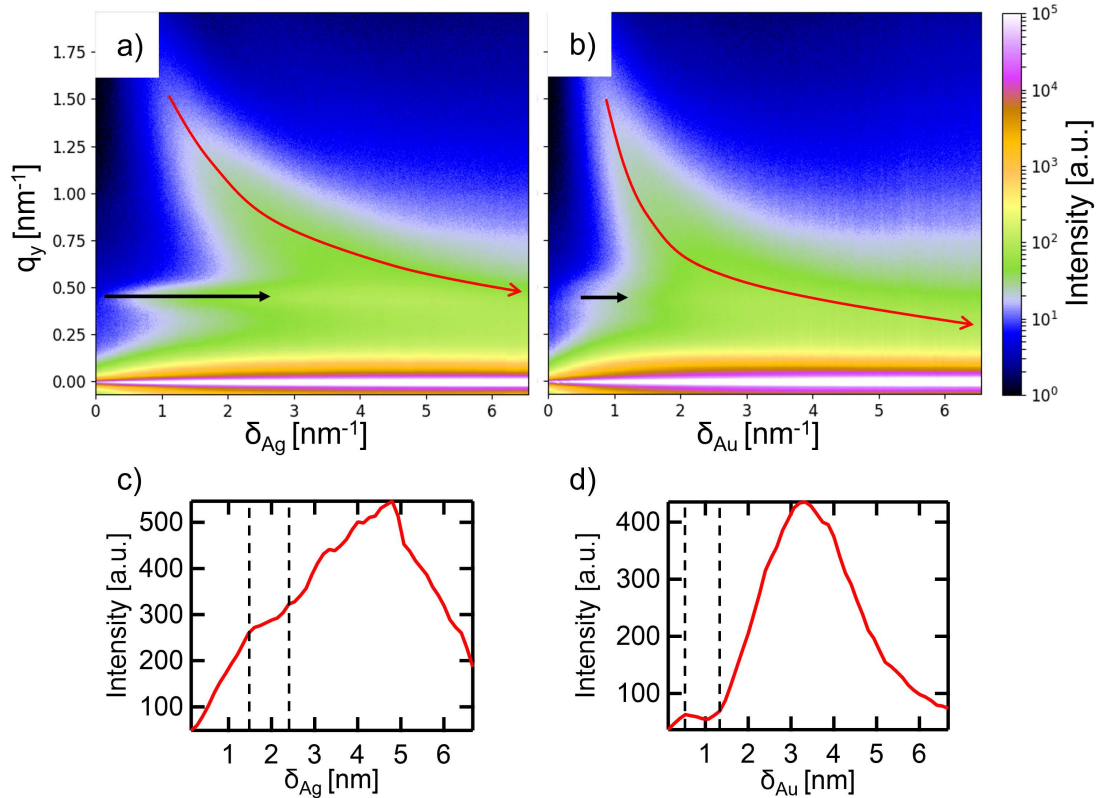


Figure 8.4.: a-b) Contour plot of Yoneda cuts from the *in situ* GISAXS data during sputter deposition of Au and Ag on PLA-*b*-P3HT as a function of effective metal thickness. The cluster peak (red arrow) and the 1st order domain peak (black line) at $q_y = 0.42 \text{ nm}^{-1}$ are highlighted. c-d) Evolution of the amplitude of the domain peak of PLA-*b*-P3HT during the metal sputter deposition.

monitored over the metal film thickness. The metal clusters both growth laterally in size, which is indicated by the change of the q_y maxima position of the cluster peak to lower q_y values. The Au seems to grow faster in size compared to Ag because the q_y maxima position grows faster to smaller q_y values. The selective wetting for both metals seems to be different on the lamella domains, since the domain peak is longer and more clearly visible in Figure 8.4a compared to Figure 8.4b. This behavior is monitored in more detail while following the intensity evolution of the copolymer domain peak during the change of metal thickness. Figure 8.4c and d show the intensity evolution of the domain peak for Au and Ag. For Ag the intensity is increasing until $\delta_{Ag} = 1.5$ nm, then a small decrease can be seen for reduced selective wetting and afterwards again an increase at $\delta_{Ag} = 2.4$ nm which can be attributed to the overlap of the domain peak and the cluster peak. The selective decoration of Au is only until $\delta_{Au} = 0.5$ nm, afterwards the selective wetting is drastically reduced and the cluster peak and the domain peak are already interconnecting at $\delta_{Au} = 1.3$ nm, which shows the large Au cluster aggregations on several lamella bundles. The higher selective decoration for Ag could be explained by the before shown high affinity of Ag to sulfur, see Figure 6.12b. The selectivity is indicated at the position of the domain peak for both metals by the length of the black arrows in Figure 8.4a and b. The difference in the cluster size evolution between Ag and Au is indicated by the different development of the red arrows in Figure 8.4a and b. For Au the q_y value moves faster to smaller values and therefore Au grows faster in cluster size.

8.3. Summary

I showed the comparison of the selective decoration between Ag and Au on the DBC template PLA-*b*-P3HT with a clear difference in the early metal growth stages. The AFM results indicate a high affinity of the Ag to P3HT and to selectively decorate the P3HT domain of the DBC template until around $\delta_{Ag} = 2$ nm. This was further confirmed with GISAXS measurements, which show a clear selective decoration for the Ag and a non selective decoration for the Au. The AFM and GISAXS measurements showed both the same results for the domain distance of around $D_L = 15$ nm, which is in the range of the exciton diffusion length. The selective Ag decoration could be useful to fabricate an OPV device with Ag nano-domains on the P3HT domains, where the Ag nano-domains are connected to a thicker metal electrode to enhance the electron collection from the excitons produced at the interface of the P3HT domains. To do so the PLA could be removed before Ag decoration as shown by Botiz *et al.* in a previous publication [53] and refilled with an acceptor material.

9. Conclusion and outlook

The sputter deposition method yields the ability to fabricate metal contacts over a large area, while the metal formation and structure can be guided by different aspects of interaction of the template and the metal. In this thesis the metal growth on different polymer types is investigated and characterized with morphological, chemical, optical and electrical sensitive methods. One of the important aspects is the chemistry between the metal and the polymer template and another one is the template morphology itself. The chemistry depends on the used metal type and the molecular components of the polymers. The morphology can be influenced by the type of the polymer such as homopolymers, homopolymer blends or DBC. The results presented in this thesis compare the influence of the metal growth on homopolymers and DBC templates to reveal a deeper understanding of the metal-polymer interaction from metal clusters to thin metal films. Different characterization methods are used to follow the metal cluster to film evolution on the polymer templates as mainly *in situ* X-ray scattering methods like GISAXS and GIWAXS offer the ability to gain high statistical information about the parameters such as the cluster size, shape and formation. The high time resolution at the synchrotron radiation source enables to track the specific parameters well. The correlation between the scattering data and complementary methods like AFM and FESEM to characterize different time stamps of the metal growth, helps to understand the metal shape and formation in detail at different metal thickness steps. Although care has to be taken as relaxation processes can enter into the process when interpreting the sputter process. Information of the chemical interaction of the metal with the polymer thin films are seen with XPS and FTIR measurements. Electrical and optical properties are measured during the metal deposition and are correlated to the other measurement methods, which reveals a deeper insight into the differences between the polymer templates or metal types. The growth of metals on polymers is generally known but a detailed knowledge about different interaction parameters as the chemistry and morphology are highly depending on the metal and polymer types.

Therefore, the study is starting with a DBC model system PS-*b*-PMMA to characterize specific properties of the Ag growth on DBC templates. The X-ray scattering data illustrates hemispherical Ag cluster growth on the DBC template for both polymer do-

mains PS and PMMA, while the selective decoration on the PS domain is much more pronounced in the beginning. For the first nanometers, Ag is embedding and starting a subsurface growth in comparison to PS, where the Ag clusters start to directly grow on the surface. This trend was further corroborated by AFM and FESEM data. In morphological terms, a difference in cluster size was observed. The Ag clusters on PS were larger compared to PMMA, which might stem from the different chemical interactions of Ag with a polymer with (PMMA) and without (PS) oxygen. This was then confirmed by XPS and FTIR measurements. Due to the different growth of the Ag clusters on PS and PMMA, the percolation of the thin metal layers was influenced. This was especially seen for the DBC template, which shifted the percolation mostly to later stages compared to the homopolymers due to the difference in morphology and mobility of the clusters between the polymer domains.

The next structured DBC template contains a semi-crystalline polymer block P3HT with a conjugated π system. P3HT is the most common conductive polymer in OPV applications. The Ag growth changed on this template compared to the previous model DBC system. The Ag clusters are growing smaller in size and distance, which is seen by the X-ray scattering data, AFM and FESEM. Furthermore, the shape of the Ag clusters is changed on the P3HT domain to a cylindrical shape, while the shape on the PMMA stays hemispherical. The FESEM measurements show additionally a preferred growth of Ag on the crystalline part of the P3HT domain. A reason for this change in cluster size, distance and shape was shown by the different chemical interaction of the Ag atoms with the sulfur of the P3HT domain. The chemical interactions were both found by XPS and FTIR measurements. The measurements confirmed a difference in the percolation related to the change of the metal formation on the polymer templates. For Ag and Al on PMMA-*b*-P3HT DBC template, the formation on the P3HT domain showed a more directed order. While for Ag the early cluster growth was directed on the crystalline part of the P3HT domain and then expand to the amorphous phase, the Al cluster growth on P3HT was dominated by large flat Al clusters merging into a wormlike nanostructure on the P3HT domain. This was illustrated with percolated pathways in the FESEM and AFM measurements. The growth of Al on PMMA-*b*-P3HT DBC template shows a clear difference compared to the that of Ag on the same DBC template. The chemical interaction of Al with sulfur is negligible and the interaction with the molecular components like oxygen and carbon of the polymers increases significantly. A high proportion of Al₂O₃ and Al-O-C compounds is formed on both PMMA and P3HT domains. The interaction highly influences the shape and formation of the hemispherical Al clusters, which are flat in the beginning and rapidly connecting to a wormlike cluster polymer mixture. On these structures newly well arranged Al clusters are forming, which are contributing to a

high UV-vis absorption measured with UV-vis spectroscopy during the metal deposition. The Al clusters induce a high absorption from plasmonic effects due to a continuous Al cluster growth with distinct distances, which is monitored at the same time with GISAXS measurements for thin Al thicknesses. FESEM and AFM measurements show the distinct Al cluster growth with a linear trend of cluster size grow over the deposited thickness as also seen by the X-ray scattering data. For the two templates PS-*b*-PMMA with Ag and PMMA-*b*-P3HT with Ag and Al sputter deposition detailed growth models were evaluated and correlated with different measurements methods. On PLA-*b*-P3HT a selective Ag decoration was demonstrated and could be useful to fabricate an OPV device with Ag nano-domains on the P3HT domains, where the Ag nano-domains are connected to a thicker metal electrode to enhance the electron collection.

The results demonstrate that the early metal cluster growth on the individual polymer domains determines the later growth stages and strongly influences the resulting nanogranular metal layer. The results from the previous chapters show that both, the difference in surface energy (mobility) of the clusters on the domains as well as the specific chemical interaction play a major role in the growth of the clusters on the polymers. These results will impact the tailoring of metal cluster layers for sensors, electrodes, organic photovoltaic applications and organic electronics using polymer-assisted sputter deposition.

The knowledge gained from the different growth mechanism could be used to fabricate an OPV device with distinct nanostructure of the donor material and refill the resulting nanostructure with an acceptor material, the produced OPV device could be correlated with the efficiency and stability of a BHJ device. Newly designed devices would need *ab initio*, molecular dynamics to fabricate more efficient specific designs for organic photovoltaics and electronics and to correlate these simulations with experimental results as presented here.

A. Appendix chapter 4

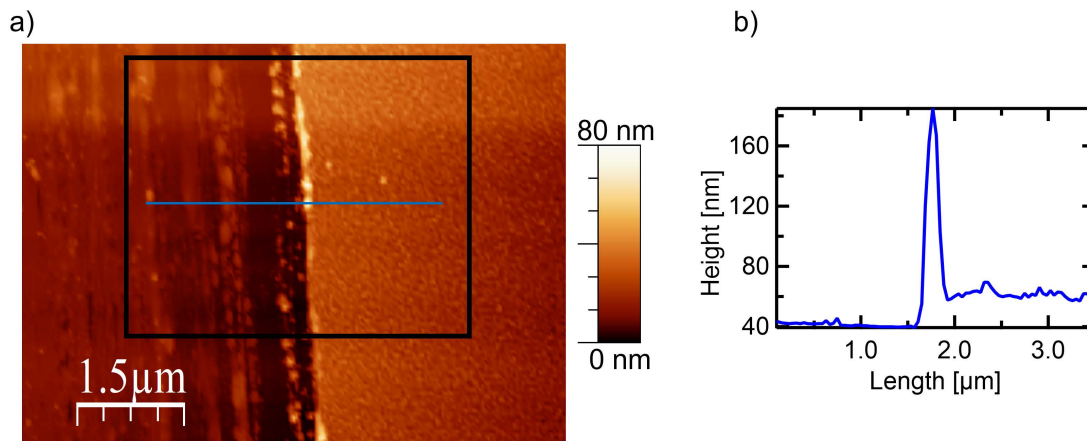


Figure A.1.: a) AFM height image of Al deposited film on silicon with a cut. The blue line marks the line-cut. The black box shows the area, which is used for the histogram. b) exemplary line-cut.

Method	Metal	thickness [nm]
AFM	Ag RF	20.3 ± 3
AFM	Ag DC	20.5 ± 3
AFM	Al DC	20.3 ± 3
AFM	Au DC	20.6 ± 3
GISAXS	Ag DC	20.1 ± 2
GISAXS	Au DC	20.7 ± 2

Table A.1.: Comparison of metal thickness determined with AFM and GISAXS measurements. RF and DC denotes the sputter deposition method.

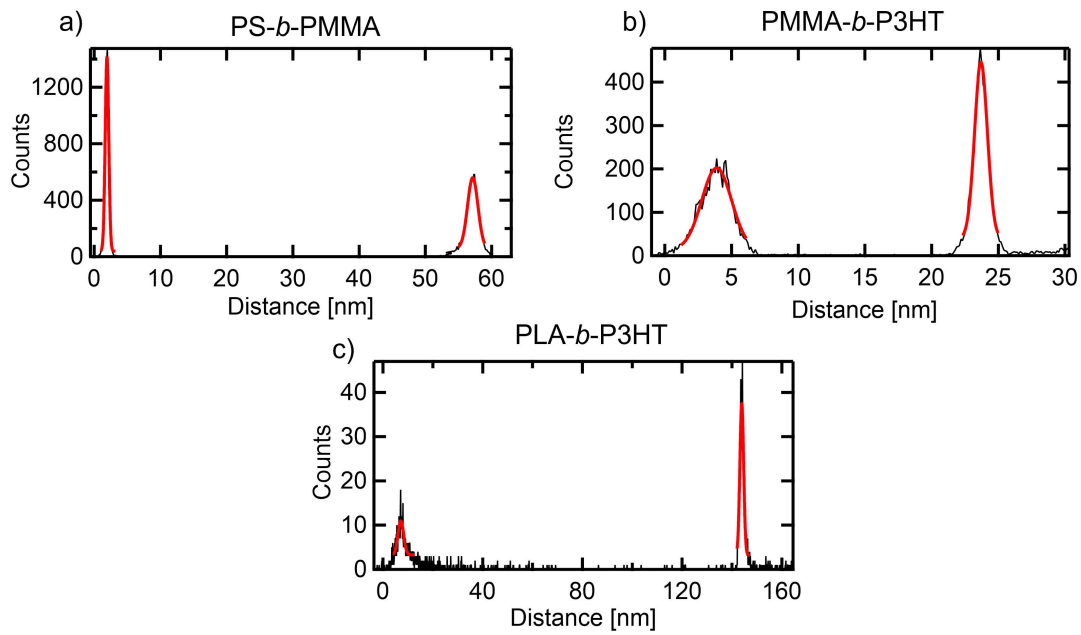


Figure A.2.: a) Histogram of the AFM height distribution of PS-*b*-PMMA. b) Histogram of the AFM height distribution of PMMA-*b*-P3HT. c) Histogram of the AFM height distribution of PLA-*b*-P3HT.

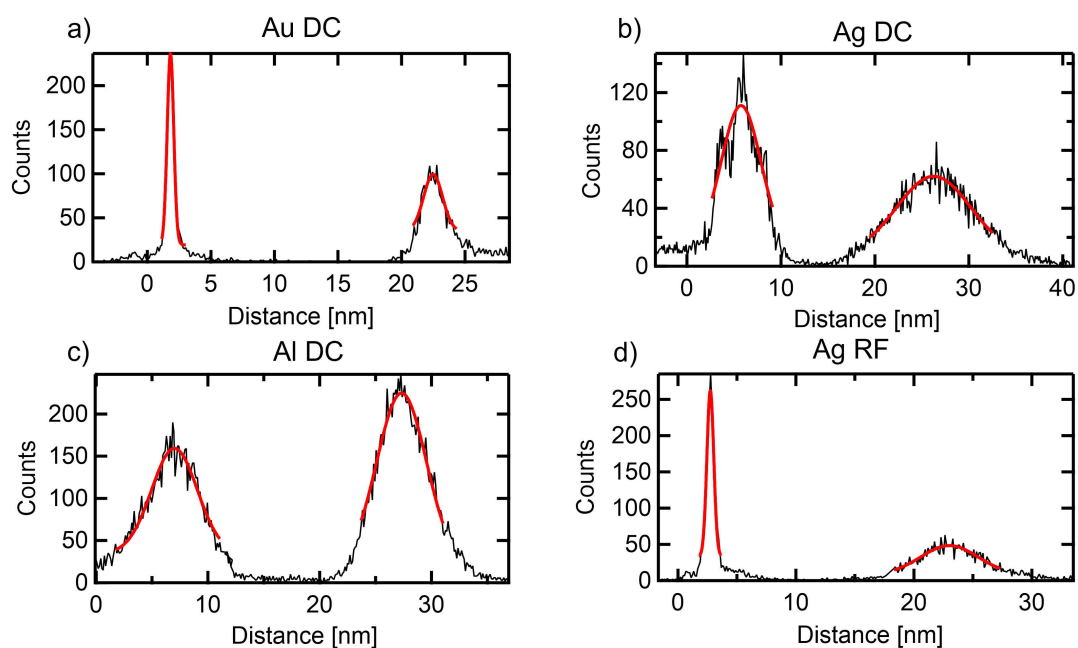


Figure A.3.: a) Histogram of AFM the height distribution of Au by DC magnetron sputtering. b) Histogram of the AFM height distribution of Ag by DC magnetron sputtering. c) Histogram of the AFM height distribution Al by DC magnetron sputtering. d) Histogram of the AFM height distribution Ag by RF sputtering.

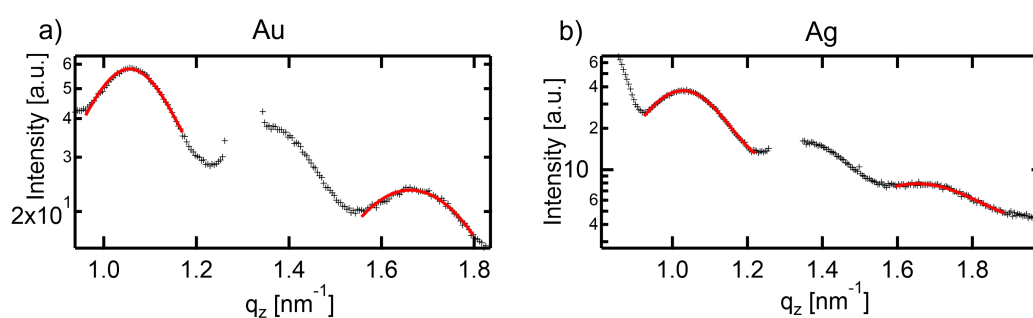


Figure A.4.: a) Vertical line-cut of a GISAXS image the DC magnetron Au deposition to determine the Au thickness. b) Vertical line-cut of a GISAXS image the DC magnetron Ag deposition to determine the Ag thickness.

B. Appendix chapter 5

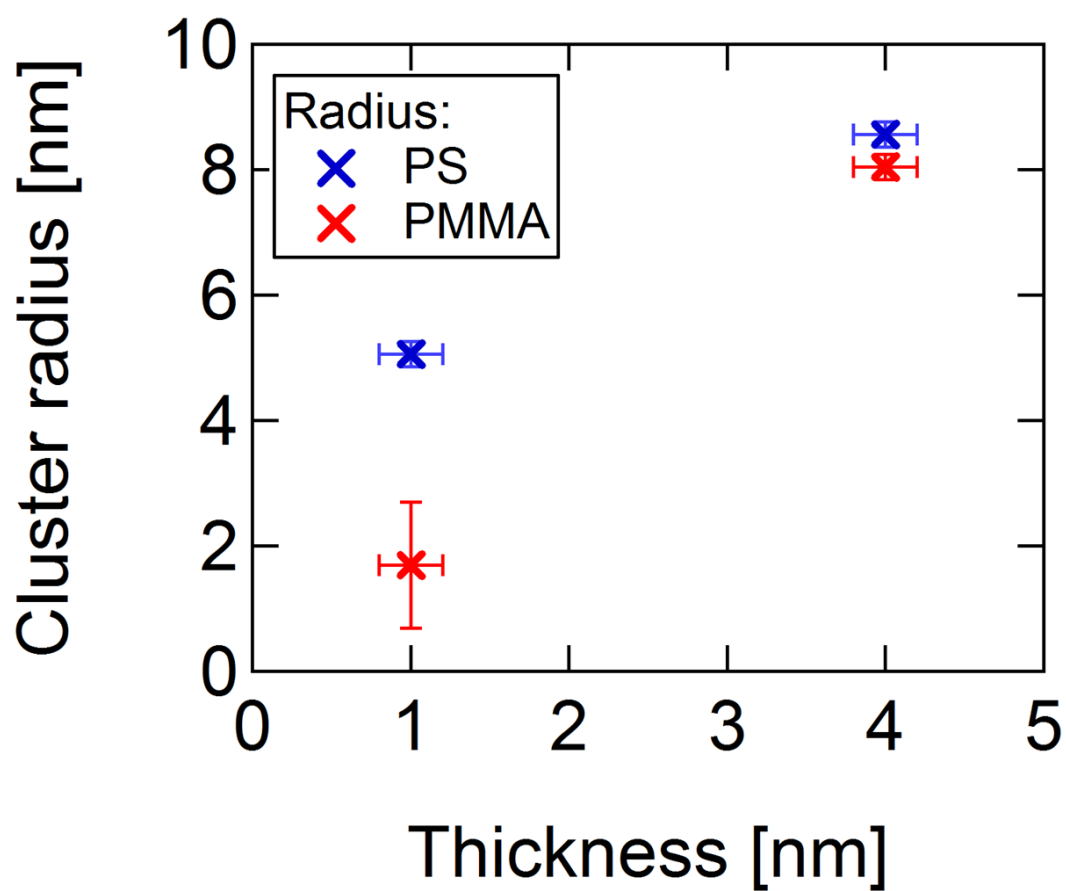


Figure B.1.: Average cluster radii derived from a hemispherical model for 1 and 4 nm of silver thickness on PS (blue symbols) and PMMA (red symbols) derived from static GISAXS pattern. The data was adopted from the Master thesis. [206] Reprinted with permission from [69]. Copyright 2019 American Chemical Society.

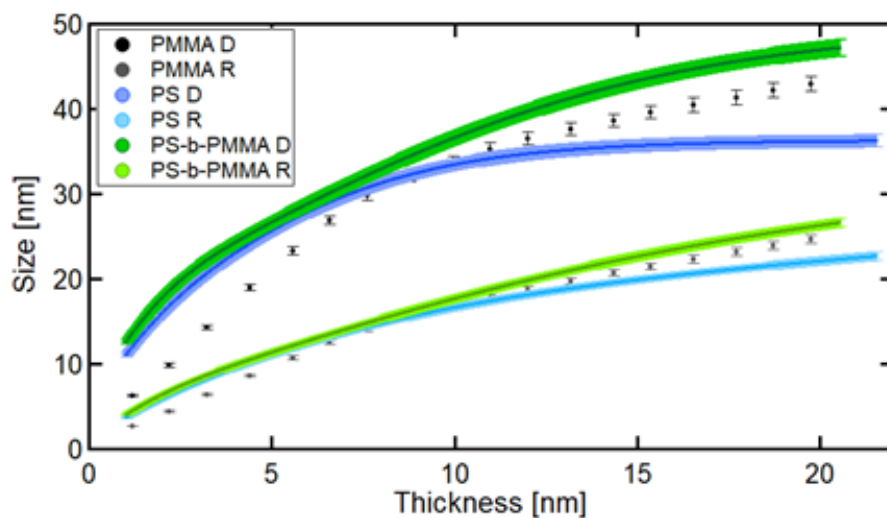


Figure B.2.: Evolution of the mean interparticle distance (D) and the cluster radius (R) of PMMA (black / grey symbols), PS (blue symbols) and PS-b-PMMA (green symbols). The data was adopted from the Master thesis. [206] Reprinted with permission from [69]. Copyright 2019 American Chemical Society.

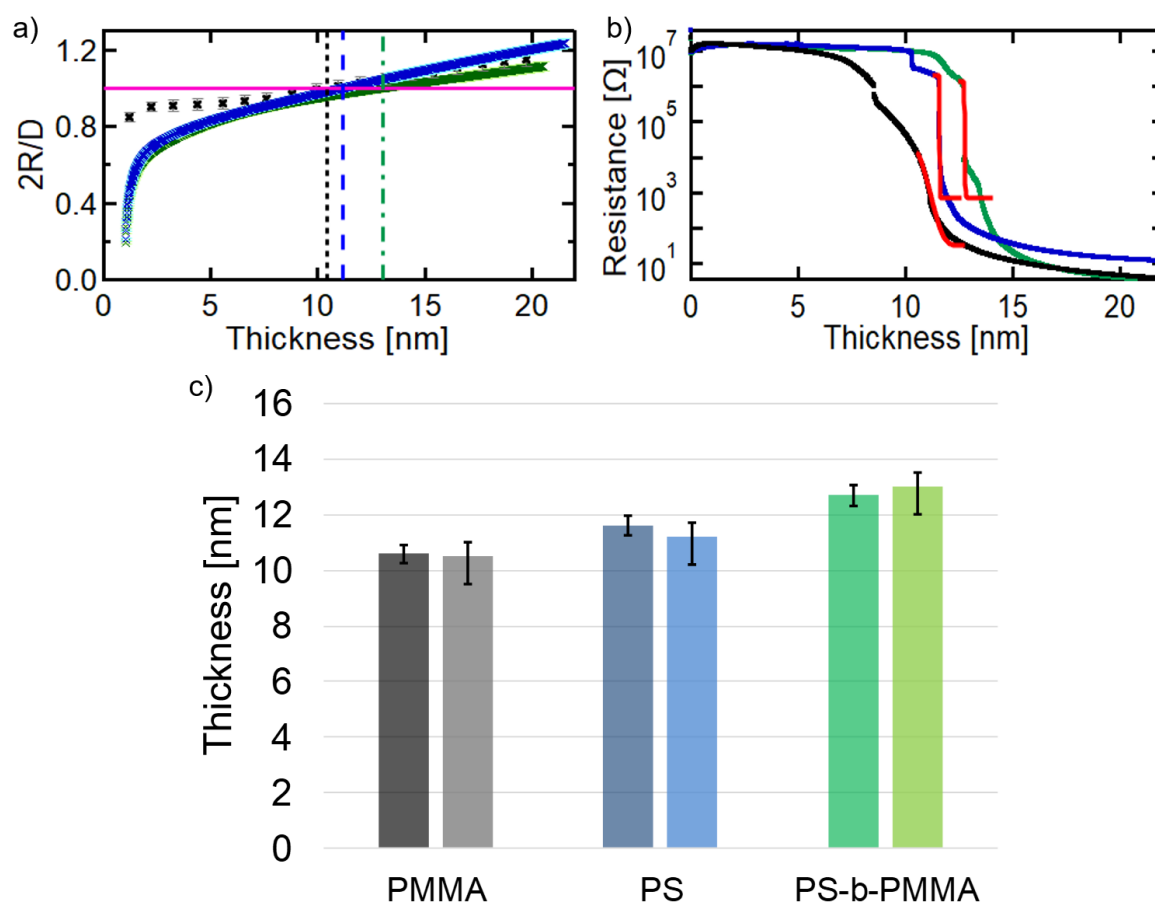


Figure B.3.: a) Evolution of ratio of average cluster diameter ($2R$) over the mean interparticle distance (D) for PMMA (black), PS (blue), PS-b-PMMA (green). When $2R/D$ equals one (pink line) the clusters start to touch each other, which can result in a conductive path. This is indicated by the short-dashed, long-dashed and dash-dotted vertical lines for the PMMA, PS, PS-b-PMMA, respectively. b) *In situ* 2-point resistance measurements during sputter deposition of Ag on PS, PMMA and PS-b-PMMA thin films. The red line is a fit using the Boltzmann sigmoidal fit function in order to determine the percolation threshold for all samples. c) Comparison of the insulator-to-metal transition (IMT) extracted from resistivity measurements and the percolation threshold p from GISAXS on PS, PMMA and PS-b-PMMA. The IMT is given by a black (PMMA), dark blue (PS) and dark green (PS-b-PMMA) column and the percolation threshold with grey (PMMA), light blue (PS) and light green (PS-b-PMMA). The data was adopted from the Master thesis. [206] Reprinted with permission from [69]. Copyright 2019 American Chemical Society.

C. Appendix chapter 7

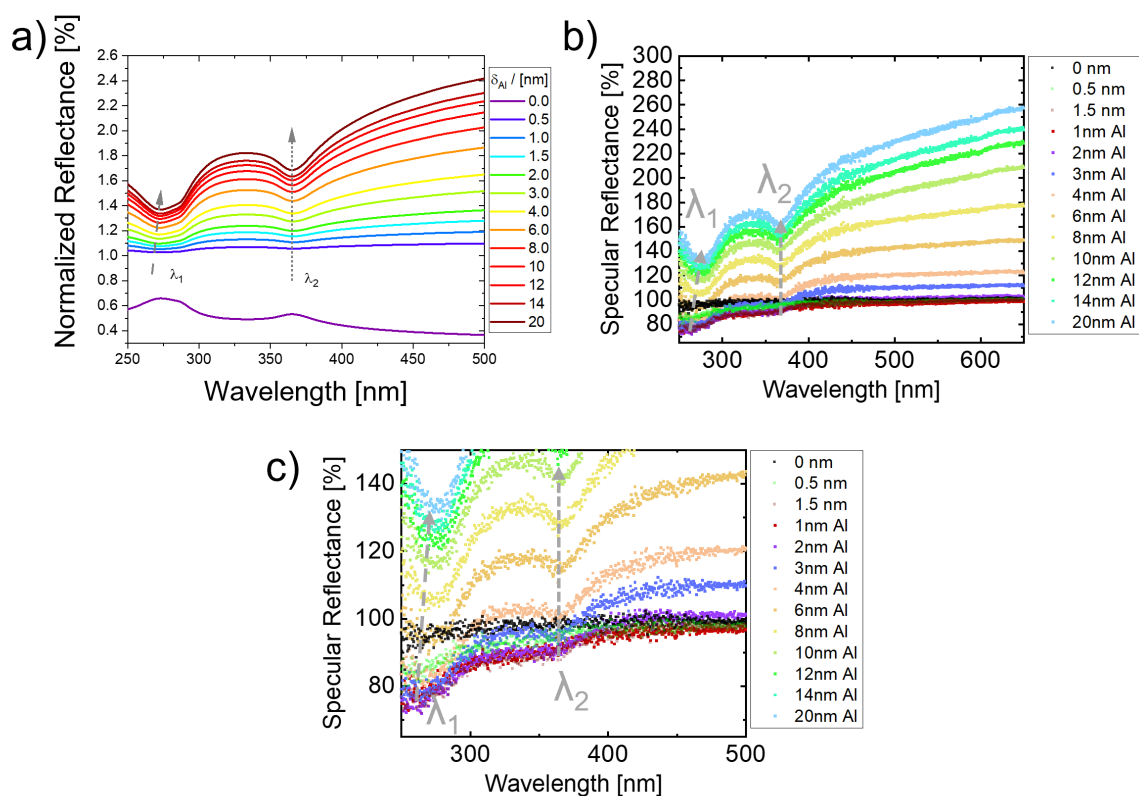


Figure C.1.: a) Simulations of SDRS spectra based on the complex-matrix form of the Fresnel equations of a growing compact (non-granular and non-plasmonic) Al layer on top of 20 nm PMMA/2nm SiO₂/Si substrate at different Al thickness (from 0 to 20 nm). Reflection features λ_1 (dashed grey arrow) and λ_2 (grey dotted arrow) appear at same positions of the template (violet spectra for 0 nm Al) and become pronounced by stratifying the different Al layers on top. b) Specular reflectance full spectra from $\delta_{Al} = 1$ nm to 20 nm. c) Zoom in UV-region of the specular reflectance from b). Reprinted with permission from [71]. Copyright 2021 American Chemical Society.

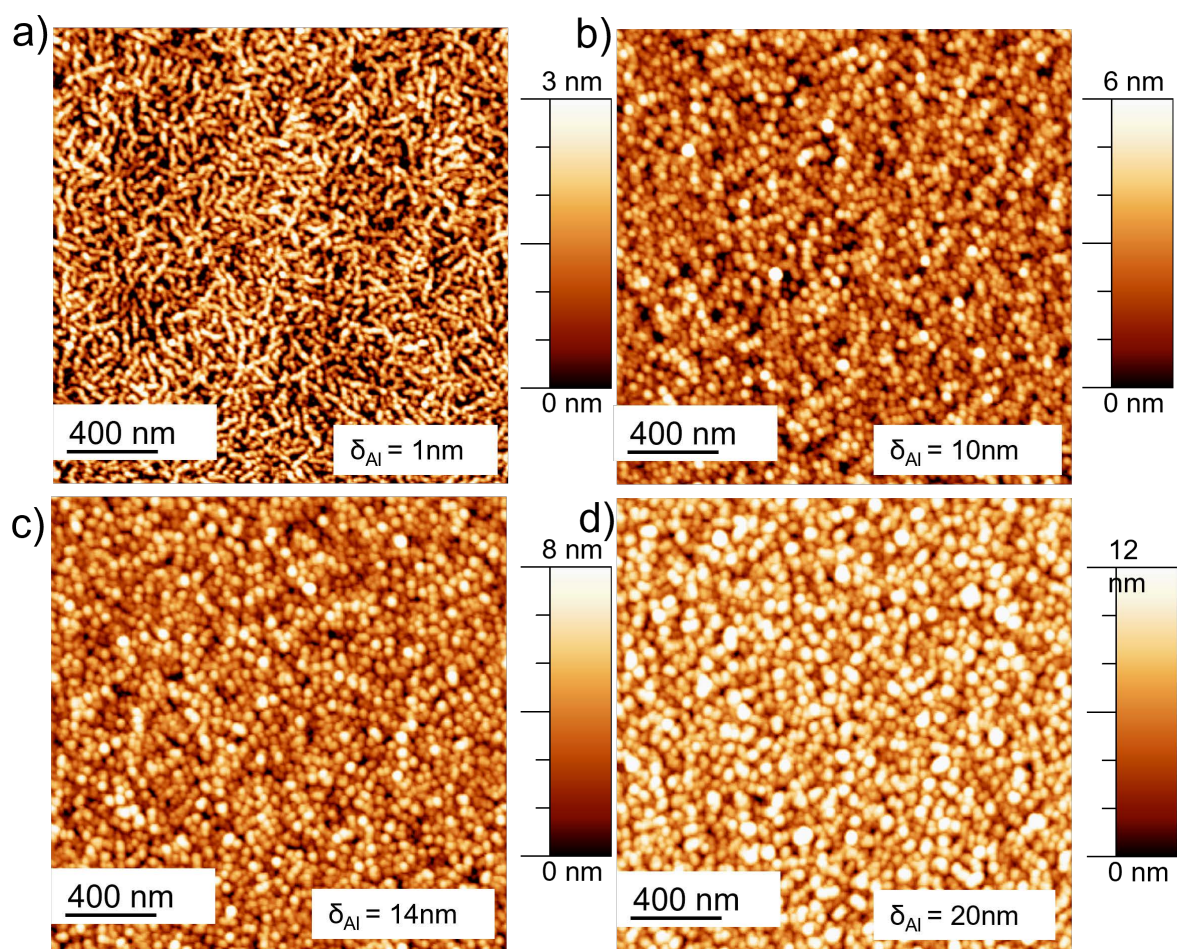


Figure C.2.: AFM height images of PMMA-*b*-P3HT films with sputter deposition of $\delta_{Al} =$ a) 1 nm, b) 10 nm, c) 14 nm and d) 20 nm. Reprinted with permission from [71]. Copyright 2021 American Chemical Society.

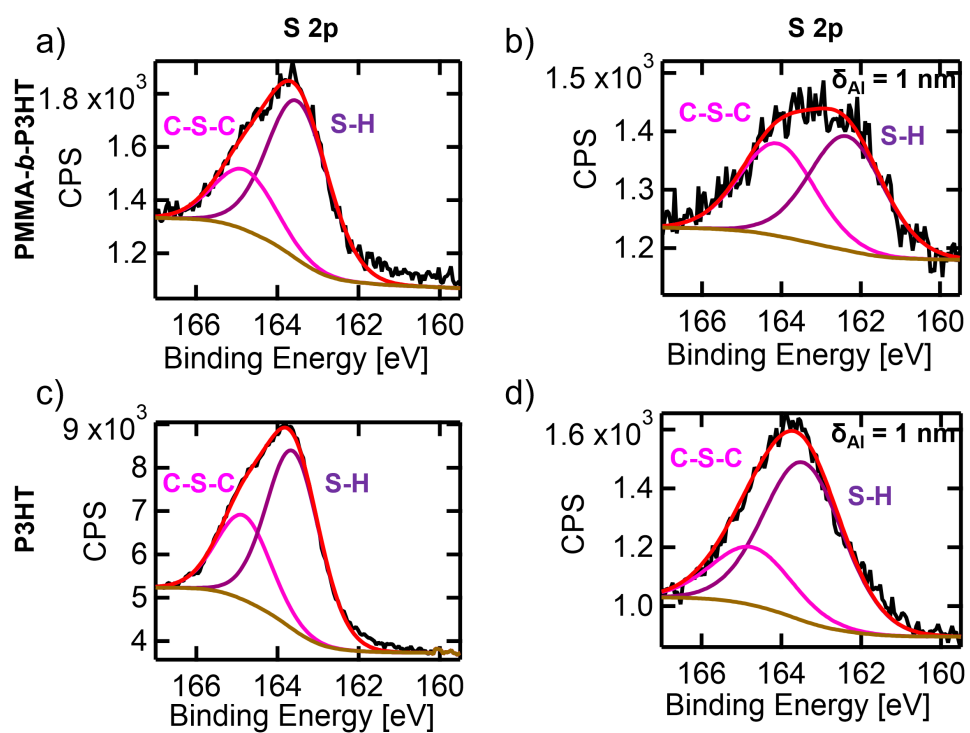


Figure C.3.: XPS spectra at the S 2p edge of a,b) PMMA-*b*-P3HT and c,d) P3HT films before and after sputter deposition of $\delta_{Al} = 1$ nm. Reprinted with permission from [71]. Copyright 2021 American Chemical Society.

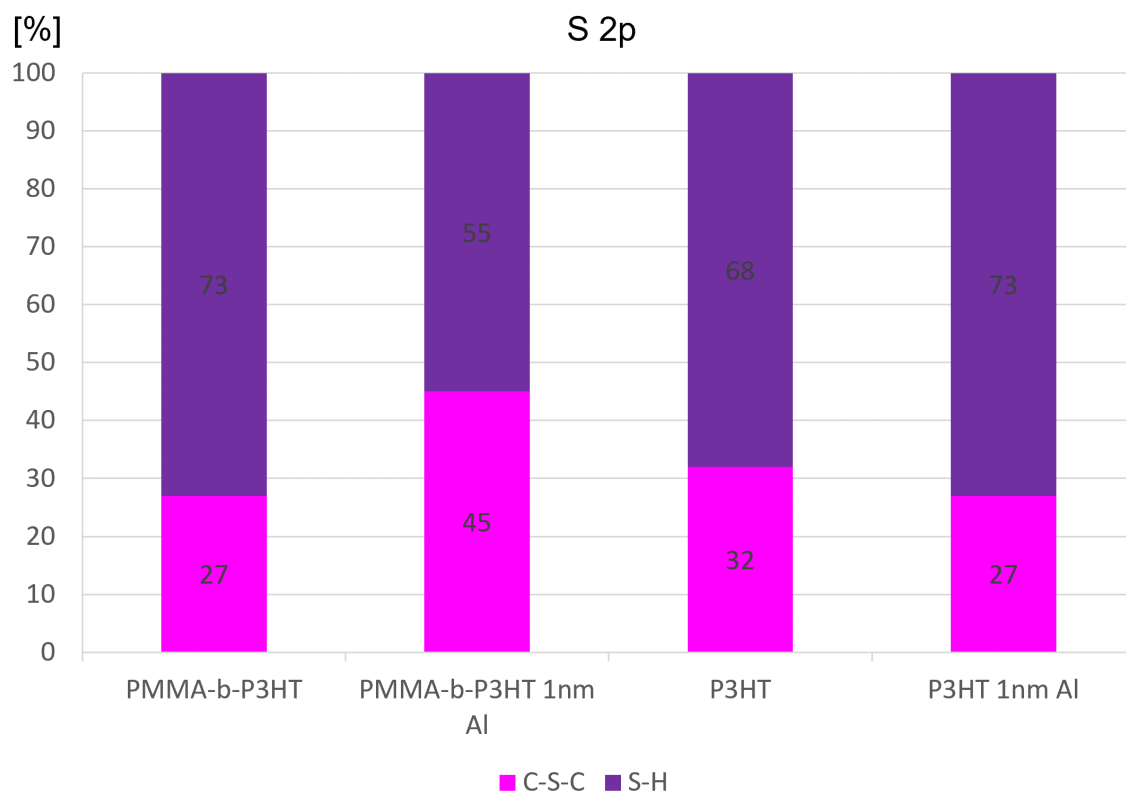


Figure C.4.: Contributions to the XPS spectra measured at the S 2p edge of P3HT and PMMA-*b*-P3HT films before and after sputter deposition of $\delta_{Al} = 1$ nm. Reprinted with permission from [71]. Copyright 2021 American Chemical Society.

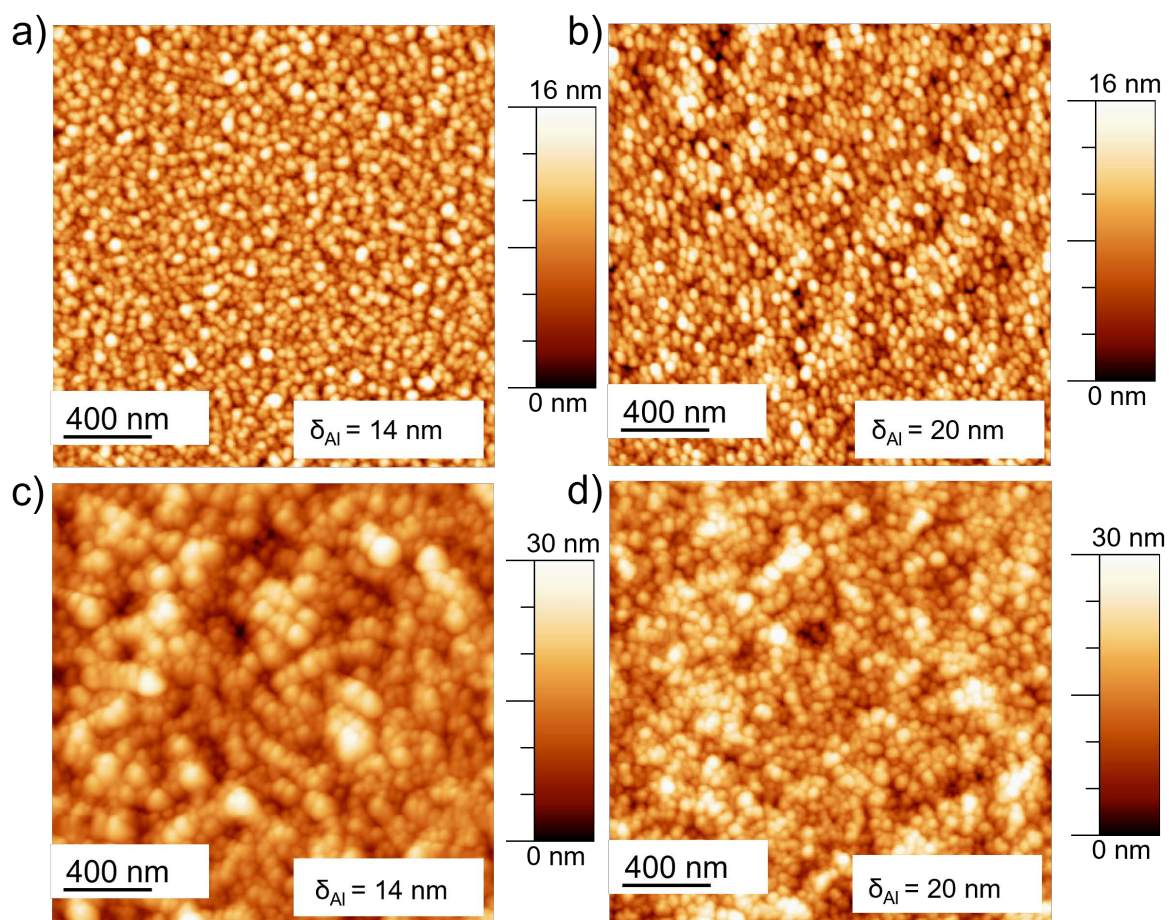


Figure C.5.: AFM topography of a,b) PMMA and c,d) P3HT with a,c) $\delta_{Al} = 14$ nm and b,d) 20 nm. Reprinted with permission from [71]. Copyright 2021 American Chemical Society.

Bibliography

- [1] S. B. Darling, N. A. Yufa, A. L. Cisse, S. D. Bader, and S. J. Sibener, “Self-Organization of FePt Nanoparticles on Photochemically Modified Diblock Copolymer Templates,” *Advanced Materials*, vol. 17, no. 20, pp. 2446–2450, 2005.
- [2] W. Cao, S. Xia, X. Jiang, M. Appold, M. Opel, M. Plank, R. Schaffrinna, L. P. Kreuzer, S. Yin, M. Gallei, M. Schwartzkopf, S. V. Roth, and P. Müller-Buschbaum, “Self-assembly of large magnetic nanoparticles in ultrahigh molecular weight linear diblock copolymer films,” *ACS Applied Materials & Interfaces*, vol. 12, pp. 7557–7564, jan 2020.
- [3] V. Suresh, M. S. Huang, M. Srinivasan, and S. Krishnamoorthy, “In situ synthesis of high density sub-50 nm ZnO nanopatterned arrays using diblock copolymer templates,” *ACS Applied Materials & Interfaces*, vol. 5, pp. 5727–5732, jun 2013.
- [4] W. A. Lopes and H. M. Jaeger, “Hierarchical self-assembly of metal nanostructures on diblock copolymer scaffolds,” *Nature*, vol. 414, pp. 735–738, 2001.
- [5] D. J. Erb, K. Schlage, and R. Röhlberger, “Uniform metal nanostructures with long-range order via three-step hierarchical self-assembly,” *Science Advances*, vol. 1, pp. 1–8, nov 2015.
- [6] P. Mansky, P. Haikin, and E. L. Thomas, “Monolayer films of diblock copolymer microdomains for nanolithographic applications,” *Journal of Materials Science*, vol. 30, no. 8, pp. 1987–1992, 1995.
- [7] P. Mansky, C. K. Harrison, P. M. Chaikin, R. A. Register, and N. Yao, “Nanolithographic templates from diblock copolymer thin films,” *Applied Physics Letters*, vol. 68, pp. 2586–2588, apr 1996.
- [8] C. Black and R. Ruiz, “Self assembly in semiconductor microelectronics: self-aligned sub-lithographic patterning using diblock copolymer thin films,” mar 2006.
- [9] T. F. Kuech and L. J. Mawst, “Nanofabrication of III–V semiconductors employing diblock copolymer lithography,” *Journal of Physics D: Applied Physics*, vol. 43, p. 183001, apr 2010.

- [10] A. Bergfelt, G. Hernández, R. Mogensen, M. J. Lacey, J. Mindemark, D. Brandell, and T. M. Bowden, “Mechanically robust yet highly conductive diblock copolymer solid polymer electrolyte for ambient temperature battery applications,” *ACS Applied Polymer Materials*, vol. 2, pp. 939–948, jan 2020.
- [11] J. Sun, X. Chen, J. Wei, L. Yan, and X. Jing, “Application of the biodegradable diblock copolymer poly(l-lactide)-block-poly(l-cysteine): Drug delivery and protein conjugation,” *Journal of Applied Polymer Science*, pp. n/a–n/a, jun 2010.
- [12] H. Kim, J. Choi, Z. Lingley, M. Brodie, Y. Sin, T. F. Kuech, P. Gopalan, and L. J. Mawst, “Selective growth of strained (in)GaAs quantum dots on GaAs substrates employing diblock copolymer lithography nanopatterning,” *Journal of Crystal Growth*, vol. 465, pp. 48–54, may 2017.
- [13] Y. S. Jung, W. Jung, H. L. Tuller, and C. A. Ross, “Nanowire conductive polymer gas sensor patterned using self-assembled block copolymer lithography,” *Nano Letters*, vol. 8, pp. 3776–3780, oct 2008.
- [14] V. D. Mitchell and D. J. Jones, “Advances toward the effective use of block copolymers as organic photovoltaic active layers,” *Polymer Chemistry*, vol. 9, no. 7, pp. 795–814, 2018.
- [15] P. D. Topham, A. J. Parnell, and R. C. Hiorns, “Block copolymer strategies for solar cell technology,” *Journal of Polymer Science Part B: Polymer Physics*, vol. 49, pp. 1131–1156, jun 2011.
- [16] I. Hamley, “Ordering in thin films of block copolymers: Fundamentals to potential applications,” *Progress in Polymer Science*, vol. 34, pp. 1161–1210, nov 2009.
- [17] F. Faupel, V. Zaporozhchenko, T. Strunskus, and M. Elbahri, “Metal-polymer nanocomposites for functional applications,” *Advanced Engineering Materials*, vol. 12, pp. 1177–1190, nov 2010.
- [18] X. Huang, P. Jiang, and L. Xie, “Ferroelectric polymer/silver nanocomposites with high dielectric constant and high thermal conductivity,” *Applied Physics Letters*, vol. 95, no. 24, pp. 1–4, 2009.
- [19] E. Stratakis and E. Kymakis, “Nanoparticle-based plasmonic organic photovoltaic devices,” *Materials Today*, vol. 16, no. 4, pp. 133–146, 2013.
- [20] J.-Y. Lee, C.-J. Lin, C.-T. Lo, J.-C. Tsai, and W.-C. Chen, “Synthesis, morphology, and field-effect transistor characteristics of crystalline diblock copolymers consisted of poly(3-hexylthiophene) and syndiotactic polypropylene,” *Macromolecules*, vol. 46, pp. 3005–3014, apr 2013.

- [21] J. Li, Y. Tao, S. Chen, H. Li, P. Chen, M. Z. Wei, H. Wang, K. Li, M. Mazzeo, and Y. Duan, "A flexible plasma-treated silver-nanowire electrode for organic light-emitting devices," *Scientific Reports*, vol. 7, no. 16468, pp. 1–9, 2017.
- [22] S. Roh, T. Chung, and B. Lee, "Overview of the characteristics of micro- and nano-structured surface plasmon resonance sensors," *Sensors*, vol. 11, no. 2, pp. 1565–1588, 2011.
- [23] E. Petryayeva and U. J. Krull, "Localized surface plasmon resonance: Nanostructures, bioassays and biosensing — a review," *Analytica Chimica Acta*, vol. 706, pp. 8–24, nov 2011.
- [24] C.-Y. Chang, H.-T. Lin, M.-S. Lai, T.-Y. Shieh, C.-C. Peng, M.-H. Shih, and Y.-C. Tung, "Flexible localized surface plasmon resonance sensor with metal–insulator–metal nanodisks on PDMS substrate," *Scientific Reports*, vol. 8, aug 2018.
- [25] H. Hoppe and N. S. Sariciftci, "Organic solar cells: An overview," *Journal of Materials Research*, vol. 19, no. 7, pp. 1924–1945, 2004.
- [26] M. Westphalen, U. Kreibig, J. Rostalski, H. Lüth, and D. Meissner, "Metal cluster enhanced organic solar cells," *Solar Energy Materials and Solar Cells*, vol. 61, no. 1, pp. 97–105, 2000.
- [27] F. Faupel, A. Thran, V. Zaporozhchenko, M. Kiene, T. Strunskus, and K. Behnke, "Nucleation, growth, interdiffusion, and adhesion of metal films on polymers," *AIP Conference Proceedings*, vol. 491, no. 1999, pp. 201–216, 1999.
- [28] J. Meyer, P. Görrn, F. Bertram, S. Hamwi, T. Winkler, H.-H. Johannes, T. Weimann, P. Hinze, T. Riedl, and W. Kowalsky, "Al₂O₃/ZrO₂ nanolaminates as ultrahigh gas-diffusion barriers—a strategy for reliable encapsulation of organic electronics," *Advanced Materials*, vol. 21, pp. 1845–1849, may 2009.
- [29] J. C. Scott, "Metal–organic interface and charge injection in organic electronic devices," *Journal of Vacuum Science & Technology A: Vacuum, Surfaces, and Films*, vol. 21, pp. 521–531, may 2003.
- [30] B. Cao, X. He, C. R. Fetterly, B. C. Olsen, E. J. Luber, and J. M. Buriak, "Role of interfacial layers in organic solar cells: Energy level pinning versus phase segregation," *ACS Applied Materials & Interfaces*, vol. 8, pp. 18238–18248, jun 2016.
- [31] M. Kim, D. K. Brown, and O. Brand, "Nanofabrication for all-soft and high-density electronic devices based on liquid metal," *Nature Communications*, vol. 11, feb 2020.
- [32] M. D. M. Faure and B. H. Lessard, "Layer-by-layer fabrication of organic photovoltaic devices: material selection and processing conditions," *Journal of Materials Chemistry C*, vol. 9, no. 1, pp. 14–40, 2021.

- [33] P. Friederich, A. Fediai, S. Kaiser, M. Konrad, N. Jung, and W. Wenzel, “Toward design of novel materials for organic electronics,” *Advanced Materials*, vol. 31, p. 1808256, apr 2019.
- [34] S. Choulis, V.-E. Choong, A. Patwardhan, M. Mathai, and F. So, “Interface modification to improve hole-injection properties in organic electronic devices,” *Advanced Functional Materials*, vol. 16, pp. 1075–1080, may 2006.
- [35] M. Rothschild, A. R. Forte, R. R. Kunz, S. C. Palmateer, and J. H. C. Sedlacek, “Lithography at a wavelength of 193 nm,” *IBM Journal of Research and Development*, vol. 41, pp. 49–55, jan 1997.
- [36] L. Sun, G. Yuan, L. Gao, J. Yang, M. Chhowalla, M. H. Gharahcheshmeh, K. K. Gleason, Y. S. Choi, B. H. Hong, and Z. Liu, “Chemical vapour deposition,” *Nature Reviews Methods Primers*, vol. 1, jan 2021.
- [37] A. Baptista, F. Silva, J. Porteiro, J. Míguez, G. Pinto, and L. Fernandes, “On the physical vapour deposition (PVD): Evolution of magnetron sputtering processes for industrial applications,” *Procedia Manufacturing*, vol. 17, pp. 746–757, 2018.
- [38] B. A. Joyce, “Molecular beam epitaxy,” *Reports on Progress in Physics*, vol. 48, pp. 1637–1697, dec 1985.
- [39] K. K. Maniam and S. Paul, “A review on the electrodeposition of aluminum and aluminum alloys in ionic liquids,” *Coatings*, vol. 11, p. 80, jan 2021.
- [40] M. Toofan and J. Toofan, *A Brief Review of the Cleaning Process for Electronic Device Fabrication*. Elsevier, 2015.
- [41] Y. Tada, S. Akasaka, H. Yoshida, H. Hasegawa, E. Dobisz, D. Kercher, and M. Takenaka, “Directed self-assembly of diblock copolymer thin films on chemically-patterned substrates for defect-free nano-patterning,” *Macromolecules*, vol. 41, pp. 9267–9276, nov 2008.
- [42] H.-W. Li and W. T. S. Huck, “Ordered block-copolymer assembly using nanoimprint lithography,” *Nano Letters*, vol. 4, pp. 1633–1636, aug 2004.
- [43] Y. S. Jung and C. A. Ross, “Orientation-controlled self-assembled nanolithography using a polystyrene-polydimethylsiloxane block copolymer,” *Nano Letters*, vol. 7, pp. 2046–2050, jun 2007.
- [44] C. M. Bates, M. J. Maher, D. W. Janes, C. J. Ellison, and C. G. Willson, “Block copolymer lithography,” *Macromolecules*, vol. 47, pp. 2–12, nov 2013.
- [45] J. Garnier, J. Arias-Zapata, O. Marconot, S. Arnaud, S. Böhme, C. Girardot, D. Buttard, and M. Zelsmann, “Sub-10 nm silicon nanopillar fabrication using fast and brushless thermal assembly of PS-b-PDMS diblock copolymer,” *ACS Applied Materials & Interfaces*, vol. 8, pp. 9954–9960, apr 2016.

- [46] J. Park, A. Khandekar, S. Park, L. Mawst, T. Kuech, and P. Nealey, "Selective MOCVD growth of single-crystal dense GaAs quantum dot array using cylinder-forming diblock copolymers," *Journal of Crystal Growth*, vol. 297, pp. 283–288, dec 2006.
- [47] D. Yu, Y.-Q. Yang, Z. Chen, Y. Tao, and Y.-F. Liu, "Recent progress on thin-film encapsulation technologies for organic electronic devices," *Optics Communications*, vol. 362, pp. 43–49, mar 2016.
- [48] G. Kaune, M. A. Ruderer, E. Metwalli, W. Wang, S. Couet, K. Schlage, R. Röhlberger, S. V. Roth, and P. Müller-Buschbaum, "In Situ GISAXS Study of Gold Film Growth on Conducting Polymer Films," *ACS Applied Materials and Interfaces*, vol. 1, no. 2, pp. 353–360, 2009.
- [49] M. Volmer and A. Weber, "Keimbildung in übersättigten gebilden," *Zeitschrift für Physikalische Chemie*, vol. 119, no. 1, pp. 277–301, 1926.
- [50] M. Y. Paik, J. K. Bosworth, D.-M. Smilges, E. L. Schwartz, X. Andre, and C. K. Ober, "Reversible morphology control in block copolymer films via solvent vapor processing: An in situ GISAXS study," *Macromolecules*, vol. 43, pp. 4253–4260, apr 2010.
- [51] X. Gu, I. Gunkel, A. Hexemer, and T. P. Russell, "Controlling domain spacing and grain size in cylindrical block copolymer thin films by means of thermal and solvent vapor annealing," *Macromolecules*, vol. 49, pp. 3373–3381, apr 2016.
- [52] K. Kim, S. Park, Y. Kim, J. Bang, C. Park, and D. Y. Ryu, "Optimized solvent vapor annealing for long-range perpendicular lamellae in PS-b-PMMA films," *Macromolecules*, vol. 49, pp. 1722–1730, feb 2016.
- [53] I. Botiz and S. B. Darling, "Self-assembly of poly(3-hexylthiophene)-block-poly lactide block copolymer and subsequent incorporation of electron acceptor material," *Macromolecules*, vol. 42, no. 21, pp. 8211–8217, 2009.
- [54] F. C. Löhner, V. Körstgens, G. Semino, M. Schwartzkopf, A. Hinz, O. Polonskyi, T. Strunskus, F. Faupel, S. V. Roth, and P. Müller-Buschbaum, "Following in Situ the Deposition of Gold Electrodes on Low Band Gap Polymer Films," *ACS Applied Materials and Interfaces*, vol. 12, pp. 1132–1141, jan 2020.
- [55] H. Yu, S. Ho, N. Barange, R. Larrabee, and F. So, "Semi-transparent vertical organic light-emitting transistors," *Organic Electronics*, vol. 55, pp. 126–132, apr 2018.
- [56] C. an Di, G. Yu, Y. Liu, X. Xu, D. Wei, Y. Song, Y. Sun, Y. Wang, D. Zhu, J. Liu, X. Liu, and D. Wu, "High-performance low-cost organic field-effect transistors with chemically modified bottom electrodes," *Journal of the American Chemical Society*, vol. 128, pp. 16418–16419, nov 2006.

- [57] G. Santoro, S. Yu, M. Schwartzkopf, P. Zhang, S. Koyiloth Vayalil, J. F. H. Risch, M. A. Rübhausen, M. Hernández, C. Domingo, and S. V. Roth, “Silver substrates for surface enhanced Raman scattering: Correlation between nanostructure and Raman scattering enhancement,” *Applied Physics Letters*, vol. 104, p. 243107, 2014.
- [58] B.-H. Jiang, H.-E. Lee, J.-H. Lu, T.-H. Tsai, T.-S. Shieh, R.-J. Jeng, and C.-P. Chen, “High-performance semitransparent organic photovoltaics featuring a surface phase-matched transmission-enhancing ag/ITO electrode,” *ACS Applied Materials & Interfaces*, vol. 12, pp. 39496–39504, aug 2020.
- [59] C. Schuster, H. Rennhofer, H. Amenitsch, H. C. Lichtenegger, A. Jungbauer, and R. Tscheliessing, “Metal–Insulator Transition of Ultrathin Sputtered Metals on Phenolic Resin Thin Films: Growth Morphology and Relations to Surface Free Energy and Reactivity,” *Nanomaterials*, vol. 11, p. 589, feb 2021.
- [60] G. Xue, Q. Dai, and S. Jiang, “Chemical Reactions of Imidazole with Metallic Silver Studied by the Use of SERS and XPS Techniques,” *Journal of the American Chemical Society*, vol. 110, no. 8, pp. 2393–2395, 1988.
- [61] A. Iwan, M. Palewicz, M. Ozimek, A. Chuchmala, and G. Pasciak, “Influence of aluminium electrode preparation on PCE values of polymeric solar cells based on P3HT and PCBM,” *Organic Electronics*, vol. 13, pp. 2525–2531, nov 2012.
- [62] M. S. Kumar and K. Balachander, “Performance analysis of different top metal electrodes in inverted polymer solar cells,” *Optik*, vol. 127, pp. 2725–2731, mar 2016.
- [63] M. Schwartzkopf, G. Santoro, C. J. Brett, A. Rothkirch, O. Polonskyi, A. Hinz, E. Metwalli, Y. Yao, T. Strunskus, F. Faupel, P. Müller-Buschbaum, and S. V. Roth, “Real-Time Monitoring of Morphology and Optical Properties during Sputter Deposition for Tailoring Metal-Polymer Interfaces,” *ACS Applied Materials and Interfaces*, vol. 7, no. 24, pp. 13547–13556, 2015.
- [64] S. V. Roth, G. Santoro, J. F. H. Risch, S. Yu, M. Schwartzkopf, T. Boese, R. Döhrmann, P. Zhang, B. Besner, P. Bremer, D. Rukser, M. A. Rübhausen, N. J. Terrill, P. A. Staniec, Y. Yao, E. Metwalli, and P. Müller-Buschbaum, “Patterned Diblock Co-Polymer Thin Films as Templates for Advanced Anisotropic Metal Nanostructures,” *ACS Applied Materials and Interfaces*, vol. 7, pp. 12470–12477, jun 2015.
- [65] B. A. Collins, J. R. Tumbleston, and H. Ade, “Miscibility, crystallinity, and phase development in P3HT/PCBM solar cells: Toward an enlightened understanding of device morphology and stability,” *Journal of Physical Chemistry Letters*, vol. 2, no. 24, pp. 3135–3145, 2011.

- [66] H. Wang, H. Y. Wang, B. R. Gao, L. Wang, Z. Y. Yang, X. B. Du, Q. D. Chen, J. F. Song, and H. B. Sun, "Exciton diffusion and charge transfer dynamics in nano phase-separated P3HT/PCBM blend films," *Nanoscale*, vol. 3, no. 5, pp. 2280–2285, 2011.
- [67] P. E. Shaw, A. Ruseckas, and I. D. Samuel, "Exciton diffusion measurements in poly(3-hexylthiophene)," *Advanced Materials*, vol. 20, no. 18, pp. 3516–3520, 2008.
- [68] M. Sim, J. Shin, C. Shim, M. Kim, S. B. Jo, J. H. Kim, and K. Cho, "Dependence of exciton diffusion length on crystalline order in conjugated polymers," *Journal of Physical Chemistry C*, vol. 118, no. 2, pp. 760–766, 2014.
- [69] M. Gensch, M. Schwartzkopf, W. Ohm, C. J. Brett, P. Pandit, S. K. Vayalil, L. Bießmann, L. P. Kreuzer, J. Drewes, O. Polonskyi, T. Strunskus, F. Faupel, A. Stierle, P. Müller-Buschbaum, and S. V. Roth, "Correlating Nanostructure, Optical and Electronic Properties of Nanogranular Silver Layers during Polymer-Template-Assisted Sputter Deposition," *ACS Applied Materials and Interfaces*, vol. 11, no. 32, pp. 29416–29426, 2019.
- [70] M. Gensch, M. Schwartzkopf, C. J. Brett, S. J. Schaper, L. P. Kreuzer, N. Li, W. Chen, S. Liang, J. Drewes, O. Polonskyi, T. Strunskus, F. Faupel, P. Müller-Buschbaum, and S. V. Roth, "Selective Silver Nanocluster Metallization on Conjugated Diblock Copolymer Templates for Sensing and Photovoltaic Applications," *ACS Applied Nano Materials*, vol. 4, no. 4, pp. 4245–4255, 2021.
- [71] M. Gensch, M. Schwartzkopf, C. J. Brett, S. J. Schaper, N. Li, W. Chen, S. Liang, J. Drewes, O. Polonskyi, T. Strunskus, F. Faupel, P. Müller-Buschbaum, and S. V. Roth, "Correlating optical reflectance with the topology of aluminum nanocluster layers growing on partially conjugated diblock copolymer templates," *ACS Applied Materials & Interfaces*, vol. 13, pp. 56663–56673, nov 2021.
- [72] G. Strobl, *The Physics of Polymers*. Springer-Verlag: Berlin Heidelberg, 2007.
- [73] M. W. Matsen and F. S. Bates, "Origins of Complex Self-Assembly in Block Copolymers," *Macromolecules*, vol. 29, no. 23, pp. 7641–7644, 1996.
- [74] F. S. Bates and G. H. Fredrickson, "Block copolymer thermodynamics: Theory and experiment," *Annual Review of Physical Chemistry*, vol. 41, pp. 525–557, oct 1990.
- [75] M. W. Matsen and F. S. Bates, "Block copolymer microstructures in the intermediate-segregation regime," *The Journal of Chemical Physics*, vol. 106, no. 6, pp. 2436–2448, 1997.
- [76] D. B. Hall, P. Underhill, and J. M. Torkelson, "Spin coating of thin and ultrathin polymer films," *Polymer Engineering & Science*, vol. 38, pp. 2039–2045, dec 1998.

- [77] C. J. Brett, N. Mittal, W. Ohm, M. Gensch, L. P. Kreuzer, V. Körstgens, M. Månsson, H. Frielinghaus, P. Müller-Buschbaum, L. D. Söderberg, and S. V. Roth, “Water-induced structural rearrangements on the nanoscale in ultrathin nanocellulose films,” *Macromolecules*, vol. 52, pp. 4721–4728, jun 2019.
- [78] F. Liu, S. Ferdous, E. Schaible, A. Hexemer, M. Church, X. Ding, C. Wang, and T. P. Russell, “Fast printing and in situ morphology observation of organic photovoltaics using slot-die coating,” *Advanced Materials*, vol. 27, no. 5, pp. 886–891, 2014.
- [79] S. Roland, R. E. Prud’homme, and C. G. Bazuin, “Morphology, thickness, and composition evolution in supramolecular block copolymer films over a wide range of dip-coating rates,” *ACS Macro Letters*, vol. 1, no. 8, pp. 973–976, 2012.
- [80] M. Li, K. Douki, K. Goto, X. Li, C. Coenjarts, D. M. Smilgies, and C. K. Ober, “Spatially controlled fabrication of nanoporous block copolymers,” *Chemistry of Materials*, vol. 16, pp. 3800–3808, sep 2004.
- [81] T. Wang, N. W. Scarratt, H. Yi, A. D. F. Dunbar, A. J. Pearson, D. C. Watters, T. S. Glen, A. C. Brook, J. Kingsley, A. R. Buckley, M. W. A. Skoda, A. M. Donald, R. A. L. Jones, A. Iraqi, and D. G. Lidzey, “Fabricating high performance, donor-acceptor copolymer solar cells by spray-coating in air,” *Advanced Energy Materials*, vol. 3, pp. 505–512, feb 2013.
- [82] M. Helgesen, J. E. Carlé, and F. C. Krebs, “Slot-die coating of a high performance copolymer in a readily scalable roll process for polymer solar cells,” *Advanced Energy Materials*, vol. 3, pp. 1664–1669, aug 2013.
- [83] H. J. Angerman, A. Johner, and A. N. Semenov, “Microphase separation in thin block copolymer films: A weak segregation mean-field approach,” *Macromolecules*, vol. 39, pp. 6210–6220, aug 2006.
- [84] M. W. Matsen and M. Schick, “Microphase separation in starblock copolymer melts,” *Macromolecules*, vol. 27, pp. 6761–6767, nov 1994.
- [85] R. Cherrabi, A. Saout-Elhak, M. Benhamou, and M. Daoud, “Phase separation in confined polymer blends,” *The Journal of Chemical Physics*, vol. 111, pp. 8174–8181, nov 1999.
- [86] H. J. Angerman and G. ten Brinke, “Weak segregation theory of microphase separation in associating binary homopolymer blends,” *Macromolecules*, vol. 32, pp. 6813–6820, sep 1999.
- [87] M. W. Matsen and M. Schick, “Stable and unstable phases of a diblock copolymer melt,” *Physical Review Letters*, vol. 72, pp. 2660–2663, apr 1994.
- [88] F. S. Bates and G. H. Fredrickson, “Block copolymers designer soft materials,” *Physics Today*, vol. 52, pp. 32–38, feb 1999.

- [89] A. K. Khandpur, S. Foerster, F. S. Bates, I. W. Hamley, A. J. Ryan, W. Bras, K. Almdal, and K. Mortensen, "Polyisoprene-polystyrene diblock copolymer phase diagram near the order-disorder transition," *Macromolecules*, vol. 28, pp. 8796–8806, dec 1995.
- [90] J. N. Albert and T. H. Epps, "Self-assembly of block copolymer thin films," *Materials Today*, vol. 13, pp. 24–33, jun 2010.
- [91] T. L. Morkved and H. M. Jaeger, "Thickness-induced morphology changes in lamellar diblock copolymer ultrathin films," *Europhysics Letters (EPL)*, vol. 40, pp. 643–648, dec 1997.
- [92] M. J. Fasolka and A. M. Mayes, "Block copolymer thin films: Physics and applications," *Annual Review of Materials Research*, vol. 31, pp. 323–355, aug 2001.
- [93] C. K. Chiang, C. R. Fincher, Y. W. Park, A. J. Heeger, H. Shirakawa, E. J. Louis, S. C. Gau, and A. G. MacDiarmid, "Electrical conductivity in doped polyacetylene," *Physical Review Letters*, vol. 39, pp. 1098–1101, oct 1977.
- [94] T. Skotheim and J. Reynolds, *Conjugated Polymers: Theory, Synthesis, Properties, and Characterization*. CRC Press, 3rd ed., Dec. 2006.
- [95] R. S. Mulliken, "Electronic population analysis on LCAO–MO molecular wave functions. i," *The Journal of Chemical Physics*, vol. 23, pp. 1833–1840, oct 1955.
- [96] J. E. Lennard-Jones, "The electronic structure of some diatomic molecules," *Transactions of the Faraday Society*, vol. 25, p. 668, 1929.
- [97] J. Pople A. and D. L. Beveridge, *Approximate molecular orbital theory*. New York Maidenhead: McGraw-Hill, 1972.
- [98] C. Janiak, H.-J. Meyer, D. Gudat, and P. Kurz, *Riedel Moderne Anorganische Chemie*. De Gruyter, may 2018.
- [99] S. A. Holgate, *Understanding Solid State Physics*. CRC Press, apr 2021.
- [100] M. Pope, *Electronic Processes in Organic Crystals and Polymers*. Oxford University Press, 2nd ed., 1999.
- [101] S. Chu, Y. Wang, C. Wang, J. Yang, and Z. Zou, "Bandgap modulation of polyimide photocatalyst for optimum h₂ production activity under visible light irradiation," *International Journal of Hydrogen Energy*, vol. 38, pp. 10768–10772, aug 2013.
- [102] H. van Mullekom, J.A.J.M.Vekemans, E.E.Havinga, and E.W.Meijer, "Developments in the chemistry and band gap engineering of donor–acceptor substituted conjugated polymers," *Materials Science and Engineering: R: Reports*, vol. 32, pp. 1–40, feb 2001.

- [103] A. V. Tunc, A. D. Sio, D. Riedel, F. Deschler, E. D. Como, J. Parisi, and E. von Hauff, "Molecular doping of low-bandgap-polymer:fullerene solar cells: Effects on transport and solar cells," *Organic Electronics*, vol. 13, pp. 290–296, feb 2012.
- [104] T.-A. Chen and R. D. Rieke, "Polyalkylthiophenes with the smallest bandgap and the highest intrinsic conductivity," *Synthetic Metals*, vol. 60, pp. 175–177, sep 1993.
- [105] S.-H. Liao, H.-J. Jhuo, Y.-S. Cheng, and S.-A. Chen, "Fullerene derivative-doped zinc oxide nanofilm as the cathode of inverted polymer solar cells with low-bandgap polymer (PTB7-th) for high performance," *Advanced Materials*, vol. 25, pp. 4766–4771, aug 2013.
- [106] Q. An, F. Zhang, L. Li, J. Wang, J. Zhang, L. Zhou, and W. Tang, "Improved efficiency of bulk heterojunction polymer solar cells by doping low-bandgap small molecules," *ACS Applied Materials & Interfaces*, vol. 6, pp. 6537–6544, apr 2014.
- [107] J. Liu, H. Choi, J. Y. Kim, C. Bailey, M. Durstock, and L. Dai, "Highly crystalline and low bandgap donor polymers for efficient polymer solar cells," *Advanced Materials*, vol. 24, pp. 538–542, dec 2011.
- [108] K.-H. Kim, S. Park, H. Yu, H. Kang, I. Song, J. H. Oh, and B. J. Kim, "Determining optimal crystallinity of diketopyrrolopyrrole-based terpolymers for highly efficient polymer solar cells and transistors," *Chemistry of Materials*, vol. 26, pp. 6963–6970, dec 2014.
- [109] Z. Li, X. Xu, W. Zhang, X. Meng, W. Ma, A. Yartsev, O. Inganäs, M. R. Andersson, R. A. J. Janssen, and E. Wang, "High performance all-polymer solar cells by synergistic effects of fine-tuned crystallinity and solvent annealing," *Journal of the American Chemical Society*, vol. 138, pp. 10935–10944, aug 2016.
- [110] W. P. Su, J. R. Schrieffer, and A. J. Heeger, "Solitons in polyacetylene," *Physical Review Letters*, vol. 42, pp. 1698–1701, jun 1979.
- [111] H. Biederman, "RF sputtering of polymers and its potential application," *Vacuum*, vol. 59, no. 2-3, pp. 594–599, 2000.
- [112] O. Kylián, A. Shelemin, P. Solař, P. Pleskunov, D. Nikitin, A. Kuzminova, R. Štefaníková, P. Kúš, M. Cieslar, J. Hanuš, A. Choukourov, and H. Biederman, "Magnetron sputtering of polymeric targets: From thin films to heterogeneous metal/plasma polymer nanoparticles," *Materials*, vol. 12, no. 15, p. 2366, 2019.
- [113] K. Seshan, *Handbook of thin film deposition*. Oxford, United Kingdom Cambridge, MA, United States: William Andrew, an imprint of Elsevier, fourth ed., 2018.
- [114] Y. Yamamura and H. Tawara, "Energy Dependence of Ion-Induced Sputtering Yields from Monatomic Solids at normal Incidence," *Atomic Data and Nuclear Data Tables*, vol. 62, pp. 149–253, mar 1996.

- [115] E. Atanassova, “Thin RF sputtered and thermal ta2o5 on si for high density DRAM application,” *Microelectronics Reliability*, vol. 39, no. 8, pp. 1185–1217, 1999.
- [116] F. M. Li, B. C. Bayer, S. Hofmann, S. P. Speakman, C. Ducati, W. I. Milne, and A. J. Flewitt, “High-density remote plasma sputtering of high-dielectric-constant amorphous hafnium oxide films,” *physica status solidi (b)*, vol. 250, no. 5, pp. 957–967, 2013.
- [117] J. A. Thornton, “Magnetron sputtering: basic physics and application to cylindrical magnetrons,” *Journal of Vacuum Science and Technology*, vol. 15, no. 2, pp. 171–177, 1978.
- [118] P. Kelly and R. Arnell, “Magnetron sputtering: a review of recent developments and applications,” *Vacuum*, vol. 56, no. 3, pp. 159–172, 2000.
- [119] G. Bräuer, B. Szyszka, M. Vergöhl, and R. Bandorf, “Magnetron sputtering – milestones of 30 years,” *Vacuum*, vol. 84, no. 12, pp. 1354–1359, 2010.
- [120] H. Adachi, *Handbook of Sputtering Technology*. Waltham, MA: Elsevier, second ed., 2012.
- [121] A. Jamnig, D. G. Sangiovanni, G. Abadias, and K. Sarakinos, “Atomic-scale diffusion rates during growth of thin metal films on weakly-interacting substrates,” *Scientific Reports*, vol. 9, apr 2019.
- [122] M. Einax, W. Dieterich, and P. Maass, “Cluster growth on surfaces: Densities, size distributions, and morphologies,” *Reviews of Modern Physics*, vol. 85, pp. 921–939, jul 2013.
- [123] R. L. Schwoebel, “Step motion on crystal surfaces. II,” *Journal of Applied Physics*, vol. 40, pp. 614–618, feb 1969.
- [124] J. A. Venables and G. D. T. Spiller, *Nucleation and Growth of Thin Films*. Springer US, 1983.
- [125] L. Rosenthal, A. Filinov, M. Bonitz, V. Zaporojtchenko, and F. Faupel, “Diffusion and growth of metal clusters in nanocomposites: A kinetic monte carlo study,” *Contributions to Plasma Physics*, vol. 51, pp. 971–980, nov 2011.
- [126] G. Ehrlich and F. G. Hudda, “Atomic view of surface self-diffusion: Tungsten on tungsten,” *The Journal of Chemical Physics*, vol. 44, pp. 1039–1049, feb 1966.
- [127] J. A. Thornton, “The microstructure of sputter-deposited coatings,” *Journal of Vacuum Science & Technology A: Vacuum, Surfaces, and Films*, vol. 4, pp. 3059–3065, nov 1986.
- [128] J. Nielsen, *Elements of modern X-ray physics*. Hoboken: Wiley, 2011.

- [129] A. Naudon, D. Babonneau, D. Thiaudière, and S. Lequien, “Grazing-incidence small-angle x-ray scattering applied to the characterization of aggregates in surface regions,” *Physica B: Condensed Matter*, vol. 283, pp. 69–74, jun 2000.
- [130] M. Tolan, *X-ray scattering from soft-matter thin films*. Berlin New York: Springer, 1999.
- [131] Y. Yoneda, “Anomalous surface reflection of X rays,” *Physical Review*, vol. 131, no. 5, pp. 2010–2013, 1963.
- [132] H. Dosch, B. W. Batterman, and D. C. Wack, “Depth-controlled grazing-incidence diffraction of synchrotron x radiation,” *Physical Review Letters*, vol. 56, pp. 1144–1147, mar 1986.
- [133] D. Jean and G. E. Alain, *X-ray and Neutron Reflectivity: Principles and Applications, Lect. Notes Phys. 770*. Springer-Verlag GmbH, Berlin Heidelberg, 2009.
- [134] P. Müller-Buschbaum, “The Active Layer Morphology of Organic Solar Cells Probed with Grazing Incidence Scattering Techniques,” *Advanced Materials*, vol. 26, pp. 7692–7709, 2014.
- [135] G. Renaud, R. Lazzari, and F. Leroy, “Probing surface and interface morphology with Grazing Incidence Small Angle X-Ray Scattering,” *Surface Science Reports*, vol. 64, pp. 255–380, aug 2009.
- [136] S. T. Chourou, A. Sarje, X. S. Li, E. R. Chan, and A. Hexemer, “HipGISAXS: a high-performance computing code for simulating grazing-incidence x-ray scattering data,” *Journal of Applied Crystallography*, vol. 46, pp. 1781–1795, nov 2013.
- [137] G. Pospelov, W. V. Herck, J. Burle, J. M. C. Loaiza, C. Durniak, J. M. Fisher, M. Ganeva, D. Yurov, and J. Wuttke, “BornAgain: software for simulating and fitting grazing-incidence small-angle scattering,” *Journal of Applied Crystallography*, vol. 53, pp. 262–276, feb 2020.
- [138] R. Lazzari, “IsGISAXS : a program for grazing-incidence small-angle X-ray scattering analysis of supported islands,” *Journal of Applied Crystallography*, vol. 35, pp. 406–421, aug 2002.
- [139] P. Müller-Buschbaum, “Grazing incidence small-angle x-ray scattering: an advanced scattering technique for the investigation of nanostructured polymer films,” *Analytical and Bioanalytical Chemistry*, vol. 376, pp. 3–10, mar 2003.
- [140] A. Hexemer and P. Müller-Buschbaum, “Advanced grazing-incidence techniques for modern soft-matter materials analysis,” *IUCrJ*, vol. 2, pp. 106–125, jan 2015.
- [141] F. Leroy, R. Lazzari, and G. Renaud, “Effects of near-neighbor correlations on the diffuse scattering from a one-dimensional paracrystal,” *Acta Crystallographica Section A Foundations of Crystallography*, vol. 60, pp. 565–581, oct 2004.

- [142] M. Schwartzkopf, R. Röhlberger, R. Gehrke, N. Stribeck, and S. V. Roth, “From atoms to layers : In situ gold cluster growth kinetics during sputter deposition,” *Nanoscale*, vol. 5, pp. 5053–5062, 2013.
- [143] Z. Jiang, “GIXSGUI: A MATLAB toolbox for grazing-incidence X-ray scattering data visualization and reduction, and indexing of buried three-dimensional periodic nanostructured films,” *Journal of Applied Crystallography*, vol. 48, pp. 917–926, 2015.
- [144] D. M. Smilgies, “Scherrer grain-size analysis adapted to grazing-incidence scattering with area detectors,” *Journal of Applied Crystallography*, vol. 42, no. 6, pp. 1030–1034, 2009.
- [145] F. J. Giessibl, “Advances in atomic force microscopy,” *Reviews of Modern Physics*, vol. 75, pp. 949–983, jul 2003.
- [146] B. Cappella and G. Dietler, “Force-distance curves by atomic force microscopy,” *Surface Science Reports*, vol. 34, pp. 1–104, jan 1999.
- [147] S. A. C. Gould, K. Burke, and P. K. Hansma, “Simple theory for the atomic-force microscope with a comparison of theoretical and experimental images of graphite,” *Physical Review B*, vol. 40, pp. 5363–5366, sep 1989.
- [148] S. Rützel, S. I. Lee, and A. Raman, “Nonlinear dynamics of atomic-force-microscope probes driven in lennard-jones potentials,” *Proceedings of the Royal Society of London. Series A: Mathematical, Physical and Engineering Sciences*, vol. 459, pp. 1925–1948, aug 2003.
- [149] A. Ikai, “STM and AFM of bio/organic molecules and structures,” *Surface Science Reports*, vol. 26, pp. 261–332, jan 1996.
- [150] D. Nečas and P. Klapetek, “Gwyddion: An open-source software for SPM data analysis,” *Central European Journal of Physics*, vol. 10, no. 1, pp. 181–188, 2012.
- [151] I. Horcas, R. Fernández, J. M. Gómez-Rodríguez, J. Colchero, J. Gómez-Herrero, and A. M. Baro, “WSXM: A software for scanning probe microscopy and a tool for nanotechnology,” *Review of Scientific Instruments*, vol. 78, no. 1, p. 013705, 2007.
- [152] M. Aziz and A. Ismail, *X-Ray Photoelectron Spectroscopy (XPS)*. Elsevier, 2017.
- [153] P. R. Griffiths, “Fourier transform infrared spectrometry,” *Science*, vol. 222, pp. 297–302, oct 1983.
- [154] J. S. Gaffney, N. A. Marley, and D. E. Jones, *Fourier Transform Infrared (FTIR) Spectroscopy*. John Wiley & Sons, Inc., oct 2012.
- [155] J. Reséndiz-Muñoz, M. A. Corona-Rivera, J. L. Fernández-Muñoz, M. Zapata-Torres, A. Márquez-Herrera, and V. M. Ovando-Medina, “Mathematical model of

- Boltzmann's sigmoidal equation applicable to the set-up of the RF-magnetron co-sputtering in thin films deposition of $\text{Ba}_x\text{Sr}_{1-x}\text{TiO}_3$," *Bulletin of Materials Science*, vol. 40, no. 5, pp. 1043–1047, 2017.
- [156] G. Benecke, W. Wagermaier, C. Li, M. Schwartzkopf, G. Flucke, R. Hoerth, I. Zizak, M. Burghammer, E. Metwalli, P. Müller-Buschbaum, M. Trebbin, S. Förster, O. Paris, S. V. Roth, and P. Fratzl, "A customizable software for fast reduction and analysis of large X-ray scattering data sets: applications of the new DPDAK package to small-angle X-ray scattering and grazing-incidence small-angle X-ray scattering," *Journal of Applied Crystallography*, vol. 47, no. 5, pp. 1797–1803, 2014.
- [157] G. Sauerbrey, "Verwendung von schwingquarzen zur wägung dünner schichten und zur mikrowägung," *Zeitschrift für Physik*, vol. 155, pp. 206–222, apr 1959.
- [158] J. Schellenberg and H.-J. Leder, "Syndiotactic polystyrene: Process and applications," *Advances in Polymer Technology*, vol. 25, no. 3, pp. 141–151, 2006.
- [159] S. Cai, B. Zhang, and L. Cremaschi, "Review of moisture behavior and thermal performance of polystyrene insulation in building applications," *Building and Environment*, vol. 123, pp. 50–65, oct 2017.
- [160] R. Abhijith, A. Ashok, and C. Rejeesh, "Sustainable packaging applications from mycelium to substitute polystyrene: a review," *Materials Today: Proceedings*, vol. 5, no. 1, pp. 2139–2145, 2018.
- [161] M. Kaseem, K. Hamad, and Y. G. Ko, "Fabrication and materials properties of polystyrene/carbon nanotube (PS/CNT) composites: A review," *European Polymer Journal*, vol. 79, pp. 36–62, jun 2016.
- [162] M. S. Zafar, "Prosthodontic applications of polymethyl methacrylate (PMMA): An update," *Polymers*, vol. 12, p. 2299, oct 2020.
- [163] S. Zidan, N. Silikas, A. Alhotan, J. Haider, and J. Yates, "Investigating the mechanical properties of ZrO_2 -impregnated PMMA nanocomposite for denture-based applications," *Materials*, vol. 12, p. 1344, apr 2019.
- [164] A. D. Mauro, C. Farrugia, S. Abela, P. Refalo, M. Grech, L. Falqui, V. Privitera, and G. Impellizzeri, "Synthesis of ZnO/PMMA nanocomposite by low-temperature atomic layer deposition for possible photocatalysis applications," *Materials Science in Semiconductor Processing*, vol. 118, p. 105214, nov 2020.
- [165] J. Macutkevic, D. Seliuta, G. Valusis, R. Adomavicius, A. Krotkus, P. Kuzhir, A. Paddubskaya, S. Maksimenko, V. Kuznetsov, I. Mazov, and I. Simonova, "Multi-walled carbon nanotubes/PMMA composites for THz applications," *Diamond and Related Materials*, vol. 25, pp. 13–18, may 2012.

- [166] S. Jung, M. Albariqi, G. Gruntz, T. Al-Hathal, A. Peinado, E. Garcia-Caurel, Y. Nicolas, T. Toupance, Y. Bonnassieux, and G. Horowitz, "A TIPS-TPDO-tetraCN-based n-type organic field-effect transistor with a cross-linked PMMA polymer gate dielectric," *ACS Applied Materials and Interfaces*, vol. 8, pp. 14701–14708, jun 2016.
- [167] B. Philip, J. K. Abraham, A. Chandrasekhar, and V. K. Varadan, "Carbon nanotube/PMMA composite thin films for gas-sensing applications," *Smart Materials and Structures*, vol. 12, pp. 935–939, nov 2003.
- [168] F. Ruffino, V. Torrisi, G. Marletta, and M. G. Grimaldi, "Effects of the embedding kinetics on the surface nano-morphology of nano-grained au and ag films on PS and PMMA layers annealed above the glass transition temperature," *Applied Physics A*, vol. 107, pp. 669–683, mar 2012.
- [169] C. Cummins, A. Bell, and M. Morris, "Creating active device materials for nano-electronics using block copolymer lithography," *Nanomaterials*, vol. 7, p. 304, sep 2017.
- [170] M. Ramanathan, Y.-C. Tseng, K. Ariga, and S. B. Darling, "Emerging trends in metal-containing block copolymers: synthesis, self-assembly, and nanomanufacturing applications," *Journal of Materials Chemistry C*, vol. 1, no. 11, p. 2080, 2013.
- [171] D. J. Lee, G. M. Kumar, P. Ilanchezhian, J.-C. Lee, S. R. Ryu, and T. W. Kang, "Vertically aligned ZnCdS nanowire arrays/p3ht heterojunctions for solar cell applications," *Journal of Colloid and Interface Science*, vol. 487, pp. 73–79, feb 2017.
- [172] M. Girtan, "On the stability of the electrical and photoelectrical properties of p3ht and p3ht:PCBM blends thin films," *Organic Electronics*, vol. 14, pp. 200–205, jan 2013.
- [173] E. L. Lim, C. C. Yap, M. A. M. Teridi, C. H. Teh, A. R. bin Mohd Yusoff, and M. H. H. Jumali, "A review of recent plasmonic nanoparticles incorporated p3ht:PCBM organic thin film solar cells," *Organic Electronics*, vol. 36, pp. 12–28, sep 2016.
- [174] B. Jana, S. Bhattacharyya, and A. Patra, "Conjugated polymer p3ht–au hybrid nanostructures for enhancing photocatalytic activity," *Physical Chemistry Chemical Physics*, vol. 17, no. 23, pp. 15392–15399, 2015.
- [175] S. Brix, O. A. Melville, N. T. Boileau, and B. H. Lessard, "The influence of air and temperature on the performance of PBDB-t and p3ht in organic thin film transistors," *Journal of Materials Chemistry C*, vol. 6, no. 44, pp. 11972–11979, 2018.

- [176] N. Y. Nia, M. Bonomo, M. Zendehdel, E. Lamanna, M. M. H. Desoky, B. Paci, F. Zurlo, A. Generosi, C. Barolo, G. Viscardi, P. Quagliotto, and A. D. Carlo, "Impact of p3ht regioregularity and molecular weight on the efficiency and stability of perovskite solar cells," *ACS Sustainable Chemistry and Engineering*, vol. 9, pp. 5061–5073, apr 2021.
- [177] S. Lee, H. Kim, and Y. Kim, "Hole injection role of p-type conjugated polymer nanolayers in phosphorescent organic light-emitting devices," *Electronics*, vol. 10, p. 2283, sep 2021.
- [178] A. Gharbi, R. Tiron, P. Pimenta Barros, M. Argoud, I. Servin, X. Chevalier, C. Nicolet, and C. Navarro, "PMMA removal options by wet development in PS- b -PMMA block copolymer for nanolithographic mask fabrication ," *Journal of Vacuum Science Technology B*, vol. 33, no. 5, p. 051602, 2015.
- [179] T. Xu, J. Stevens, J. A. Villa, J. T. Goldbach, K. W. Guarini, C. T. Black, C. J. Hawker, and T. P. Russell, "Block copolymer surface reconstruction: A reversible route to nanoporous films," *Advanced Functional Materials*, vol. 13, no. 9, pp. 698–702, 2003.
- [180] C. Zhang, D. Zhao, D. Gu, H. Kim, T. Ling, Y.-K. R. Wu, and L. J. Guo, "An ultrathin, smooth, and low-loss al-doped ag film and its application as a transparent electrode in organic photovoltaics," *Advanced Materials*, vol. 26, pp. 5696–5701, jun 2014.
- [181] S. D. Yambem, K.-S. Liao, and S. A. Curran, "Flexible ag electrode for use in organic photovoltaics," *Solar Energy Materials and Solar Cells*, jul 2011.
- [182] J.-D. Yang, I.-W. Ok, J.-M. Cho, D.-H. Park, W.-S. Shin, K.-G. Kim, S.-J. Moon, K.-H. Yoo, and W.-K. Choi, "Ag interlayered transparent conducting electrode for photovoltaic cells," *Japanese Journal of Applied Physics*, vol. 51, p. 10NE07, oct 2012.
- [183] M. Bockstaller, R. Mickiewicz, and E. Thomas, "Block copolymer nanocomposites: Perspectives for tailored functional materials," *Advanced Materials*, vol. 17, pp. 1331–1349, may 2005.
- [184] M. Karttunen, P. Ruuskanen, V. Pitkänen, and W. M. Albers, "Electrically conductive metal polymer nanocomposites for electronics applications," *Journal of Electronic Materials*, vol. 37, pp. 951–954, apr 2008.
- [185] S. Park, B. Kim, A. Cirpan, and T. P. Russell, "Preparation of metallic line patterns from functional block copolymers," *small*, vol. 5, pp. 1343–1348, jun 2009.
- [186] M. López-Heras, I. G. Theodorou, B. F. Leo, M. P. Ryan, and A. E. Porter, "Towards understanding the antibacterial activity of ag nanoparticles: electron microscopy in

- the analysis of the materials-biology interface in the lung,” *Environmental Science: Nano*, vol. 2, no. 4, pp. 312–326, 2015.
- [187] S. Deshmukh, S. Patil, S. Mullani, and S. Delekar, “Silver nanoparticles as an effective disinfectant: A review,” *Materials Science and Engineering: C*, vol. 97, pp. 954–965, apr 2019.
- [188] C. Zhao, Y. Zhu, Y. Su, Z. Guan, A. Chen, X. Ji, X. Gui, R. Xiang, and Z. Tang, “Tailoring plasmon resonances in aluminium nanoparticle arrays fabricated using anodic aluminium oxide,” *Advanced Optical Materials*, vol. 3, pp. 248–256, nov 2014.
- [189] S. Mandal, J. Wang, R. E. Winans, L. Jensen, and A. Sen, “Quantum size effects in the optical properties of ligand stabilized aluminum nanoclusters,” *Journal of Physical Chemistry C*, vol. 117, pp. 6741–6746, mar 2013.
- [190] T. R. Andersen, N. A. Cooling, F. Almyahi, A. S. Hart, N. C. Nicolaidis, K. Feron, M. Noori, B. Vaughan, M. J. Griffith, W. J. Belcher, and P. C. Dastoor, “Fully roll-to-roll prepared organic solar cells in normal geometry with a sputter-coated aluminium top-electrode,” *Solar Energy Materials and Solar Cells*, vol. 149, pp. 103–109, may 2016.
- [191] B. Pint, “The role of chemical composition on the oxidation performance of aluminium coatings,” *Surface and Coatings Technology*, vol. 188-189, pp. 71–78, 2004.
- [192] F. Ostermann, *Anwendungstechnologie Aluminium*. Springer Berlin Heidelberg, 2014.
- [193] S. V. Roth, M. Burghammer, C. Riekel, P. Müller-Buschbaum, A. Diethert, P. Panagiotou, and H. Walter, “Self-assembled gradient nanoparticle-polymer multilayers investigated by an advanced characterization method: microbeam grazing incidence x-ray scattering,” *Applied Physics Letters*, vol. 82, no. 12, pp. 1935–1937, 2003.
- [194] S. V. Roth, H. Walter, M. Burghammer, C. Riekel, B. Lengeler, C. Schroer, M. Kuhlmann, T. Walther, A. Sehrbrock, R. Domnick, and P. Müller-Buschbaum, “Combinatorial investigation of the isolated nanoparticle to coalescent layer transition in a gradient sputtered gold nanoparticle layer on top of polystyrene,” *Applied Physics Letters*, vol. 88, no. 2, pp. 1–3, 2006.
- [195] P. Müller-Buschbaum, “Influence of surface cleaning on dewetting of thin polystyrene films,” *The European Physical Journal E*, vol. 12, pp. 443–448, nov 2003.
- [196] D. W. Schubert and T. Dunkel, “Spin coating from a molecular point of view: its concentration regimes, influence of molar mass and distribution,” *Materials Research Innovations*, vol. 7, pp. 314–321, oct 2003.

- [197] D. W. Schubert, "Spin coating as a method for polymer molecular weight determination," *Polymer Bulletin*, vol. 38, pp. 177–184, feb 1997.
- [198] C. Sinturel, M. Vayer, M. Morris, and M. A. Hillmyer, "Solvent vapor annealing of block polymer thin films," *Macromolecules*, vol. 46, pp. 5399–5415, jun 2013.
- [199] A. V. Berezkin, F. Jung, D. Posselt, D.-M. Smilgies, and C. M. Papadakis, "In situ tracking of composition and morphology of a diblock copolymer film with GISAXS during exchange of solvent vapors at elevated temperatures," *Advanced Functional Materials*, vol. 28, p. 1706226, mar 2018.
- [200] J. Zhang, D. Posselt, A. Sepe, X. Shen, J. Perlich, D.-M. Smilgies, and C. M. Papadakis, "Structural evolution of perpendicular lamellae in diblock copolymer thin films during solvent vapor treatment investigated by grazing-incidence small-angle x-ray scattering," *Macromolecular Rapid Communications*, vol. 34, pp. 1289–1295, jul 2013.
- [201] Y. Xuan, J. Peng, L. Cui, H. Wang, B. Li, and Y. Han, "Morphology development of ultrathin symmetric diblock copolymer film via solvent vapor treatment," *Macromolecules*, vol. 37, pp. 7301–7307, aug 2004.
- [202] J. Peng, D. H. Kim, W. Knoll, Y. Xuan, B. Li, and Y. Han, "Morphologies in solvent-annealed thin films of symmetric diblock copolymer," *Journal of Chemical Physics*, vol. 125, p. 064702, aug 2006.
- [203] Y. Wang, X. Hong, B. Liu, C. Ma, and C. Zhang, "Two-dimensional ordering in block copolymer monolayer thin films upon selective solvent annealing," *Macromolecules*, vol. 41, pp. 5799–5808, jul 2008.
- [204] R. Döhrmann, S. Botta, A. Buffet, G. Santoro, K. Schlage, M. Schwartzkopf, S. Bommel, J. F. H. Risch, R. Mannweiler, S. Brunner, E. Metwalli, P. Müller-Buschbaum, and S. V. Roth, "A new highly automated sputter equipment for in situ investigation of deposition processes with synchrotron radiation," *The Review of scientific instruments*, vol. 84, no. 4, p. 043901, 2013.
- [205] M. Schwartzkopf, A. Hinz, O. Polonskyi, T. Strunskus, F. C. Löhner, V. Körstgens, P. Müller-Buschbaum, F. Faupel, and S. V. Roth, "Role of Sputter Deposition Rate in Tailoring Nanogranular Gold Structures on Polymer Surfaces," *ACS Applied Materials and Interfaces*, vol. 9, no. 6, pp. 5629–5637, 2017.
- [206] M. Gensch, "In situ conductivity measurement on metallized block copolymer," Master's thesis, Universität Hamburg, 2017.
- [207] U. Guler and R. Turan, "Effect of particle properties and light polarization on the plasmonic resonances in metallic nanoparticles," *Optics Express*, vol. 18, no. 16, p. 17322, 2010.

- [208] K. Jain, M. Klosner, M. Zemel, and S. Raghunandan, “Flexible electronics and displays: High-resolution, roll-to-roll, projection lithography and photoablation processing technologies for high-throughput production,” *Proceedings of the IEEE*, vol. 93, no. 8, pp. 1500–1510, 2005.
- [209] G. Bauer, J. Hassmann, H. Walter, J. Haglmüller, C. Mayer, and T. Schalkhammer, “Resonant nanocluster technology—from optical coding and high quality security features to biochips,” *Nanotechnology*, vol. 14, no. 12, pp. 1289–1311, 2003.
- [210] C. Park, J. Yoon, and E. L. Thomas, “Enabling nanotechnology with self assembled block copolymer patterns,” *Polymer*, vol. 44, no. 22, pp. 6725–6760, 2003.
- [211] Y. Lin, J. A. Lim, Q. Wei, S. C. B. Mannsfeld, A. L. Briseno, and J. J. Watkins, “Co-operative assembly of hydrogen-bonded diblock copolythiophene/fullerene blends for photovoltaic devices with well-defined morphologies and enhanced stability,” *Chemistry of Materials*, vol. 24, no. 3, pp. 622–632, 2012.
- [212] L. Xue, J. Zhang, and Y. Han, “Phase separation induced ordered patterns in thin polymer blend films,” *Progress in Polymer Science*, vol. 37, no. 4, pp. 564–594, 2012.
- [213] S. Ham, C. Shin, E. Kim, D. Y. Ryu, U. Jeong, T. P. Russell, and C. J. Hawker, “Microdomain Orientation of PS-b-PMMA by Controlled Interfacial Interactions,” *Macromolecules*, vol. 41, no. 17, pp. 6431–6437, 2008.
- [214] F. Ruffino, V. Torrisi, G. Marletta, and M. G. Grimaldi, “Growth morphology of nanoscale sputter-deposited Au films on amorphous soft polymeric substrates,” *Applied Physics A: Materials Science and Processing*, vol. 103, pp. 939–949, 2011.
- [215] W. A. Lopes, “Nonequilibrium self-assembly of metals on diblock copolymer templates,” *Physical Review E*, vol. 65, p. 031606, feb 2002.
- [216] E. Metwalli, V. Körstgens, K. Schlage, R. Meier, G. Kaune, A. Buffet, S. Couet, S. V. Roth, R. Röhlberger, and P. Müller-Buschbaum, “Cobalt Nanoparticles Growth on a Block Copolymer Thin Film : A Time-Resolved GISAXS Study,” *Langmuir*, vol. 29, no. 21, pp. 6331–6340, 2013.
- [217] E. Metwalli, S. Couet, K. Schlage, R. Röhlberger, V. Körstgens, M. Ruderer, W. Wang, G. Kaune, S. V. Roth, and P. Müller-Buschbaum, “In situ GISAXS investigation of gold sputtering onto a polymer template,” *Langmuir: the ACS journal of surfaces and colloids*, vol. 24, pp. 4265–72, apr 2008.
- [218] M. Schwartzkopf, S.-J. Wöhnert, V. Waclawek, N. Carstens, A. Rothkirch, J. Rubeck, M. Gensch, J. Drewes, O. Polonskyi, T. Strunskus, A. M. Hinz, S. J. Schaper, V. Körstgens, P. Müller-Buschbaum, F. Faupel, and S. V. Roth, “Real-time insight into nanostructure evolution during the rapid formation of ultra-thin gold layers on polymers,” *Nanoscale Horizons*, vol. 6, no. 2, pp. 132–138, 2021.

- [219] H. Kang, S.-S. Kim, S. I. Yoo, and B.-H. Sohn, "Dichroic plasmon superstructures of au nanorods over macroscopic areas via directed self-assemblies of diblock copolymers," *Advanced Materials Interfaces*, vol. 6, p. 1901257, sep 2019.
- [220] S. Gopinath, N. N. Adarsh, P. R. Nair, and S. Mathew, "Shape-memory polymer nanocomposites of poly(ϵ -caprolactone) with the polystyrene-block-polybutadiene-block-polystyrene-triblockcopolymer encapsulated with metal oxides," *ACS Omega*, vol. 6, no. 9, pp. 6261–6273, 2021.
- [221] Z. Ding, M. Ding, C. Gao, C. Boyer, and W. Zhang, "In situ synthesis of coil–coil diblock copolymer nanotubes and tubular ag/polymer nanocomposites by RAFT dispersion polymerization in poly(ethylene glycol)," *Macromolecules*, vol. 50, no. 19, pp. 7593–7602, 2017.
- [222] S. Mahieu, K. Van Aeken, D. Depla, D. Smeets, and A. Vantomme, "Dependence of the sticking coefficient of sputtered atoms on the target-substrate distance," *Journal of Physics D: Applied Physics*, vol. 41, no. 15, pp. 1–4, 2008.
- [223] L. Bachmann and J. J. Shin, "Measurement of the sticking coefficients of silver and gold in an ultrahigh vacuum," *Journal of Applied Physics*, vol. 37, no. 1, pp. 242–246, 1966.
- [224] B. Emmoth and H. Bergsaker, "Sticking of sputtered particles to different surfaces," *Nuclear Instruments and Methods in Physics Research Section B: Beam Interactions with Materials and Atoms*, vol. 33, no. 1-4, pp. 435–437, 1988.
- [225] O. Belaidi, M. Adjim, T. Bouchaour, and U. Maschke, "FT-IR and FT-Raman spectra of 2-hydroxyethyl methacrylate – a conformational and vibrational analysis," *Spectrochimica Acta Part A: Molecular and Biomolecular Spectroscopy*, vol. 148, pp. 396–404, sep 2015.
- [226] S. Yu, G. Santoro, K. Sarkar, B. Dicke, P. Wessels, S. Bommel, R. Döhrmann, J. Perlich, M. Kuhlmann, E. Metwalli, J. F. H. Risch, M. Schwartzkopf, M. Drescher, P. Müller-Buschbaum, and S. V. Roth, "Formation of Al Nanostructures on Alq₃: An in Situ Grazing Incidence Small Angle X-ray Scattering Study during Radio Frequency Sputter Deposition," *The Journal of Physical Chemistry Letters*, vol. 4, no. 18, pp. 3170–3175, 2013.
- [227] S. Grachev, M. D. Grazia, E. Barthel, E. Søndergård, and R. Lazzari, "Real-time monitoring of nanoparticle film growth at high deposition rate with optical spectroscopy of plasmon resonances," *Journal of Physics D: Applied Physics*, vol. 46, no. 37, p. 375305, 2013.
- [228] Z. Li, C.-C. Chueh, and A. K.-Y. Jen, "Recent advances in molecular design of

- functional conjugated polymers for high-performance polymer solar cells,” *Progress in Polymer Science*, vol. 99, p. 101175, 2019.
- [229] W. Hou, Y. Xiao, G. Han, and J.-Y. Lin, “The applications of polymers in solar cells: A review,” *Polymers*, vol. 11, no. 1, p. 143, 2019.
- [230] Y. Wu, Y. Liu, T. Emrick, and T. P. Russell, “Polymer design to promote low work function surfaces in organic electronics,” *Progress in Polymer Science*, vol. 103, p. 101222, 2020.
- [231] X. Guo, M. Baumgarten, and K. Müllen, “Designing π -conjugated polymers for organic electronics,” *Progress in Polymer Science*, vol. 38, no. 12, pp. 1832–1908, 2013.
- [232] B. Nketia-Yawson and Y.-Y. Noh, “Organic thin film transistor with conjugated polymers for highly sensitive gas sensors,” *Macromolecular Research*, vol. 25, no. 6, pp. 489–495, 2017.
- [233] L. Wang, M. Liu, C. Gao, L. Ma, and D. Cui, “A pH-, thermo-, and glucose-, triple-responsive hydrogels: Synthesis and controlled drug delivery,” *Reactive and Functional Polymers*, vol. 70, no. 3, pp. 159–167, 2010.
- [234] A. Rösler, G. W. Vandermeulen, and H.-A. Klok, “Advanced drug delivery devices via self-assembly of amphiphilic block copolymers,” *Advanced Drug Delivery Reviews*, vol. 64, pp. 270–279, 2012.
- [235] L. Britnell, R. M. Ribeiro, A. Eckmann, R. Jalil, B. D. Belle, A. Mishchenko, Y. Kim, R. V. Gorbachev, T. Georgiou, S. V. Morozov, A. N. Grigorenko, A. K. Geim, C. Casiraghi, A. H. C. Neto, and K. S. Novoselov, “Strong Light-Matter Interactions Thin Films,” *Science*, vol. 340, pp. 1311–1315, June 2013.
- [236] H.-C. Liao, C.-S. Tsao, T.-H. Lin, M.-H. Jao, C.-M. Chuang, S.-Y. Chang, Y.-C. Huang, Y.-T. Shao, C.-Y. Chen, C.-J. Su, U.-S. Jeng, Y.-F. Chen, and W.-F. Su, “Nanoparticle-Tuned Self-Organization of a Bulk Heterojunction Hybrid Solar Cell with Enhanced Performance,” *ACS Nano*, vol. 6, pp. 1657–1666, feb 2012.
- [237] L. Cojocar, C. Olivier, T. Toupance, E. Sellier, and L. Hirsch, “Size and shape fine-tuning of SnO₂ nanoparticles for highly efficient and stable dye-sensitized solar cells,” *Journal of Materials Chemistry A*, vol. 1, no. 44, pp. 13789–13799, 2013.
- [238] J. Wang, B. Tian, and E. Sahlin, “Integrated Electrophoresis Chips/Amperometric Detection with Sputtered Gold Working Electrodes,” *Analytical Chemistry*, vol. 71, pp. 3901–3904, sep 1999.
- [239] S. Sutthana, N. Hongstith, and S. Choopun, “AZO/ag/AZO multilayer films prepared by DC magnetron sputtering for dye-sensitized solar cell application,” *Current Applied Physics*, vol. 10, pp. 813–816, may 2010.

- [240] S. Zenoozi, S. Agbolaghi, M. Nazari, and F. Abbasi, “Thermal and optical properties of nano/micro single crystals and nanofibers obtained from semiconductive-dielectric poly(3-hexylthiophene) block copolymers,” *Materials Science in Semiconductor Processing*, vol. 64, pp. 85–94, jun 2017.
- [241] C. A. Schneider, W. S. Rasband, and K. W. Eliceiri, “NIH Image to ImageJ: 25 years of image analysis,” *Nature Methods*, vol. 9, no. 7, pp. 671–675, 2012.
- [242] F. Ferrarese Lupi, T. J. Giammaria, G. Seguíni, M. Laus, P. Dubček, B. Pivac, S. Bernstorff, and M. Perego, “GISAXS Analysis of the In-Depth Morphology of Thick PS-b-PMMA Films,” *ACS Applied Materials and Interfaces*, vol. 9, no. 12, pp. 11054–11063, 2017.
- [243] M. W. Knight, N. S. King, L. Liu, H. O. Everitt, P. Nordlander, and N. J. Halas, “Aluminum for plasmonics,” *ACS Nano*, vol. 8, pp. 834–840, dec 2013.
- [244] W. Li, K. Ren, and J. Zhou, “Aluminum-based localized surface plasmon resonance for biosensing,” *TrAC Trends in Analytical Chemistry*, vol. 80, pp. 486–494, jun 2016.
- [245] G. H. Chan, J. Zhao, G. C. Schatz, and R. P. V. Duyne, “Localized surface plasmon resonance spectroscopy of triangular aluminum nanoparticles,” *The Journal of Physical Chemistry C*, vol. 112, pp. 13958–13963, aug 2008.
- [246] J. Liu, B. Cankurtaran, G. McCredie, M. J. Ford, L. Wiczorek, and M. B. Cortie, “Investigation of the optical properties of hollow aluminium ‘nano-caps’,” *Nanotechnology*, vol. 16, pp. 3023–3028, oct 2005.
- [247] M. B. Ross and G. C. Schatz, “Radiative effects in plasmonic aluminum and silver nanospheres and nanorods,” *Journal of Physics D: Applied Physics*, vol. 48, p. 184004, dec 2014.
- [248] Y. Ekinici, H. H. Solak, and J. F. Löffler, “Plasmon resonances of aluminum nanoparticles and nanorods,” *Journal of Applied Physics*, vol. 104, p. 083107, oct 2008.
- [249] Z. Jiang, X. Chen, X. Lin, X. Jia, J. Wang, L. Pan, S. Huang, F. Zhu, and Z. Sun, “Amazing stable open-circuit voltage in perovskite solar cells using AgAl alloy electrode,” *Solar Energy Materials and Solar Cells*, vol. 146, pp. 35–43, 2016.
- [250] A. Khalil, Z. Ahmed, F. Touati, and M. Masmoudi, “Review on organic solar cells,” *13th International Multi-Conference on Systems, Signals and Devices, SSD 2016*, pp. 342–353, 2016.
- [251] O. Polonskyi, O. Kylián, M. Drábik, J. Kousal, P. Solař, A. Artemenko, J. Čechvala, A. Choukourov, D. Slavínská, and H. Biederman, “Deposition of Al nanoparticles and their nanocomposites using a gas aggregation cluster source,” *Journal of Materials Science*, vol. 49, no. 9, pp. 3352–3360, 2014.

- [252] Y. Zhou, H. Cheun, W. J. Potscavage, C. Fuentes-Hernandez, S. J. Kim, and B. Kippelen, "Inverted organic solar cells with ITO electrodes modified with an ultra-thin Al₂O₃ buffer layer deposited by atomic layer deposition," *Journal of Materials Chemistry*, vol. 20, no. 29, pp. 6189–6194, 2010.
- [253] H. R. Yeom, J. Heo, G. H. Kim, S. J. Ko, S. Song, Y. Jo, D. S. Kim, B. Walker, and J. Y. Kim, "Optimal top electrodes for inverted polymer solar cells," *Physical Chemistry Chemical Physics*, vol. 17, no. 3, pp. 2152–2159, 2015.
- [254] G. Kaune, E. Metwalli, R. Meier, V. Körstgens, K. Schlage, S. Couet, R. Röhlberger, S. V. Roth, and P. Müller-Buschbaum, "Growth and Morphology of Sputtered Aluminum Thin Films on P3HT Surfaces," *ACS Applied Materials & Interfaces*, vol. 3, pp. 1055–1062, apr 2011.
- [255] M. Bou, J. Martin, T. L. Mogne, and L. Vovelle, "Chemistry of the interface between aluminium and polyethyleneterephthalate by XPS," *Applied Surface Science*, vol. 47, pp. 149–161, feb 1991.
- [256] C. Hinnen, D. Imbert, J. Siffre, and P. Marcus, "An in situ XPS study of sputter-deposited aluminium thin films on graphite," *Applied Surface Science*, vol. 78, pp. 219–231, jul 1994.
- [257] B. R. Strohmeier, "Characterization of an activated alumina claus catalyst by XPS," *Surface Science Spectra*, vol. 3, pp. 141–146, apr 1994.

List of publications

Publications related to the thesis

- M. Gensch, M. Schwartzkopf, W. Ohm, C. J. Brett, P. Pandit, S. K. Vayalil, L. Bießmann, L. P. Kreuzer, J. Drewes, O. Polonskyi, T. Strunskus, F. Faupel, A. Stierle, P. Müller-Buschbaum, and S. V. Roth, “Correlating Nanostructure, Optical and Electronic Properties of Nanogranular Silver Layers during Polymer-Template-Assisted Sputter Deposition”, *ACS Applied Materials and Interfaces*, vol. 11, no. 32, pp. 29416–29426, 2019
- M. Gensch, M. Schwartzkopf, C. J. Brett, S. J. Schaper, L. P. Kreuzer, N. Li, W. Chen, S. Liang, J. Drewes, O. Polonskyi, T. Strunskus, F. Faupel, P. Müller-Buschbaum, and S. V. Roth, “Selective Silver Nanocluster Metallization on Conjugated Diblock Copolymer Templates for Sensing and Photovoltaic Applications”, *ACS Applied Nano Materials*, vol. 4, no. 4, pp. 4245–4255, 2021
- M. Gensch, M. Schwartzkopf, C. J. Brett, S. J. Schaper, N. Li, W. Chen, S. Liang, J. Drewes, O. Polonskyi, T. Strunskus, F. Faupel, P. Müller-Buschbaum, and S. V. Roth, “Correlating Optical Reflectance with the Topology of Aluminum Nanocluster Layers Growing on Partially Conjugated Diblock Copolymer Templates”, *ACS Applied Materials and Interfaces*, vol. 13, no. 47, pp. 56663–56673, 2021

Further publications

- C. J. Brett, N. Mittal, W. Ohm, M. Gensch, L. P. Kreuzer, V. Körstgens, M. Mansson, H. Frielinghaus, P. Müller-Buschbaum, L. D. Söderberg, and S. V. Roth, “Water-Induced Structural Rearrangements on the Nanoscale in Ultrathin Nanocellulose Films”, *Macromolecules* vol. 52, pp. 4721, 2019
- Q. Chen, C. J. Brett, A. Chumakov, M. Gensch, M. Schwartzkopf, V. Körstgens, L. D. Söderberg, A. Plech, P. Zhang, P. Müller-Buschbaum, and S. V. Roth, “Layer-by-Layer Spray-Coating of Cellulose Nanofibrils and Silver Nanoparticles for Hydrophilic Interfaces”, *ACS Appl. Nano Mater.* vol. 4, pp. 503, 2021

- M. Schwartzkopf, S.-J. Wöhnert, V. Waclawek, N. Carstens, A. Rothkirch, J. Rubeck, Marc Gensch, J. Drewes, O. Polonskyi, T. Strunskus, A. M. Hinz, S. J. Schaper, V. Körstgens, P. Müller-Buschbaum, F. Faupel, and S. V. Roth, “Real-time insight into nanostructure evolution during the rapid formation of ultra-thin gold layers on polymers”, *Nanoscale Horizons* vol. 6, pp. 132, 2021
- L. O. Akinsinde, T. E. Glier, M. Schwartzkopf, M. Betker, M. Nissen, M. Witte, S. Scheitz, C. Nweze, B. Grimm-Lebsanft, M. Gensch, A. Chumakov, I. Baev, U. Schürmann, T. Dankwort, F. Fischer, M. Martins, S. V. Roth, L. Kienle, M. Rübhausen, “Surface characterization and resistance changes of silver-nanowire networks upon atmospheric plasma treatment”, *Appl. Surf. Sci.* vol. 550, pp. 149362, 2021
- S. Liang, W. Chen, S. Yin, S. J. Schaper, R. Guo, J. Drewes, N. Carstens, T. Strunskus, M. Gensch, M. Schwartzkopf, F. Faupel, S. V. Roth, Y. Cheng, P. Müller-Buschbaum, “Tailoring the optical properties of sputter-deposited gold nanostructures on nanostructured titanium dioxide templates based on in situ grazing-incidence small-angle x-ray scattering determined growth laws”, *ACS Appl. Mater. Interfaces* vol. 13, pp. 14728, 2021
- A. Chumakov, C. J. Brett, K. Gordeyeva, D. Menzel, L. O. Akinsinde, M. Gensch, M. Schwartzkopf, W. Cao, S. Yin, M. A. Reus, M. A. Rübhausen, P. Müller-Buschbaum, D. Söderberg, S. V. Roth, “Sprayed Nanometer-Thick Hard-Magnetic Coatings with Strong Perpendicular Anisotropy for Data Storage Applications”, *ACS Appl. Nano Mater.* vol. 5, pp. 8741, 2022

Scientific reports

- M. Gensch, M. Schwartzkopf, C. J. Brett, S. J. Schaper, L. P. Kreuzer, N. Li, W. Chen, S. Liang, J. Drewes, O. Polonskyi, T. Strunskus, F. Faupel, P. Müller-Buschbaum, and S. V. Roth: “In situ GISAXS investigation of silver sputter deposition on conjugated block copolymer thin films”, E13 Annual Report, 2018
- M. Gensch, M. Schwartzkopf, C. J. Brett, S. J. Schaper, L. P. Kreuzer, N. Li, W. Chen, S. Liang, J. Drewes, O. Polonskyi, T. Strunskus, F. Faupel, P. Müller-Buschbaum, and S. V. Roth: “Correlating Nanostructure, Optical and Electronic Properties of Nanogranular Silver Layers during Polymer-Template Assisted Sputter Deposition”, E13 Annual Report, 2019

- M. Gensch, M. Schwartzkopf, C. J. Brett, S. J. Schaper, N. Li, W. Chen, S. Liang, J. Drewes, O. Polonskyi, T. Strunskus, F. Faupel, P. Müller-Buschbaum, and S. V. Roth: “In situ GISAXS investigation of aluminium sputter deposition on conjugated diblock copolymer thin films”, E13 Annual Report, 2020
- M. Gensch, M. Schwartzkopf, C. J. Brett, S. J. Schaper, N. Li, W. Chen, S. Liang, J. Drewes, O. Polonskyi, T. Strunskus, F. Faupel, P. Müller-Buschbaum, and S. V. Roth: “Investigation of the selective wetting of noble metals on PLA-*b*-P3HT”, Lehrstuhl für Funktionelle Materialien”, E13 Annual Report, 2021

Conference talks

- M. Gensch, M. Schwartzkopf, W. Ohm, C. J. Brett, P. Pandit, S. K. Vayalil, L. Bießmann, L. P. Kreuzer, J. Drewes, O. Polonskyi, T. Strunskus, F. Faupel, A. Stierle, P. Müller-Buschbaum, and S. V. Roth: “Optoelectronic properties of metal clusters on polymer thin films during sputter deposition”, DPG Frühjahrstagung, Berlin (Germany), 11 - 16 Mar 2018
- M. Gensch, M. Schwartzkopf, W. Ohm, C. J. Brett, P. Pandit, S. K. Vayalil, L. Bießmann, L. P. Kreuzer, J. Drewes, O. Polonskyi, T. Strunskus, F. Faupel, A. Stierle, P. Müller-Buschbaum, and S. V. Roth, “Optoelectronic properties of metal clusters on polymer thin films during sputter deposition”, 4th German-Czech Workshop on Nanomaterials, Budweis (Czech Republic), 10 - 11 May 2018
- M. Gensch, M. Schwartzkopf, W. Ohm, C. J. Brett, P. Pandit, S. K. Vayalil, L. Bießmann, L. P. Kreuzer, J. Drewes, O. Polonskyi, T. Strunskus, F. Faupel, A. Stierle, P. Müller-Buschbaum, and S. V. Roth, “Optoelectronic properties of metal clusters on polymer thin films during sputter deposition”, The 7th Synchrotron Radiation in Polymer Science (SRPS) conference, Gyeongju (South Korea), 4 - 7 Sep 2018
- M. Gensch, M. Schwartzkopf, C. J. Brett, S. J. Schaper, L. P. Kreuzer, N. Li, W. Chen, S. Liang, J. Drewes, O. Polonskyi, T. Strunskus, F. Faupel, P. Müller-Buschbaum, and S. V. Roth, “Selective Silver Nanocluster Metallization on Conjugated Diblock Copolymer Templates for Sensing and Photovoltaic Applications”, DPG Frühjahrstagung, Regensburg (Germany), 31 Mar - 4 Apr 2019

- M. Gensch, M. Schwartzkopf, C. J. Brett, S. J. Schaper, L. P. Kreuzer, N. Li, W. Chen, S. Liang, J. Drewes, O. Polonskyi, T. Strunskus, F. Faupel, P. Müller-Buschbaum, and S. V. Roth, “Sputter deposition of Ag and Al on nanostructured PMMA-b-P3HT copolymer thin films”, Petra III Beamline Review, Hamburg (Germany), Feb 2021

Conference poster presentations

- M. Gensch, M. Schwartzkopf, C. J. Brett, S. J. Schaper, L. P. Kreuzer, N. Li, W. Chen, S. Liang, J. Drewes, O. Polonskyi, T. Strunskus, F. Faupel, P. Müller-Buschbaum, and S. V. Roth, Nanostructured diblock copolymers as templates for metal sputter deposition”, DESY Photon Science Users Meeting, Hamburg (Germany), Jan 2018
- M. Gensch, M. Schwartzkopf, C. J. Brett, S. J. Schaper, L. P. Kreuzer, N. Li, W. Chen, S. Liang, J. Drewes, O. Polonskyi, T. Strunskus, F. Faupel, P. Müller-Buschbaum, and S. V. Roth, “Nanostructured diblock copolymers as templates for metal sputter deposition”, From Matter to Materials and Life (MML) Workshop, Dresden, 13 - 15 Feb 2019
- M. Gensch, M. Schwartzkopf, C. J. Brett, S. J. Schaper, L. P. Kreuzer, N. Li, W. Chen, S. Liang, J. Drewes, O. Polonskyi, T. Strunskus, F. Faupel, P. Müller-Buschbaum, and S. V. Roth, “Sputter deposition of Ag on nanostructured PMMA-b-P3HT and PS-b-PMMA copolymer thin films”, MSE Interdisciplinary Winter School: Food and Energy, 18 - 22 Feb 2019
- M. Gensch, M. Schwartzkopf, C. J. Brett, S. J. Schaper, L. P. Kreuzer, N. Li, W. Chen, S. Liang, J. Drewes, O. Polonskyi, T. Strunskus, F. Faupel, P. Müller-Buschbaum, and S. V. Roth, “Selective Silver Nanocluster Metallization on Conjugated Diblock Copolymer Templates for Sensing and Photovoltaic Applications”, 4th Internal Biennial Science Meeting of the MLZ, Grainau (Germany), 24 - 27 Jun 2019
- M. Gensch, M. Schwartzkopf, C. J. Brett, S. J. Schaper, L. P. Kreuzer, N. Li, W. Chen, S. Liang, J. Drewes, O. Polonskyi, T. Strunskus, F. Faupel, P. Müller-Buschbaum, and S. V. Roth, “Sputter deposition of Ag on nanostructured PMMA-b-P3HT and PS-b-PMMA copolymer thin films”, Nano- and materials science (NanoMat day 2020), Hamburg (Online, Germany), 6 Feb 2020

-
- M. Gensch, M. Schwartzkopf, C. J. Brett, S. J. Schaper, L. P. Kreuzer, N. Li, W. Chen, S. Liang, J. Drewes, O. Polonskyi, T. Strunskus, F. Faupel, P. Müller-Buschbaum, and S. V. Roth, “Sputter deposition of Ag on nanostructured PMMA-b-P3HT copolymer thin films”, DPG Frühjahrstagung, Online (Germany), 11 - 16 Mar 2020
 - M. Gensch, M. Schwartzkopf, C. J. Brett, S. J. Schaper, L. P. Kreuzer, N. Li, W. Chen, S. Liang, J. Drewes, O. Polonskyi, T. Strunskus, F. Faupel, P. Müller-Buschbaum, and S. V. Roth, “Sputter deposition of Ag on nanostructured PMMA-b-P3HT and PS-b-PMMA copolymer thin films”, 10th Energy Colloquium of the Munich School of Engineering, Online (Germany), 30 Jul 2020
 - M. Gensch, M. Schwartzkopf, C. J. Brett, S. J. Schaper, L. P. Kreuzer, N. Li, W. Chen, S. Liang, J. Drewes, O. Polonskyi, T. Strunskus, F. Faupel, P. Müller-Buschbaum, and S. V. Roth, “Sputter deposition of silver on nanostructured PMMA-b-P3HT copolymer thin films”, MLZ User Meeting, Online (Germany), 8 - 10 Dez 2020

Acknowledgments

My time as a PhD student at the TUM in collaboration with DESY was shaped by great experiences in diverse areas. I have to thank many people, who were involved in the work and who I would like to acknowledge. First, I would like to thank my two supervisors Prof. Dr. Peter Müller-Buschbaum and Adj. Prof. Stephan Roth for allowing me to join the Chair of Functional Materials and the P03 DESY beamline Team. They helped me to get the best out of me and my PhD topic of the metallization of conjugated diblock copolymer templates. I am very grateful that I was able to present my topic at conferences, workshops and meetings and even out of Europe. It was a great experience to accompany them to south korea and present my work there.

This work could only be done by a lot of collaborations as with the group of Franz Faupel from the CAU in Kiel. Therefore I would like to thank him very much. Further I would like to thank all the members of his group with which I worked together of the last years. Especially I would like to thank Jonas Drewes and Thomas Strunskus, who were always a great support and became friends to me. Also I would like to thank Oleksandr Polonskyi and Niko Carstens from the group for their great technical support.

During my work at the Chair for Functional Materials and at the P03 beamline at DESY I got to know so many nice people and many of them became also friends. I hope everyone I met gets the right thanks from me for their incredible help and support during my work.

Now I would like to thank my group in Munich for their big support for the guy who is in their group but abroad in the north of Germany in Hamburg. So many people here I have to thank because of the always very nice talks besides the PhD and fun that we had when I visited Munich or when they came to Hamburg. Here I would like to thank especially Lucas Kreuzer, Lorenz Bießmann, Franziska Löhner, Sebastian Grott, Florian Jung, Manuel Reus, Dominik Schwaiger, Johannes Schlipf, Christian Weindl, Tobias Widmann, Anna-Lena Oechsle, Nuri Hohn, Nian Li, Shanshan Yin, Wei Chen, Simon Jakob Schaper, Jenny Lebert, Oliver Filonik, Mihael Čorić, Nitin Saxena, Lennart Reb, Julian Heger, Christina Geiger, Xinyu Jiang, Apostolos Vagias and Volker Körstgens. All the people of E13 supported me so much and we had so much fun together. I look

back and remember very well the trip to the MLZ Summer School in Grainau in 2019, where we were hiking, swimming and had so much nice discussions.

Between all the scientific meetings and discussions there are people who makes this even possible and they do so much work for the scientists to help us make the best work we can. Thank you Christina Newiger, who was always there for me in Hamburg at DESY and supported me with all the problems we faced. Thank you Carola Kappauf and Marion Waletzki, for all the help and the support with the administrative and bureaucratic tasks, even tough I was not often around, everything was perfectly communicated to me and helped me to feel more integrated into the E13 group in Munich. Especially I remember one of my first visits to Munich to the stark beer festival in Munich, where Marion told me a lot about the group and helped me to introduce me to everybody.

I would like to thank My summer students at DESY for their help supporting my work: Thank you Kateryna Chunikhina and Letizia Ferbel.

I would especially like to thank my group in Hamburg. Here, I have to thank so many people along the way we faced together over the last years: Jan Rubeck, Matthias Schwartzkopf, Calvin Brett, Sven-Jannick Wöhnert, Andre Chumakov, Wiebke Ohm, Constantin Harder, Yusuf Bulut, Marie Betker, Qing Chen, Elisabeth Erbes, Susann Frenzke, Pallavi Pandit, Vivian Waclawek thank you all so much.

Finally, I would like to thank my family for all their support. My mother who I can always talk to about everything or my father who supports me in everything I started. Furthermore my brothers which when we became older also grow to my deepest friends. I want to thank my grandparents who helped me grow up and always hold our family together. I would like to thank my aunts, uncles and my cousin. I want also to thank all my friends, who supported me during this time. My biggest thanks is to my wife who always supported me and listen to me even tough I was stressed out.